INFORMATION TO USERS

Calibration of photon and electron beams with an extrapolation chamber

Corey E. Zankowski

Physics Department
McGill University, Montreal
August 1997

A thesis submitted to the Faculty of Graduate Studies in Research in partial

fulfillment of the requirements for the degree of Doctor of Philosophy

Canada

Abstract

A variable air-volume, parallel-plate, extrapolation chamber forming an integral part of a Solid-Water^{TM} phantom was built to determine the absorbed dose in Solid-Water^{TM} directly. The sensitive air-volume of the extrapolation chamber is controlled through the movement of the chamber piston by means of a micrometer mounted to the phantom body. The relative displacement of the piston is monitored by a mechanical distance travel indicator with a precision on the order of 0.002 mm. Irradiations were carried out with cobalt-60 gamma rays, x-ray beams ranging from 4 to 18 MV, and electron beams between 6 and 22 MeV. The absorbed dose at a given depth in Solid-Water^{TM} is proportional to the ionization gradient measured in the Bragg–Gray cavity region with a Solid-Water^{TM} embedded extrapolation chamber. Measured charge is corrected for ion recombination and ion diffusion in the chamber air volume according to a comprehensive model for charge loss in an ionization chamber. The discrepancies between doses determined with our uncalibrated phantom-embedded extrapolation chamber and doses obtained with calibrated Farmer-type cylindrical ionization chambers following the AAPM-TG21 and AAPM-TG25 dosimetry protocols are less than 1% for photon and electron beams at all clinical megavoltage energies. Uncalibrated extrapolation chambers thus offer a simple and practical alternative to other techniques used in output measurements of megavoltage photon and electron beams.

Résumé

Une chambre à extrapolation avec deux électrodes parallèles à séparation variable a été construite intégralement dans un phantôme Solid-Water^{TM}. Cette chambre peut déterminer directement la dose absorbée par le phantôme. La séparation des électrodes est contrôlée par le mouvement du piston à chambre à l'aide d'un micromètre attaché au corps du phantôme. La position relative du piston est mesurée par un indicateur mécanique de distance avec une précision de l'ordre de 0.002 mm. La chambre a été irradiée par des faisceaux de rayons gamma produits par le cobalt-60, des rayons x dont l'énergie varie de 4 à 18 MV, et des électrons d'énergie variante de 6 à 22 MeV. La dose à une profondeur donnée dans le Solid-Water^{TM} est proportionelle au gradient d'ionization mesuré par la chambre à extrapolation PEEC sous les conditions de cavité requises à l'application de la théorie Bragg–Gray. La charge mesurée a été corrigée pour la perte due à la recombinaison et la diffusion des ions selon le modèle proposé par Böhm. Les differences entre les doses mesurées par notre chambre non-calibrée et les chambres d'ionisation calibrées de type Farmer sont de l'ordre de 1% pour les faisceaux de photons et d'électrons à haute énergie. Par conséquent, les chambres d'ionisation à extrapolation non-calibrées représentent une alternative simple et pratique aux techniques présentement utilisées pour la détermination de la dose absorbée par les faisceaux de photons et d'électrons à hautes énergies.

Original Contribution

Several reports on the use of extrapolation chambers for absolute beam output calibrations appeared in the literature since the 1950s. However, the approach has never been considered seriously, mainly because the chambers used in the past were not water-equivalent and fluence corrections were required when calculating the dose in water from the extrapolation chamber measurements. The design of our phantom-embedded extrapolation chamber is an improvement over typical extrapolation chambers in that the chamber is built as an integral part of the dosimetric phantom. The integration of the chamber and the dosimetric phantom permits the direct measurement of dose absorbed in the phantom without having to incorporate fluence corrections accounting for the difference between the chamber wall material and the dosimetric phantom.

Investigation of the ionization gradient as a function of the relative electrode separation in order to test the validity of the Bragg–Gray cavity conditions is also an original contribution to extrapolation chamber dosimetry. In the region where the Bragg–Gray cavity conditions are satisfied, the measured ionization gradient stabilizes as the electrode separation is varied making a reliable determination of the ionization gradient possible.

A method for the determination of the collection efficiency which includes the effects of general recombination, initial recombination, and diffusion loss, in addition to charge multiplication in the chamber volume has been described in detail. Initial recombination, diffusion loss, and charge multiplication have an observable effect on charge measurements at chamber potentials typically used for clinical dosimetry. We demonstrate this fact, and develop a technique to separate the parameters of initial recombination, general recombination, and diffusion loss from the non-dosimetric contribution of charge

iv

multiplication and extract the correct saturation charge, and hence the chamber collection efficiency, from measured data.

We are the first group to attempt to measure the output of a clinical proton beam with an extrapolation chamber. Given the excellent performance of our phantom-embedded extrapolation chamber in high energy photon and electron beams, we are confident that with further study, a phantom-embedded extrapolation chamber can be used reliably for the calibration of proton beams as well.

Acknowledgments

Table of Contents

CHAPTER 5   Ion collection in parallel-plate ionization chambers 108

CHAPTER 6   Experimental apparatus and techniques . . 135

CHAPTER 1

Introduction

Radiotherapy, also referred to as radiation therapy or radiation oncology, is a clinical specialty which incorporates ionizing radiation in the treatment of malignant disease. The aim of radiotherapy is to deliver a precisely measured dose of radiation to a well-defined tumour volume with minimal damage to the surrounding healthy tissue.

Radiation dosimetry is concerned with an accurate quantification of ionizing radiation used in the treatment of cancer, and thus is an important aspect of radiotherapy. Quantitative measurements of ionizing radiation are made in order to establish or to use numerical relationships between measured quantities and biological effects produced by the radiation. These effects can be expressed in terms of a series of complex interactions between the radiation field and the medium. It is thus necessary to investigate the nature of ionizing radiations and their interactions with matter before an adequate attempt can be made to quantify the effect of ionizing radiation on a specific medium such as tissue.

I. Ionizing radiations

When a beam of high-energy radiation traverses a medium, some of its energy is transferred to the medium through various interactions. If the amount of energy imparted to the medium exceeds a minimum level of a few electron-volts (eV), molecular bonds in

the medium can be broken or atoms may be ionized, ultimately resulting in the production of ion pairs in the medium. Radiation energetic enough to cause the dissociation of matter into positive and negative ions is called *ionizing radiation*.

The ICRU[1] (International Commission on Radiation Units and Measurement) has defined two classes of ionizing radiations according to the different processes through which charged and uncharged radiations interact with matter:

(i) *Directly ionizing radiations*, consisting of fast charged particles (electrons, protons, α-particles, heavy ions) which transfer their kinetic energy to matter directly through numerous small Coulomb interactions that occur along the track of the particle, and

(ii) *Indirectly ionizing radiations*, consisting of uncharged radiations (photons, neutrons) which first transfer their energy to charged particles in the medium. The resulting energetic charged particles subsequently deposit their energy in matter directly through numerous Coulomb interactions.

The transfer of energy to matter from directly ionizing radiation is a continuous process, while the energy transfer from indirectly ionizing radiation is a two-step process. The action of ionizing radiations on matter is shown schematically in Fig. 1.1. The passage of ionizing radiation initially results in the dissociation of the medium into free electrons and positively charged ions (atoms missing one or more electrons). An atom A may have an electron knocked out of one its outer shells by ionizing radiation and the process can be described by the following equation:

$$A \rightarrow A^+ + e^- . \qquad (1.1)$$

Almost immediately, the free electron produced in the initial interaction is captured by

```
                        ┌─────────────────────┐
                        │ Ionizing radiations │
                        └─────────────────────┘
                           /               \
                          /                 \
          ┌──────────────────────┐   ┌──────────────────────┐
          │  indirectly ionizing │   │   directly ionizing  │
          │     ( x, γ, n )      │   │   ( e⁻, e⁺, p, α)    │
          └──────────────────────┘   └──────────────────────┘
                     │                          │
                     ▼                          │
          ┌──────────────────────┐              │
          │   directly ionizing  │              │
          │       ( e⁻, p )      │              │
          └──────────────────────┘              │
                     │                          │
                     ▼                          ▼
              ┌───────────────────────────────────┐
              │   free electrons + positive ions  │
              └───────────────────────────────────┘
                               │
                               ▼
          ┌───────────────────────────────────────────┐
          │  negative ions, positive ions, free radicals │
          └───────────────────────────────────────────┘
                               │
                               ▼
                  ┌───────────────────────┐
                  │  *biological damage*  │
                  └───────────────────────┘
```
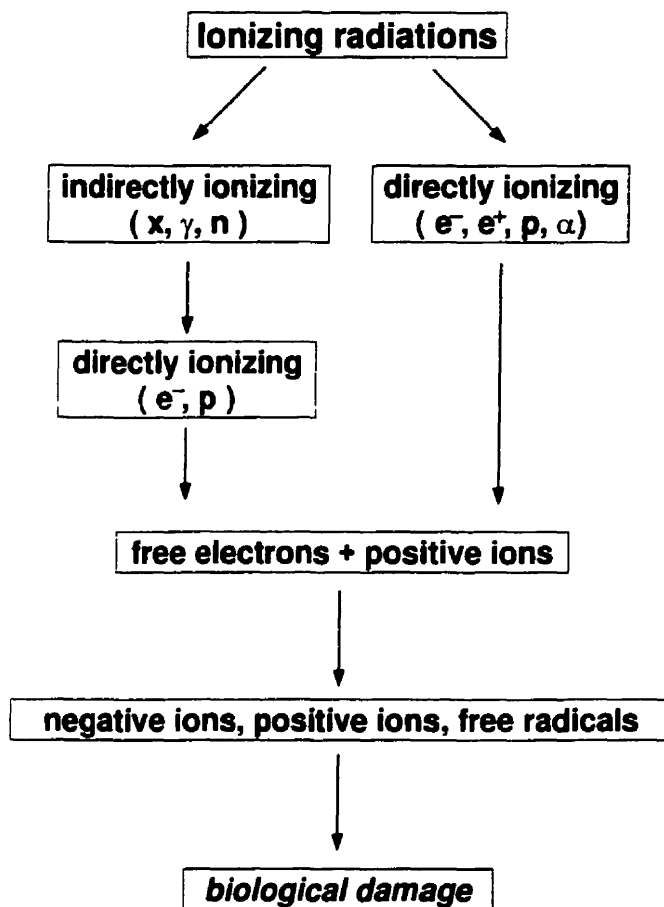
FIGURE 1.1. Illustration of the energy deposition in matter by directly and indirectly ionizing radiations. The chart emphasizes that in order to describe the action of indirectly ionizing radiations in matter, an additional step is required as compared to directly ionizing radiations.

some electronegative molecule B in the medium to form a negative ion:

$$B + e^- = B^- . \qquad (1.2)$$
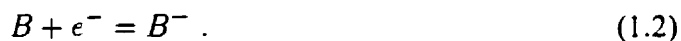
The ions, A^+ and B^-, are called an ion pair. Ion pairs have a lifetime of the order of 10^{-10} s.

The biological damage is produced by the ion pairs or solvated electrons which react with the medium to produce *free radicals*. Free radicals have a lifetime on the order of 10^{-5} s which is very much longer than that of ion pairs. A free radical does not

carry an excess *charge* but carries excess *energy* and is highly reactive because of the presence of an unpaired electron in its outer shell. It is helpful to illustrate the production of free radicals in water with a specific example. Suppose a molecule of water interacts with ionizing radiation and loses an orbital electron in a manner which can be expressed mathematically as

$$H_2O \rightarrow H_2O^+ + e^- \; . \tag{1.3}$$

The ionized water molecule may then react with another water molecule to form the highly reactive hydroxyl radical $OH^\bullet$ according to the following equation:

$$H_2O^+ + H_2O \rightarrow H_3O^+ + OH^\bullet \; . \tag{1.4}$$
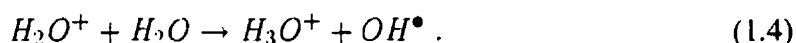
In practice, the situation is much more complicated than this, but Eq. (1.4) is sufficient to describe the general process by which ionizing radiation produces biological damage. In general, a molecule CD is acted upon by directly ionizing radiation to produce a positive ion CD^+ and an electron:

$$CD \rightarrow CD^+ + e^- \; . \tag{1.5}$$
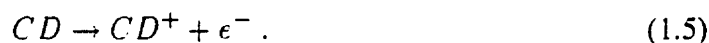
The positive ion CD^+ breaks up or interacts with the medium to form an ion and a free radical:

$$CD^+ \rightarrow C^+ + D^\bullet \; . \tag{1.6}$$

The positive ion C^+ carries the excess charge while the radical $D^\bullet$ has the excess energy and is highly reactive because of the unpaired electron. The free radical and, to a lesser extent, the ion may then produce a chain of events which precipitate chemical changes in the medium.

Biological systems are particularly susceptible to damage by ionizing radiations. The absorption from ionizing radiation of a relatively small amount of energy ($\sim$4 J/kg) distributed throughout the human body is likely to result in death, although the same amount of heat energy is capable of raising the overall body temperature by only 0.001°C. The lethal effect of such a small amount of ionizing energy exists because ionizing radiations have the ability to deposit energy in local concentrations sufficiently high to kill a cell directly or to form highly reactive chemical species, such as free radicals, in the water which constitutes the bulk of the biological material. The highly reactive free radicals then migrate through the cell disrupting chemical reactions and molecular structures necessary for cell survival.

The ionizing properties of high-energy radiations can be exploited in the treatment of malignant disease. Malignant cells, unlike healthy cells, lack a mechanism for regulating cell growth and proliferation, thus they cease to function in their normal biological capacity and grow uncontrollably into cell masses which eventually inhibit the function of their host organ. Exposure of cells to ionizing radiation can damage cellular DNA and consequently can destroy the cells' ability to reproduce. Cells which attempt to divide under these circumstances will die. Healthy biological cells, which undergo normal cell cycles, allow enough time for the repair of damage incurred by the radiation before attempting cell division. In contrast, malignant cells experience accelerated cell division and do not allow adequate time for the repair of damaged DNA, hence malignant cells are preferentially killed by ionizing radiation. The methods for the treatment of malignant tumours with radiation are numerous and excellent review of current radiobiological knowledge and techniques can be found in the literature.[2, 3]

Sources of ionizing radiation used in medicine are classified into *continuous* and *pulsed* radiation:

(i)   *Continuous radiation* is produced naturally by radioisotopes which decay at a constant rate. Some low-energy x-ray therapy machines which use a constant potential to accelerate a steady stream of electrons from the cathode to the anode target also produce continuous beams of bremsstrahlung photons.

(ii)   *Pulsed radiation.* Some x-ray therapy machines accelerate electrons to sufficiently high energy that lengthy exposure to electron bombardment can damage the target. For this reason the electrons and the subsequent bremsstrahlung spectrum are delivered in short bursts. For MeV therapy machines commonly used in radiotherapy, such as medical linear accelerators (linacs), betatrons and cyclotrons, the charged particle accelerating process results in pulsed beams of photons, electrons, or other particle beams.

The distinction between continuous and pulsed radiations is based not on the ability of either type of beam to ionize the medium but rather on the difference in the relative amount of ion recombination which occurs in the two kinds of beams. Ion recombination will be discussed in detail in Chapter 5.

II.   Radiation dosimetry techniques

Several techniques have been developed to determine the dose absorbed by a medium exposed to a given source of ionizing radiation. These techniques are divided into two main groups: *absolute dosimetry* and *relative dosimetry*. Absolute dosimetry measures the absorbed dose deposited in a sensitive volume without requiring calibration in a known radiation field, while relative dosimetry requires calibration of detector response in a known radiation field.

There are many types of relative dosimeters, of which standard ionization cham-

bers, solid-state detectors, film and thermoluminescent detectors are the most common in radiation dosimetry. Currently, there are only three accepted absolute dosimetry techniques of varying degrees of absoluteness. In decreasing order of absoluteness, these are calorimetry, chemical dosimetry, and free-air ionization chamber dosimetry. In this thesis we present a detailed study of a phantom-embedded extrapolation chamber which could also be considered an absolute dosimeter equal in absoluteness to the free-air ionization chamber.

II.A. Calorimetry

Suitably designed calorimeters have the fundamental merit that they measure energy deposition directly. This constitutes a major advantage over other dosimetric techniques which infer the absorbed dose from measurements of secondary processes. The design and composition of a calorimeter is influenced and often greatly limited by features of the energy absorption processes.

In calorimetry, the absorbed dose is determined by measuring the change in temperature of the medium after being exposed to a radiation source. Thermistors, devices whose electrical resistance varies with temperature (usually 5% per degree), typically serve as the temperature measuring instrument. Thermistors used in radiation dosimetry are often the size of a pinhead and have resistances on the order of 10^3 to 10^5 ohms.

The temperature rise per unit dose absorbed by a material depends on the specific-heat c_p of the material which is expressed in J/kg °C. For a sensitive volume of mass m, containing a material with specific-heat c_p and thermal defect δ_t, that absorbs an amount of energy E, the temperature increase of the medium will be

$$\Delta T = \left(\frac{E}{m}\right)\frac{(1-\delta_t)}{c_p} = D\frac{(1-\delta_t)}{c_p} . \qquad (1.7)$$

in which D is the absorbed dose in the sensitive volume. Rearranging terms will permit

the calculation of the absorbed dose as a function of the increase in temperature of the sensitive volume,

$$D = \frac{\Delta T \, c_p}{(1 - \delta_t)}.$$ (1.8)

The thermal defect, if any, is the fraction of E that goes into chemical reactions and does not appear as heat.

Since the specific heat of water is 10^3 cal/kg °C, 1 Gy of radiation produces a temperature rise ΔT of

$$\Delta T = 1 \, \frac{J}{kg} \times \frac{1}{4.18} \frac{cal}{J} \times 10^{-3} \frac{kg}{cal} \, °C = 2.39 \times 10^{-4} \, °C.$$

The small temperature change induces a small change in the resistance of the thermistor which can be measured precisely using a carefully designed Wheatstone bridge.

If the specific-heat of the core is not known to a sufficiently high degree of precision, then Eq. (1.7) may not provide an adequate solution for absolute dosimetry. In this case, a known amount of electrical energy E_h can be dissipated in the core of the calorimeter and the corresponding temperature rise ΔT_h recorded. The energy absorbed from irradiation E_r will then be related to the temperature rise of the core during irradiation ΔT_r by the simple relationship,

$$E_r = E_h \frac{\Delta T_r}{\Delta T_h}.$$ (1.9)

The measurement of temperature rise comes the closest of any dosimetric technique to direct measurement of the absorbed dose, granting calorimetry the highest degree of absoluteness. Almost any material can be employed as the detector sensitive volume, making calorimeters versatile. As well, the response of calorimeters is independent of the dose rate and calorimeters work equally well with photon, electron, neutron or α-particle beams, and are stable against radiation damage at high dose rates.

Historically, the use of calorimetry for the measurement of ionizing radiations has been rather limited, mainly because ionizing radiations impart a very small amount of energy to the medium, requiring that the calorimeter be extremely sensitive. Additionally, calorimetric apparatus is normally complex, bulky, and not commercially available, and requires long periods of time to reach thermal stability. Consequently, calorimetry is normally restricted to standards laboratories or to sophisticated research applications.

II.B.   Chemical dosimetry

Chemical dosimetry is concerned with relating a quantitative chemical change in an appropriate medium to the absorbed dose. The most appropriate medium for medical purposes normally consists of a chemical substance in aqueous solution owing to the tissue equivalence of water. Chemical dosimeters currently in use include Fricke dosimeters and, more recently, BANG-gel dosimeters. Of these two dosimeters, only Fricke is capable of absolute dosimetry, while BANG-gels are used for relative dosimetry.

Most aqueous dosimeters are dilute, therefore, it can be assumed that the radiation interacts with water to produce chemically active species, such as free radicals like $OH^\bullet$, or ion pairs like H^+ and OH^-, close to the particle track. After a short time, diffusion processes tend to homogenize the spatial distribution of the reactive species throughout the medium, and the species interact chemically throughout the solution to produce a measurable product X.

The *radiation chemical yield*, $G(X)$ describes the number of molecules of X produced per joule of energy absorbed (mol/J). The absorbed dose D can be determined by measurement of the quantity of X produced during exposure to radiation:

$$D = \frac{\Delta M}{\rho G(X)},$$ (1.10)

where ΔM (mol/l) is the change in molar concentration of the product X due to irradiation

and ρ is the solution density (1 g/cm^3 = 1 kg/l). Equation (1.10) assumes that $G(X)$ applies throughout the entire range ΔM.

The most common chemical dosimeter currently in use is the Fricke ferrous sulfate dosimeter. It has a linear dose response curve in the range from 40 to 400 Gy and is extendable down to 4 Gy. The Fricke dosimeter consists of a solution containing ferrous (Fe^{2+}) ions which are converted into ferric (Fe^{3+}) ions in the presence of ionizing radiations.

The quantity of ferric ions produced during irradiation can be measured by chemical titration methods which determine ΔM directly. A more practical method is based on spectrophotometry in which a laser beam is shone through a small irradiated sample of the solution and the optical transmission is compared to the transmission of a similar but unirradiated sample. The ratio of transmitted light intensity through the irradiated and unirradiated sample is

$$\frac{I}{I_0} = 10^{-\Delta(OD)} ,$$

where $\Delta(OD)$ is the corresponding increase in optical density given by

$$\Delta(OD) = \epsilon l \Delta M , \qquad\qquad (1.12)$$

in which ϵ is the molar extinction coefficient for Fe^{3+}, and l is the optical width of the sample. Substituting Eq. (1.12) into Eq. (1.10) gives

$$D = \frac{\Delta(OD)}{\epsilon l \rho G(Fe^{+3})} , \qquad\qquad (1.13)$$

where typically,

$$\epsilon = 2187 \; l/mol \text{ at } 304 \text{ nm and } 25°C,$$

$$l = 1 \text{ cm},$$

$$G(Fe^{3+}) = 1.607 \times 10^{-6} \text{ mol/J for } {}^{60}Co \; \gamma - rays,$$

$$\rho = 1.024 \text{ kg/l at } 25°C.$$

Being composed mainly of water gives aqueous chemical dosimeters the advantage of tissue-equivalence as well as the ability to have any shape desired. The primary disadvantages of chemical dosimetry are that the chemical solutions are very expensive and difficult to prepare, $G(X)$ is sensitive to the temperature of solution during irradiation and during the readout phase, and often these solutions are toxic. Furthermore, normally $G(X)$ is not known to better than 2% accuracy.

II.C. Free-air ionization chamber dosimetry

One way to determine the absorbed dose at a point of interest is to determine the *exposure* in air at that point and then to calculate the dose in air from this by applying the following equation:

$$D_{air} = X \cdot \overline{W}_{air} \tag{1.14}$$

where $X = dQ/dm$ is the exposure and $\overline{W}_{air}$ (33.97 eV/ion pair) is the mean energy required for ionizing radiation to produce an ion pair in air.[4] The ICRU[5] defines exposure as "the quotient of dQ by dm, where the value of dQ is the absolute value of the total charge of the ions of one sign produced in air when all the electrons (negatrons and positrons) liberated by photons in air of mass dm are completely stopped in air." This definition of exposure requires the measurement of the total ionization produced by energetic electrons arising from photon interactions with a known mass of air.
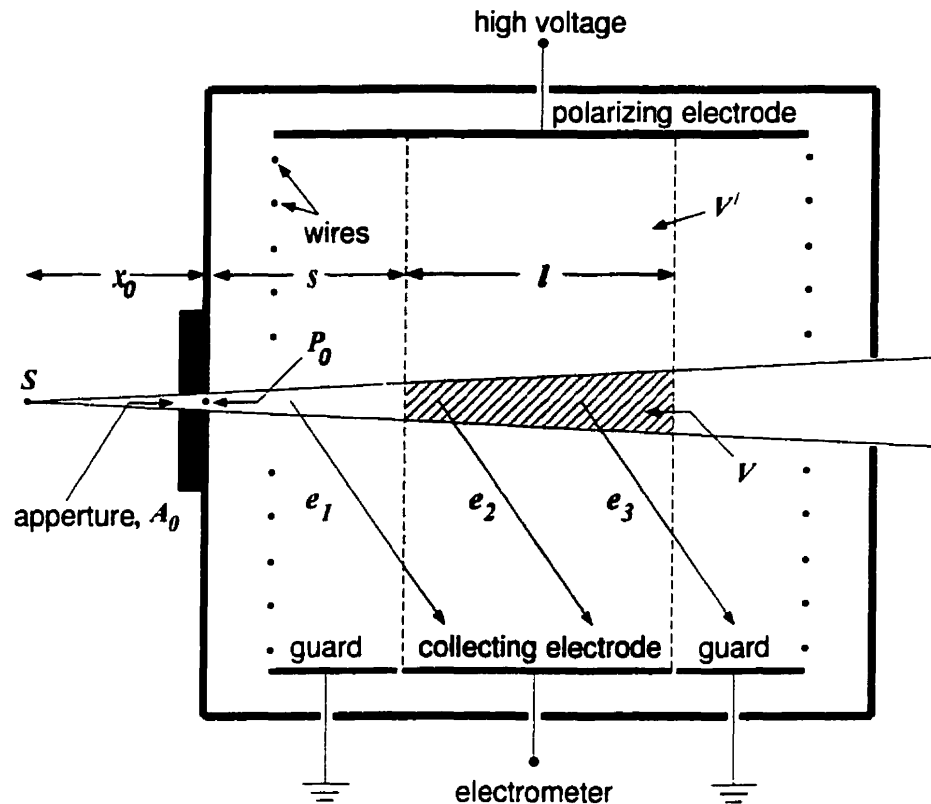
FIGURE 1.2. Schematic diagram of a free-air ionization chamber illustrating the relationship between the charge collecting volume V' and the ideal volume V where secondary electrons are produced for collection (e_2). The number of electrons produced in V and escape collection in V' (e_3) is exactly balanced by electrons produced outside of V (e_1) and enter V' for collection.

The free-air ionization chamber is specially designed to measure the exposure in air and relies on the establishment of charged particle equilibrium to satisfy the ICRU definition of exposure. Figure 1.2 is a schematic diagram of a free-air ionization chamber designed by Wyckoff and Attix.[6] The chamber is shielded from scattered photons and stray sources of radiation by a lead container and the entrance diaphragm of the chamber is aligned with the central axis of the x-ray beam and has a cross section of area A_0. Axial point P_0 is the location where the exposure is referenced; consequently, P_0 is the point at which cavity chambers are centered for calibration with the free-air ionization chamber.

The photon beam enters the free-air ion chamber through the aperture A_o and intersects the charge collecting volume V' defining a volume V that is common to both V' and the volume of air occupied by the beam itself. The definition of exposure implies that we wish to measure only the ionization in air due to secondary electrons produced in V. Some electrons (e_2) are generated in V and never leave the collecting volume V' and thus satisfy the constraints of the definition, *i.e.*, only ionization produced by secondary electrons originating in V must be collected. However, it is difficult to separate and measure the ionization caused exclusively by secondary electrons originating in V because some of these electrons follow paths which take them out of the charge collecting volume V' (e_3). Hence some of the secondary electrons produced in V ionize the air outside of V' and generate ions that are not measured by the collecting electrode. Furthermore, some secondary electrons not produced in V may cross into V' (e_1) and subsequently produce ions that are collected. The lateral dimensions of the detector, therefore, are chosen to ensure that charged particle equilibrium exists throughout V', *i.e.*, all components of the free-air ionization chamber, including the polarizing, collecting, and guard electrodes, and the walls of the lead box are located at a distance far enough from the boundaries of V that they cannot be reached by electrons produced within V.

The existence of charged particle equilibrium guarantees that the number of secondary electrons that are produced in V and escape V' is exactly balanced by electrons that are produced outside of V and enter V'. This implies that the amount of ionization produced in V' is equal to the amount of ionization resulting from secondary electrons originating in V. Thus, on the basis of charged particle equilibrium, it is possible to segregate and measure the ionization produced by electrons originating in a known volume of air, and thereby determine the exposure in accordance with the ICRU definition.

Referring to Fig. 1.2, we see that the aperture of area A_o is located a distance

13

x_o from the x-ray source S. A disc-shaped element of air of thickness dx located in the plane of the aperture has a mass of $dm_o = \rho A_o dx$. A photon beam with energy fluence ψ_o is incident on the mass element dm_o containing the point P_o. The electrons resulting from interactions within dm_o when allowed to dissipate all of their kinetic energy in air will produce a charge of either sign equal to

$$dQ_o = \frac{\psi_o}{W_{air}} \left(\frac{\mu_{ab}}{\rho} \right)_{air} dm_o = K_o dm$$

$$= K_o \rho A_o dx . \tag{1.15}$$

where $(\mu_{ab}/\rho)_{air}$ is the mass energy-absorption coefficient for air (see Chapter 2, Section III.H).

If we now consider a second mass element of air dm, located a distance x from the source and lying inside the volume V, then

$$dm = \rho A dx = \rho A_o \left(\frac{x}{x_o} \right)^2 dx . \tag{1.16}$$

The photon energy fluence $\psi(x)$ at this point is related to the fluence at the aperture ψ_o by the inverse-square law and exponential attenuation of the primary beam

$$\psi(x) = \psi_o \left(\frac{x_o}{x} \right)^2 e^{-\mu(x-x_o)} . \tag{1.17}$$

The charge dQ produced by secondary electrons originating in dm can be found by combining Eqs. (1.16) and (1.17) as follows:

$$dQ = \frac{\psi(x)}{W_{air}} \left(\frac{\mu_{ab}}{\rho} \right)_{air} dm = K_o e^{-\mu(x-x_o)} \left(\frac{x}{x_o} \right)^2 \rho A_o \left(\frac{x_o}{x} \right)^2 dx$$

$$= K_o e^{-\mu(x-x_o)} \rho A_o dx . \tag{1.18}$$

The total charge produced by electrons set in motion within V can be found by integrating Eq. (1.18) between $x_o + s$ and $x_o + s + l$ where s is the distance from the aperture to the boundary of the collecting volume V' and l is the width of the collecting electrode, *i.e.*, the width of V'. Thus, the total charge is given by

$$Q = K_o \rho A_o e^{\mu x_0} \int_{x_o + s}^{x_o + s + l} e^{-\mu x} dx$$

$$= K_o \rho A_o \left(\frac{e^{\mu s}}{\mu} \right) \left[1 - e^{-\mu l} \right]$$

$$\approx K_o \rho A_o \left(\frac{e^{\mu s}}{\mu} \right) [1 - (1 - \mu l)] = K_o \rho A_o l e^{-\mu s} . \tag{1.19}$$

Consider the mass M_c of the cylindrical volume $A_o l$ where $M_c = \rho A_o l$, then $Q/M_c = K_o e^{-\mu s}$ and, recalling Eq. (1.15), the exposure $X_o = dQ_o/dm_o$ at point P_o is determined from the measured exposure Q/M_c using

$$X_o = \frac{dQ_o}{dm_o} = \frac{Q}{M_c} e^{\mu s} . \tag{1.20}$$

Thus the exposure at P_o where a cavity detector is to be calibrated is the same as the exposure measured in the free-air ionization chamber corrected for attenuation of the photon beam in air.

Standard free-air ionization chambers are large and lack mobility making them impractical for use outside of a standards laboratory. To get an idea of the size of such chambers, consider that the range in air of electrons set in motion by monoenergetic photons of energy 3 MeV is 1.5 m. Thus the polarizing, collecting, and guard electrodes must be separated by a distance of over 3 m, and the length of the lead shielding-box should be over 4 m. A thickness of air 1.5 m in length will attenuate a 3 MeV photon

beam by more than 5%, rendering the free-air ionization chamber unsatisfactory for photon beams with energy in excess of 3 MeV.

II.D. Phantom-embedded extrapolation chamber dosimetry

Radiotherapy clinics most commonly determine the output of photon and electron machines used in radiotherapy with parallel-plate or cylindrical thimble chambers following one of several national or international protocols (*e.g.*, ICRU[7, 8], AAPM-TG21[9], AAPM-TG25[10], *etc.*). These protocols are based on standard Bragg-Gray[11, 12] or Spencer-Attix[13] cavity theories which provide linear relationships between the dose D_{med} to a point in the medium and the ratio Q/m, where Q is the ionization charge collected in the mass m of the gas inside the chamber cavity.

Unlike the charge Q which is easily measured with a high degree of accuracy, the effective mass of the gas in the cavity is difficult to determine. Instead, ionization chambers are normally taken to national standards laboratories where they are given a calibration factor. The geometry and composition of the chamber as well as the type of radiation source influence the ionization chamber calibration factor.

According to the Spencer-Attix[13] cavity theory, the dose to the medium D_{med} can be found by measuring the ionization Q in a small cavity of air of mass m located in the medium through the following relationship:

$$D_{med} = \frac{Q}{m} \overline{W}_{air} \left(\frac{\overline{L}}{\rho} \right)_{air}^{med} . \qquad (1.21)$$

where $\left(\overline{L}/\rho \right)_{air}^{med}$ is the ratio of the restricted mass electron stopping powers in the medium and in air, respectively.

We have designed a variable-volume parallel-plate extrapolation chamber which is embedded directly into a commercially available water-equivalent phantom material: the *phantom-embedded extrapolation chamber* (PEEC). The PEEC is able to determine

the derivative dQ/dm through a measurement of the *change* in the charge dQ produced in the cavity per *change* in the mass dm of the sensitive air-volume. The standard cavity theory equation [Eq. (1.21)] can be modified to incorporate the ionization gradient $dQ/(\rho A\,dz)$, in which $dm = \rho A\,dz$, instead of the ratio Q/m, thereby obviating the need for chamber calibration. The modified Spencer–Attix equation for dose measurement with the PEEC is as follows:

$$D_{med} = \frac{dQ}{dz}\frac{1}{\rho A}\,\overline{W}_{air}\left(\frac{\overline{L}}{\rho}\right)^{med}_{air}. \tag{1.22}$$

The PEEC is thus an uncalibrated air-ionization chamber which offers a simple and practical alternative to other techniques used in the measurement of the output of megavoltage photon and electron machines. The PEEC could be considered to have the same level of absoluteness as a free-air ionization chamber with the ability to calibrate photon beams of energy in excess of 3 MeV. Moreover, the PEEC constitutes a method for the *in-phantom* determination of absorbed dose which is in step with the philosophy of new absorbed-dose protocols currently under development.[14]

By making the PEEC directly out of the dosimetry standard water-equivalent phantom material, several correction factors normally associated with the use of commercially produced ionization chambers are eliminated, as will be shown in Chapter 4.

III. Summary

For the purposes of radiation dosimetry, ionizing radiation can be divided into two classifications, namely directly and indirectly ionizing radiations, corresponding to charged and uncharged radiations, respectively. While the transfer of energy to matter

from directly ionizing radiation is a continuous process, the energy transfer from indirectly ionizing radiation is a two step process.

The passage of ionizing radiation through matter results in the dissociation of molecules in the medium into positive and negative ions and the subsequent production of free radicals. The products of ionizing radiation in the medium are of a highly reactive nature and are capable of causing large scale biological damage in living tissue. The ionizing properties of high-energy radiations can be exploited in the treatment of malignant disease by concentrating the delivery of the radiation to the afflicted area of tissue.

Radiation dosimetry is concerned with the accurate quantification of ionizing radiation in order to obtain and use numerical relationships between measured quantities and the biological effects of the radiation on tissue. Several techniques have been developed to determine the dose absorbed by a medium exposed to a given source of ionizing radiation. These techniques can be divided into absolute and relative dosimetry techniques. Absolute dosimetry measures the absorbed dose without requiring calibration in a known radiation field, while relative dosimetry requires that the response of the dosimeter is calibrated in a known radiation field. As for absolute dosimetry techniques, there are currently only three accepted techniques: calorimetry, chemical dosimetry, and free-air ionization chamber dosimetry. We propose to introduce a fourth absolute dosimetry technique based on the use of phantom-embedded extrapolation chambers.

References

1. ICRU, "Radiation quantities and units," Report 19, International Commission on Radiation Units and Measurement, Bethesda, Maryland, 1971.

2. E. J. Hall, *Radiobiology for the Radiologist* (Harper & Row, Maryland, 1973).

3. E. L. Travis, *Primer of Medical Radiobiology* (Year Book Medical, Chicago, 1982).

4. M. Boutillon and A. M. Perroche, "Effect of a change of stopping-power values on the W value recommended by ICRU for electrons in dry air," Report CCEMRI(I)85–8, Bureau International des Poids et Mesures, Sèvres, 1985.

5. ICRU, "Radiation quantities and units," Report 33, International Commission on Radiation Units and Measurement, Bethesda, Maryland, 1980.

6. H. Wyckoff and F. Attix, "Design of free-air ionization chambers," Handbook 64, National Bureau of Standards, Washington, DC, 1957.

7. ICRU, "Measurement of absorbed dose in a phantom irradiated by a single beam of x or gamma rays," Report 23, International Commission on Radiation Units and Measurement, Washington, D.C., 1973.

8. ICRU, "Radiation dosimetry: electron beams with energies between 1 and 50 MeV," Report 35, International Commission on Radiation Units and Measurement, Washington, D.C., 1984.

9. AAPM Task Group 21 of the Radiation Therapy Committee, "A protocol for the determination of absorbed dose from high-energy photon and electron beams," Med. Phys. **10**, 741–771 (1983).

10. AAPM Task Group 25 of the Radiation Therapy Committee, "Clinical electron-beam dosimetry," Med. Phys. **18**, 73–109 (1991).

11. W. H. Bragg, *Studies in Radioactivity* (Macmillan, New York, 1912).

12. L. H. Gray, "An ionization method for the absolute measurement of γ-ray energy," Proc. R. Soc. A. (London) **156**, 578–596 (1936).

13. L. V. Spencer and F. H. Attix, "A theory of cavity ionization," Radiat. Res. **3**, 239–254 (1955).

14. D. W. O. Rogers, in *Teletherapy: present and future*, edited by T. R. Mackie and J. R. Palta, pp. 319–356 (Advanced Medical Publishing, Madison, Wisconsin, 1996), Proceedings of the AAPM 1996 summer school.

CHAPTER 2

Interactions of photons with matter

Interactions of x-ray and γ-ray photons with matter are characterized by the elimination of the photon from the primary beam accompanied by the release of a high energy particle (electron, positron, neutron, *etc.*) and sometimes a scattered photon. On a microscopic scale, x-ray and γ-ray photons can interact directly with atomic nuclei, with electrons orbiting the nuclei, or with the electric field surrounding the nuclei and the orbital electrons of the medium. The three interactions between photons and matter which are of most interest in clinical medical dosimetry are the *photoelectric effect*, the *Compton effect*, and *pair production*. Each of these interactions results in the transfer of energy from photons to electrons or positrons in the medium which in turn deposit their energy in numerous subsequent Coulomb interactions as they move through the medium. A fourth photon interaction with matter, *Raleigh* or *coherent* scattering, does not involve a transfer of kinetic energy between the photon and the medium; therefore, a detailed presentation of this phenomenon is not included in this thesis.

The relative importance of each of the three primary photon interactions is a function of the photon energy $h\nu$ and the atomic number Z of the absorbing medium. Figure 2.1 is a two dimensional surface plot in $h\nu$–space, mapping the regions in which each of the above processes represents the dominant interaction. The solid curves indicate the Z and $h\nu$ coordinates at which the atomic interaction coefficients of neighboring

21

effects are equal. For a given medium of atomic number Z, the photoelectric effect is the predominant interaction at photon energies that are comparable to the electron binding energies of the medium ($h\nu \leq 0.1$ MeV). The photoelectric effect becomes increasingly important as the atomic number of the medium increases. It can be seen from the graph that for low Z materials, such as water and human tissue, the Compton effect has a very broad energy range over which it is the most important photon interaction. However, this energy range gradually narrows with increasing Z, and for high Z materials the Compton effect becomes less influential. Figure 2.1 shows that on average, the Compton effect is most important at photon energies in the range from 1 to 5 MeV, while at energies beyond 10 MeV, pair production begins to dominate the other interactions. Pair production is strongest for high Z materials and is the most important photon interaction at photon energies above ~15 MeV.

I.   Kinematics of photon interactions

I.A.   Photoelectric effect

The photoelectric effect is the most important interaction of relatively low-energy photons with matter. It is a phenomenon which involves the interaction of a low-energy photon with an atom, resulting in the ejection of one of the orbital electrons from the atom. A schematic diagram of the photoelectric process is given in Fig. 2.2.

During a photoelectric interaction, the incident photon is totally absorbed by the interaction and transfers practically all of its energy to the bound electron. A small fraction ($\sim 10^{-5}$) of the incident photon energy is absorbed by the atom as a whole in order to conserve momentum. The electron is ejected from the atom with a kinetic energy of $T_{e^-} = h\nu - |E_b|$, where E_b is the electron binding energy. Interactions of this type can
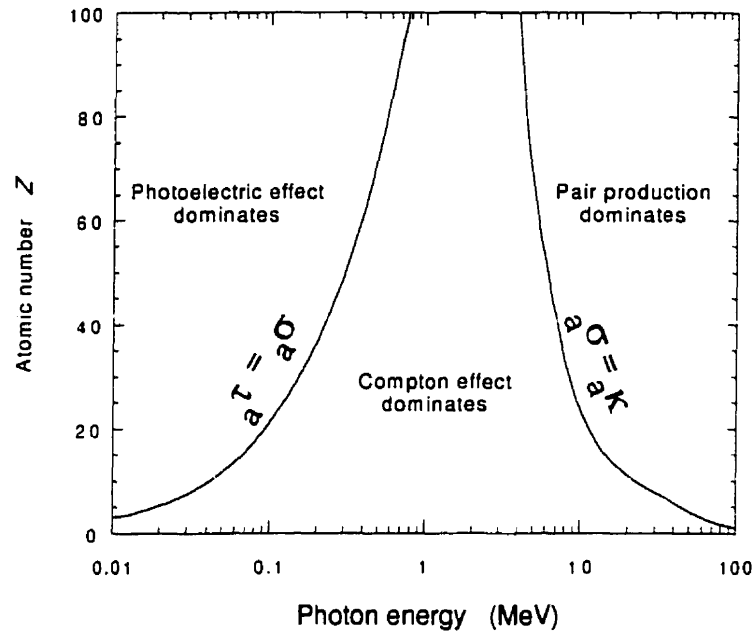
FIGURE 2.1. Relative importance of the three main photon interactions with matter as a function of the photon energy $h\nu$ and the atomic number Z of the medium. The solid lines indicate values of $h\nu$ and Z for which the atomic interaction coefficients of neighboring effects are just equal.

occur with electrons from any of the electron shells, but are most probable when the photon energy $h\nu$ is roughly equal to or slightly greater than the electron binding energy.

At low photon energies, $h\nu \leq 20$ keV, the photoelectrons are ejected at right angles to the incident photon, whereas for $h\nu \geq 1$ MeV, photoelectrons are emitted primarily in the forward direction.[1]

The ejection of a bound electron leaves the atom in an excited state with a vacancy in one of the electron shells. The excess atomic energy may be released by one of several processes which will be discussed in Section II. Ultimately, the inner shell vacancy is exchanged for one or more outer shell vacancies which are in turn filled by an appropriate

number of thermal electrons captured from the environment by the electric field of the nucleus.

I.B.   Compton effect

The Compton effect arises when a photon with initial energy $h\nu$ collides elastically with a *free* electron of the medium. The electron is considered free if the momentum transferred to it by the photon exceeds the electrons initial momentum within the atom,[2] *i.e.*, $h\nu >> E_b$. The incident photon transfers some of its energy to the free electron and is scattered by an angle φ with respect to its original direction and carries away the remainder of the energy $h\nu'$. The free electron recoils with kinetic energy T_e- at an angle of θ with respect to the direction of the incident photon. The Compton scattering process is depicted schematically in Fig. 2.3. The ejection of the Compton recoil electron results in an electron orbital vacancy which will be filled by the processes described in Section II.

Application of the law of conservation of momentum and energy to the above
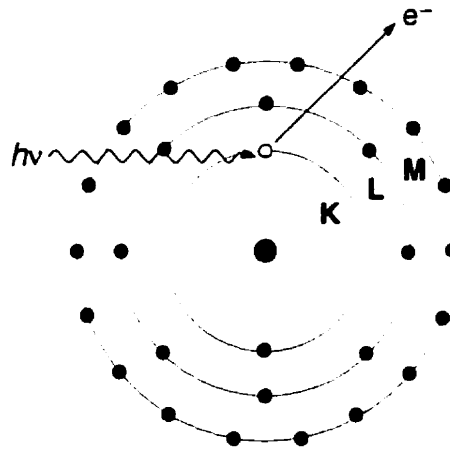
FIGURE 2.2. Schematic diagram illustrating the photoelectric effect. A photon with energy $h\nu \approx E_K$ interacts with an atomic electron from the K-shell resulting in ejection of the atomic electron.
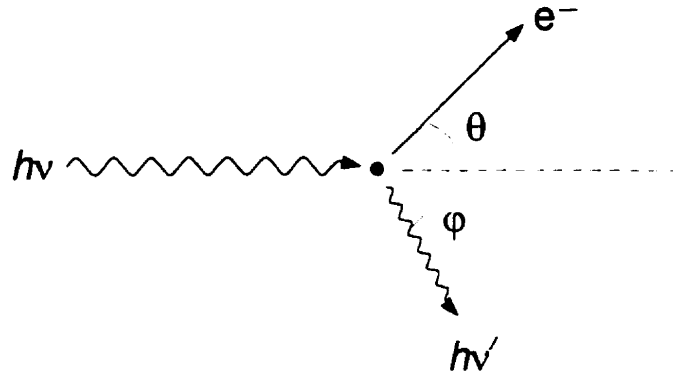
FIGURE 2.3. Schematic diagram of the Compton effect. An incident photon with energy $h\nu$ interacts with a free electron at rest. The photon is scattered at an angle φ while the electron recoils with angle θ with respect to the incident photon direction.

collision leads to the following important relationships:

$$T_{e^-} = h\nu \frac{\alpha(1-\cos\varphi)}{1+\alpha(1-\cos\varphi)} \ . \tag{2.1}$$

$$h\nu' = \frac{h\nu}{1+\alpha(1-\cos\varphi)} \ . \tag{2.2}$$

$$\lambda' - \lambda = \frac{hc}{m_o c^2}(1-\cos\varphi) \ .$$

and,

$$\cot\theta = (1+\alpha)\tan(\varphi/2) \ ,$$

where $\alpha = h\nu/m_o c^2$, $m_o c^2$ is the rest energy of the electron (0.511 MeV), h is Planck's constant, and λ and

$$\lambda' \tag{2.5}$$

are the wavelengths of the initial and scattered photons, respectively.
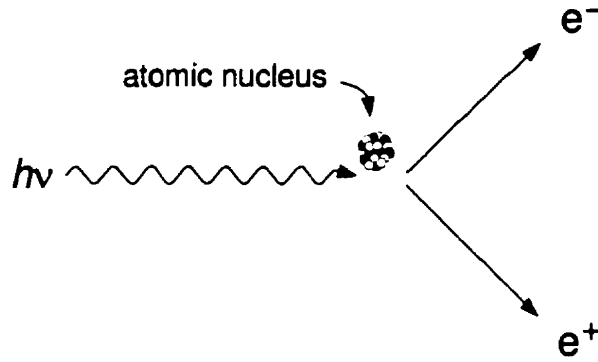
FIGURE 2.4. Schematic diagram of pair production in the field of the nucleus. The incident photon is totally absorbed in the creation of an electron-positron pair.

I.C. Pair production

Pair production is an interaction process in which a photon is absorbed and an electron-positron pair is created. Pair production can occur only in the Coulomb field which exists near an atomic nucleus and is illustrated in Fig. 2.4. In this interaction, the whole of the photon energy is converted into the mass and kinetic energy of the electron-positron pair. Sometimes pair production occurs in the Coulomb field of a single orbital electron and the effect is then called *triplet production* because the products consist of three electrons: the recoil electron and the electron-positron pair. The presence of the nucleus (or the electron) is necessary for the conservation of energy and momentum.

The threshold photon energy for pair production is the energy required to produce an electron-positron pair at rest, *i.e.*, $h\nu > 2m_0c^2 = 1.022$ MeV. If the incident photon energy is in excess of the threshold energy, the remaining energy is distributed between the kinetic energies of electron and positron pair, T_{e^-} and T_{e^-}, respectively:

$$T_{e^-} + T_{e^+} = h\nu - 2m_0c^2 .$$

(2.6)

The electron and the positron share the total kinetic energy available to them and any distribution of the kinetic energy between the two particles is possible. The particles tend to be emitted primarily in the same direction as the incident photon.

Triplet production is analogous to pair production but has a photon energy threshold of $h\nu \geq 4m_oc^2 = 2.044$ MeV. The excess photon energy is shared by the electron-positron pair and the recoil electron in the field of which the interaction occurred.

II. Post-interaction atomic processes

Atoms in the ground state possess electron shells which have a full complement of electrons. The ejection of an electron from any interaction process creates an electron shell vacancy and leaves the atom in an excited state. In order to revert back to the ground state, an electron from a higher energy shell makes a transition to fill the vacancy accompanied by the emission of either a characteristic x-ray photon (especially in high-Z elements) or an Auger electron (especially in low-Z elements).

II.A. Characteristic radiation

The x-ray photon emitted during the transition of an electron from an outer shell to an inner shell vacancy is referred to as *characteristic radiation* or *fluorescence radiation*. The characteristic photon has an energy equal to the difference between the binding energies of the donor and recipient shells. For example, suppose a K-shell electron is ejected as a result of the photoelectric effect and an electron from the L-shell moves to fill the K-shell vacancy, the corresponding characteristic photon will have an energy $h\nu = E_K - E_L$, where E_K and E_L are the binding energies of the K- and L-shells, respectively (Fig. 2.5(a)). The atom remains in an excited state because a vacancy

(a)   Characteristic radiation   (b)   Auger electrons
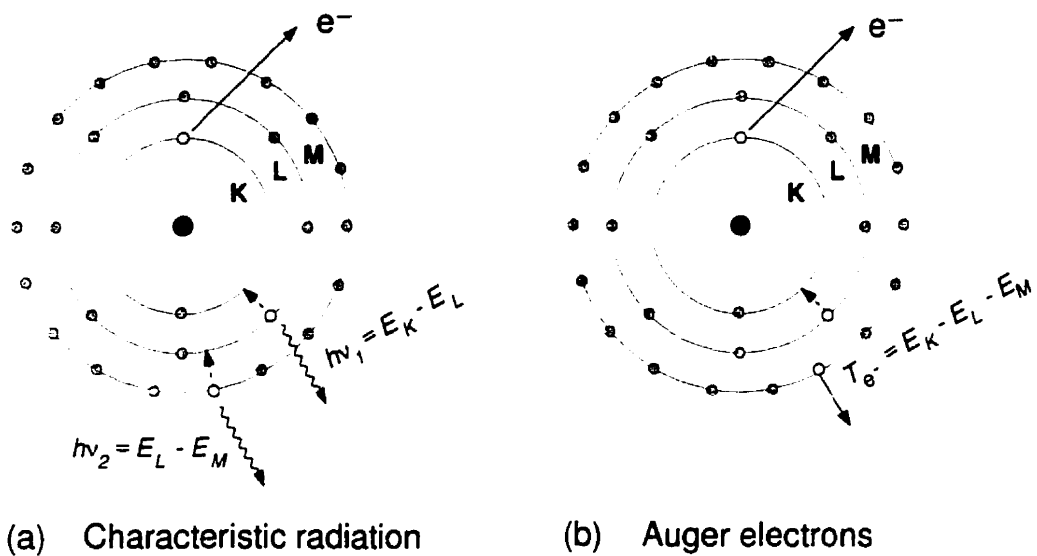
FIGURE 2.5. When an electron is removed from an inner electron-shell, an electron from a less-tightly bound shell will make the transition to fill the vacancy. The transition is followed either by (a) the emission of characteristic radiation, or (b) the ejection of one or more Auger electron from a less-tightly bound shell.

now exists in the L-shell. Another electron from an even higher-energy shell, such as the M-shell, may fill the vacancy in the L-shell followed by the emission of a second characteristic photon of energy $h\nu = E_L - E_M$, where E_M is the binding energy of the M-shell, or by the ejection of an Auger electron. This cascade process continues until a thermal electron from the surrounding medium is captured by the atom.

II.B. Auger effect

The Auger effect provides an alternative mechanism for the atom to return to the ground state. In the Auger process, the atom ejects one or more orbital electrons which carry away the excess atomic energy (Fig. 2.5(b)). The kinetic energy of the Auger electron is equal to the binding energy of the recipient shell (*i.e.*, the shell of the original vacancy) minus the binding energy of the donor electron minus the binding energy of the Auger electron. Consider a KLM Auger process in which there exists a vacancy in the K-shell that is filled by an electron from the L-shell followed by the ejection of an M-shell Auger electron. The kinetic energy T_{e^-} of the Auger electron is $T_{e^-} = E_K - E_L - E_M$.

Now the atom is left with two vacancies: one in the L-shell and one in the M-shell. These vacancies will be filled by electrons residing in even higher-energy shells. The electrons which make the transition from these higher-energy shells to fill the vacancies may produce characteristic radiation of even more Auger electrons.

It is thus possible for the atom to emit a number of Auger electrons in a sort of chain reaction in which an energetic "deep" inner-shell vacancy is exchanged for a number of relatively "shallow" outer-shell vacancies. As is the case following the emission of characteristic radiation, the outer-shell vacancies are eventually filled by thermal electrons which become bound to the atom.

An Auger electron which originates in the same shell as the donor electron is referred to as a Coster-Kronig electron. Coster-Kronig electrons are a special case of Auger electrons including Auger electrons of the form KLL, KMM, LMM, *etc.*.

II.C. Fluorescence yield

The probability that the transition of an electron from one shell to another is accompanied by the emission of a characteristic photon is called the *fluorescence yield*,
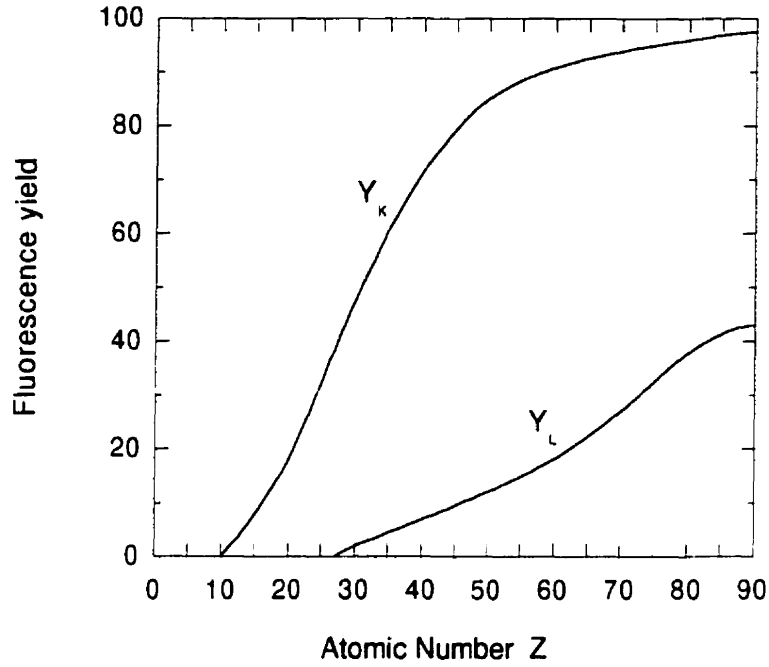
FIGURE 2.6. Fluorescence yields Y_K and Y_L for the K- and L-shells, respectively, as a function of the atomic number Z of the medium. Y_K was calculated from Lederer and Shirley[3] and Y_L from Burhop.[4]

Y. Each electron shell has its own fluorescence yield; Y_K and Y_L are the fluorescence yields for the K- and L-shells, respectively. Y_K is defined as the number of K x-rays emitted per vacancy in the K-shell. For K-shell interactions one can write,

$$Y_K = \frac{N_K}{N_{V_K}} ,$$

(2.7)

where N_K is the number of photons emitted from the K-shell and N_{V_K} is the number of K-shell vacancies produced.

The empirical values Y_K and Y_L are plotted in Fig. 2.6 as a function of the atomic number. With an increasing Z, Y_K is seen to rise sharply for Z > 10 and approaches unity gradually for large Z. Y_L is nearly zero for Z < 30, gradually rising to 0.42 for high Z. The probability for characteristic x-ray emission is negligible during the filling of vacancies in the M-shell and in higher shells.

30

III. Photon attenuation coefficients

The previous sections dealt with the major processes by which photons interact with matter. Although the various relationships between the incident photon energy and the resulting kinetic energy transferred to the electrons were described, nothing has yet been said about the probability of a given interaction for a given photon of energy $h\nu$ with a medium of atomic number Z.

III.A. Cross sections and attenuation coefficients

Indirectly ionizing radiations, such as photons, are not subject to long-range Coulomb forces; therefore, interaction processes occur randomly along the trajectory of the radiation through the medium. For this reason, it is meaningful to speak only of the probability of an interaction between an indirectly ionizing particle and the medium. The probability of a given process can be expressed in terms of interaction cross sections or of interaction coefficients. An interaction cross section can be thought of as the apparent area of an interaction centre presented to the incident radiation. The interaction cross section, denoted by σ, is defined as

$$\sigma = \sum_i \sigma_i = \frac{1}{\phi} \sum_i P_i \qquad (2.8)$$

where ϕ is the fluence of indirectly ionizing radiation, and σ_i and P_i are the cross section and the probability of the interaction i, respectively, with i representing the photoelectric effect, Compton effect, pair-production, or any other possible interaction. The SI unit for interaction cross sections is m^2, however, a more convenient unit, the barn b, equal to 10^{-28} m^2 is frequently used.

Electronic versus atomic cross section. If the interaction centre in question is a single electron, as in the case of the Compton effect, then the fundamental interaction is

31

expressible in terms of the cross section per electron, or the electronic cross section. The Compton electronic cross section $_e\sigma$ can be expressed in cm^2/electron. For a material of atomic number Z, the Compton cross section per atom, or the Compton atomic cross section $_a\sigma$ can be written as

$$_a\sigma = Z \cdot _e\sigma ,$$
(2.9)

which has dimensions of cm^2/atom. In general, the atomic cross section is equal to Z times the electronic cross section.

Linear attenuation coefficient. Often it is desirable to know by what fraction the incident photon fluence will be attenuated by a given thickness of absorber. The linear attenuation coefficient of a given material can be derived from the known atomic interaction cross sections.

The number of atoms present in one gram of any element is given by (N_A/A) where N_A is Avogadro's number $(6.022 \times 10^{23}$ atoms/gram-atom) and A is the atomic mass (g/gram-atom). The number N of atoms per cm^3 of a given element is found by multiplying the number of atoms per gram by the density ρ (g/cm^3),

$$N = \rho\left(\frac{N_A}{A}\right) .$$
(2.10)

Thus, the probability that a Compton interaction, say, occurs when a photon traverses 1 cm of an element can be found by multiplying Eq. (2.9) and Eq. (2.10) to obtain

$$\sigma = _a\sigma \cdot \rho\left(\frac{N_A}{A}\right) = _e\sigma \cdot \rho Z\left(\frac{N_A}{A}\right) ,$$
(2.11)

where σ is the linear Compton attenuation coefficient, expressed in cm^{-1}.

Consider a material with linear attenuation coefficient μ that is bombarded by a monodirectional photon beam of fluence ϕ. The change in the fluence $d\phi$ per unit pathlength dx is proportional to the fluence and the linear attenuation coefficient μ,

$$\frac{d\phi}{dx} = -\mu\phi .$$ (2.12)

The differential equation, Eq. (2.12) can be solved for ϕ as a function of the distance x travelled in the medium giving

$$\phi(x) = \phi_o\, e^{-\mu x} ,$$ (2.13)

where ϕ_o is the initial photon fluence.

Mass attenuation coefficient. Clearly, the attenuation produced by a layer of medium depends on the number of interaction centres present in the layer. If the layer were compressed to half its original thickness, it would still have the same number of interaction centres thus it would still attenuate the particle beam to the same extent, and, of course, its linear attenuation coefficient μ would be twice as large. It is evident from Eq. (2.11) that the linear attenuation coefficient is dependent on the density of the absorbing medium. The linear attenuation coefficient in Eq. (2.13) can be replaced with the mass attenuation coefficient (μ/ρ), a more fundamental coefficient to describe the attenuation of photons in matter, which is obtained by dividing the linear attenuation μ coefficient by the density ρ. In this way, the dependence on the density of the medium apparent in Eq. (2.11) is eliminated. Equation (2.13) can then be rewritten in terms of the mass attenuation coefficient (μ/ρ) and the mass-thickness of absorber $X = \rho x$ (g/cm^2):

$$\phi(X) = \phi_o\, e^{-\left(\frac{\mu}{\rho}\right)X} .$$ (2.14)

III.B. Photoelectric cross section

A theoretical description of the photoelectric effect is quite complicated owing to considerations of the electron binding energy. There are no simple equations which represent the differential photoelectric cross section; however, satisfactory solutions to the problem have been discussed in the literature.[5, 6] Published values for photoelectric cross sections are based on experiment and supplemented by theoretical interpolations for various photon energies and media.

A photoelectric interaction with a given atomic electron cannot occur unless the incident photon energy is at least as great as the binding energy of that electron. Consider the situation of photons passing through lead which has a K-shell binding energy of 0.088 MeV. For photon energies just below the K-edge, $h\nu < E_k$ and no electrons in the K-shell can interact via the photoelectric effect. For photon energies greater than the K-shell binding energy $h\nu > E_k$, K-shell electrons can participate in the interaction. Thus, at $h\nu = E_k$ there exists a discontinuity in the photoelectric atomic cross section $_a\tau$ called the K-edge. Similar absorption edges related to the three electron L-orbitals also exist and are shown in Fig. 2.7 , in which the mass-attenuation coefficient for lead is plotted as a function of $h\nu$.

In the energy region $h\nu \leq 0.1$ MeV where the photoelectric effect is most important, for photon energies greater than the atomic binding energy, the photoelectric atomic interaction cross section $_a\tau$ varies roughly as Z^4 and as $(h\nu)^{-3}$, or

$$_a\tau \, \widetilde{\propto} \, \frac{Z^4}{(h\nu)^3} \qquad (2.15)$$

When $h\nu$ is near 5 MeV, photoelectric atomic cross section[7] varies as $(h\nu)^{-1}$. The relationship between the photoelectric mass-attenuation coefficient shown in Fig. 2.7 and the photon energy follows the $(h\nu)^{-3}$ dependence predicted by Eq. (2.15).

III.C. Compton cross section

J.J. Thomson was the first to provide a theoretical description of photon-electron scattering based on classical electromagnetism. The Thomson theory assumes that the electron is free to oscillate under the influence of the photon electric vector and absorbs the photon energy for prompt reradiation in a different direction. The electron thus retains none of the incident photon energy as a result of this elastic scattering event.

Thomson deduced that the differential cross section per electron for a photon scattered at an angle φ per unit solid angle is:

$$\frac{d_e\sigma}{d\Omega_\varphi} = \frac{r_o^2}{2}(1 + \cos^2 \varphi) \ . \tag{2.16}$$

where $r_o = \frac{1}{4\pi\epsilon_o}\frac{e^2}{m_o c^2}$, the *classical electron radius* (2.82 fm). The Thomson cross section agrees with experiment for $h\nu < 0.01$ MeV.[7]
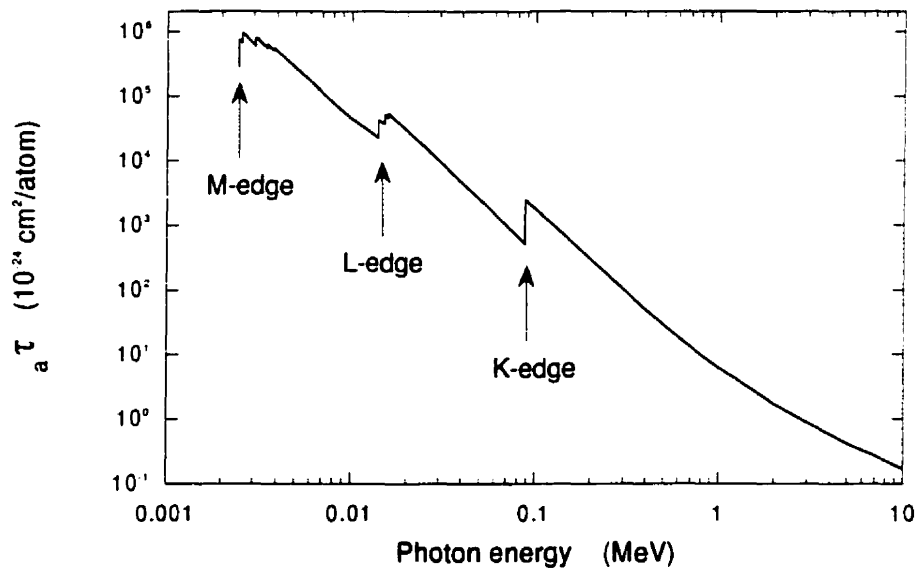
FIGURE 2.7. The photoelectric mass attenuation coefficient for lead illustrating the discontinuities known as the K-, L- and M-edges.

An improved theory for the prediction of Compton scattering was provided by Klein and Nishina[8] who applied the relativistic theory of the electron developed by Dirac. The Klein–Nishina theory predicts the correct experimental cross section while retaining the simple assumption that the electron is unbound and at rest. The differential cross section per electron for a photon scattered at an angle φ, per unit solid angle may be rewritten as follows:

$$\frac{d_e\sigma}{d\Omega_\varphi} = \frac{r_o^2}{2}\left(\frac{h\nu'}{h\nu}\right)^2\left(\frac{h\nu}{h\nu'} + \frac{h\nu'}{h\nu} - \sin^2\varphi\right). \tag{2.17}$$

in which $h\nu'$ is given in Eq. (2.2). For low photon energies $h\nu \approx h\nu'$ and Eq. (2.17) reduces to the Thomson equation given in Eq. (2.16). For photon energies where the Compton effect is most important, the differential Compton cross section varies roughly as $(h\nu)^{-1}$.

The total Klein–Nishina cross section for Compton scattering per electron can be found by integrating Eq. (2.17) over all photon scattering angles φ:

$$_e\sigma = 2\pi \int_0^\pi \left(\frac{d_e\sigma}{d\Omega_\varphi}\right)\sin\varphi\, d\varphi$$

$$= 2\pi r_o^2\left\{\frac{1+\alpha}{\alpha^2}\left[\frac{2(1+\alpha)}{1+2\alpha} - \frac{\ln(1+2\alpha)}{\alpha}\right] + \frac{\ln(1+2\alpha)}{2\alpha} - \frac{1+3\alpha}{(1+2\alpha)^2}\right\} \tag{2.18}$$

where $\alpha = h\nu/m_oc^2$. The Compton electronic cross section is plotted in Fig. 2.8 as a function of the incident photon energy $h\nu$.

Since the Compton effect involves only *free* electrons, it does not depend on the atomic number Z of the medium but rather on the electron density of the medium. For most materials, except hydrogen which has $Z/A = 1$, Z/A ranges from 0.5 to 0.4 and tends to decrease as Z is increased.[9, 7] Thus the Compton mass attenuation coefficient (σ/ρ) is nearly the same for all materials.

III.D. Pair production cross section

Bethe and Heitler[10] developed a theory to describe the interaction cross section for pair production. The Bethe–Heitler theory predicts that the atomic differential cross section $d_a \kappa$ for pair production for the creation of a positron of kinetic energy T_{e^+} can be written

$$\frac{d_a \kappa}{dT_{e^+}} = \frac{r_o^2}{137} \frac{Z^2 P}{h\nu - 2m_o c^2} ,$$ (2.19)

where P is a parameter dependent on $h\nu$ and Z. The dependence of P on Z is slight[7] and is generally ignored.

The total pair-production cross section may be found by integrating Eq. (2.19)
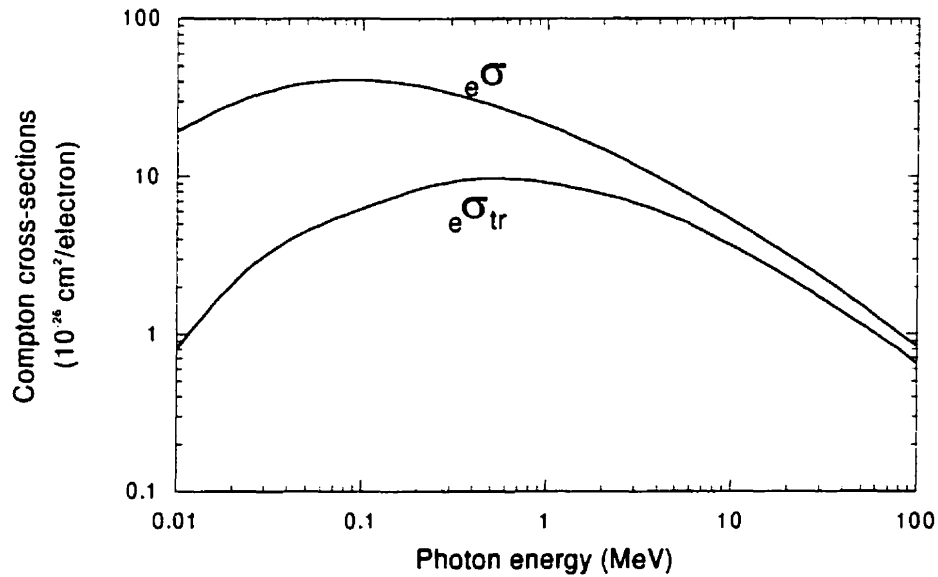
FIGURE 2.8. Compton effect cross section and energy-transfer coefficient per electron, $_e\sigma$ and $_e\sigma_{tr}$, respectively, calculated using the Klein–Nishina equation for lead as a function of the primary photon energy $h\nu$.
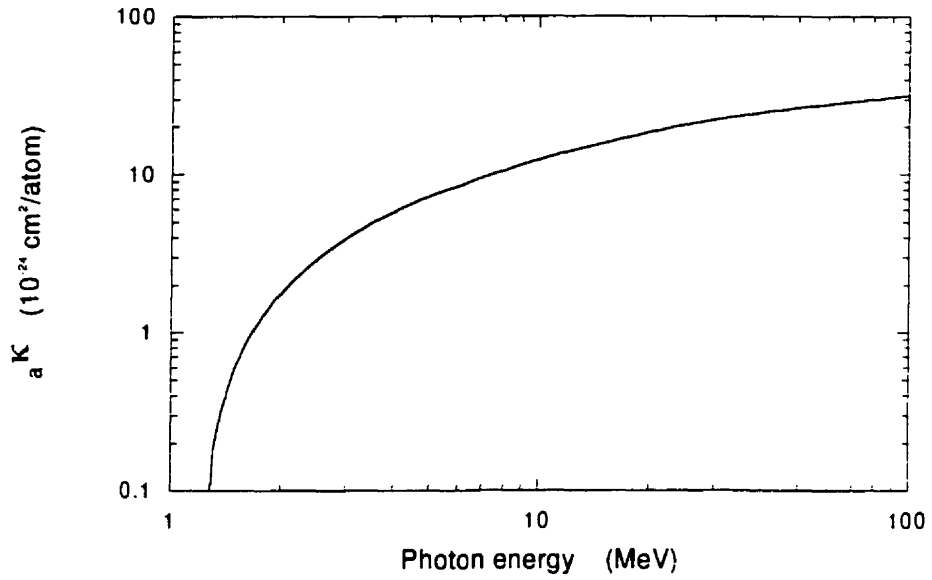
FIGURE 2.9. Pair production atomic cross section $_a\kappa$ plotted as a function of the incident photon energy $h\nu$ in lead.

over all possible T_{e^+}:

$$_a\kappa = \frac{r_o^2}{137}Z^2 \int_0^{(h\nu - 2m_oc^2)} \frac{P}{h\nu - 2m_oc^2}dT_{e^+}$$

$$= \frac{r_o^2}{137}Z^2 \int_0^1 P\, d\left(\frac{T_{e^+}}{h\nu - 2m_oc^2}\right)$$

$$= \frac{r_o^2}{137}Z^2\overline{P} .\tag{2.20}$$

where $\overline{P}$ has no Z–dependence, varies roughly as the logarithm of $h\nu$, and tends toward a constant value independent of $h\nu$ for large $h\nu$ because of electron screening of the nuclear field.[7] It is therefore possible to say that $_a\kappa \cong Z^2$ and $(\kappa/\rho) \propto Z$. The pair production atomic cross section is plotted in Fig. 2.9 as a function of the incident photon energy $h\nu$.

38
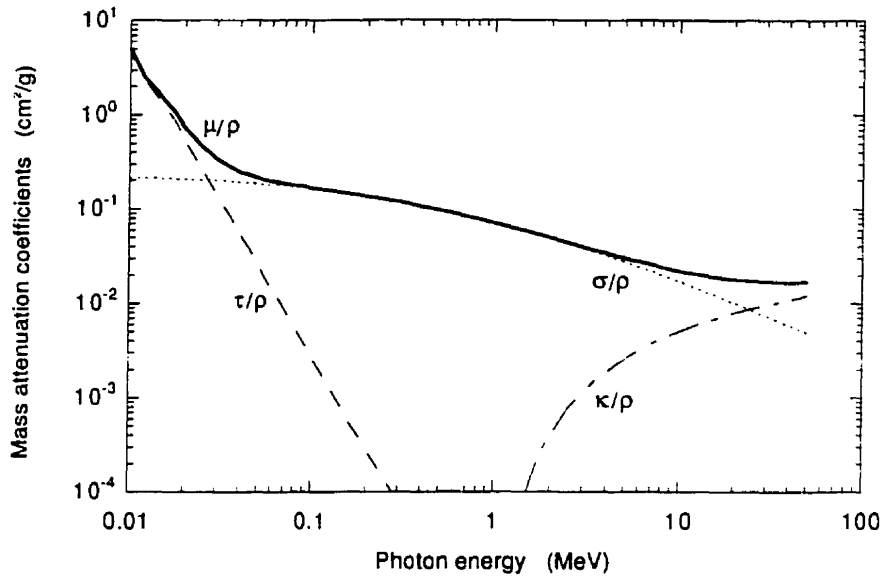
FIGURE 2.10. Plot showing the contributions of the photoelectric (τ/ρ), Compton (σ/ρ), and pair-production (κ/ρ) mass attenuation coefficients to the total mass attenuation coefficient (μ/ρ) of water as a function of the photon energy.

III.E. Total mass attenuation coefficient

Recalling Eqs. (2.8) and (2.14), we can express the total mass attenuation coefficient (μ/ρ) in a given medium as a sum of the photoelectric (τ/ρ), Compton (σ/ρ), Raleigh (σ_R/ρ), and pair-production (κ/ρ) mass attenuation coefficients, or

$$\frac{\mu}{\rho} = \frac{\tau}{\rho} + \frac{\sigma}{\rho} + \frac{\sigma_R}{\rho} + \frac{\kappa}{\rho} . \tag{2.21}$$

In Fig. 2.10 the photoelectric, Compton, and pair-production mass attenuation coefficients which contribute to the total mass attenuation coefficient of photons in water are depicted. The solid line of Fig. 2.10 indicates the total mass attenuation coefficient (μ/ρ).

III.F. Summary of interactions

The degree to which a photon beam is attenuated as it passes through a medium depends on the photon energy $h\nu$ and the atomic number Z of the medium. For matter with large Z, a thick electron cloud surrounds the nucleus with which low energy photons interact strongly via the photoelectric effect. The photoelectric effect is therefore an interaction between a photon and the entire atom and is the dominant interaction for low photon energies where $h\nu \gtrsim E_b$, the binding energy of the atomic electrons. For low atomic number media and photon energies where $h\nu \gg E_b$, electrons can be considered unbound. Under these conditions, the Compton effect, a photon interaction with "free" electrons in the medium, dominates when $h\nu$ is below the threshold energy for pair production. For large Z materials where the Coulomb field around the nucleus is particularly strong, and for high-energy photons ($h\nu \geq 1.022$ MeV) that are able to penetrate the electron cloud, pair production is the most important photon interaction with matter.

Table 2.1 summarizes the dependence on $h\nu$ and Z of the photoelectric, Compton, and pair production coefficients important in radiotherapy. It is important to note that in calculating the Z–dependence of the mass attenuation coefficients Z/A was assumed constant. (Recall that with the exception of hydrogen, most materials have approximately the same number of electrons per gram,[7, 9] although the number of electrons per gram of an element decreases slowly with atomic number.)

Table 2.1. Summary of the dependence on $h\nu$ and Z of photoelectric, Compton, and pair production coefficients in radiotherapy. Shown are the electronic and atomic cross sections as well as the linear and mass attenuation coefficients.

	Photoelectric	Compton	Pair production
electronic cross-section	${}_e\tau \propto \frac{Z^3}{(h\nu)^3}$	${}_e\sigma \propto \frac{Z^0}{h\nu}$	${}_e\kappa \propto Z \ln(h\nu)$
atomic cross-section	${}_a\tau \propto \frac{Z^4}{(h\nu)^3}$	${}_a\sigma \propto \frac{Z}{h\nu}$	${}_a\kappa \propto Z^2 \ln(h\nu)$
linear attenuation coefficient	$\tau \propto \frac{\rho Z^3}{(h\nu)^3}$	$\sigma \propto \frac{\rho Z^0}{h\nu}$	$\kappa \propto \rho Z \ln(h\nu)$
mass attenuation coefficient	$\frac{\tau}{\rho} \propto \frac{Z^3}{(h\nu)^3}$	$\frac{\sigma}{\rho} \propto \frac{Z^0}{h\nu}$	$\frac{\kappa}{\rho} \propto Z \ln(h\nu)$

III.G. Mass energy-transfer coefficient

The mass attenuation coefficient is used to describe the fraction of incident photons that are removed from the primary beam; however, it says nothing about the fraction of the incident photon energy that is removed. The mass energy-transfer coefficient is used to describe the fraction of energy that is transferred from the incident photons to secondary electrons in the medium, and is related to the mass attenuation coefficient through the following relationship:

$$\frac{\mu_{tr}}{\rho} = \frac{\mu}{\rho} \frac{\langle E_{tr} \rangle}{h\nu},$$ (2.22)

in which $\langle E_{tr} \rangle$ is the mean energy transferred to the recoil electron for a large number of interactions. The method for determining $\langle E_{tr} \rangle$ for each of the major photon interactions is discussed below.

Energy transfer in the photoelectric effect. The fraction of energy transferred

41

to the photoelectron is simply

$$\frac{T_{e^-}}{h\nu} = \frac{h\nu - E_i}{h\nu} , \qquad (2.23)$$

where E_i is the binding energy of the ith shell. This is the first approximation to the total fraction of $h\nu$ which is transferred to all electrons. Most of the electron binding energy will be radiated away in the form of characteristic energy and is not transferred to the medium. However, recall that some of the electron binding energy may be reclaimed by Auger electrons; therefore, Eq. (2.23) will underestimate the mean energy transferred to the medium.

The *mean* mass energy transfer coefficient $\langle \tau_{tr}/\rho \rangle$ must account for the different processes which may follow the photoelectric interaction. The fluorescence yield Y_i of the ith shell must be considered along with the probability of a photoelectric interaction P_i with that shell in order to determine the mean mass energy-transfer coefficient. The fraction χ of the incident photon energy which gets reradiated, *i.e.*, <u>not</u> transferred to electrons in the medium, may be written as

$$\chi = \sum_i P_i Y_i |E_i| . \qquad (2.24)$$

where $|E_i|$ is the absolute value of the binding energy of the ith shell. The mean mass energy transfer coefficient for the photoelectric effect is then:

$$\left\langle \frac{\tau_{tr}}{\rho} \right\rangle = \left(\frac{h\nu - \chi}{h\nu} \right) \frac{\tau}{\rho} . \qquad (2.25)$$

Energy transfer in the Compton effect. To calculate the Compton energy-transfer coefficient per electron, it is necessary to revert to the integration over all photon scattering angles of a modified form of the Klein–Nishina cross section. The differential Klein–Nishina energy-transfer cross section per electron $d_e\sigma_{tr}/d\Omega_\varphi$ is written as follows:

$$\frac{d_e\sigma_{tr}}{d\Omega_\varphi} = \frac{r_o^2}{2} \left(\frac{h\nu'}{h\nu} \right)^2 \left(\frac{h\nu}{h\nu'} + \frac{h\nu'}{h\nu} - \sin^2\varphi \right) \left(\frac{h\nu - h\nu'}{h\nu} \right) , \qquad (2.26)$$

where $(h\nu - h\nu')/h\nu$ represents the fraction of the incident photon energy transferred to the recoil electron. Integrating Eq. (2.26) over all photon scattering angles yields the Klein–Nishina energy-transfer cross section $_e\sigma_{tr}$:

$$_e\sigma_{tr} = 2\pi \int_0^\pi \left(\frac{d_e\sigma_{tr}}{d\Omega_\varphi} \right) \sin\varphi \, d\varphi$$

$$= 2\pi r_o^2 \left[\frac{2(1+\alpha)^2}{\alpha^2(1+2\alpha)} - \frac{1+3\alpha}{(1+2\alpha)^2} - \frac{(1+\alpha)(2\alpha^2 - 2\alpha - 1)}{\alpha^2(1+2\alpha)^2} \right.$$

$$\left. - \frac{4\alpha^2}{3(1+2\alpha)^3} - \left(\frac{1+2\alpha}{\alpha^3} - \frac{1}{2\alpha} \right) \ln(1+2\alpha) \right]. \tag{2.27}$$

The Klein–Nishina energy transfer coefficient $_e\sigma_{tr}$ per electron for the Compton effect is plotted in Fig. 2.8 for photons in lead.

The mean kinetic energy transferred to the Compton recoil electrons generated by photons of energy $h\nu$ can be found from the following relationship:

$$\frac{\langle T_{e^-} \rangle}{h\nu} = \frac{_e\sigma_{tr}}{_e\sigma}. \tag{2.28}$$

The mean Compton recoil electron energy $\langle T_{e^-} \rangle$ is different from the maximum kinetic energy transferred to the recoil electron $T_{e^-}^{max}$ which can be found from Eq. (2.1) by setting $\phi = \pi$. Figure 2.11 is a plot of the maximum and mean fractions of the incident photon energy $T_{e^-}^{max}/h\nu$ and $\langle T_{e^-} \rangle/h\nu$, respectively, which is transferred to the recoil electron as a function of the photon energy. $T_{e^-}^{max}$ is calculated from the Klein–Nishina equation. The mean mass energy transfer coefficient $\langle \sigma_{tr}/\rho \rangle$ for the Compton interaction, hence, is

$$\left\langle \frac{\sigma_{tr}}{\rho} \right\rangle = \left(\frac{\langle T_{e^-} \rangle}{h\nu} \right) \frac{\sigma}{\rho}, \tag{2.29}$$

where $\langle T_{e^-} \rangle/h\nu$ can be found from Fig. 2.11.

Energy transfer in pair production. For pair-production, the mean mass energy transfer coefficient may be calculated from Eq. (2.6). Since the entire photon energy is absorbed to produce the electron-positron pair, one may write,

$$\left\langle \frac{\kappa_{tr}}{\rho} \right\rangle = \left(1 - \frac{2m_0 c^2}{h\upsilon} \right) \frac{\kappa}{\rho} .$$
(2.30)

Total mass energy-transfer coefficient. It is useful to relate the total mass attenuation coefficient to the total mass energy transfer coefficient. Using the general expressions for the individual energy-transfer coefficients, the total mass energy-transfer coefficient may be written as

$$\left\langle \frac{\mu_{tr}}{\rho} \right\rangle = \left\langle \frac{\tau_{tr}}{\rho} \right\rangle + \left\langle \frac{\sigma_{tr}}{\rho} \right\rangle + \left\langle \frac{\kappa_{tr}}{\rho} \right\rangle .$$
(2.31)
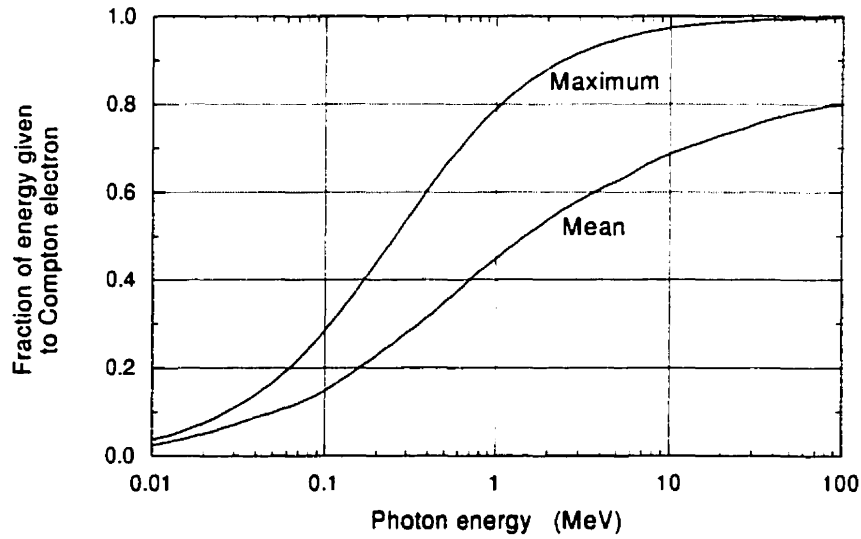
FIGURE 2.11. Plot of the maximum and mean kinetic energy transferred to the recoil electron in a Compton interaction as a fraction of the incident photon energy. The maximum kinetic energy of the recoil electron is found from Eq. (2.1) and the mean kinetic energy can be calculated from Eqs. (2.28) and (2.27).

It is possible to calculate the total mean mass energy transfer coefficient by substituting Eqs. (2.25), (2.29), and (2.30) into Eq. (2.21), so that

$$\left\langle \frac{\mu_{tr}}{\rho} \right\rangle = \frac{1}{\rho} \left\{ \tau \frac{(h\nu - \chi)}{h\nu} + \sigma \frac{\langle T_e - \rangle}{h\nu} + \kappa \left(1 - \frac{2m_0 c^2}{h\nu} \right) \right\} . \tag{2.32}$$

The mean energy transferred to the medium $\langle E_{tr} \rangle$ per photon interaction may be calculated from the following equation:

$$\langle E_{tr} \rangle = \frac{\left\langle \frac{\mu_{tr}}{\rho} \right\rangle}{\left(\frac{\mu}{\rho} \right)} h\nu . \tag{2.33}$$

III.H. Mass energy-absorption coefficient

Radiation dosimetry is concerned with the amount of energy that is absorbed per unit mass of medium. Although the mass attenuation and mass energy-transfer coefficients are important quantities, they are insufficient to describe the energy actually *absorbed* by the medium. A new quantity, the mass energy-absorption coefficient (μ_{ab}/ρ) is introduced to complete the discussion of the interactions of indirectly ionizing radiations with matter.

The mass energy-absorption coefficient is related to the mass energy-transfer coefficient by the following expression:

$$\frac{\mu_{ab}}{\rho} = \frac{\mu_{tr}}{\rho} (1 - g) , \tag{2.34}$$

in which g represents the average fraction of secondary-electron kinetic energy that is given up to radiative interactions with the medium. Radiative interactions with the medium consist of bremsstrahlung for electrons and in-flight annihilation for positrons. An evaluation of g will be given in Section V of Chapter 3.

For low values of $h\nu$ and Z, only a small amount of the secondary-electron kinetic energy is lost to radiative interactions so that $g \to 0$ and $\mu_{ab}/\rho \approx \mu_{tr}/\rho$. As

hν or *Z* increases, *g* gradually increases. For *hν* = 10 MeV passing through lead,

$\mu_{ab}/\rho = 0.74\,\mu_{tr}/\rho$.[ref.7]

The mean energy absorbed by the medium $\langle E_{ab} \rangle$ per photon interaction is given by the following equation:

$$\langle E_{ab} \rangle = \frac{\left\langle \frac{\mu_{ab}}{\rho} \right\rangle}{\left(\frac{\mu}{\rho} \right)} h\nu \, . \tag{2.35}$$

IV. Summary

The three primary interactions between high-energy photons and matter of concern in medical radiation dosimetry are the photoelectric effect, the Compton effect, and pair production. The relative importance of each of these interactions is a complicated function of the photon energy *hν* and the atomic number of the medium *Z*.

Following the ejection of an orbital electron from a photoelectric or Compton interaction, or the annihilation of an orbital electron with the positron created during pair production, the atom is left with an electron shell vacancy. In order to revert back to the atomic ground state, an electron from a higher energy shell makes a transition to fill the vacancy in the lower energy shell. The electron transition may be followed either by the emission of a characteristic photon or an Auger electron, which serve to remove some of the excess energy from the atom. Ultimately, the electron shell vacancies are transferred to the valence shell where they are filled by thermal electrons from the medium which are captured by the Coulomb field of the atomic nucleus.

The probability of any of the above processes may be expressed in terms of interaction cross sections which are directly related to various interaction coefficients, such as the linear and mass attenuation coefficients, the mass energy-transfer coefficient,

and the mass energy-absorption coefficient. The total interaction coefficient due to all processes is determined simply by summing over the individual interaction coefficients.

The total mass energy-absorption coefficient is of primary importance in radiation dosimetry as it describes the fraction of the incident photon beam energy that is absorbed by the medium.

References

1. G. N. Whyte, *Principles of Radiation Dosimetry* (Wiley, New York, 1959).

2. J. R. Greening, *Fundamentals of Radiation Dosimetry (Medical Physics Handbook 6)* (Adam Hilger Ltd., Bristol, Great Briton, 1981).

3. C. M. Lederer and V. S. Shirley, *Table of Isotopes* (Wiley-Interscience, New York, 7th edition, 1979).

4. E. H. S. Burhop, *The Auger Effect* (Cambridge University Press, England, 1952).

5. R. D. Evans, *The Atomic Nucleus* (Krieger, Malabar, Florida, 1955).

6. J. Hubbell, "Photon cross sections, attenuation coefficients from 10 keV to 100 GeV," Report NSRDS-NBS29, U.S. National Bureau of Standards, Washington, D.C., 1969.

7. F. H. Attix, *Introduction to Radiological Physics and Radiation Dosimetry* (John Wiley & Son, New York, 1986).

8. O. Klein and Y. Nishina, Physik **52**, 853 (1929).

9. H. E. Johns and J. R. Cunningham, *The Physics of Radiology* (Charles C. Thomas, Springfield, Illinois, 4th edition, 1983).

10. H. Bethe and W. Heitler, "On the stopping of fast particles and on the creation of positive electrons," Proc. Roy. Soc. A. (London) **146**, 83–112 (1934).

CHAPTER 3

Interactions of electrons with matter

It was shown in Chapter 2 that photons may interact with matter and cause the release of energetic recoil electrons in the medium. In this chapter, the transfer of kinetic energy from these recoil electrons to the medium will be described. Charged particles lose their energy in a manner which is very distinct from that of uncharged radiations. A photon or neutron is capable of passing through a medium without any interactions at all and, consequently, without any energy loss. When a photon interacts with the medium, it is usually removed from the primary beam by means of a catastrophic event in which most of its energy is transferred to a secondary electron in the medium.

The Coulomb field that surrounds a charged particle, such as an electron, causes it to interact with one or more electrons, or with the nucleus of practically every atom it passes. In contrast to the situation of photons passing through matter, the probability that an electron (or any charged particle) traverses the medium without an interaction is zero. A 1 MeV electron undergoes $\sim 10^5$ interactions before coming to rest in the medium. Most of these interactions individually transfer only a small fraction of the electron kinetic energy to the medium.

The combination of a large number of interactions and a relatively small energy transfer per interaction slows down the electrons as if they were acted upon by friction. This friction-like action of the medium on directly ionizing radiations has led to the

development of the "continuous slowing down approximation" (CSDA) for charged particles. The CSDA for charged particles assumes that the particle loses its energy linearly with penetration into the medium and eventually comes to rest at a depth in the medium known as the *electron range*. The electron range in a medium is dependent on the density of the medium and on the initial kinetic energy of the electron. Mathematically, the electron range is the expectation value for the mean pathlength of an electron of a given kinetic energy in a given medium.

I. Types of electron interactions

Electromagnetic interactions between electrons and matter may be categorized according to the relative size of the classical impact parameter b and the atomic radius a. There are in general three types of electron interactions with the medium which correspond to $b >> a$ (soft collisions), $b \sim a$ (hard collisions), and $b << a$ (radiative collisions).

I.A. "Soft" collisions ($b >> a$)

Owing to its Coulomb field, an electron, as it traverses a medium, is most likely to interact from a large distance ($b >> a$) with a great number of atoms. When $b >> a$, the Coulomb field surrounding the electron will interact with the atom as a whole, perturbing the orbiting electrons of the atom and leading to excitation of the atom and possibly ionization of some valence electrons. Furthermore, the large impact parameter means that interactions between the electron and an individual atom are "soft", implying that little net kinetic energy is transferred to the medium. "Soft" collisions are the most common type of electron interaction, and they account for roughly half of the total

energy transferred from the electron to the medium.

In condensed media, such as water or tissue, the passage of a charged particle can lead to the polarization of the medium. The polarization of the medium tends to decrease the electric field experienced by the energetic electron, resulting in a decrease in the amount of energy imparted to the medium. This phenomenon is known as the *density effect* and is of considerable importance in radiation dosimetry. A correction for the density effect will be described in Section III.A.

I.B. "Hard" collisions (*b* ~ *a*)

When the impact parameter *b* is on the order of the atomic radius *a* of a particular atom, it becomes more likely that the incident electron will interact with an individual electron orbiting the nucleus. A collision of this nature will cause the orbital electron to be ejected from the atom with a considerable kinetic energy. If this secondary electron has sufficient energy to produce its own ion track, it is referred to as a δ ray. The δ ray deposits its energy at some distance away from the interaction site, thus the energy transferred to the medium cannot be considered locally absorbed.

Should a hard collision cause the ejection of an inner-shell electron, the collision will be followed by the emission of a characteristic photon or the ejection of an Auger electron, just as if the bound electron had been ejected through a photon interaction (see Chapter 2, Section II). This is important to note because in hard collisions, some of the energy transferred to the medium may be carried away by photons as well as by δ rays, and will not contribute to the locally absorbed dose.

Although hard collisions are less numerous than soft collisions, the amount of energy lost per hard collision is much greater, so that on average a comparable fraction of the incident electron kinetic energy is given to hard and soft collisions. The probability of

a hard collision depends on the quantum-mechanical spin of the incident charged particle, therefore, the form of the stopping power equation is different for electrons and positrons (see Section III).

I.C.   Radiative collisions ($b \ll a$)

When the impact parameter of the electron is much smaller than the atomic radius, the electron is most likely to interact within the Coulomb-field of the nucleus. In 98% of such encounters, the electron is scattered elastically and does not emit an x-ray photon or excite the nucleus.[1] Nuclear scattering, therefore, is not an important mechanism for energy transfer from an energetic electron to the medium, but is a very important means of deflecting electrons.

In the other 2% of encounters between an energetic electron and an atomic nucleus, the electron experiences a violent change of direction followed by the emission of an x-ray photon. As the electron is deflected and slowed down in the field of the nucleus, the electron loses a large proportion (up to 100%) of its kinetic energy to the photon. Such photons are called *bremsstrahlung*, the German word for "braking radiation," and will be described in Section II.B. Bremsstrahlung photons are often energetic enough to escape from the medium, consequently, their energy is not absorbed by the medium.

II.   Electron energy loss in the medium

II.A.   Collisional energy loss

The most important mechanism for electron energy loss in the medium by an energetic electron traversing the medium involves a large number of collisions between the energetic electron and the atomic electrons. These collisions may be soft or hard, as

described above, and result in the ionization and excitation of the medium.

Consider the case of an electron moving with velocity v and colliding with an atomic electron via the electromagnetic force. Classical theory[2] indicates that in order to calculate the energy transfer during a collision, one must calculate the momentum impulse caused by the electric field of the incident particle at the position of the atomic electron. The momentum gained Δp by the atomic electron can be calculated as follows:

$$\Delta p = \int_{-\infty}^{\infty} F_c dt = \frac{1}{4\pi\epsilon_0} \int_{-\infty}^{\infty} \frac{e^2}{(x^2+b^2)} \frac{dx}{v} = \frac{e^2}{4\pi\epsilon_0} \frac{2}{bv} , \tag{3.1}$$

where F_c is the Coulomb force, e is the electron charge and b the impact parameter, and dt was replaced by the incremental distance dx divided by the electron velocity v. Using Eq. (3.1), the non-relativistic energy transferred to the atomic electron can be written as

$$\Delta T_{e^-} = \frac{(\Delta p)^2}{2m_0} = \left(\frac{e^2}{4\pi\epsilon_0}\right)^2 \frac{2}{m_0 v^2} \frac{1}{b^2} . \tag{3.2}$$

For non-relativistic electrons, the electron kinetic energy is $T = \frac{1}{2}m_0 v^2$, thus Eq. (3.2) may be expressed in terms of T:

$$\Delta T_{e^-} = \frac{1}{T}\left(\frac{e^2}{4\pi\epsilon_0}\right)^2 \frac{1}{b^2} . \tag{3.3}$$

As the electron approaches relativistic energies, its velocity approaches the speed of light and, according to Eq. (3.2), the energy transferred to the atomic electron should approach a constant value. However, Eq. (3.3), which is expressed in terms of the incident electron kinetic energy, suggests that the incremental energy loss dT of the charged particle along an increment of path length dx should decrease for increasing T. Surprisingly, the collisional stopping power $(dT/dx)_c$ begins to increase slightly for relativistic electrons, as shown in Fig. 3.1 for electrons passing through water. This increase in the collisional
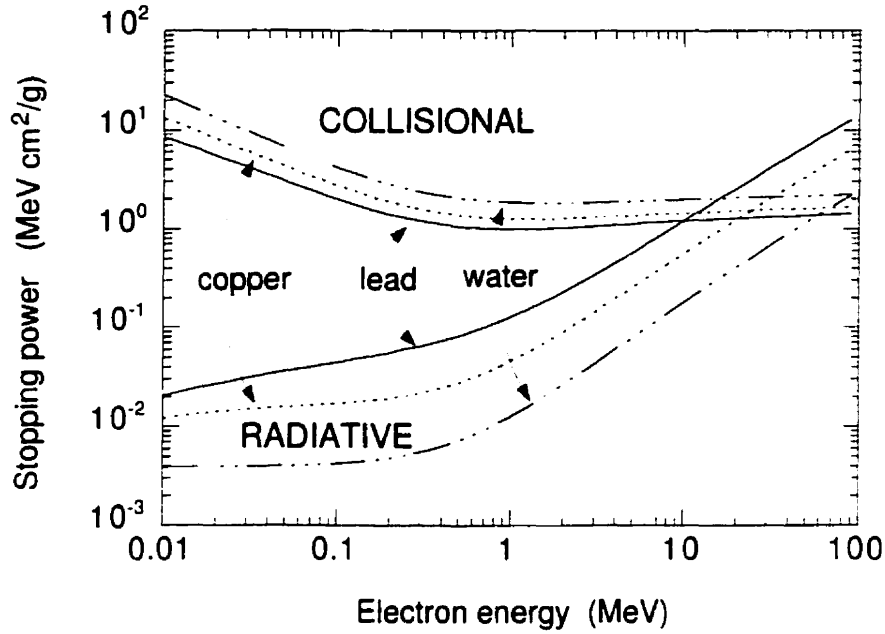
FIGURE 3.1. Plot of the collisional and radiative electron mass stopping power in copper, lead and water. Note the slight increase in the collisional stopping power at relativistic energies. The radiative collisional loss becomes important at energies above 10 MeV and highest for large Z materials.

stopping power for relativistic electrons is due to the contraction of the electric field which makes distant interactions more probable.

The energy transfer varies as the inverse of the square of the impact parameter. This shows clearly that for large impact parameters ($b >> a$), ΔT_{e^-} is small, and for $b \sim a$, ΔT_{e^-} becomes quite large. The maximum energy that can be transferred from one electron to another is $\Delta T_{e^-}^{max} = \frac{(\gamma-1)}{2} m_0 c^2$. If this is substituted into the left hand side of Eq. (3.2), the lower limit of the impact parameter b_{min} can be approximated as follows:

$$b_{min} \approx \left(\frac{e^2}{4\pi\epsilon_0} \right) \frac{2}{\beta\sqrt{(\gamma - 1)}} \frac{1}{m_0 c^2} . \tag{3.4}$$

Equation (3.2) is valid only for impact parameters greater than b_{min} given in Eq. (3.4).

II.B. Radiative energy loss

According to classical electromagnetic theory, when a free charged particle undergoes an acceleration a, it radiates energy at a rate proportional to a^2. The Larmor equation for a non-relativistic accelerated charged particle states that the rate of energy loss dE/dt is given by

$$\frac{dE}{dt} = \frac{e^2 a^2}{6\pi \epsilon_o c^3} ,$$

(3.5)

where z is the charge of the particle and Z is the atomic number of the nucleus. For a charged particle in the field of a nucleus, $a \propto zZ/M$ where M is the charged particle mass. The rate of energy loss dE/dt to bremsstrahlung for an energetic charged particle, therefore, is proportional to the square of the product of the nuclear and incident charged particle charges divided by the mass of the charged particle:

$$\frac{dE}{dt} \propto \left(\frac{zZ}{M}\right)^2 .$$

(3.6)

Given that the rate of energy loss to radiation is inversely proportional to the square of the incident particle mass, bremsstrahlung production is significant only for light particles, such as electrons. For an incident electron $z = 1$.

Radiative energy loss increases with electron energy and is roughly proportional to the electron kinetic energy. In tissue, at electron kinetic energies above 100 MeV, more of the electron energy is lost to radiation than to collision.[3] From Eq. (3.6) it is evident that bremsstrahlung production becomes important in high Z elements, such as lead. In Fig. 3.1, radiative energy loss in lead is shown to dominate for electron energies above 10 MeV.

III.   Electron stopping powers

The expectation value of the rate of kinetic energy loss per unit path length of the charged particle dT/dx is known as the stopping power S. A useful quantity in radiotherapy is the mass stopping power (S/ρ) expressed in MeV cm^{2}g^{-1}, where ρ is the density of the medium.

Since radiation dosimetry is interested in the deposition of energy in the medium, it is convenient to divide the stopping power into two separate categories, namely *collisional stopping power* and *radiative stopping power*. Collisional stopping power refers to the rate of energy loss resulting from the sum of both soft and hard collisions, described in Section II.A. Radiative stopping power refers to the rate of energy loss resulting from radiative interactions, discussed in Section II.B. Energy given to collision generally contributes to the dose absorbed in the vicinity of the ion track produced by the charged particle, while energy lost to radiation is carried away from the interaction site by the photons.

The energy loss of particles passing through matter has been investigated by several authors[4-8] using various models for the energy loss process. The theory and related calculations are rather involved and will be omitted in this discussion.

III.A.   Mass collisional stopping power

The collisional stopping power results from energy transfers between the incident electron and bound atomic electrons in the medium. A general form of the mass collisional stopping power is given by

$$\left(\frac{S}{\rho}\right)_c = \frac{N_A}{M_A} Z \int\limits_{0}^{W_{max}} W \frac{d\sigma}{dW} dW \, , \qquad (3.7)$$

where N_A is Avogadro's number, M_A is the molar mass of the medium in g/mol, Z is

the atomic number of the medium, and $d\sigma/dW$ is the differential electronic cross section resulting in an energy transfer of W. Recall that collisional energy loss may be divided into soft and hard collisions, thus the mass collisional stopping power may be expressed as a sum of the soft and hard collision components, or

$$\left(\frac{S}{\rho}\right)_c = \frac{N_A}{M_A}Z\left[\int_0^{W_c} W\frac{d\sigma}{dW}dW + \int_{W_c}^{W_{max}} W\frac{d\sigma}{dW}dW\right]$$

$$= \left(\frac{S}{\rho}\right)_c^{W<W_c} + \left(\frac{S}{\rho}\right)_c^{W>W_c} . \tag{3.8}$$

in which W_c represents the somewhat arbitrary value for energy transfer which separates hard and soft collisions. For Eq. (3.8) to be valid, W_c must be large compared to the binding energies of the atomic electrons of the medium.

Electrons and positrons are quantum mechanically related and differ only in that the signs of their charge and magnetic spins are opposite. It is not surprising, then, that the calculation of the mass collisional stopping power of electrons and positrons are also similar with some slight differences owing to the charge and magnetic spin. For positrons, the maximum energy transfer to electrons in the medium is $W_{max} = T$, while for electrons, $W_{max} = T/2$, where T is the kinetic energy of the incident charged particle. From Eq. (3.8), one sees that the formulae consist of a portion that is common to both electrons and positrons $(S/\rho)_c^{W<W_c}$, and a portion unique to either electrons or positrons $(S/\rho)_c^{W>W_c}$. A general formula for the mass collisional stopping power exists in terms of $\tau \equiv T/m_o c^2$:

$$\left(\frac{S}{\rho}\right)_c = 2\pi r_o^2 \left(\frac{N_A Z}{A}\right)\frac{m_o c^2}{\beta^2}\left\{\ln\left[\frac{\tau^2(\tau+2)}{2(I/m_o c^2)^2}\right] + F^{\pm}(\tau) - \delta\right\} , \tag{3.9}$$

in which r_o^2 is the classical electron radius, $(N_A Z/A)$ is the number of electrons per gram of medium, $\beta = v/c$, and δ is the *density-effect* correction parameter. In Eq. (3.9) $F^{\pm}(\tau)$ is written[9] for electrons as:

$$F^{-}(\tau) = 1 - \beta^2 + \frac{\tau^2/8 - (2\tau + 1)\ln 2}{(\tau + 1)^2} ,$$

(3.10)

and for positrons as:

$$F^{+}(\tau) = 2\ln 2 - \frac{\beta^2}{12}\left[23 + \frac{14}{\tau + 2} + \frac{10}{(\tau + 2)^2} + \frac{4}{(\tau + 2)^3} \right] .$$

(3.11)

The mean excitation energy I in Eq. (3.9) is the geometric-mean value of all ionization and excitation energies of the atoms in the medium. In general, I cannot be calculated from atomic theory to a useful degree of accuracy and is determined experimentally. Berger and Seltzer[10] have provided an extensive review of I–values, stopping powers, and electron and positron ranges in various media.

Density-effect correction, δ. The passage of a charged particle through matter results in the polarization of atoms near the track of the particle. The polarization of the medium results in a decrease in the Coulomb field in the vicinity of the particle thereby reducing the stopping power of the medium. In gases, the atoms are sufficiently separated so that each atom can be considered independent of the next and the polarization effect is negligible. For high density materials, such as solids and liquids, the reduction in the stopping power is particularly strong and is called, therefore, the *density effect*. The density effect increases with particle momentum by virtue of the Lorentz contraction which makes distant collisions more important. At high enough electron energies, the density effect becomes important even for gases.

The density effect was first predicted by Swann[11] and calculated by Fermi.[12] Sternheimer was successful in developing a model for the density effect which is
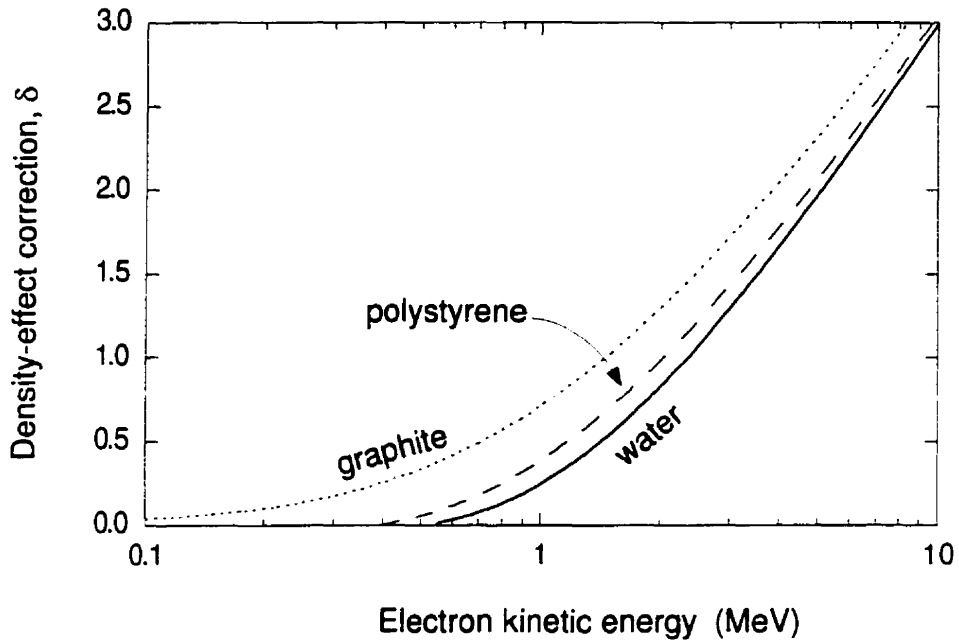
FIGURE 3.2. Sternheimer density-effect δ correction for electrons in water, polystyrene, and graphite as a function of the electron kinetic energy.

consistent with the experimental value of the mean excitation energy for the medium.[13] A plot of Sternheimer density-effect data published by the ICRU[14] as a function of the kinetic energy for electrons in water, polystyrene, and graphite is shown in Fig. 3.2.

III.B. Mass radiative stopping power

The mass radiative stopping power $(S/\rho)_r$ is the rate of bremsstrahlung production by electrons or positrons and can be written as

$$\left(\frac{S}{\rho}\right)_r = \frac{1}{137}\left(\frac{e^2}{m_o c^2}\right)^2 \frac{N_A Z^2}{A}(T + m_o c^2)\overline{B}_r , \tag{3.12}$$

in which T is the kinetic energy of the incident electron and $\overline{B}_r$ is a slowly varying function of Z and T having a value of roughly 6 for $T = 1$ MeV, 12 for 10 MeV, and 15 for 100 MeV.[ref. 1] It should be noted that $\overline{B}_r Z^2$ is a dimensionless quantity.

III.C. Total mass stopping power

The total mass stopping power simply is equal to the sum of the mass collisional stopping power and the mass radiative stopping power:

$$\left(\frac{S}{\rho}\right) = \left(\frac{S}{\rho}\right)_c + \left(\frac{S}{\rho}\right)_r . \tag{3.13}$$

IV. Restricted mass stopping power

Just as the total mass stopping power is divided into a collisional and radiative part to account for energy which escapes the interaction site, the collisional part may be subdivided into two components. The soft portion of the collisional stopping power refers to interactions in which very low-energy secondary electrons are produced and locally absorbed. In contrast, the δ rays produced in hard collisions are energetic enough to carry and, consequently, deposit some of their kinetic energy a significant distance from the original electron track. Consideration of energetic δ rays becomes particularly important when calculating the dose to a thin foil traversed by an electron beam as the δ rays will escape the foil and not contribute to the dose at all. Thus the use of the mass collisional stopping power will overestimate the dose, unless δ–ray equilibrium exists so that for each δ ray escaping the foil, a δ ray from upstream enters the foil.

The *restricted mass collisional stopping power* $(L/\rho)_\Delta$ includes all soft collisions and those hard collisions resulting in the production of secondary electrons having kinetic energy less than some cutoff value Δ. The cutoff value is usually selected to correspond to the energy of electrons which have a mean range in the medium appropriate to the geometry of the dose deposition region. Thus for a thicker foil, a higher Δ may be selected. The restricted mass collisional stopping power is calculated by substituting Δ

for W_{max} in the limit of the integral in Eq. (3.8). If Δ is increased to equal W_{max} ($T/2$ for electrons and T for positrons) then

$$\left(\frac{S}{\rho}\right)_c = \left(\frac{L}{\rho}\right)_{\Delta=W_{max}} = \left(\frac{L}{\rho}\right)_\infty . \tag{3.14}$$

where $\left(\frac{L}{\rho}\right)_\infty$ is referred to as the *unrestricted collisional stopping power*.

Let $\eta = \Delta/\tau$, then for electrons and positrons, the restricted mass stopping power may be written as follows:[14]

$$\left(\frac{L}{\rho}\right)_\Delta = 2\pi r_o^2 \left(\frac{N_A Z}{A}\right) \frac{m_o c^2}{\beta^2} \left\{ \ln \left[\frac{\tau^2(\tau+2)}{2(I/m_o c^2)^2} \right] + G^\pm(\tau,\eta) - \delta \right\} . \tag{3.15}$$

which is similar to Eq. (3.9) except that for electrons, one uses

$$G^-(\tau,\eta) = -1 - \beta^2 + \ln[4(1-\eta)\eta] + \frac{1}{(1-\eta)}$$
$$+ (1-\beta^2)\left[\frac{\tau^2\eta^2}{2} + (2\tau+1)\ln(1-\eta)\right] . \tag{3.16}$$

and for positrons, substituting $\xi = (\tau+2)^{-1}$,

$$G^+(\tau,\eta) = \ln 4\eta - \beta^2 \times [1 + (2-\xi^2)\eta - (3+\xi^2)\left(\frac{\xi\tau}{2}\right)\eta^2$$
$$+ (1+\xi\tau)\left(\frac{\xi^2\tau^2}{3}\right)\eta^3 - \left(\frac{\xi^3\tau^3}{4}\right)\eta^4] . \tag{3.17}$$

Note that $G^-(\tau,1/2) = F^-(\tau)$ and $G^+(\tau,1) = F^+(\tau)$.

V.   Radiation yield

Now that the mass collisional and radiative stopping powers have been defined, it is possible to introduce the *radiation yield* $Y(T_o)$ of an electron having initial kinetic energy T_o. The radiation yield is defined as the fraction of energy that is emitted in the form of electromagnetic radiation as the electron is brought to rest in the medium. For electrons, only bremsstrahlung contributes to $Y(T_o)$; for positrons, in-flight annihilation is also a factor, although, it is normally ignored in the calculation of $Y(T_o)$.

For an electron of instantaneous kinetic energy T we can define $y(T)$ as

$$y(T) = \frac{(S/\rho)_r}{(S/\rho)} \, . \tag{3.18}$$

The radiation yield for an electron with initial kinetic energy T_o is then calculated as follows:

$$Y(T_o) = \frac{\int\limits_{T_o}^{0} y(T)dT}{\int\limits_{T_o}^{0} dT} = \frac{1}{T_o} \int\limits_{0}^{T_o} y(T)dT \, . \tag{3.19}$$

The amount of energy radiated per electron is then $E_r = T_o \cdot Y(T_o)$.

In the calculation of the mass absorption coefficient in Section III.H of Chapter 2, a factor g was introduced in Eq. (2.34). The g–factor is defined as the average value of $Y(T_o)$ for all electrons and positrons of various starting energies present, thus one can write

$$g = \overline{Y}(T_{max}) = \frac{\int\limits_{0}^{T_{max}} \Phi_e Y(T_o)dT}{\int\limits_{0}^{T_{max}} \Phi_e dT} \, , \tag{3.20}$$

where Φ_e is the secondary electron spectrum produced by photon interactions in the medium.

VI. Energy absorbed by the medium

At this stage it is possible to determine the dose absorbed by the medium. The absorbed dose is equal to the amount of energy absorbed per unit mass of absorber and is measured in grays (Gy), where 1 Gy = 1 J/Kg.

Consider a monoenergetic electron beam of energy T passing through a foil made of a known medium. The dose D absorbed by the medium simply will equal the product of the monoenergetic electron fluence Φ_T (cm^{-2}), the mass restricted stopping power $(L/\rho)_\Delta^T$ (MeV cm^2 g^{-1}) for electrons with kinetic energy T, and a conversion factor relating MeV/g to Gy,

$$D = 1.602 \times 10^{-10}\ \Phi_T \left(\frac{L}{\rho}\right)_\Delta^T. \tag{3.21}$$

This calculation assumes that in a thin foil, radiative photons and δ rays will escape and thus not contribute to the absorbed dose.

Rarely, in practice, does one deal with a monoenergetic beam of electrons. In most circumstances one is interested in calculating the dose from a polyenergetic beam of electrons traversing the medium. Rigorously, the absorbed dose should be expressed as

$$D = 1.602 \times 10^{-10} \int_\Delta^{T_{max}} \Phi_e(T)\left(\frac{L(T)}{\rho}\right)_\Delta dT + \sum N_\Delta \cdot \Delta. \tag{3.22}$$

where Δ is the lowest energy for which electrons are considered as part of the electron spectrum $\Phi_e(T)$ (MeV^{-1}cm^{-2}), and the summation accounts for the dose contributed by "track-end electrons" whose energy falls below Δ. Roughly 5–10% of the absorbed dose can be attributed to such track-end electrons.[15]

In subsequent chapters, when the absorbed dose from a spectrum Φ_e of electron energies is required, Eq. (3.21) will be expressed as

$$D = 1.602 \times 10^{-10}\ \Phi_e \left(\frac{L}{\rho}\right)_\Delta, \tag{3.23}$$

where $(\overline{L}/\rho)_\Delta$ represents the mean restricted stopping power found from Eq. (3.22).

VII. Summary

There are, in general, three types of electron interactions with the medium which correspond to $b >> a$ (soft collisions), $b \sim a$ (hard collisions), and $b << a$ (radiative collisions). Soft collisions describe the numerous low-energy interactions which occur between the kinetic electron and the atoms of the medium. Hard collisions describe the relatively infrequent interactions between the kinetic electron and an individual orbital electron resulting in a large transfer of kinetic energy to the orbital electron followed by its subsequent ejection from the atom. Although hard collisions are much less numerous than soft collisions, on average, a comparable fraction of the incident electron energy is lost to hard and soft collisions. When the impact parameter of the kinetic electron is less than the atomic radius, the electron is likely to interact with the Coulomb-field of the nucleus. In 98% of such collisions, the electron is scattered elastically; in the other 2% of interactions with the nucleus, the electron loses a large portion of its kinetic energy to bremsstrahlung production.

The expectation value of the rate of kinetic energy loss per unit path length of the charged particle is known as the stopping power S. Stopping powers are calculated based on the continuous slowing down approximation of charged particles in matter and can be divided into collisional and radiative stopping powers. Energy lost to collision generally contributes to the locally absorbed dose, while energy lost to radiation is carried away from the interaction site.

Occasionally, a δ ray is produced in the medium which can transport kinetic energy a large distance from the interaction site. This δ–ray energy does not contribute

to the locally absorbed dose and must be accounted for in many cases of radiation dosimetry. The restricted stopping power considers δ–ray production and includes only those collisions in the medium in which the secondary electron has a kinetic energy less than some cutoff value Δ which corresponds to the dimensions of a typical ionization chamber.

As radiation dosimetry is concerned with the amount of energy absorbed by the medium from an electron beam, a method for computing the absorbed dose from an electron beam was developed. The energy locally absorbed from a monoenergetic beam of electrons can be calculated from the product of the monoenergetic electron fluence, the electron stopping power for the electron energy, and a conversion factor relating MeV/g to Gy. For a an electron beam comprised of a spectrum of electron energies, the individual contributions of each electron energy must be summed in order to arrive at the total energy locally absorbed.

References

1. F. H. Attix, *Introduction to Radiological Physics and Radiation Dosimetry* (John Wiley & Son, New York, 1986).

2. J. D. Jackson, *Classical Electrodynamics* (Wiley, New York, second edition, 1975).

3. J. R. Greening, "Saturation characteristics of parallel-plate ionization chambers," Phys. Med. Biol. **9**, 143–154 (1964).

4. H. A. Bethe, "Zur Theorie des Durchgangs schneller Korpuskularstrahlen durch Materie," Ann. Physik **5**, 325 (1930).

5. H. A. Bethe, "Bremsformel für Elektronen relativistischer Geschwindigkeit," Z. Physik **76**, 293 (1932).

6. E. J. Williams, "The passage of α– and β–particles through matter and Born's theory of collisions," Proc. Roy. Soc. A (London) **135**, 108–142 (1932).

7. M. S. Livingston and H. A. Bethe, "Nuclear physics," Rev. Mod. Phys. **9**, 245 (1937).

8. P. Marmier and E. Sheldon, *Physics of Nuclei and Particles* Volume 1 (Academic Press, New York, 1969).

9. E. A. Uehling, "Penetration of heavy charged particles in matter," Annual Rev. Nucl. Sci. **4**, 315–350 (1954).

10. M. J. Berger and S. M. Seltzer, "Stopping powers and ranges of electrons and positrons," Report NBSIR 82–2550–A, National Bureau of Standards, Washington, D.C., 1983.

11. W. F. G. Swann, "Theory of energy loss of high energy particles," J. Franklin Inst. **226**, 598 (1938).

12. E. Fermi, "The ionization loss of energy in gasses and in condensed materials," Phys. Rev. **57**, 485 (1940).

13. R. M. Sternheimer, "The density effect for the ionization loss in various materials," Phys. Rev. **88**, 851–859 (1952).

14. ICRU, "Radiation dosimetry: electron beams with energies between 1 and 50 MeV," Report 35, International Commission on Radiation Units and Measurement, Washington, D.C., 1984.

15. D. W. O. Rogers, in *Advances in Radiation Oncology Physics*, edited by J. A. Purdy, pp. 181–223 (American Institute of Physics, Lawrence, Kansas, 1990), Proceedings of the AAPM 1990 summer school.

CHAPTER 4

Measurement of absorbed dose

The goal of radiation dosimetry is the measurement and quantification of absorbed dose. Several techniques exist for the measurement of absorbed dose, the most important of which were mentioned in Chapter 1. A proper discussion of radiation dosimetry must begin with an introduction to the quantities used to characterize a radiation beam, followed by a description of the mechanisms by which energy is transferred to and subsequently absorbed by the medium. With respect to radiation dosimetry a very important quantity used to describe a beam of radiation is the radiation fluence. Fluence can refer to a beam of either directly or indirectly ionizing particles, and can also refer to secondary particles produced in the medium.

I.   Concepts in radiation dosimetry

I.A.   Photon fluence

Some naturally occurring radioisotope photon sources of clinical interest produce monoenergetic or quasi-monoenergetic photon beams. X ray generating machines, in contrast, produce beams which consist of photons comprising an entire spectrum of energies. The photon fluence ϕ of a monoenergetic photon beam was defined by the ICRU[1] as the number of photons dN that intersect a sphere of cross-sectional area dA:

$$\phi = \frac{dN}{dA}.$$ (4.1)

If the photon beam is comprised of photons of various energies, the photon fluence

described by Eq. (4.1) is implicitly understood as

$$\phi(h\nu) = \frac{dN(h\nu)}{dA},\qquad(4.2)$$

where $h\nu$ is the photon energy. Alternatively, a beam of photons may be described in terms of the photon energy fluence ψ, or the amount of energy $d(N \cdot h\nu)$ carried by a beam of photons through a sphere of cross-sectional area dA, where

$$\psi = \frac{dN \cdot h\nu}{dA}.\qquad(4.3)$$

Although the concept of photon fluence is simple, the actual representation of a photon beam in terms of its fluence or its energy fluence is difficult because it requires the knowledge of the exact number and energy of each photon comprising the beam. Characterizing a beam of radiation in terms of its fluence can, however, be a useful abstraction and forms the basis for the Bragg–Gray cavity theory (see Section III.A).

I.B. Energy transfer to the medium: kerma

In previous chapters, it was shown that the transfer of energy from a beam of photons to the medium is a two-step process. The first step involves the interaction of photons with the medium and the subsequent transfer of photon energy to electrons in the medium. A quantity kerma K has been introduced for the purpose of describing the initial transfer of energy from the photon beam to kinetic energy of electrons in the medium. Kerma is an acronym for kinetic energy released in matter, and has been defined by the ICRU[1] as

$$K = \frac{d\overline{E}_{tr}}{dm},\qquad(4.4)$$

where $d\overline{E}_{tr}$ is the mean energy *transferred* from photons to electrons within a mass element dm of the medium. The mean energy transferred from a large number of photons

was described in Section III.G of Chapter 2 to be a function of the photon energy and can be calculated from Eq. (2.32).

The kerma can be expressed in terms of the photon fluence ϕ as

$$K = \phi\left(\frac{\mu}{\rho}\right)\overline{E}_{tr} ,$$

(4.5)

where (μ/ρ) is the photon mass attenuation coefficient in the medium and $\overline{E}_{tr}$ is the mean energy transferred to an electron per interaction. The product $\phi(\mu/\rho)$ represents the expectation value for the number of photon interactions per unit mass of medium.

For a photon beam containing a spectrum of photon energies the kerma can be expressed as the integral over all photon energies $\xi = h\nu$ comprising the beam spectrum. Thus, kerma can then be written as follows:

$$K = \int_{\xi=0}^{\xi=h\nu_{max}} \frac{d\phi(\xi)}{d\xi}\left(\frac{\mu(\xi)}{\rho}\right)\overline{E}_{tr}(\xi)\,d\xi .$$

(4.6)

The unit of measurement for kerma is J/kg.

I.C.   Energy absorbed by the medium: absorbed dose

The quantity of most importance in radiotherapy is the absorbed dose. The ICRU[1] has defined the absorbed dose D as

$$D = \frac{d\overline{E}_{ab}}{dm} .$$

(4.7)

where $d\overline{E}_{ab}$ is the mean energy *absorbed* from ionizing radiation by a mass element dm of medium. The elemental mass dm must be sufficiently small to be considered a point on a macroscopic scale, yet not so small that statistical fluctuations in the energy deposition become significant. Absorbed dose has been given a special unit of measurement, the gray, or Gy, which is equal to 1 J/kg.
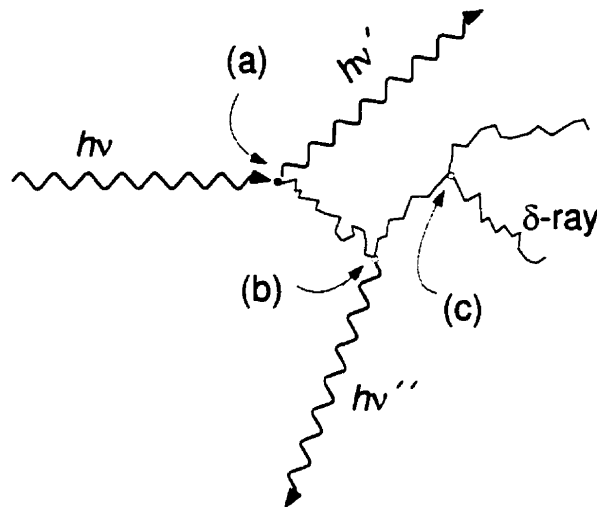
FIGURE 4.1. Schematic representation of the transfer of energy from a photon of energy $h\nu$ to the medium. *Kerma*: An incident photon transfers $h\nu - h\nu'$ of energy to an electron in the medium at (a). *Absorbed dose*: the medium absorbs the electron kinetic energy all along the electron track. Energy lost to bremsstrahlung (b) and δ-ray production (c) is not locally absorbed and does not contribute to the absorbed dose.

The difference between absorbed dose and kerma is clarified with the aid of Fig. 4.1. An incident photon of energy $h\nu$ is scattered at (a) and is left with energy $h\nu'$. An amount of energy $E = h\nu - h\nu'$ is transferred to an atomic electron in the form of kinetic energy. This transfer of kinetic energy to the electron from the incident photon represents the kerma. The electron then travels through the medium, losing its kinetic energy mostly in small collisions along its track. The small amounts of energy lost by the electron along its track are locally absorbed by the medium and contribute to the absorbed dose. At point (b) the electron interacts with a nucleus to produce a bremsstrahlung photon which carries its energy out of the region. At (c) the electron interacts violently in an electron-electron collision and loses a large quantity of energy to a secondary electron called a δ ray. The δ ray is sufficiently energetic to carry its energy away from the interaction site (c) and produce its own ion track. Clearly, the absorbed dose occurs over

a relatively large volume of the medium and is equal to the kerma, which occurs entirely at point (a) less the energy lost to bremsstrahlung photons (b) and δ rays (c).

I.D.   Electronic equilibrium

The fact that absorbed dose and kerma do not occur at the same point has some interesting ramifications in radiation dosimetry. Although Eq. (4.6) gives a simple relation between the photon fluence and the kerma, there is no similar way to calculate absorbed dose unless a state of electronic equilibrium exists at the point of interest. Absorbed dose can be conceptualized with the aid of an illustration of the energy absorption process as provided schematically in Fig. 4.2. As the photon beam traverses the medium, it continually produces secondary electrons, such as the one shown in Fig. 4.1, which move through the medium causing ionization and excitation.

Figure 4.2 (a) illustrates a large number of secondary electrons produced by a beam of photons as it passes through the medium. For simplicity, it is assumed that electrons are slowed down continuously in the medium, and that they all travel with the same small angle relative to the direction of the photon beam.

The density of secondary electron tracks shown in Fig. 4.2 (a) represents the fluence of secondary electrons in the medium. From the diagram, it is evident that the density of secondary electron tracks increases from zero at the phantom surface and reaches a maximum value at a depth nearly equal to the electron range in the medium. At this depth, the number of electrons leaving a given volume of medium is exactly equal to the number of electrons entering the volume, and electronic equilibrium is assumed to exist.

Consider first the simplified case in which a photon beam generates electrons in the medium, but does not suffer appreciable attenuation. Given that there is no attenuation

electrons set in motion in the medium
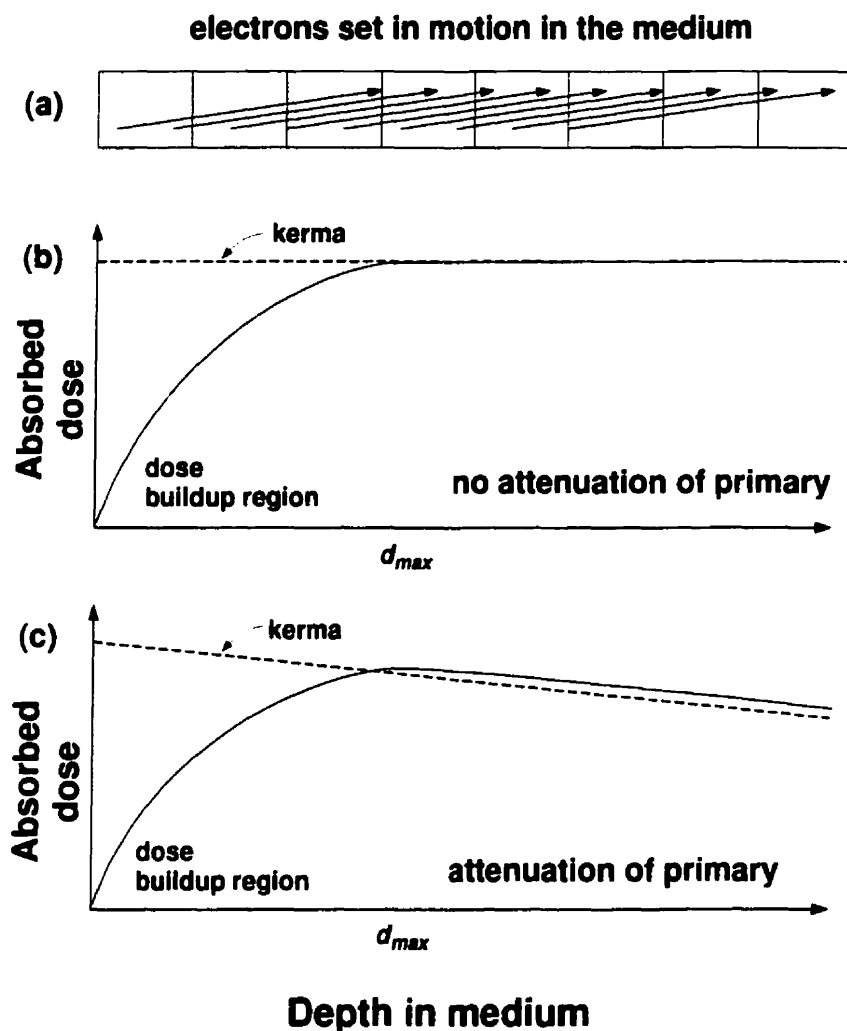

Depth in medium

FIGURE 4.2. Illustration of absorbed dose and kerma. (a) Electrons are set in motion in the medium and are continually slowed down by the medium. (b) No photon attenuation occurs in the medium, therefore the kerma remains constant with depth. The absorbed dose increases from zero (at the phantom surface) to its maximum value (at d_{max}) equal to the kerma. (c) The photon beam is attenuated by the medium and kerma decreases exponentially. Here, the absorbed dose rises to a maximum value at d_{max} and then decreases with depth following the decay of the kerma.

of the photon beam, the kerma, *i.e.*, the number of secondary electrons set in motion in the medium by photons, remains constant with depth in the medium as shown in Fig. 4.2 (b). Equation (3.23) states that the absorbed dose D is proportional to the flux of electron tracks passing through any point in the medium, thus D begins at zero on the

phantom surface and gradually increases to a constant value characteristic of electronic equilibrium. The depth at which the absorbed dose reaches a maximum value is called the depth dose maximum d_{max}, and the region between the phantom surface and d_{max} is referred to as the dose buildup region. At depths beyond d_{max}, in the absence of bremsstrahlung, the absorbed dose is exactly equal to the kerma. For a photon beam that is not attenuated by the medium, wherever electronic equilibrium is said to exist, the absorbed dose may be expressed in terms of the kerma as follows:

$$D = \phi \left(\frac{\mu}{\rho} \right) \overline{E}_{ab} = K(1 - g) , \qquad (4.8)$$

where the mean energy absorbed per photon interaction $\overline{E}_{ab}$, and the fraction of energy that is lost to bremsstrahlung g, were defined in Chapter 2, Section III.H.

If one now considers the situation in which the photon beam is exponentially attenuated by the medium, then the kerma is an exponentially decreasing function of the depth in medium. In this situation, electronic equilibrium is never truly established; however, a state of *transient electronic equilibrium* is eventually reached. The absorbed dose D increases until it reaches a maximum value at d_{max} and then decreases essentially exponentially with depth, following the exponential decrease in the kerma. In Fig. 4.2 (c), the absorbed dose at depth d, where $d \gtrsim d_{max}$, is shown to be always greater than the kerma in the transient equilibrium region. This is because the absorbed dose arises from electrons produced at points downstream from the point of measurement, *i.e.*, in regions where the kerma is larger than it is at d.

Normally, the curves for the absorbed dose and the kerma run parallel to each other, and the curve for absorbed dose is higher than that for kerma by a nearly constant factor β. Hence, the absorbed dose $D(d)$ at depth d in the medium, under conditions of transient electronic equilibrium, may be found from the kerma $K(d)$ at depth d according

to the following equation:

$$D(d) = \phi(d) \left(\frac{\mu}{\rho}\right) \overline{E}_{ab}\beta = K(d)\,\beta(1-g) \ . \tag{4.9}$$

II. Dose to a small mass of medium in air

Following the basic discussion of kerma and absorbed dose, it is possible to calculate the absorbed dose from measurements of the exposure in air. The exposure X in air has been defined in Section II.C of Chapter 1 as dQ/dm, the amount of charge produced per unit mass of air by the passage of ionizing radiation. A given beam of radiation will produce an exposure X in air at point P as shown in Fig. 4.3 (a) which can be related to the air kerma through a conversion factor κ,

$$K_{air} = \kappa X \ , \tag{4.10}$$

where $\kappa = 0.876$ cGy/R and exposure is measured in Roentgens. If a small mass Δm of medium is placed at P, such as in Fig. 4.3 (b), the kerma in the small mass $K_{\Delta m}$ can be found from the following equation:

$$K_{\Delta m} = K_{air} \left(\frac{\mu_{tr}}{\rho}\right)_{air}^{\Delta m} \ , \tag{4.11}$$

where $(\mu_{tr}/\rho)_{air}^{\Delta m}$ denotes the ratio of the mass energy transfer coefficients of the small mass of medium Δm to that of air, *i.e.*, $(\mu_{tr}/\rho)_{\Delta m}/(\mu_{tr}/\rho)_{air}$.

For the purposes of dose calibration, a sufficient quantity of material must be added around Δm in order to establish electronic equilibrium at P [Fig. 4.3 (c)]. With the additional medium surrounding Δm, the kerma at P will be reduced by a small factor $k(r_{med})$ which accounts for attenuation of the photon beam in the medium. The
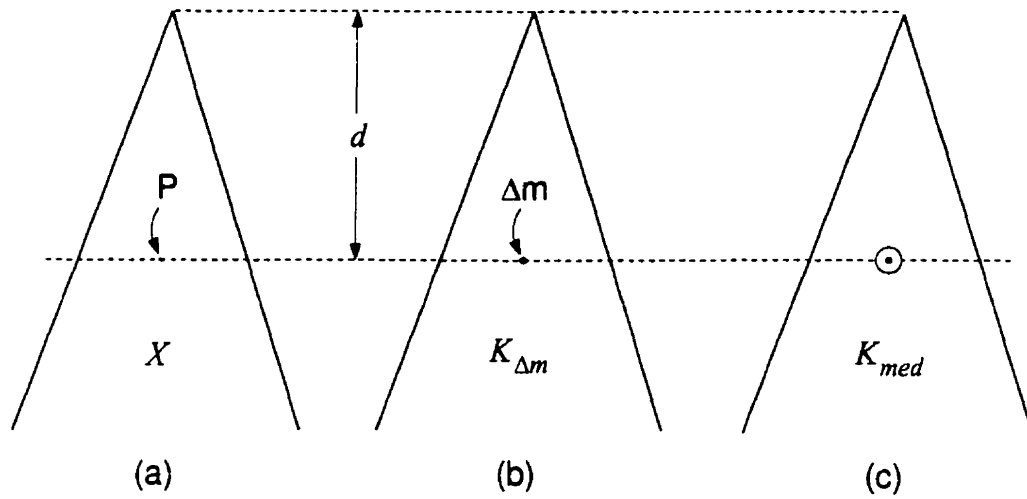
75

FIGURE 4.3. (a) Measurement of exposure X at a point P in air, (b) determination of kerma to a small mass of medium $K_{\Delta m}$, and (c) determination of kerma to a practical mass of medium K_{med} in which electronic equilibrium is established. The distance between the radiation source and point P is f.

correction factor $k(r_{med})$ is simply

$$k(r_{med}) = \exp\left\{-\left(\frac{\mu_{ab}}{\rho}\right)_{med} \rho_{med} r\right\}$$ (4.12)

where r is the radius of material required to assure electronic equilibrium. Thus, if the medium surrounding Δm is of the same composition as Δm itself, the kerma at the center of the mass of medium K_{med} may be written in terms of $K_{\Delta m}$ as follows:

$$K_{med} = K_{\Delta m} k(r_{med}) = 0.876 \cdot X \left(\frac{\mu_{tr}}{\rho}\right)_{air}^{med} k(r_{med}).$$ (4.13)

The absorbed dose to the mass of medium D_{med} in air may be found from substitution of Eq. (4.13) into Eq. (4.8) giving

$$D_{med} = K_{med}(1 - g)\beta = 0.876 \cdot X\beta \left(\frac{\mu_{tr}}{\rho}\right)_{air}^{med} (1 - g)\, k(r_{med})$$

$$= 0.876 \cdot X \beta \left(\frac{\mu_{ab}}{\rho} \right)^{med}_{air} k(r_{med}) \ ,$$ (4.14)

in which the relation $(\mu_{ab}/\rho) = (\mu_{tr}/\rho)(1 - g)$ was used.

III. Cavity theory

In order to determine the dose absorbed by a given medium through an indirect means, such as by the insertion of an ionization chamber into a dosimetric phantom, it is first necessary to determine the dose absorbed by the gas in the ionization chamber and then relate this dose to that which would be absorbed in the phantom were the ionization chamber not present. A number of theories have been developed which relate the dose measured by a given instrument to the dose in the unperturbed medium. The most notable of these "cavity" theories was developed by W. H. Bragg and L. H. Gray in the first half of this century.

III.A. Bragg–Gray cavity theory

The underlying principles of cavity theory are contained in Eq. (3.23). If a mono-energetic electron beam of fluence Φ_T and kinetic energy T passes through an interface between two media, g and m, as shown in Fig. 4.4 then the dose absorbed on the g side of the interface is given by

$$D_g = \Phi_T \left(\frac{S_T}{\rho} \right)_g ,$$ (4.15)

and on the m side by

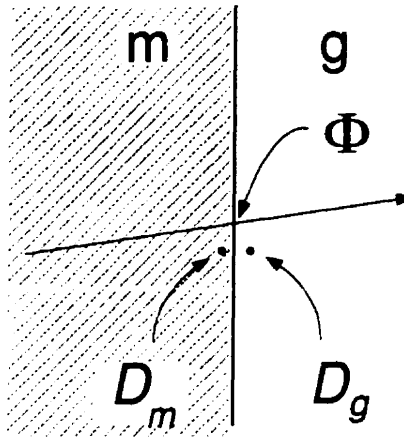$$D_m = \Phi_T \left(\frac{S_T}{\rho} \right)_m ,$$ (4.16)

FIGURE 4.4. The electron fluences immediately on either side of the interface between m and g are identical, therefore, the absorbed dose on either side of the interface may be related through Eq. (4.17).

where $(S_T/\rho)_g$ and $(S_T/\rho)_m$ represent the mass collision stopping power ratios for electrons of energy T travelling through media g and m, respectively.

Ignoring backscatter, the electron fluences are identical on either side of the interface, thus,

$$\frac{D_g}{D_m} = \frac{(S_T/\rho)_g}{(S_T/\rho)_m} = \left(\frac{S}{\rho}\right)^g_m .$$

(4.17)

where $(S/\rho)^g_m$ represents the ratio of mass collision stopping powers in media g and m for electrons of appropriate kinetic energy T.

W. H. Bragg[2] and L. H. Gray[3] applied Eq. (4.17) to the problem of relating the absorbed dose in a cavity gas to the dose which would be absorbed in the surrounding medium in the absence of the cavity. Consider a cavity of medium g surrounded by some medium m, as depicted in Fig. 4.5. For Eq. (4.17) to remain valid, the mass thickness of the g–layer must be small compared to the electron range in g so that the presence of
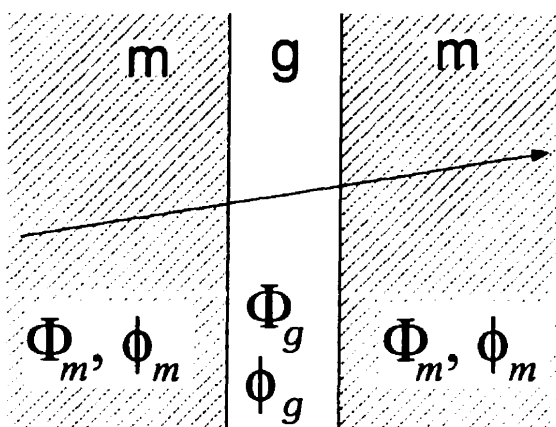
78

FIGURE 4.5. Schematic diagram of a simple Bragg–Gray cavity in which the thin mass-layer of medium g is surrounded by medium m. The electron and photon fluences in the medium Φ_m and ϕ_m, respectively, are unperturbed by g and thus are equivalent to Φ_g and ϕ_g. The doses D_m and D_g are related through Eq. (4.20).

the cavity does not perturb the electron fluence to an appreciable extent, *i.e.*, the electron fluence in cavity g must be the same as the fluence in the undisturbed medium m, or $\Phi_T^m = \Phi_T^g$. This is known as the *first Bragg–Gray condition*. In addition, the scattering properties of g must be similar to those of medium m so that if g were replaced by an equal mass-layer of m, the electrons would experience the same amount of scattering.

The *second Bragg–Gray condition* stipulates that the *absorbed dose in the cavity is deposited entirely by electrons crossing the cavity*. Implicit in this statement is that (1) all electrons crossing the cavity originate outside the cavity, *i.e.*, no electrons originate inside the cavity, and (2) no electrons are stopped within the cavity.

Under the two Bragg–Gray conditions, Eq. (4.17) will give the ratio of absorbed dose in media g and m, respectively, for each monoenergetic component of the spectrum of electrons crossing g. To calculate the ratio of absorbed dose due to a spectrum of

incident electron energies, the *mean* mass electron collision stopping power for each medium must be calculated. In medium g, the average mass collision stopping power is given by

$$\left(\frac{\overline{S}}{\rho}\right)_g = \frac{\int_0^{T_{max}} \Phi(T) \cdot \left(\frac{S(T)}{\rho}\right)_g dT}{\int_0^{T_{max}} \Phi(T) dT} = \frac{D_g}{\Phi}, \tag{4.18}$$

and in medium m, it is given by

$$\left(\frac{\overline{S}}{\rho}\right)_m = \frac{\int_0^{T_{max}} \Phi(T) \cdot \left(\frac{S(T)}{\rho}\right)_m dT}{\int_0^{T_{max}} \Phi(T) dT} = \frac{D_m}{\Phi}, \tag{4.19}$$

where $\Phi(T)$ refers to the *primary* electron energy fluence spectrum.

The ratio of the absorbed dose in media m to g is therefore

$$\frac{D_m}{D_g} = \frac{(\overline{S}/\rho)_m}{(\overline{S}/\rho)_g} = \left(\frac{\overline{S}}{\rho}\right)_g^m. \tag{4.20}$$

For ionization chambers, the medium g filling the cavity is usually a gas (typically air). The dose D_{gas} absorbed by the cavity gas can be expressed in terms of the charge Q produced in the gas by ionizing radiation using the following equation:

$$D_{gas} = \frac{Q}{m_{gas}} \overline{W}_{gas}, \tag{4.21}$$

where Q is expressed in coulombs, m_{gas} is the mass (kg) of the cavity gas in which Q was produced, and $\overline{W}_{gas}$ is the mean energy required to produce an ion pair in air. The currently accepted value[4, 5] for $\overline{W}_{air}$ in dry air is 33.97 eV/ion pair or 33.97 J/C.

By substituting Eq. (4.21) into Eq. (4.20), the Bragg–Gray relation in terms of the cavity ionization is found:

$$D_{med} = \frac{Q}{m_{gas}} \overline{W}_{gas} \left(\frac{\overline{S}}{\rho}\right)_{gas}^{med}. \tag{4.22}$$

Equation (4.22) permits the calculation of absorbed dose D_{med} to the medium in the immediate vicinity of the cavity from measurement of the ionization within the cavity.

III.B. Spencer–Attix derivation of the Bragg–Gray theory

In 1955 the Bragg–Gray theory was improved upon by L. V. Spencer and F. H. Attix[6] who proposed a theory using a more general method than did Bragg and Gray. Although the cavity theories are valid when charged particle equilibrium does not exist, the Spencer–Attix approach was to investigate the behaviour of the electron spectrum under conditions of charged particle equilibrium. When charged particle equilibrium exists, the dose at any point within a infinite homogeneous medium m that emits N identical charged particles per gram, each having kinetic energy T_0, can be stated as

$$D_m = NT_o .\qquad(4.23)$$

At any point in the medium, there will exist an equilibrium charged-particle fluence spectrum $_e\Phi$, where the subscript e denotes equilibrium. Similarly to Eq. (3.22), the dose can be expressed in terms of $_e\Phi$ as

$$D_m = \int_0^{T_0} {}_e\Phi(T) \cdot \left(\frac{S(T)}{\rho}\right)_m dT .\qquad(4.24)$$

where $(S/\rho)_m$ is the mass collision stopping power in the absence of bremsstrahlung for medium m.

Equating Eqs. (4.23) and (4.24) and differentiating with respect to T_0 leads to the following relationship for the equilibrium spectrum of charged particles in medium m:

$$_e\Phi(T) = \frac{N}{(S/\rho)_m} .\qquad(4.25)$$

Thus, the equilibrium fluence of charged particles in the medium is directly proportional to the number of charged particles released in the medium and inversely proportional

to the mass collision stopping power at each energy. Figure 4.6 is a plot of the equilibrium spectrum of primary electrons resulting from Eq. (4.25) in an aqueous solution containing two sources of electrons, one emitting electrons at $T_0 = 5$ MeV and the other at $T_0 = 0.5$ MeV. The dashed curve in Fig. 4.6 represents the primary electron spectrum which results from the source emitting the 5 MeV electrons. The solid line is the total primary electron spectrum in the aqueous solution resulting from both sources. The primary electron equilibrium spectrum calculated from Eq. (4.25) is based on the continuous slowing down approximation and is, therefore, itself only a first approximation to the true equilibrium spectrum that would actually develop in the medium. Hence, the spectra plotted in Fig. 4.6 are not entirely realistic as secondary electron production has
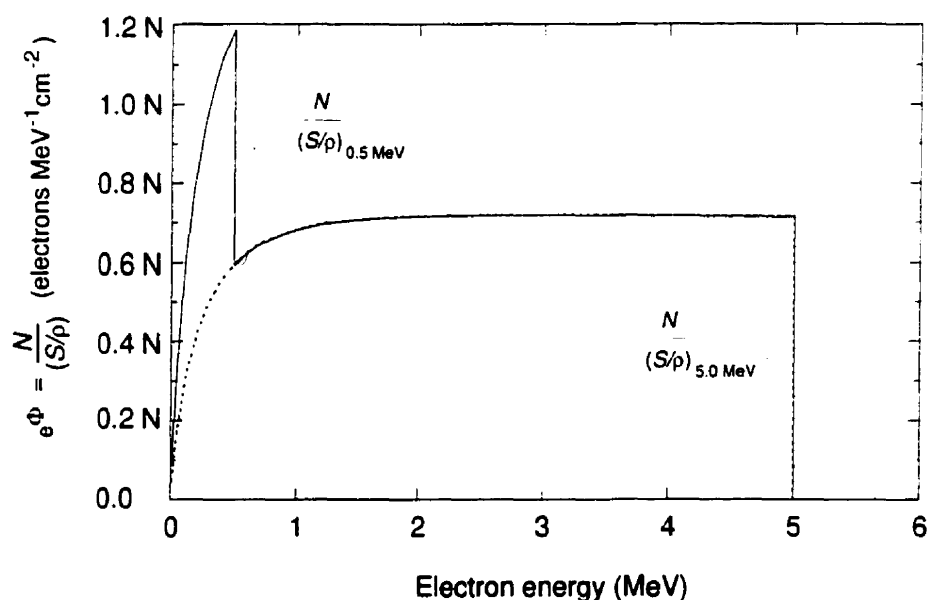

FIGURE 4.6. Example of an equilibrium fluence spectrum, $_e\Phi(T) = N/(S/\rho)$, of primary electrons under conditions of charged particle equilibrium in water assuming the continuous slowing down approximation. The dashed curve represents the primary electron spectrum resulting from a 5 MeV electron source in the aqueous solution. The solid curve is the total primary electron spectrum in the aqueous solution resulting from both 0.5 MeV and 5 MeV sources.

been ignored. In reality, as the incident electrons are slowed down in the water, several lower-energy secondary electrons are produced resulting in an overall enhancement of the low-energy portion of the spectrum.

If a small cavity filled with medium g is placed within the medium m, the same equilibrium charged particle fluence that exists in the medium will cross the cavity. The dose absorbed in the cavity D_g may then be written as

$$D_g = \int_0^{T_o} {}_e\Phi(T) \cdot \left(\frac{S}{\rho}\right)_g dT = N \int_0^{T_o} \frac{(S/\rho)_g}{(S/\rho)_m} dT \ . \tag{4.26}$$

in which ${}_e\Phi$ was replaced with Eq. (4.25). The ratio of the dose in m to the dose in g is found by dividing Eq. (4.26) by Eq. (4.23) to get

$$\frac{D_g}{D_m} = \frac{1}{T_o} \int_0^{T_o} \left(\frac{S}{\rho}\right)_m^g dT = \left(\frac{\overline{S}}{\rho}\right)_m^g \ . \tag{4.27}$$

which is the same as the Bragg–Gray relation given in Eq. (4.20).

The equivalence of Eqs. (4.27) and (4.20) is not immediately apparent, and can be shown explicitly as follows:

(i)   From the Bragg–Gray derivation one has the mean stopping power in the gas as

$$\left(\frac{\overline{S}}{\rho}\right)_g = \frac{\int_0^{T_o} {}_e\Phi(T) \cdot \left(\frac{S(T)}{\rho}\right)_g dT}{\int_0^{T_o} {}_e\Phi(T) dT} = \frac{1}{{}_e\Phi} \int_0^{T_o} {}_e\Phi(T) \cdot \left(\frac{S(T)}{\rho}\right)_g dT$$

$$= \frac{N}{{}_e\Phi} \int_0^{T_o} \left(\frac{S(T)}{\rho}\right)_m^g dT = \frac{D_g}{{}_e\Phi} \ , \tag{4.28}$$

where ${}_e\Phi(T)$ was calculated in Eq. (4.25).

(ii)   Likewise, the mean stopping power in the surrounding medium is given by

$$\left(\frac{\overline{S}}{\rho}\right)_m = \frac{\int_0^{T_o} {}_e\Phi(T) \cdot \left(\frac{S(T)}{\rho}\right)_m dT}{\int_0^{T_o} {}_e\Phi(T)dT} = \frac{N}{{}_e\Phi} \int_0^{T_o} \left(\frac{S}{\rho}\right)_m dT$$

$$= \frac{NT_o}{{}_e\Phi} = \frac{D_m}{{}_e\Phi} . \tag{4.29}$$

(iii)   Thus, the ratio of mean stopping powers is

$$\left(\frac{\overline{S}}{\rho}\right)_m^g = \frac{1}{T_o} \int_0^{T_o} \left(\frac{S}{\rho}\right)_m^g dT = \frac{D_g}{D_m} . \qquad \text{Q.E.D.}$$

The Spencer–Attix treatment of the Bragg–Gray cavity theory described above can be generalized to accommodate bremsstrahlung production in the medium by rewriting Eq. (4.23) as

$$D_m = NT_o[1 - Y_m(T_o)] . \tag{4.31}$$

in which $Y_m(T_o)$ is the radiation yield in medium m for charged particles of energy T_0 as defined in Chapter 3, Section V. The use of Eq. (4.31) in the Spencer–Attix formalism leads to the following relationship which includes bremsstrahlung production:

$$\frac{D_g}{D_m} = \frac{1}{T_o[1 - Y_m(T_o)]} \int_0^{T_o} \left(\frac{S}{\rho}\right)_m^g dT = \left(\frac{\overline{S}}{\rho}\right)_m^g . \tag{4.32}$$

III.C. Spencer–Attix cavity theory

The Spencer–Attix cavity theory is based on the Bragg–Gray theory and thus begins with the same basic assumptions, namely that (1) the two Bragg–Gray conditions

are satisfied, and (2) bremsstrahlung production is absent. However, two modifications

to the Bragg–Gray theory were introduced by Spencer and Attix which significantly

improve the original theory.

The first modification to the Bragg–Gray theory is the inclusion of δ rays in

the equilibrium electron spectrum. The Spencer–Attix equilibrium electron fluence is

denoted by $^\delta_e\Phi$ to emphasize the inclusion of δ rays and to differentiate it from the

primary equilibrium spectrum $_e\Phi$ employed in the Bragg–Gray theory.

The second modification to the original cavity theory involves the characterization

of the cavity with respect to a parameter Δ, which represents the mean energy of electrons

having a projected range just large enough to cross the cavity. Thus, in the Spencer–Attix

formalism, the equilibrium charged particle fluence $^\delta_e\Phi$ is divided into two components

comprising fast and slow electrons:

(i)   *Fast electrons:* electrons with kinetic energies $T \geq \Delta$ and capable of transporting

        energy through the medium. These electrons have enough energy to cross the

        cavity if they strike it.

(ii)   *Slow electrons:* electrons with kinetic energies $T < \Delta$ assumed to have *zero*

        range in the medium and thus do not transport energy across the cavity. These

        electrons are produced in the medium but cannot enter the cavity. This last

        assumption does not introduce any errors to the theory since secondary charged

        particle equilibrium is said to exist.

The second Spencer–Attix modification to the Bragg–Gray cavity theory naturally

leads to the use of the *restricted mass collision stopping power* (L/ρ) in the calculation of

the absorbed dose. Recall from Section IV of Chapter 3 that the restricted mass collision

stopping power is that fraction of the mass collision stopping power that includes only

energy transfers W to the medium in which $W < \Delta$.

According to the Spencer–Attix formalism of the cavity theory, the absorbed dose at any point in the medium m where charged particle equilibrium exists is

$$D_m = NT_o = \int_{\Delta}^{T_o} {}_e^{\delta}\Phi(T) \cdot \left(\frac{L_{\Delta}(T)}{\rho} \right)_m dT + \sum N_{\Delta} \cdot \Delta \, . \qquad (4.33)$$

where $(L_{\Delta}(T)/\rho)_m$ is the restricted mass collision stopping power in medium m for electrons of kinetic energy T, excluding energy losses to the medium in excess of Δ. The integral in Eq. (4.33) has a lower limit of Δ because electrons of lesser energy are assumed to have zero range.

Following the same series of steps which led to Eq. (4.20), and using (L_{Δ}/ρ) rather than (S/ρ) with the appropriate limits of integration, one can show that in the Spencer–Attix formalism, the ratio of absorbed doses in the medium and the cavity is given by

$$\frac{D_m}{D_g} = \left(\frac{\overline{L}}{\rho} \right)_g^m \, . \qquad (4.34)$$

The Spencer–Attix theory gives a somewhat better agreement with experimental observations by taking into account the production of δ rays in the medium and by incorporating the cavity size in the calculation of the absorbed dose. However, the Spencer–Attix cavity theory still relies on the Bragg–Gray conditions and can be expected to fail if these conditions are violated.

Ionization chamber wall correction factors. The standard Bragg–Gray and hence the Spencer–Attix cavity theories are both based on the assumption that the presence of the cavity does not perturb the photon fluence or the electron fluence in the medium. In reality, however, the fluence in the medium is perturbed by the cavity and

the extent to which the particle fluence is perturbed depends on the cavity geometry. For dose measurement, the cavity consists of a volume of air surrounded by a wall material that usually differs in composition from the medium in which the dose is measured.

The wall material has two effects on the dosimetry. Firstly, the chamber wall attenuates the primary photon beam differently than the medium and thus may affect the photon fluence at the depth of measurement. Secondly, the wall generates electrons of its own that will contribute to the ionization in the cavity and may prevent electrons produced in the medium from entering the cavity.

The photon fluence at the center of an air cavity, such as that shown in Fig. 4.7 will be higher than that which would be present in the absence of the cavity since air is less attenuating than any water-equivalent medium. The presence of the wall in an ionization chamber can either raise or lower the photon fluence at the depth of measurement depending on the choice of wall material and the type of medium. A correction factor k_c accounts for the difference in photon attenuation in the presence of the cavity relative to that in the absence of the cavity:

$$k_c = \frac{e^{-\mu_{ab}^{med}c}}{e^{-\mu_{ab}^{air}a} \times e^{-\mu_{ab}^{wall}(c-a)}} \approx \frac{e^{-\mu_{ab}^{med}c}}{e^{-\mu_{ab}^{wall}(c-a)}} = \frac{k(c_{med})k(a_{wall})}{k(c_{wall})} . \qquad (4.35)$$

where a and c are the inner and outer radii of the chamber wall, respectively. The attenuation correction factor k_c along with a correct factor for scatter generated in the chamber wall are combined into a wall correction factor, A_{wall}.

For a cavity with a wall composed of the same material as the surrounding medium, *i.e.*, effectively having no wall at all when inserted into the medium, the dose to the cavity gas is related to the dose in the surrounding medium by Eq. (4.34). For photon beam irradiation, if the wall material differs from the medium and is thick enough to stop all electrons generated in the medium from reaching the air cavity, the dose to the medium
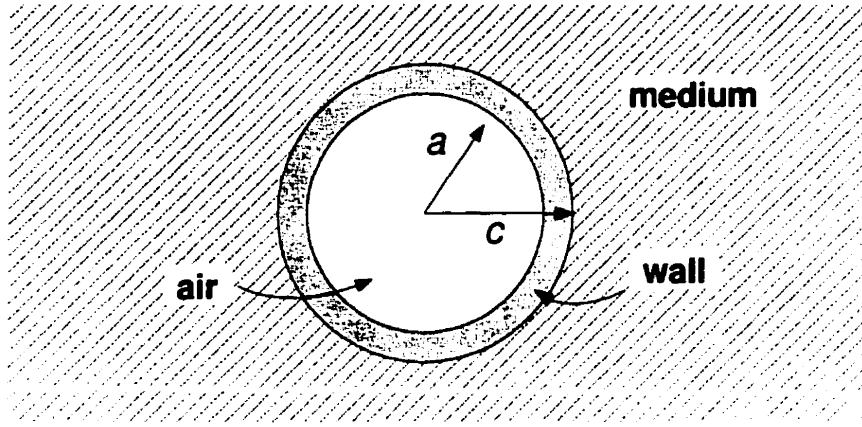
FIGURE 4.7. Illustration of a typical air cavity of radius a used in radiation dosimetry. The cavity is normally surrounded by a conducting material that forms the chamber wall. The chamber of outer radius c is inserted into the medium for dose measurement.

is expressed in terms of the dose to the wall, or

$$D_{med} = D_{wall}\left(\frac{\mu_{ab}}{\rho}\right)_{wall}^{med} = D_{gas}\left(\frac{L}{\rho}\right)_{gas}^{wall}\left(\frac{\mu_{ab}}{\rho}\right)_{wall}^{med}. \tag{4.36}$$

in which the dose to the thick wall was calculated using Eq. (4.34) with the wall replacing the medium.

For a typical ionization chamber, the thickness of the wall is such that some of the ionization in the cavity gas is due to electrons originating in the wall, and some of the ionization comes from electrons generated in the medium. The fraction α of electrons which originate in the chamber wall can be used to combine Eqs. (4.34) and (4.36) to estimate the true dose to the medium and leads to the following expression for the dose to the medium D_{med}:

$$D_{med} = \alpha D_{wall}\left(\frac{\mu_{ab}}{\rho}\right)_{wall}^{med} + (1-\alpha)D_{gas}\left(\frac{L}{\rho}\right)_{gas}^{med}$$

$$= D_{gas}\left[\alpha\left(\frac{L}{\rho}\right)_{gas}^{wall}\left(\frac{\mu_{ab}}{\rho}\right)_{wall}^{med} + (1-\alpha)\left(\frac{L}{\rho}\right)_{gas}^{med}\right]. \tag{4.37}$$

In order to determine the true dose to the medium D_{med} accurately, Eq. (4.37) must be

multiplied by k_c [Eq. (4.35)] to correct for the perturbation of the photon fluence at the

center of the cavity, *i.e.*,

$$D_{med} = D_{gas}\left[\alpha\left(\frac{\bar{L}}{\rho}\right)_{gas}^{wall}\left(\frac{\mu_{ab}}{\rho}\right)_{wall}^{med} + (1-\alpha)\left(\frac{\bar{L}}{\rho}\right)_{gas}^{med}\right]k_c \ . \qquad (4.38)$$

It can be shown that large changes in the value for α produce only a small effect in the

dose calculated with Eq. (4.38). Values for α have been measured by Lempert *et al.*[7]

and are plotted in Figure 7 of the AAPM-TG21 calibration protocol.[8]

The wall correction factor P_{wall} is a factor that accounts for the effects of the

chamber wall and is defined as the ratio of the dose-to-medium in the absence of the wall

to that when wall effects are included, or the quotient of Eq. (4.37) and Eq. (4.34):

$$P_{wall} = \frac{\alpha\left(\frac{\bar{L}}{\rho}\right)_{gas}^{wall}\left(\frac{\mu_{ab}}{\rho}\right)_{wall}^{med} + (1-\alpha)\left(\frac{\bar{L}}{\rho}\right)_{gas}^{med}}{\left(\frac{\bar{L}}{\rho}\right)_{gas}^{med}}$$

$$= 1 - \alpha\left(1 - \left(\frac{\bar{L}}{\rho}\right)_{med}^{wall}\left(\frac{\mu_{ab}}{\rho}\right)_{wall}^{med}\right) \ . \qquad (4.39)$$

For chambers with thin, low atomic number walls, P_{wall} will be very nearly equal to 1.00.

IV.   The AAPM-TG21 protocol: Calibration of photon beams

The purpose of the protocol introduced by the Task Group 21 (TG21) of the

Radiation Therapy Committee of the American Association of Physicists in Medicine

(AAPM) was to provide an accurate method for the determination of absorbed dose

in water for high-energy photon and electron beams. The TG21 protocol covers the

calibration of ^{60}Co γ rays and x rays with nominal accelerating potentials between 2

and 50 MV. The TG21 protocol also deals with the calibration of electron beams in the

energy range from 5–50 MeV.

The TG21 protocol requires that the primary dosimeter be an ionization chamber

having a calibration factor for ^{60}Co γ rays that is directly traceable to a national standards

laboratory (in Canada, National Research Council, Ionizing Radiation Standards Group,

Ottawa; in the United States, National Institute of Science and Technology, Washington,

D.C.). The characterization of ionization chambers at a national standards laboratory

assures both accurate and consistent calibration of radiotherapy machines.

The topics dealt with by the protocol can be divided into four categories:

(i)   The apparatus, including dosimeters and phantoms,

(ii)   The determination of chamber calibration factors at the standards laboratory,

(iii)   The calculation of the dose-to-medium D_{med} in the clinic, and

(iv)   The transfer of D_{med} to the dose-to-water D_{water}.

These topics are discussed in detail below.

IV.A. Calibration apparatus

Dosimeters. The TG21 protocol recommends the use of ionization chambers

of either the cylindrical thimble design or the plane-parallel guarded design. For a

cylindrical chamber placed with its axis perpendicular to the direction of the photon

beam, the protocol sets an upper limit of 1 cm on the internal diameter of the air cavity.

Limiting the dimensions of the ionization chamber cavity used in the protocol helps to

ensure that the chamber behaves like a Bragg–Gray cavity and reduces the magnitude

of the factors used to correct for perturbation of the electron and photon fluence due to

the presence of the cavity.

Available data suggest that the effective depth of measurement for cylindrical ionization chambers should be shifted towards the source by between 0.67 r and 0.75 r from the center of the chamber, where r is the internal radius of the chamber. However, in the TG21 protocol, the central axis of the cylindrical chamber is taken as the depth of measurement. A fluence gradient factor is introduced to correct for the fact that at the proximal surface of a cylindrical cavity the fluence is more intense than the fluence at the central axis, *i.e.*, at the depth of measurement, when the cavity is removed. Replacement corrections for Farmer-type cylindrical chambers used at the Montreal General Hospital are typically less than 0.8% in photon beams.

It is recommended that ionization chambers of the plane-parallel design have a guarded central electrode having a diameter on the order of 2 cm and an electrode separation of roughly 2 mm. The depth of measurement of plane-parallel ionization chambers is accurately defined at the proximal surface of the polarizing electrode and replacement factors associated with these chambers are much smaller than those for cylindrical chambers.

Dosimetry phantoms. The calibration of high-energy photon therapy machines may be conducted in polystyrene or acrylic plastics as well as in water. The solid plastic phantoms are easier to use in practice and offer clinical advantages over water tanks. A suitable dosimetry phantom is chosen to closely mimic the electron density and photon attenuation properties of tissue for the type of radiation to be measured. Regardless of the choice of phantom material the ionization chamber must be placed at a location in the medium where transient electronic equilibrium is established. This means that for photon beams, the depth of calibration in phantom must lie somewhere beyond d_{max}, the depth of dose maximum.

Dosimetry geometry. When plastic phantoms are used, the irradiation geometry must be altered so that the chamber is exposed to the same photon fluence as would be present in a water phantom. The extent to which the irradiation geometry is altered depends on the density of the phantom material. It is recommended that the source-detector distance (SDD) remain constant, but that the thickness of overlying material be scaled so that the attenuation of the incident beam in plastic is equal to that in water.

The calibration of a medical linear accelerator is normally carried out at a depth d_{water} of 5 cm in water and a source–surface distance (SSD) of 100 cm. In a Solid-Water^{TM} phantom, for instance, the SDD should remain constant at 105 cm, however, the depth of measurement d_{sw} must be scaled to correct for attenuation and scatter of the photon beam. Thus the depth of measurement in Solid-Water^{TM} phantom should be

$$d_{sw} = d_{water}\,\frac{\mu_{water}}{\mu_{sw}}\,.\tag{4.40}$$

For a 10 MV photon beam, $\mu_{water}/\mu_{sw} = 1.024$ [ref. 9], thus 1 cm of water is equivalent to 1.024 cm of Solid-Water^{TM} for this beam. A comparison of irradiation geometries for water and Solid-Water^{TM} is illustrated in Fig. 4.8 for a 10 MV photon beam.

The TG21 protocol requires all doses to be reported in terms of dose-to-water, thus, once the dose to the plastic phantom is established, it must be converted to the dose that would have been measured in water. In the case of dose calibration in a water tank, no photon fluence correction or dose conversion factors are required. However, the ionization chamber must be waterproofed when a water tank is employed. It is recommended that a thin, low-atomic number sheath be used for waterproofing the ionization chamber so as to introduce minimal uncertainty to the dose calculation.

IV.B. Ionization chamber calibration factors: N_x and N_{gas}

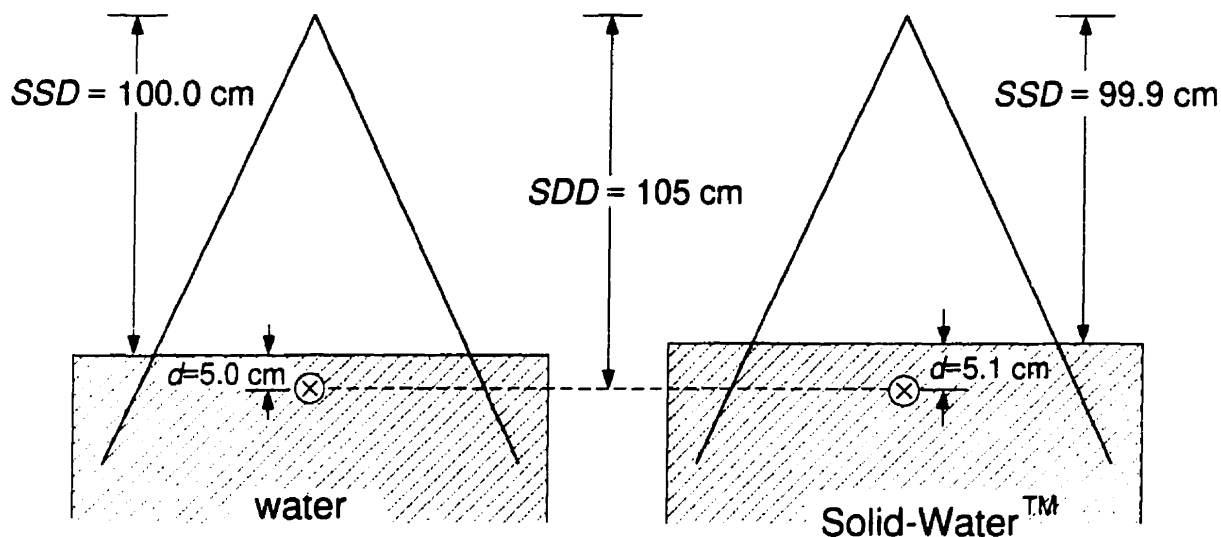The determination of the dose to the medium which surrounds an ionization cham-

FIGURE 4.8. Comparison of the calibration geometry for water and Solid-Water™ phantoms in a 10 MV photon beam.

ber during the calibration of a high-energy photon beam is given by the Spencer–Attix cavity theory which serves as the basis for the TG21 calibration protocol. The theory can be divided into two distinct sections: the first involves the calculation of the dose-to-gas D_{gas} in the cavity from ionization measurements, while the second consists of the conversion of D_{gas} to D_{med}, the dose to the medium in the absence of the chamber cavity. The direct application of the first step of the dose calculation requires the mass of the sensitive volume of the ionization chamber to be known with an uncertainty considerably smaller than the maximum acceptable uncertainty in the dose to the absorbing medium. As the effective sensitive air mass is often difficult to determine in practice, the TG21 protocol suggests that each ionization chamber be calibrated at a national standards laboratory before being used clinically.

The determination of the chamber calibration factors for ^{60}Co γ rays at a national

standards laboratory is a prerequisite for the TG21 protocol. At the national standards

laboratory, the user's chamber is placed in a calibrated radiation field and given a known

exposure X. The ^{60}Co exposure calibration factor N_x for the ionization chamber can be

calculated from the following equation:

$$X = N_x \cdot M ,$$ (4.41)

where M is the electrometer reading for the dosimeter normalized to normal temperature

and pressure (NTP) of 22°C and 101.3 kPa, respectively, but not corrected for ion

recombination. From N_x, a new parameter, the cavity-gas calibration N_{gas} is calculated

based on the theory of Section I. N_{gas} is unique to each ionization chamber, is a constant

for all radiation qualities for which $\overline{W}_{air} = 33.97$ J/C,[a] and is independent of the

dosimetry phantom. The cavity-gas calibration factor is such that the product of N_{gas} and

the electrometer reading M corrected for temperature, pressure, and ion recombination

gives the dose-to-gas, or

$$D_{gas} = \frac{N_{gas} \cdot M}{A_{ion}} ,$$ (4.42)

in which A_{ion} is the ionization collection efficiency at the time of the calibration at the

national standards laboratory. It is recommended that the bias potential be high enough

to ensure that A_{ion} is greater than 0.995. Further discussion of the theoretical ionization

collection efficiency is given in Chapter 5.

By equating the dose-to-medium calculated from in-air measurements [Eq. (4.14)]

to the dose-to-medium calculated from in-phantom measurements [Eq. (4.38)], the semi-

empirical expression for N_{gas} can be found in terms of N_x:

$$N_{gas} = 0.876 \, N_x \frac{\beta \, A_{wall} A_{ion}}{\left[\alpha \left(\frac{\overline{L}}{\rho} \right)_{gas}^{wall} \left(\frac{\mu_{ab}}{\rho} \right)_{wall}^{air} + (1 - \alpha) \left(\frac{\overline{L}}{\rho} \right)_{gas}^{med} \left(\frac{\mu_{ab}}{\rho} \right)_{med}^{air} \right]} .$$ (4.43)

---

[a]   At the time when TG21 was published, the accepted value for $\overline{W}_{air}$ was 33.7 J/C.

in which $A_{wall} = k(c_{wall})/k(a_{wall})$, α is the fraction of ionization due to electrons originating in the chamber wall, and $(1-\alpha)$ is the fraction of ionization from electrons originating in the medium. It must be pointed out that all of the parameters in the equation for N_{gas} are evaluated at the time of calibration in the ^{60}Co beam for dry air at NTP.

IV.C. Calculating the dose-to-phantom D_{med} in a photon beam

The calculation of the dose-to-phantom is based entirely on the Spencer–Attix cavity theory. Since the dose-to-gas is given by the product of N_{gas} and the electrometer reading M, adjusted for temperature and pressure and corrected for ion recombination, the dose to medium is given by

$$D_{med} = M \, N_{gas} \left(\frac{\bar{L}}{\rho}\right)_{gas}^{med} P_{ion} \, P_{repl} \, P_{wall} . \qquad (4.44)$$

P_{ion} is a factor that corrects for ion recombination losses occurring *at the time of measurement*, and is in form, the inverse of A_{ion} (which is determined *at the time of the ion chamber calibration* in a ^{60}Co beam). P_{repl} is a replacement correction which depends on the type and energy of the radiation, the gradient of the depth dose curve at the point of measurement, as well as the design of the ionization chamber. In plane-parallel chambers at measurement depths beyond d_{max}, P_{repl} is equal to 1.00. For cylindrical chambers in use at the Montreal General Hospital, P_{repl} varies between 0.992 and 0.994 depending on the chamber and the energy of the beam. P_{wall} was described in Section III.C and accounts for the different materials used for the chamber wall and the dosimetric phantom.

IV.D. Calculating the dose-to-water D_{water} in photon beam dosimetry

When the spectral distribution and fluence of primary and secondary photons at the point of measurement in a plastic phantom are the same as at a comparable point in

water, the dose-to-water is given by

$$D_{water} = D_{med}\left(\frac{\overline{\mu}_{ab}}{\rho}\right)^{water}_{med} ,$$ (4.45)

where $(\overline{\mu}_{ab}/\rho)^{water}_{med}$ is the ratio of the average mass energy-absorption coefficient for water to that of plastic.

The amount of scatter is proportional to the volume and density of the irradiated material. If the plastic phantom has a higher electron density than water, it will produce more scatter per unit area than will water. The fraction of excess scattered photons which occurs in plastic phantoms can be approximated by taking the ratio of the tissue air ratios (TAR) in water for the unscaled field size to the TAR for the field size scaled to account for the relative electron density c of the plastic phantom to water:

$$ESC = \frac{TAR(F.d)}{TAR(cF.d)} .$$ (4.46)

where ESC is the excess scatter correction, F is the field size, cF is the scaled field size, and d is the depth of measurement.

Thus, when the recommended geometry is employed (Fig. 4.8), the dose-to-water is calculated from the measured dose-to-plastic according to

$$D_{water} = D_{med}\left(\frac{\overline{\mu}_{ab}}{\rho}\right)^{water}_{med} \cdot ESC .$$ (4.47)

Finally, the absolute dose-to-water can be found from ionization measurements conducted according to the procedures outlined in the TG21 protocol by using the following equation:

$$D_{water} = M \cdot N_{gas}\left(\frac{\overline{L}}{\rho}\right)^{med}_{gas}\left(\frac{\overline{\mu}}{\rho}\right)^{water}_{med} \cdot ESC \cdot P_{ion} \cdot P_{repl} \cdot P_{wall} .$$ (4.48)

V.   The AAPM-TG21 protocol: Calibration of electron beams

The calibration of clinical electron beams is dealt with in the TG21 protocol for the dosimetry of high-energy photon and electron beams. The TG21 protocol was developed with the philosophy that the approach to the calibration of radiotherapy machines should be the same for both electron and photon beams. It is not surprising then that many of the suggestions for the calibration of photon beams also apply to the calibration of electron beams. It is understood that an ionization chamber used in the calibration of electron beams maintains the same ^{60}Co (N_x) and cavity-gas (N_{gas}) calibration factor it uses for photon measurements.

Spencer–Attix cavity theory is a completely general theory which applies to any type of ionizing radiation so long as the Bragg–Gray conditions are met. The theory is thus applicable to electron beams as well as photon beams. First, from ionization measurements a determination of the dose-to-gas is made which is then related to the dose to the surrounding medium according to the Spencer–Attix theory with appropriate correction factors [Eq. (4.44)]

$$D_{med} = M\ N_{gas} \left(\frac{\overline{L}}{\rho}\right)^{med}_{gas} P_{ion} P_{repl} P_{wall} \ . \tag{4.49}$$

Several difficulties arise in the calibration of electron beams stemming from the fact that the electron energy spectrum and fluence vary considerably with depth in the medium. Application of Eqs. (4.44) and (4.49), therefore, is not a simple matter and involves some analysis.

V.A.   The electrometer reading M_{corr}

Irradiation of the collecting electrode, the stem, or the cable of the ionization chamber by high energy electrons can lead to considerable spurious ionization current.

Low energy electrons that are deposited directly on the collecting electrode or in the central wire of the cables will be included as part of the ionization current and will add or subtract from the measured current depending on the polarity of the chamber at the time of measurement. In addition, some high-energy electrons may cause the emission of secondary electrons from any of these components and will alter the measured ionization current. To account for these effects it is necessary that electron beam measurements are made for both positive and negative polarities of the collecting electrode and the mean value is used for M in Eq. (4.44).

The true electrometer reading M_{corr} is given by

$$M_{corr} = \frac{|M_+| + |M_-|}{2} , \qquad (4.50)$$

where $|M_+|$ and $|M_-|$ are the absolute values of the electrometer readings for positive and negative polarities, respectively. By using Eq. (4.50), the spurious currents which do not change sign when the polarity is changed, such as irradiation of the stem and cable, are removed. However, effects which change sign with the polarity of the chamber will remain. An excellent list of the causes of polarity effects in ionization chambers is provided by Boag,[10] although some of these effects are not significant to clinical dosimetry.

V.B. Replacement factor P_{repl} in electron beam dosimetry

The replacement correction factor in electron beam dosimetry is comprised of two major components: the gradient correction, and the electron fluence correction. Because the ionization-gradient in electron beams is large everywhere except at the depth of dose maximum d_{max}, the protocol recommends that electron calibrations be performed only at d_{max} where the ionization-gradient is zero.

The electron fluence correction arises as a result of two opposing factors. Firstly, the number of electrons crossing the cavity is enhanced because fewer electrons are scattered out of the cavity by the gas than are scattered into the cavity by the surrounding medium. This results in a dose to the gas which is greater than that which would occur in the unperturbed medium. Secondly, electrons are scattered less in the gas than in the medium, thus electron path-lengths in the gas are longer than those in the unperturbed medium, resulting in a dose-to-gas which is lower than the dose-to-unperturbed medium. In general, guarded plane-parallel chambers require no correction factors due to in-scattering effects, while cylindrical chamber readings must be corrected. Electron fluence correction factors for cylindrical ionization chambers in acrylic phantoms are presented in Table VIII of the TG21 protocol. It is recommended that the acrylic values be used for water and polystyrene until comparable data become available for these materials.

V.C. Wall correction factor P_{wall} in electron beam dosimetry

Work by Johansson *et al.*[11] shows that the response of low atomic-number, thin-walled ionization chambers is unaffected by the wall composition. Based on this conclusion, P_{wall} is unity for electron beams.

V.D. Choice of correct mean restricted stopping powers for $\left(\overline{L}/\rho\right)_{gas}^{med}$

Strictly speaking, in order to evaluate correctly the ratio of the mean restricted mass stopping power of the medium to that of the gas $\left(\overline{L}/\rho\right)_{gas}^{med}$, the electron spectrum at every depth must be known. As this is virtually impossible, the electron beam is characterized instead in terms of the mean electron energy E_d as a function of the depth d in medium. As $\left(\overline{L}/\rho\right)_{gas}^{med}$ is not very sensitive to small changes in electron energy, this approximation is adequate and introduces relatively small uncertainties in the final result. Several studies have been made with the goal of determining the mean electron

energy at a given depth from in-phantom ionization measurements.[12–16]

The correct choice for the electron energy at which to evaluate the ratio of mean restricted mass stopping powers of the medium to the gas is complicated by the fact that the electron energy spectrum degrades rapidly with depth in the phantom. Consequently, the mean restricted stopping power may change considerably with depth. Fortunately, however, the *ratio* of mean restricted stopping powers in different media changes very little with depth. The procedure for determining the mean electron energy at depth will be outlined below.

Electron beam ionization curve. For every electron beam energy to be calibrated with an ionization chamber, the depth of dose maximum d_{max}, and the practical range R_p of the electron beam must be found from plotting Q_{corr} (where $Q_{corr} = M_{corr} \cdot P_{ion}$) as a function of the depth d in phantom. The practical range is determined from the depth-dose or depth-ionization curves and is the depth at which the line tangent to the inflection point of the dose fall-off region intersects the bremsstrahlung tail. The plot of Q_{corr} vs d is called the electron ionization curve. The depth at which the ionization chamber reading is reduced to 50% of its maximum value d_{50} is used to determine the mean incident energy of electrons $\overline{E}_o$ on the phantom surface (see below). A typical electron ionization curve is shown in Fig. 4.9 indicating the various parameters of interest.

For plane-parallel chambers, the effective point of measurement is taken as the depth of the polarizing electrode located at the proximal surface of the collecting volume. For cylindrical chambers, however, the TG25 protocol recommends that the effective point of measurement be shifted by $0.5\ r$ in the direction of the electron beam where r is the inner radius of the cylindrical chamber. Thus, the depth d along the x-axis of the ionization curve is the depth of measurement for plane-parallel chambers or is $d = d_{center} - 0.5r$ for cylindrical chambers.
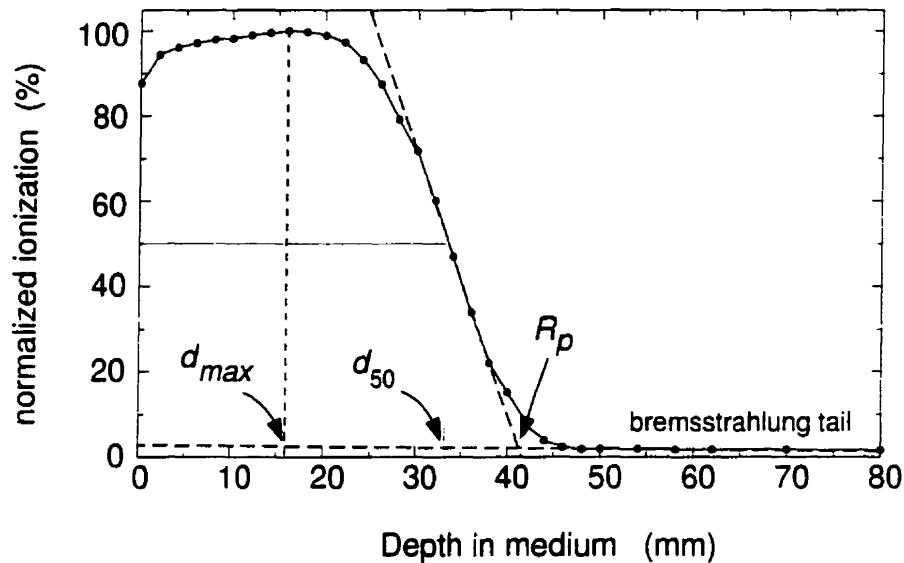
FIGURE 4.9. Electron beam depth-ionization curve for a 9 MeV electron beam in Solid-Water™ phantom.

Energy determination. For electron beams, the mean energy of the electron beam incident on the phantom surface can be determined by multiplying the d_{50} by a numerical constant 2.33 MeV/cm. The value was obtained from depth-dose curves calculated by Berger and Seltzer[13] for parallel-plate ionization chambers. In principle, the electron ionization curve should be measured for very large field sizes when d_{50} is to be used in the calculation of $\overline{E}_o$. When phantom other than water are used, it was found[17] that d_{50} must be scaled to account for differences between the plastic phantoms and water. Thus, in the TG21 protocol,

$$\overline{E}_o = 2.33 \times f \times d_{50} , \qquad\qquad (4.51)$$

where f is the scaling factor.

The mean electron energy at the phantom surface $\overline{E}_o$ is used to look up the

correct mass restricted stopping power ratio from tables provided in the TG21 protocol. Tables V-VII of the protocol list the restricted stopping power ratio for medium to air at various depths in the medium for water, polystyrene, and acrylic, respectively. Recently, a method relating the electron physical range R_p to the most probable electron energy at the phantom surface $E_{p,0}$ and subsequently to the mean electron energy $\overline{E}(d)$ at depth d in the phantom has been developed by Ding[18] *et al.*

Calculation of dose-to-water D_{water} in electron beam dosimetry. At this stage, all of the parameters required for the determination of the absorbed dose to the medium D_{med} are available for substitution into Eq. (4.44). The dose-to-medium is transferred to the dose-to-water D_{water} following a procedure that is different for electron beams than for photon beams. For electron beams,

$$D_{water} = D_{med} \left(\frac{\overline{S}_{col}}{\rho} \right)_{med}^{water} \Phi_{med}^{water} . \tag{4.52}$$

where $\left(\overline{S}_{col}/\rho \right)_{med}^{water}$ is the ratio of mean unrestricted collision mass stopping power in water to that of the plastic phantom, and Φ_{med}^{water} is the ratio of the electron fluence at d_{max} that would occur in water to that in plastic.

Similarly to the procedure for determining the correct value for $\left(\overline{L}/\rho \right)_{gas}^{med}$ in Eq. (4.44), the mean electron energy at depth E_d is the electron energy at which $\left(\overline{S}_{col}/\rho \right)_{med}^{water}$ is evaluated. The ratio of electron fluences at d_{max} for polystyrene to water as a function of the most probable electron energy at the phantom surface E_p are given in Table XVI in the TG21 protocol and range from 1.039 for $E_p = 5$ MeV to 1.009 for $E_p = 16$ MeV.

VI. Summary

When a beam of ionizing radiation traverses a medium, it imparts some of its energy to the medium. The objective of radiation dosimetry is to determine the quantity of energy imparted to the medium from the ionizing radiation beam. For indirectly ionizing radiation, such as photons, a quantity known as the kerma was developed to represent the kinetic energy released in the medium, which can be related to the absorbed dose through Eq. (4.9) wherever charged particle equilibrium can be said to exist. The concepts of kerma and charged particle equilibrium lead naturally to the calculation of the theoretical absorbed dose in a small mass of medium from measurements of the exposure in air.

Following a different method, but using similar arguments, Bragg and Gray developed a theory for relating the dose absorbed in a small cavity to the dose absorbed in the surrounding medium assuming that the presence of the cavity does not alter the photon and electron fluence in the medium. The basic conditions for the Bragg–Gray theory to be applicable are that the cavity dimensions are small relative to the range of the crossing charged particles, and that no charged particles are generated or stopped within the cavity. According to the Bragg–Gray cavity theory, if the dose in the cavity is known, then can the dose in the medium be determined.

The Bragg–Gray theory had a few shortcomings in that it did not include the effects of δ ray production in the medium. Spencer and Attix rederived the Bragg–Gray cavity theory following a more restrictive approach and then modified the theory to include the contribution δ rays to the equilibrium charged particle spectrum, considering fast, or energetic, electrons separately from slow electrons.

In an air ionization chamber, the dose absorbed by the cavity gas is directly

proportional to the ionization of the gas and is easily calculated if the ionization per unit

mass of the air in the chamber is accurately known, and is given by Eq. (4.21). Since

the mass of the sensitive volume of the ionization chamber is often difficult to determine

in practice, several international protocols have been developed for the determination of

absorbed dose in megavoltage photon and electron beams based on the Spencer–Attix

cavity theory.

In North America, the current protocol for the calibration of high-energy photons

and electrons are the TG21 and TG25 protocols, respectively, which have the requirement

that every ionization chamber for use in the protocols is calibrated, or can trace its

calibration back to a national standards laboratory. An ionization chamber is first

calibrated against a calorimeter in a known radiation field and is given a chamber

calibration factor N_x or N_{gas}. A calibrated chamber can then be used to calibrate the

output of a clinical radiation therapy machine.

The calibration protocols make various suggestions for the composition and

design of ionization chambers and dosimetry phantoms, as well as for the geometry

of clinical calibration measurements. The use of such protocols ensures a certain degree

of uniformity in dosimetric techniques between various institutions worldwide. The

calibration protocols also summarize the various small correction factors which account

for the perturbation of the radiation fluence by the cavity. Thus, the dosimetry of ionizing

radiations has evolved from simple arguments and relationships into a very comprehensive

and accurate procedure.

In recent years numerous changes and clarifications were made to TG21. A

thorough summary of these changes is given by Rogers.[19] Despite these improvements,

the TG21 protocol is still recommended and widely used in output calibrations of clinical

photon and electron beams. Currently, a new task group of the AAPM is assigned to

incorporate the recent changes into a new updated protocol for the dosimetry of high-energy photon and electron beams.

References

1. ICRU, "Radiation quantities and units," Report 33, International Commission on Radiation Units and Measurement, Bethesda, Maryland, 1980.

2. W. H. Bragg, "Consequences of the corpuscular hypothesis of the gamma and x rays, and the ranges of beta rays," Phil. Mag. **20**, 385 (1910).

3. L. H. Gray, "Absorption of penetrating radiation," Proc. R. Soc. A. (London) **122**, 647 (1929).

4. M. Boutillon and A. M. Perroche, "Effect of a change of stopping-power values on the W value recommended by ICRU for electrons in dry air," Report CCEMRI(I)85–8, Bureau International des Poids et Mesures, Sèvres, 1985.

5. M. Boutillon and A. M. Perroche, "Re-evaluation of the w value for electrons in dry air," Phys. Med. Biol. **32**, 213–219 (1987).

6. L. V. Spencer and F. H. Attix, "A theory of cavity ionization," Radiat. Res. **3**, 239–254 (1955).

7. G. Lempert, R. Nath, and R. J. Shulz, "Fraction of ionization from electrons arising in the wall of an ionization chamber," Med. Phys. **10**, 1–3 (1983).

8. AAPM Task Group 21 of the Radiation Therapy Committee, "A protocol for the determination of absorbed dose from high-energy photon and electron beams," Med. Phys. **10**, 741–771 (1983).

9. A. K. Ho and B. R. Paliwal, "Stopping power and mass energy absorption coefficient ratios for Solid Water," Med. Phys. **13**, 403–404 (1986).

10. J. W. Boag, in *Radiation Dosimetry*, edited by F. H. Attix and W. C. Roesh, Chapter 1 (Academic Press, New York, 1966).

11. K. Johansson, L. Mattson, L. Lindborg, and H. Svensson, Report SM-222/35, IAEA, Vienna, Austria, 1977.

12. ICRU, "Radiation dosimetry: electron beams with energies between 1 and 50 MeV," Report 35, International Commission on Radiation Units and Measurement, Washington, D.C., 1984.

13. M. J. Berger and S. M. Seltzer, "Stopping powers and ranges of electrons and positrons," Report NBSIR 82-2451-A, National Bureau of Standards, Washington, D.C., 1982.

14. A. Brahme and H. Svensson, "Specification of electron beam quality from the central-axis depth absorbed-dose distribution," Med. Phys. **3**, 95–102 (1976).

15. NACP, "Electron beams with mean energies at the phantom surface below 15 MeV," Acta Radiol. Oncol. Rad. Phys. **20**, 402–415 (1981).

16. D. W. O. Rogers and A. F. Bielajew, "Differences in electron depth-dose curves calculated with EGS and ETRAN and improved energy-range relationships," Med. Phys. **13**, 687–691 (1986).

17. R. Loevinger, C. Karzmark, and M. Weissbluth, Radiology **77**, 906 (1961).

18. G. Ding and D. Rogers, "Mean energy, energy-range relationships and depth-scaling factors for clinical electron beams," Med. Phys. **23**, 361–376 (1996).

19. D. W. O. Rogers, in *Advances in Radiation Oncology Physics*, edited by J. A. Purdy, pp. 181–223 (American Institute of Physics, Lawrence, Kansas, 1990), Proceedings of the AAPM 1990 summer school.

CHAPTER 5

Ion collection in parallel-plate ionization chambers

I.   Introduction

In most radiotherapy clinics the dose to a given point in the medium is determined by measuring the amount of charge Q produced in a small cavity located at that point in the medium. The cavity is usually an ionization chamber filled with air at ambient temperature and pressure. Ionizing radiation creates positive ions and free electrons in the air cavity. As described in Chapter 1, Section I, in electronegative gases the free electron attaches itself to a neutral gas molecule to form a negative ion. The dose to the medium can be calculated from the total charge, or saturation charge, produced in the air cavity according to the Spencer–Attix[1] cavity theory as described in Chapter 4, Section III.C.

The charge $Q(V)$ measured at a given chamber potential V is generally smaller than the saturation charge Q_{sat} because some charge is lost to recombination of positive and negative ions within the air cavity and to thermal diffusion of ions against the applied electric field. The ratio $Q(V)/Q_{sat}$ for a given chamber potential V is defined as the charge collection efficiency or ion collection efficiency $f(V)$:

$$f(V) = \frac{Q}{Q_{sat}} .$$

(5.1)

The ion collection efficiency of the chamber is increased by raising the electric potential between the polarizing and collecting electrodes. When all other conditions

remain constant, as the polarizing potential is increased from zero to some large value, the quantity of charge collected increases at first rapidly and almost linearly, while at higher voltages the increase in collected charge is more gradual and asymptotically approaches the saturation charge Q_{sat}. A plot of the collected charge Q versus the polarizing voltage V results in the *saturation curve*. A typical saturation curve is illustrated in Fig. 5.1. The ion chamber collection efficiency curve is found by dividing the saturation curve by Q_{sat} (*i.e.*, normalizing the saturation curve to 1).

Figure 5.1 shows that charge loss in an ionization chamber decreases with increasing polarizing potential V. However, there is an upper limit to the voltage which can be applied across the plates of the chamber because of the onset of either electrical breakdown of the insulators constituting the chamber or charge multiplication in the chamber sensitive gas. Charge multiplication occurs when an ion drifting in the cavity,
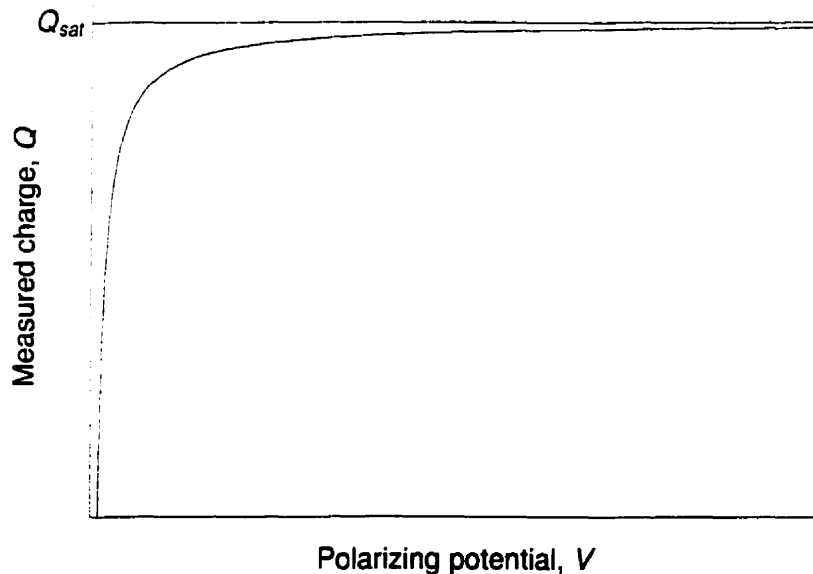
FIGURE 5.1. Typical plot of measured charge Q as a function of the chamber polarizing potential V. The measured charge increases almost linearly for low voltages and approaches asymptotically the saturation charge Q_{sat} at higher voltages.

between two successive collisions with air molecules in the cavity, gains enough kinetic energy from the applied electric field to ionize the air.[2] Thus a single ion as it travels toward the anode can give rise to a cascade of charges. It has been found[2-4] that charge multiplication in air at ambient temperature and pressure becomes an important factor for electric fields above 2000 V/mm. At electric field strengths greater than 2000 V/mm the chamber is said to be in the charge multiplication region; the measured charge becomes dependent on the applied voltage and less dependent on the rate of initial charge production in the chamber. Thus for ionization measurements in radiation dosimetry, it is important that the applied chamber potential is selected such that the chamber operates in the near saturation region yet well below the charge multiplication region.

Determination of the collection efficiency can be accomplished easily in practice assuming that no pockets of low field-strength exist in the chamber volume as a result of poor chamber geometry where ion recombination may persist. If the collection efficiency of a chamber is known for a given electrode separation and polarizing potential, Q_{sat} can be determined through a measurement of $Q(V)$ using Eq. (5.1).

The appropriate Q_{sat} to be used for dose determination in radiation dosimetry is calculated from the measured charge Q following various models for charge loss from ion recombination and ion diffusion. There are two types of recombination processes, namely *initial recombination* and *general recombination*; the latter is treated separately for each of the three categories of ionizing radiations (continuous, pulsed, and pulsed-scanned). Therapy machines at the Montreal General Hospital are capable of producing only continuous and pulsed radiation beams; therefore, this thesis is concerned with these two modalities.

Initial recombination represents the recombination that occurs between ions produced within the track of a single ionizing particle and is thus independent of dose rate.

For initial recombination, $1/Q$ was shown[5-7] to vary linearly with $1/V$. General re-combination, in contrast to initial recombination, depends on dose rate and applies to ions produced in different ion tracks which meet and recombine. For general recom-bination, $1/Q$ in the near saturation region ($f \geq 0.7$) was found to vary linearly with $1/V^2$ in continuous beams[7-11] and linearly with $1/V$ in pulsed beams.[9, 12-14] In elec-tronegative gases it was shown that in the near saturation region, initial recombination is negligible[4, 6, 7, 14] in comparison with general recombination. For thermal diffusion of ions against the applied chamber potential it was found[15] that $1/Q$ also follows a linear relationship with $1/V$.

II.   Theoretical background

II.A.   Recombination rate

The probability that an ion pair recombines in the chamber volume is a function of the concentration of positive and negative ions at a given location in the chamber and the ion interaction time. The number of ions per unit volume dN/dV lost to recombination per unit time dt is called the recombination rate and can be found from the following relationship:[16]

$$\frac{d}{dV}\left(\frac{dN}{dt}\right) = \alpha C^+ C^- .$$ (5.2)

where α is a constant of proportionality called the recombination coefficient, and C^+ and C^- are the positive and negative ion concentrations, respectively.

Equation (5.2) can be expressed in terms of the amount of charge lost to recombi-nation $q = eN$ and as a function of the positive and negative charge densities $\rho^+ = eC^+$ and $\rho^- = eC^-$, respectively, where e is the electron charge. The rate at which charge is

lost to recombination is then given as follows:

$$\frac{d}{dV}\left(\frac{dq}{dt}\right) = \frac{d\rho}{dt} = \frac{\alpha}{e}\rho^+\rho^- \ . \tag{5.3}$$

The exact ion concentrations at a given point in the chamber volume and the interaction time are directly related to the polarizing potential V, the electrode separation d, and the positive and negative ion mobilities in the chamber gas, k^+ and k^-, respectively.

Inside a polarized ionization chamber positive ions drift toward the cathode while negative ions drift towards the anode. The ions have drift velocities that are proportional to the electric field E in the chamber; positive ions drift toward the cathode with a velocity of $v^+ = k^+E$ and negative ions toward the anode with a velocity of $v^- = k^-E$. In air and other electronegative gases which have high electron affinities, free electrons produced by ionizing radiation quickly attach themselves to a gas molecule, resulting in a heavy negative ion, thus $k^- \approx k^+$. In inert gases, electrons do not combine with gas molecules, thus the negative charge carriers are free electrons which have mobilities k^- about 3 orders of magnitude greater than k^+. The ion mobility greatly influences the recombination rate in the chamber. For high ion mobility, ions will have less time in which to interact, consequently, the probability of recombination will be lower.

II.B. Collection efficiency for general recombination in continuous radiation beams

Boag and Wilson,[11] expanding the work of Mie,[8] developed a straightforward theory for general recombination in a continuous beam of radiation. Consider a parallel-plate ionization chamber exposed to a field of ionizing radiation which produces a uniform charge per unit volume of chamber gas per unit time. If there is no recombination of ions in the chamber volume then the ion current I at the collecting electrode will be

$$I = \dot{\rho}_c Ad \ , \tag{5.4}$$

where $\dot{\rho}_c$ is the rate of ion production per unit volume of the chamber by a continuous source of radiation, A is the area of the collecting electrode, and d is the electrode separation. Under the influence of the electric field, positive ions produced in the cavity volume will migrate towards the negative electrode **N** with a velocity of k^+V/d and negative ions will migrate towards the positive electrode **P** with velocity k^-V/d. The steady flow of ions will create a charge gradient between the electrodes **N** and **P**. Under steady-state conditions, the positive charge density ρ_c^+ will increase linearly from zero at **P** until it reaches a maximum value at **N**. Let $\rho_c^+(x)$ be the positive charge density a distance x from the positive electrode **P**. The current $I(x)$ can be found from the quantity of charge per second crossing a plane located at x and parallel to the electrode plates, thus at **N** one finds:

$$I(d) = \rho_c^+(d) \cdot A \cdot \frac{k^+V}{d} \, . \tag{5.5}$$

The positive charge density at **N** can be calculated by equating Eqs. (5.4) and (5.5):

$$\rho_c^+(d) = \frac{\dot{\rho}_c d^2}{k^+V} \, . \tag{5.6}$$

By linearly interpolating between zero and the result of Eq. (5.6) it is possible to solve for the positive charge density at any distance x from **P**:

$$\rho_c^+(x) = \frac{\dot{\rho}_c d}{k^+V} x \, . \tag{5.7a}$$

Analogously, the negative charge density at a distance x from **P** may be expressed as:

$$\rho_c^-(x) = \frac{\dot{\rho}_c d}{k^+V}(d - x) \, . \tag{5.7b}$$

A schematic diagram of the steady-state positive and negative ion density that develops between the polarizing and collecting electrodes of a parallel-plate ionization chamber is shown in Fig. 5.2.
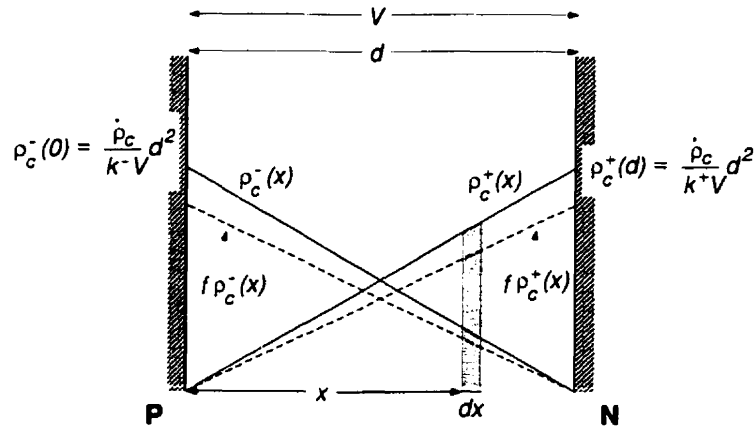
FIGURE 5.2. Schematic diagram of a parallel-plate chamber in which charge is continuously produced uniformly throughout the chamber volume. The densities of the positive and negative charge carriers are shown as a function of the distance x from the positive electrode **P**.

If Eqs. (5.7a) and (5.7b) are substituted into Eq. (5.3), one can solve for the charge lost to recombination per second dq/dt in a volume of area A and infinitesimal thickness dx:

$$\frac{dq}{dt} = \left(\frac{\alpha}{e}\right)\frac{\dot{\rho}_c^2 d^2}{k^+k^-V^2}x(d-x)A\,dx \ . \tag{5.8}$$

To obtain the total charge lost to recombination per second throughout the entire chamber volume, this expression must be integrated from $x = 0$ to $x = d$ giving:

$$A\left(\frac{\alpha}{e}\right)\frac{\dot{\rho}_c^2 d^2}{k^+k^-V^2}\int\limits_{x=0}^{x=d} x(d-x)dx = \frac{A}{6}\left(\frac{\alpha}{e}\right)\frac{\dot{\rho}_c^2 d^5}{k^+k^-V^2} \ . \tag{5.9}$$

Dividing Eq. (5.9) by the ideal ion current I [Eq. (5.4)] one obtains the fraction f_r' of charge produced by ionizing radiation which recombines in the chamber cavity:

$$f_r' = \left(\frac{\alpha}{e}\right)\frac{\dot{\rho}_c d^4}{6k^+k^-V^2} = \frac{1}{\zeta^2} \ , \tag{5.10}$$

where,

$$\zeta^2 = 6\left(\frac{e}{\alpha}\right)\frac{k^+k^-}{\dot{\rho}_c d^4}V^2 \ .$$

If ion recombination in the chamber is non-negligible, then Eq. (5.10) will over-estimate the fraction of ions lost to recombination since the charge density is assumed to be maximal at all points along the integration. We can attempt to improve the solution found in Eq. (5.10) by postulating that the charge densities at each electrode are only a fraction f of the total current, *i.e.*, $\rho_c^+(d) = f\dot{\rho}_c d^2/k^+V$ and $\rho_c^-(0) = f\dot{\rho}_c d^2/k^-V$ instead of the values given in Eqs. (5.7a) and (5.7b). Repeating the calculations leading up to Eq. (5.10) with this reduced value for the charge densities predicts that the fraction of charge f'' lost to recombination in the chamber is then,

$$f_r'' = \frac{f^2}{\zeta^2}.$$

(5.11)

The above expression, however, underestimates the fraction of charge recombination because a minimum charge distribution is assumed at all points along the integration. The actual charge distributions do not remain linear with distance from the electrodes, in fact they are slightly sigmoidal in shape due to the influence of space charge on the electric field. A more detailed analysis of the charge distribution was presented by Mie[8] and simplified by Greening[9] for ionization in air. This work leads to an estimation of the actual fraction of charge f_r lost to recombination in the chamber which is the geometric mean of Eqs. (5.10) and (5.11), giving

$$f_r = \frac{f}{\zeta^2}.$$

(5.12)

One can express the fraction of the ionization which is measured at the collecting electrode as $f = (1 - f_r)$. Rearranging Eq. (5.12) and solving for f gives

$$f = \frac{1}{1 + \frac{1}{\zeta^2}}.$$

(5.13)

Thus, the charge collection efficiency $f_g^c(V)$ for general recombination as a function of applied potential V in an ionization chamber containing an electronegative

gas and irradiated by a continuous radiation field with a constant dose rate is given by the following expression:

$$f_g^c(V) = \frac{Q(V)}{Q_{sat}} = \frac{1}{1 + \frac{\Lambda_g^c}{V^2}} \, , \tag{5.14}$$

in which the constant Λ_g^c is expressed as

$$\Lambda_g^c = \left(\frac{\alpha}{e}\right) \frac{\dot{\rho}_c d^4}{6k^+ k^-} \, , \tag{5.15}$$

where the superscript c denotes *continuous radiation* and the subscript g denotes *general recombination*. The relationship was found to be valid in the near saturation region ($f_g^c \geq 0.7$) and may also be written in the following form:

$$\frac{1}{Q} = \frac{1}{Q_{sat}} + \frac{\lambda_g^c}{V^2} \, . \tag{5.16}$$

where constants Λ_g^c and λ_g^c contain chamber and air parameters and are related through $\lambda_g^c = \Lambda_g^c / Q_{sat}$.

Equation (5.16) implies that when data of Q measured as a function of V are plotted in the form $1/Q$ vs $1/V^2$, a straight line should result which, when extrapolated to $1/V^2 = 0$, yields $1/Q_{sat}$. The extrapolation to $1/V^2 = 0$ should provide a reliable method to correct for general recombination in the case of continuous radiation. A simplified version of this approach is the so-called two-voltage method in which the collected charge is measured only at two voltages, V_H and V_L, assuming, of course, that Eq. (5.16) is valid in the region spanned by the two voltage points.[17-20] If Q_H and Q_L are the charges measured at V_H and V_L, respectively, then $f_g^c(V_H)$ can be written as

$$f_g^c(V_H) = \frac{Q_H}{Q_{sat}} = \frac{Q_H/Q_L - (V_H/V_L)^2}{1 - (V_H/V_L)^2} \, . \tag{5.17}$$
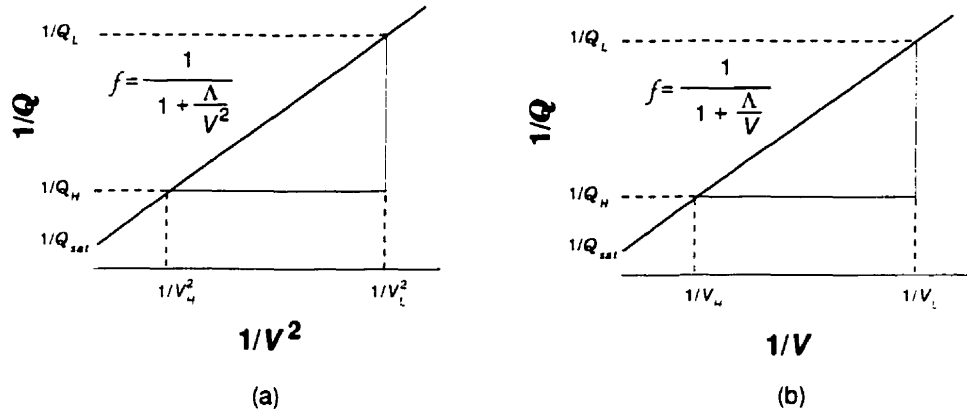
FIGURE 5.3. Determination of Q_{sat} through a linear extrapolation of (a) $1/Q$ vs $1/V^2$ for general recombination with continuous radiation for which the collection efficiency has the form $f = \frac{1}{1+\Lambda/V^2}$, and (b) $1/Q$ vs $1/V$ for collection efficiencies having the form $f = \frac{1}{1+\Lambda/V}$.

Equation (5.17) can be derived geometrically from the graph of $1/Q$ vs $1/V^2$ shown in Fig. 5.3(a).

In the AAPM-TG21 protocol[21] which deals with the calibration of high-energy photon and electron beams, Eq. (5.17) is further simplified by using $V_H = 2 V_L$ (typically, $V_H = 300$ V and $V_L = 150$ V) so that the collection efficiency for general recombination in continuous radiation beams $f_g^c(V_H)$ may be found from

$$f_g^c(V_H) = \frac{Q_H}{Q_{sat}} = \frac{4}{3} - \frac{Q_H}{3Q_L} .$$ (5.18)

II.C. Collection efficiency for general recombination in pulsed radiation beams

For an ionization chamber containing an electronegative gas irradiated by a *pulsed* radiation field (*e.g.*, x rays or electron beams from a medical linac) at a constant dose rate, where the pulse duration is short compared to the mean ion transit time in the cavity, the calculation of the chamber collection efficiency differs from that described in

117

Section II.B. The pulse duration for a typical linac is on the order of a few microseconds, while the ion transit time is on the order of 100–300 μs.[4]

In pulsed radiation beams one assumes that no steady-state ion density is developed in the chamber volume and the ionization produced during each pulse of radiation must be considered separately. One can assume that the total charge density per pulse ρ_p occurs instantaneously.[22]

Between pulses, the ions drift to the oppositely charged electrodes and three distinct regions develop in the chamber sensitive volume: (1) a positive ion region near the cathode N, (2) a negative ion region near the anode P, and (3) a recombination region in which positive and negative charges coexist. The three regions are shown schematically in Fig. 5.4. The width w of the envelope of the recombination region can be expressed by the following equation:

$$w(t) = d - t(k^+ + k^-)\frac{V}{d}.$$

(5.19)

Thus at time $t = 0$ the width $w(0)$ of the region in which positive and negative charges can interact to recombine is equal to the electrode separation d. At some time T, the width of the recombination region will have decreased to zero. After this time recombination is no longer possible. The period of recombination T can be solved for by setting the width $w(T) = 0$ and solving for T, the time during which ion recombination can occur:

$$T = \frac{d^2}{(k^+ + k^-)V}.$$

(5.20)

When the gas is ionized by radiation, an equal number of positive and negative ions is produced. Since a negative ion necessarily recombines with a positive ion, the positive and negative charge densities are always equal, and one can insert $\rho = \rho^+ = \rho^-$ into
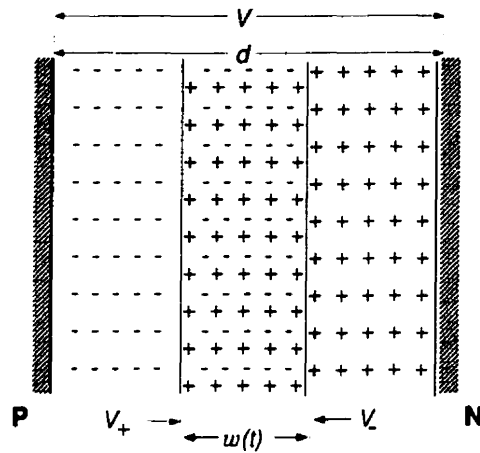
FIGURE 5.4. Schematic diagram of a parallel-plate chamber in which a pulsed radiation beam has produced a uniform distribution of positive and negative charges. Positive charges drift toward the negative electrode N with velocity V_+, while negative charges drift toward the positive electrode P with velocity V_-. Charge recombination is possible only in the overlap region having a width w that decreases with time.

Eq. (5.3) to get

$$\frac{d\rho}{dt} = -\frac{\alpha}{e}\rho^2 \, . \tag{5.21}$$

Integrating this equation and solving for the charge density ρ at a given time t yields

$$\rho(t) = \frac{\rho_p}{1 + \left(\frac{\alpha}{e}\right)\rho_p t} \, . \tag{5.22}$$

where ρ_p is the instantaneous charge density produced during each pulse. There is a finite probability for ion recombination as long as there exists some overlap of the positive and negative ions in the chamber volume. The fraction of ions which recombine in the chamber volume in a pulsed radiation field is a function of the positive and negative electron densities, the size of the ion overlap region, and the electric polarizing potential. The recombination fraction f_r may be expressed as

$$f_r = \frac{A}{(\rho_p A d)} \int_0^T \left(\frac{\alpha}{e}\right)\rho^2(t)w(t)dt \, , \tag{5.23}$$

where A is the electrode area, $\rho(t)$ is given by Eq. (5.22), and $w(t)$ is from Eq. (5.19). The integral can be divided into two parts and easily solved[12] to give

$$f_r = \left[1 - \frac{1}{u}\ln(1+u)\right],$$
(5.24)

where

$$u = \left(\frac{\alpha}{e}\right)\frac{\rho_p d^2}{(k^+ + k^-)V}.$$

Hence, the collection efficiency $f = 1 - f_r$ is given by the following relationship:

$$f = \frac{1}{u}\ln(1+u).$$
(5.25)

The approximation to the collection efficiency f for $V \to \infty$, *i.e.*, for $u \to 0$ is found by expanding $\ln(1+u)$ for $u \to 0$,

$$f = \frac{u - \frac{u^2}{2} + \frac{u^3}{3}}{u} \approx 1 - \frac{u}{2} \approx \frac{1}{1 + \frac{u}{2}}.$$
(5.26)

In the near saturation region, a modified expression for the charge collection efficiency in a pulsed radiation beam can be written as:

$$f_g^p(V) = \frac{Q(V)}{Q_{sat}} = \frac{1}{1 + \frac{\lambda_g^p}{V}}.$$
(5.27)

where $\lambda_g^p = \alpha \rho_p d^2/2(k^+ + k^-)eV$. Equation (5.27) may also be written as

$$\frac{1}{Q} = \frac{1}{Q_{sat}} + \frac{\lambda_g^p}{V},$$
(5.28)

with the constant λ_g^p defined as $\lambda_g^p = \Lambda_g^p/Q_{sat}$.

Equation (5.28) implies that for pulsed radiation beams $1/Q$ measured at several values of V can be plotted as a function of $1/V$ and the resulting straight line extrapolated linearly to $1/V = 0$ to obtain $1/Q_{sat}$. Again, a two-voltage technique can be derived

from Eq. (5.28) for use in determining Q_{sat}. If Q_H and Q_L are the charges measured at V_H and V_L, respectively, then $f_g^p(V_H)$ can be written as:

$$f_g^p(V_H) = \frac{Q_H}{Q_{sat}} = \frac{Q_H/Q_L - (V_H/V_L)}{1 - (V_H/V_L)} .$$ (5.29)

Similarly to the situation with Eq. (5.17) and Fig 5.3(a), Eq. (5.29) can be derived geometrically from Fig. 5.3(b). A half-voltage technique analogous to that for irradiations with continuous beams is suggested in the AAPM-TG21 protocol[21] to determine the collection efficiency for pulsed radiation beams. With $V_H = 2V_L$, Eq. (5.29) reduces to

$$f_g^p(V_H) = 2 - Q_H/Q_L .$$ (5.30)

II.D. Collection efficiency for initial recombination

A theoretical treatment of initial recombination was first given by Jaffé,[23-26] followed by Lea[27] and Zanstra.[5] Jaffé's theory of initial recombination reduces to a problem of simple Brownian motion under the influence of two forces: (1) the Coulomb attraction between oppositely charged ions produced in the same charged particle ion track and (2) the applied electric field in an ionization chamber. The theory assumes a constant linear ion density of N_0 ion-pairs per centimeter following a Gaussian distribution around the charged particle track. Initial recombination is always present in an ion chamber and is dependent only on the density of ions produced along the track of the ionizing particle, thus initial recombination is independent of the dose rate.

When dealing with electron or photon beams monitored by typical ionization chambers under standard clinical conditions (air at 101.3 kPa or less, with electric fields less than 1000 V/cm), initial recombination has been found to be negligible compared to general recombination.[4, 6, 7, 14] Current theory suggests that initial recombination is significant when the ion density of the track is high (such as in the tracks produced by α-particles, or by electrons travelling through a very high-pressure gas) or when the charge

mobility is low enough so that ions do not readily migrate far from their point of creation (such as in gases with very low electric field strengths). Since initial recombination is probable only when the density of ions produced in a single track is high, significant dispersion of the ion track precludes the possibility of initial recombination in the chamber gas. The disappearance of the charged particle track is brought about by diffusion, ion recombination, and ion drift in the applied electric field.

Jaffé found that the collection efficiency in an ion chamber with a collecting field normal to the ion track of E (V/cm) for initial recombination could be expressed as follows:

$$f_i = \frac{Q}{Q_{sat}} = \frac{1}{1 + gh(x)} , \qquad (5.31)$$

where

$$h(x) = e^x \left(\frac{i\pi}{2} \right) H_0^{(1)}(ix) . \qquad (5.32)$$

and $x \propto E^2 = (V/d)^2$. The constant $g = \alpha N_o / 8\pi D$ with α the coefficient of recombination and D the diffusion coefficient of the ions. Thus, from Eq. (5.31) the collection efficiency for initial recombination depends only on N_0 and the electric field strength E normal to the ion track. For large x, Eq. (5.32) has the asymptotic approximation $h(x) \to \sqrt{\pi/2x}$ which is accurate enough to permit, for large polarizing potentials, Eq. (5.31) to be written in the following form:

$$f_i = \frac{Q}{Q_{sat}} = \frac{1}{1 + \frac{\lambda_i}{V}} , \qquad (5.33)$$

where λ_i is a parameter incorporating various chamber and gas parameters and is proportional to the electrode separation d.

Work by Jaffé and others [28, 29] demonstrated that Jaffé's theory of initial recombination permits the consistent extrapolation of measured data to the saturation charge

Q_{sat}. Scott and Greening[7], and Ritz and Attix[30] showed that for *initial recombination*, one should find that

$$\frac{1}{Q} = \frac{1}{Q_{sat}} + \frac{\lambda_i}{V} , \qquad (5.34)$$

where Q is the measured charge, Q_{sat} is the saturation charge, V is the polarizing potential, and $\lambda_i = \Lambda_i / Q_{sat}$. According to Eq. (5.34), a plot of $1/Q$ vs $1/V$, as shown in Fig. 5.3(b), will provide a straight line which intercepts the ordinate-axis at $1/Q_{sat}$.

II.E. Collection efficiency for ion diffusion

In addition to general and initial recombination, some charge loss in a polarized ionization chamber may result from thermal diffusion of ions against the applied electric field. The diffusion of ions in the chamber is a natural result of Brownian motion in which identical gas particles become evenly distributed throughout the chamber volume. Diffusion acts in such a way as to reduce the ion gradient which is established as ions migrate to the oppositely charged electrodes. An ensemble of ions originally concentrated around a point will diffuse out as the time t increases with a mean square fluctuation of $\langle r^2(t) \rangle = 2Dt$ where D is the ion diffusion constant. Thus after a time t on the order of $t \approx z^2/D$ where z is the relative electrode separation, some ions will diffuse thermally and reach the polarizing electrode and escape detection.

In solving this problem, Langevin[15] set up a series of differential equations for the transport of ions between parallel electrodes:

$$\frac{d}{dz}\left(D^+ \frac{d\rho^+}{dz} - k^+ h\rho^+ \right) = \alpha\rho^+\rho^- - \dot{\rho} , \qquad (5.35)$$

$$\frac{d}{dz}\left(D^- \frac{d\rho^-}{dz} + k^- h\rho^- \right) = \alpha\rho^+\rho^- - \dot{\rho} , \qquad (5.36)$$

$$\frac{dh}{dz} = \frac{4\pi}{\kappa}\left(\rho^+ - \rho^- \right) , \qquad (5.37)$$

where the $D d\rho/dz$ terms represent the rate of diffusion with respect to the instantaneous

ion gradient; k^+ and k^- are the positive and negative ion mobilities, respectively; the $kh\rho$

terms represent the ion drift velocities with respect to the applied electric field; $\alpha\rho^+\rho^-$ is

the rate of ion recombination; $\dot{\rho}$ is the rate of charge production per unit volume of gas;

κ is the dielectric constant of the gas; and h represents the local electric field. Langevin's

equations are derived directly from the continuity equation ($\nabla \cdot \vec{J} = -d\rho/dt$).

The boundary conditions for this problem are such that the ion densities are zero

at the electrode plates, $\rho^+(0) = \rho^+(d) = 0$ and $\rho^-(0) = \rho^-(d) = 0$, where $z = 0$ defines

the positive electrode, and $z = d$ defines the negative electrode. One must also have that

$\int_0^d h \, dz = V$, where V is the applied potential.

To calculate the current per unit area i under the influence of thermal diffusion,

the rate of flow of positive and negative ions per unit area parallel to the electrode

surfaces must be calculated. Along the z-axis, the positive and negative current flow,

i^+ and i^-, respectively are found from the left hand side of Eqs. (5.35) and (5.36) and

can be written as:

$$i^+ = D^+ \frac{d\rho^+}{dz} - k^+ h \rho^+ \tag{5.38}$$

and

$$i^- = D^- \frac{d\rho^-}{dz} + k^- h \rho^- \tag{5.39}$$

for positive and negative ions, respectively. To a first approximation, the current flow at

the collecting electrode $\left(\rho^+ = \rho^- = 0\right)$ may be found from:

$$i = \left(i^- - i^+\right), \tag{5.40}$$

in which the currents $i^- = D^- \left(d\rho^-/dz\right)_0$ and $i^+ = D^+ \left(d\rho^+/dz\right)_0$ represent the diffusion

of negative and positive charges against the charge gradient.

Langevin proposed to develop a solution to the Eqs. (5.35—5.37) based on a series

expansion of the unknowns $\rho^+, \rho^-, i^+, i^-, h$ in terms of ρ:

$$\rho^+ = \rho_1^+ \dot\rho + \rho_2^+ \dot\rho^2 + \ldots + \rho_n^+ \dot\rho^n + \ldots , \qquad (5.41a)$$

$$\rho^- = \rho_1^- \dot\rho + \rho_2^- \dot\rho^2 + \ldots + \rho_n^- \dot\rho^n + \ldots , \qquad (5.41b)$$

$$i^+ = i_1^+ \dot\rho + i_2^+ \dot\rho^2 + \ldots + i_n^+ \dot\rho^n + \ldots , \qquad (5.41c)$$

$$i^- = i_1^- \dot\rho + i_2^- \dot\rho^2 + \ldots + i_n^- \dot\rho^n + \ldots . \qquad (5.41d)$$

$$h = h_o + h_1 \dot\rho + \ldots . \qquad (5.41e)$$

where all the ρ_i disappear at the electrode surfaces, and for $j > 1$. h_j satisfy the integral

$$\int_0^d h_j \, dz = 0.$$

If we consider only the terms that are first order in $\dot\rho$, then Eqs. (5.35—5.37)

become

$$\frac{d}{dz}\left(D^+ \frac{d\rho_1^+}{dz} - k^+ h_o \rho_1^+\right) = -1 . \qquad (5.42)$$

$$\frac{d}{dz}\left(D^- \frac{d\rho_1^-}{dz} + k^- h_o \rho_1^-\right) = -1 , \qquad (5.43)$$

$$\frac{dh_1}{dz} = \frac{4\pi}{\kappa}\left(\rho_1^+ - \rho_1^-\right) . \qquad (5.44)$$

Recalling that $\rho^+(0) = \rho^-(0) = 0$, integration of Eqs. (5.42–5.44) with respect to z gives

$$k^+ h_o \rho_1^+ - D^+ \frac{d\rho_1^+}{dz} = -i_1^+ + z \qquad (5.45)$$

and

$$k^- h_o \rho_1^- + D^- \frac{d\rho_1^-}{dz} = i_1^- - z \ . \tag{5.46}$$

If we substitute $\rho_1^+ = \beta_1 \exp\left(\frac{k^+ h_o}{D^+} z\right)$ into Eq. (5.45) where β_1 disappears on the

electrode surfaces, then we get

$$k^+ h_o \beta_1 \exp\left(\frac{k^+ h_o}{D^+} z\right) - D^+ \left(\frac{k^+ h_o \beta_1}{D^+} + \frac{d\beta_1}{dz}\right) \exp\left(\frac{k^+ h_o}{D^+} z\right)$$

$$= -i_1^+ + z \ . \tag{5.47}$$

which reduces to

$$D^+ \frac{d\beta_1}{dz} = (i_1^+ - z) \exp\left(-\frac{k^+ h_o}{D^+} z\right) \ . \tag{5.48}$$

Integrating Eq. (5.48) between the limits $z = 0$ and $z = d$ gives the solution for i_1^+ as

$$i_1^+ = d\left[\frac{1}{m^+} - \frac{e^{-m^+}}{1 - e^{-m^+}}\right] \ . \tag{5.49}$$

Here, the parameter $m^+ = k^+ h_o d / D^+ = k^+ V / D^+$. (Recall that $\int\limits_0^d h\, dz = V$.) A similar

approach may be followed to solve for i_1^- giving,

$$i_1^- = d\left[\frac{e^{m^-}}{1 - e^{m^-}} - \frac{1}{m^-}\right] \ . \tag{5.50}$$

Recalling Eqs. (5.41), and substituting Eqs. (5.49) and (5.50) into Eq. (5.40) and

dividing by the saturation current $I = Ad\rho$ gives the following relationship for the ion

collection efficiency for thermal diffusion loss in an ion chamber:

$$f = \frac{iA}{I} = \frac{e^{m^-}}{e^{m^-} - 1} - \frac{1}{m^-} + \frac{e^{-m^+}}{1 - e^{-m^+}} - \frac{1}{m^+} \ . \tag{5.51}$$

For an electronegative gas we may assume that $m^+ = m^- = m$. Therefore, for large m (*i.e.*, large applied potential):

$$f \cong \frac{e^m}{e^m - 1} - \frac{2}{m} \approx 1 - \frac{2\overline{D}}{\overline{k}V},$$ (5.52)

where $\overline{D}$ and $\overline{k}$ are the mean diffusion constant and mobility, respectively, for positive and negative ions. It can be shown[31] that $\frac{\overline{k}}{\overline{D}} = \frac{e}{kT}$, where e is the electronic charge, k is Boltzmann's constant, and T is the absolute temperature. Therefore, Eq. (5.52) becomes

$$f = 1 - \frac{2kT}{eV}.$$ (5.53)

Thus, if we assume that Eq. (5.53) represents the first term in a series expansion, then the collection efficiency for thermal diffusion may be represented by the following equation:

$$f_d = \frac{1}{1 + \frac{\lambda_d}{V}}.$$ (5.54)

i.e.,

$$\frac{1}{Q} = \frac{1}{Q_{sat}} + \frac{\lambda_d}{V}.$$ (5.55)

where the diffusion constant $\lambda_d = 2\,kT/e = \lambda_d Q_{sat}$. At room temperature, λ_d is equal to 0.0506 V.

Equation (5.55), similarly to Eqs. (5.28) and (5.34), implies that a plot of $1/Q$ vs $1/V$ results in a straight line, which, when extrapolated to $1/V = 0$, gives $1/Q_{sat}$.

II.F. Comprehensive model for ion loss

Böhm[14] expressed the total collection efficiency f as a product of three terms f_i, f_g, and f_d, representing collection efficiencies for initial recombination, general

recombination, and diffusion loss, respectively. This approach is not entirely correct—initial recombination is independent of general recombination and ion diffusion, but general recombination and ion diffusion occur simultaneously and are mutually competing processes. However, for the purpose of our study where f is always larger than 0.7, it is adequate to assume that general recombination and ion diffusion are independent processes, and that Böhm's approach is valid.

For continuous beams of radiation, Böhm's approach leads to the following relationship:

$$f^c = f_g^c f_i f_d = \left\{ \left[1 + \frac{\Lambda_g^c}{V^2} \right] \left[1 + \frac{\Lambda_i}{V} \right] \left[1 + \frac{\Lambda_d}{V} \right] \right\}^{-1}$$

$$= \left\{ 1 + \frac{\Lambda_i + \Lambda_d}{V} + \frac{\Lambda_g^c + \Lambda_i \Lambda_d}{V^2} + \vartheta \left(\frac{1}{V^3} \right) \right\}^{-1}. \tag{5.56}$$

Analyzing the relative importance of the three terms of Eq. (5.56), Böhm concluded that for x rays in air at atmospheric pressure, initial recombination and ion diffusion loss play a negligible role in comparison with general recombination, implying that in Eq. (5.56) $\Lambda_i = \Lambda_d = 0$. Several other investigators[4, 6, 7] also concluded that for continuous beams in air at atmospheric pressures, loss of ions through initial recombination is negligible in comparison with general recombination; however, they dealt with electric fields typically below 50 V/mm. These investigators recommend that for use in radiation dosimetry, f and Q_{sat} be determined from measured $Q(V)$ data assuming the predominance of general recombination and an approach to saturation expressed by a linear relationship between $1/Q$ and $1/V^2$.

These assumptions lead to the following method to determine Q_{sat}, and subsequently the collection efficiency $f(V)$ from measured charge Q at applied potential V in continuous radiation beams:

(i)   a sufficiently high polarizing voltage is applied to ensure that all charges Q are measured in the near saturation region,

(ii)   initial recombination and diffusion loss are ignored and the predominance of general recombination is assumed,

(iii)   the collection efficiency f_g^c is determined from the two–voltage technique [Eq. (5.17)] which was derived from the assumed linear relationship in the near saturation region between $1/Q$ and $1/V^2$, and

(iv) Q_{sat} is calculated from the ratio $Q(V)/f_g^c$.

We believe and show in Chapter 7 that the current methodology is in error and that initial recombination and ion diffusion should not be neglected when calculating the collection efficiency. For high polarizing potentials, Eq. (5.56) suggests that the relative importance of the terms in $1/V$ will be such that a failure to account for them may lead to errors of up to 0.5% in the determination of Q_{sat}.

Similarly to Eq. (5.56), for pulsed radiation beams Böhm's treatment leads to the following simple equation for the collection efficiency:

$$f^p = f_g^p f_i f_d = \left\{ \left[1 + \frac{\Lambda_g^p}{V} \right] \left[1 + \frac{\Lambda_i}{V} \right] \left[1 + \frac{\Lambda_d}{V} \right] \right\}^{-1}$$

$$= \left\{ 1 + \frac{\Lambda_g^p + \Lambda_i + \Lambda_d}{V} + \vartheta \left(\frac{1}{V^2} \right) \right\}^{-1} . \tag{5.57}$$

Since general recombination in pulsed beams varies as $1/V$, the inclusion of initial recombination and diffusion loss, which also vary as $1/V$, does not affect the functional relationship between Q and V, and the collection efficiency f^p for pulsed beams can still be determined from a plot of $1/Q$ vs $1/V$.

II.G. A_{ion} and P_{ion}

The cavity-gas calibration factor N_{gas} can be calculated from the exposure calibration factor N_x provided by a national standards laboratory (see Chapter 4, Section IV.B). For a given ionization chamber, the saturation charge Q_{sat} is related to D_{gas}, the absorbed dose in a cavity gas[21] through $D_{gas} = N_{gas} \cdot Q_{sat}$. The saturation charge used in this calibration is found by dividing the measured charge by the collection efficiency calculated using the two-voltage technique for continuous beams [Eq. (5.17)]. The collection efficiency f determined at the time of calibration in a continuous radiation beam at the standards laboratory is denoted A_{ion}, and Q_{sat} is calculated from A_{ion} as follows:

$$Q_{sat} = \frac{Q}{A_{ion}} \ . \tag{5.58}$$

In standard dosimetry an assumption is generally made that A_{ion} is equal to 1.0.[ref. 32] For clinical calibrations of radiotherapy treatment beams, to avoid confusion with A_{ion}, a new parameter P_{ion} was introduced, defined as $P_{ion} = 1/f$. Thus for clinical applications, Q_{sat} is determined from measured Q and P_{ion} according to the following expression:

$$Q_{sat} = Q \cdot P_{ion} \ . \tag{5.59}$$

III.   Summary

There are three mechanisms for charge loss in an ionization chamber: general recombination, initial recombination, and ion diffusion. General recombination occurs when a positive and negative ion from different charged particle tracks meet and recombine in the chamber volume. In continuous radiation beams the general recombination parameter Λ_g^c depends on the ionization rate $\dot{\rho}$ and the electrode separation d, such that $\Lambda_g^c \propto \dot{\rho} d^4$. In pulsed beams the general recombination parameter Λ_g^p is proportional

to $\rho_p d^2$, where ρ_p is the instantaneous charge density per pulse. Initial recombination describes the recombination of a positive and negative ion from the same particle track; its recombination parameter increases with the electrode separation d and with the linear ion density of the charged particle track N_o, such that $\Lambda_i \propto dN_o$. Ion diffusion against the applied electric field is a result of Brownian motion and, the diffusion parameter Λ_d varies linearly with temperature T, *i.e.*, $\Lambda_d \propto T$.

In current radiation dosimetry protocols initial recombination and diffusion loss are ignored and the collection efficiency is determined assuming that the approach to saturation for both continuous and pulsed beams is governed by general recombination. We will show in Chapter 7 that this approach can result in errors in the determination of the collection efficiency f^c in continuous beams on the order of 0.5% because the final approach to saturation is actually governed by initial recombination and ion diffusion rather than by general recombination. However, failure to account for initial recombination and diffusion loss explicitly should not affect the determination of f^p since the functional relationship between the measured charge and the applied voltage for these processes is similar to that of general recombination in pulsed beams.

References

1. L. V. Spencer and F. H. Attix, "A theory of cavity ionization," Radiat. Res. **3**, 239–254 (1955).

2. F. H. Attix, *Introduction to Radiological Physics and Radiation Dosimetry* (John Wiley & Son, New York, 1986).

3. P. N. Jeffery, J. W. Boag, and H. E. Johns, "Electron avalanche amplification in x-ray imaging devices," Phys. Med. Biol. **19**, 593–604 (1974).

4. J. W. Boag, in *The Dosimetry of Ionizing Radiation*, edited by K. R. Kase, B. E. Bjärngard, and F. H. Attix, Volume 2, Chapter 3 (Academic Press, Orlando, 1987).

5. H. Zanstra, "A rapid method for determining the saturation current by the Jaffé theory of columnar ionization," Physica (Amsterdam) **2**, 817–824 (1935).

6. M. Boutillon and M. T. Niatel, "A study of a graphite cavity chamber for absolute exposure measurements of Co-60 gamma rays," Metrologica **9**, 139–146 (1973).

7. P. B. Scott and J. R. Greening, "The determination of saturation currents in free-air ionization chambers by extrapolation methods," Phys. Med. Biol. **8**, 51–57 (1963).

8. G. Mie, "Der elektrische Strom in ionisierter Luft in einem ebenen Kondensator," Ann. Physik **13**, 857–889 (1904).

9. J. R. Greening, "Saturation characteristics of parallel-plate ionization chambers," Phys. Med. Biol. **9**, 143–154 (1964).

10. J. S. Townsend, *Electricity in Gasses* (Clarendon Press, Oxford, 1915).

11. J. W. Boag and T. Wilson, "The saturation curve at high ionization intensity," Br.

J. Appl. Phys. **3**, 222–229 (1952).

12. J. W. Boag, "Ionization measurements at very high intensities I. Pulsed radiation beams," Br. J. Radiol. **23**, 601–611 (1950).

13. J. W. Boag, "The saturation curve for ionization measurements in pulsed radiation beams," Br. J. Radiol. **25**, 649–650 (1952).

14. J. Böhm, "Saturation corrections for plane parallel ionization chambers," Phys. Med. Biol. **21**, 754–759 (1976).

15. P. Langevin, "Mesure de la valence des ions dans les gaz," Le Radium **10**, 113–124 (1913).

16. H. E. Johns and J. R. Cunningham, *The Physics of Radiology* (Charles C. Thomas, Springfield, Illinois, 4th edition, 1983).

17. J. W. Boag and J. Currant, "Current collection and ionic recombination in small cylindrical ionization chambers exposed to pulsed radiation," Br. J. Appl. Phys. **53**, 471–478 (1980).

18. P. R. Almond, "Use of a Victoreen 500 electrometer to determine ionization chamber collection efficiencies," Med. Phys. **8**, 901–904 (1981).

19. F. H. Attix, "Determination of A_{ion} and P_{ion} in the new AAPM radiotherapy dosimetry protocol," Med. Phys. **11**, 714–716 (1984).

20. M. S. Weinhouse and J. A. Meli, "Determining P_{ion}, the correction factor for recombination losses in an ionization chamber," Med. Phys. **11**, 846–849 (1984).

21. AAPM Task Group 21 of the Radiation Therapy Committee, "A protocol for the determination of absorbed dose from high-energy photon and electron beams," Med. Phys. **10**, 741–771 (1983).

22. J. W. Boag, in *Radiation Dosimetry*, edited by F. H. Attix and W. C. Roesh, Chapter 1 (Academic Press, New York, 1966).

23. G. Jaffé, "On the theory of ionization in columns, I. (in German)," Ann. Physik (Leipzig) **42**, 303–344 (1913).

24. G. Jaffé, "Collumnar ionization. (in French)," Le Radium **10**, 126–134 (1913).

25. G. Jaffé, "On the theory of ionization in columns, II. (in German)," Ann. Physik (Leipzig) **1**, 977–1008 (1929).

26. G. Jaffé, "On the theory of recombination," Phys. Rev. **58**, 968–976 (1940).

27. D. Lea, "The theory of ionization measurements in gasses at high pressures," Proc. Cambridge Philos. Soc. **30**, 80–101 (1934).

28. W. R. Kanne and J. A. Bearden, "Collumnar ionization," Phys. Rev. **50**, 935–938 (1936).

29. A. Muller, "On the behaviour of columnar ionization in pure gasses (in German)," Z. Physik **145**, 469–485 (1956).

30. V. H. Ritz and F. H. Attix, "An ionization chamber for kilocalorie source calibrations," Radiat. Res. **16**, 401–415 (1962).

31. R. K. Pathria, *Statistical Mechanics* (Pergamon Press, Oxford, 1972).

32. F. H. Khan, *The Physics of Radiation Therapy* (Williams and Wilkins, Maryland, second edition, 1992).

CHAPTER 6

Experimental apparatus and techniques

I. Phantom-embedded extrapolation chamber

The phantom-embedded extrapolation chamber (PEEC) is a variable air-volume, parallel-plate ionization chamber designed to form an integral part of a Solid-Water™ phantom with dimensions of $30 \times 30 \times 10$ cm^3. Solid-Water™ material (model 457; RMI, Middleton, Wisconsin) was the ideal choice for the construction of the PEEC because it is the primary plastic dosimetry phantom used in most radiotherapy facilities. The elemental composition and radiation characteristics of the Solid-Water™ (model 457) have been published by other investigators.[1, 2]

As shown schematically in Fig. 6.1, a 7 cm diameter, 10 cm height Solid-Water™ piston was fashioned to move inside a cylindrical aperture bored along the centre of the Solid-Water™ phantom. Various polarizing electrodes ranging from 0.5 to 2.0 mm in thickness can be fixed to the top of the aperture. A layer of graphite dag of thickness ≤ 0.05 mm was spray-painted directly onto pieces of Solid-Water™ to form the electrode surfaces. The measuring and guard electrodes are attached to the top of the movable piston such that the sensitive volume of the PEEC is defined by the volume of air separating the polarizing and measuring electrodes. The electrode separation, determined by the displacement of the piston, is controlled by means of a micrometer which is connected to the bottom of the piston through a ball-bearing mechanism. The micrometer
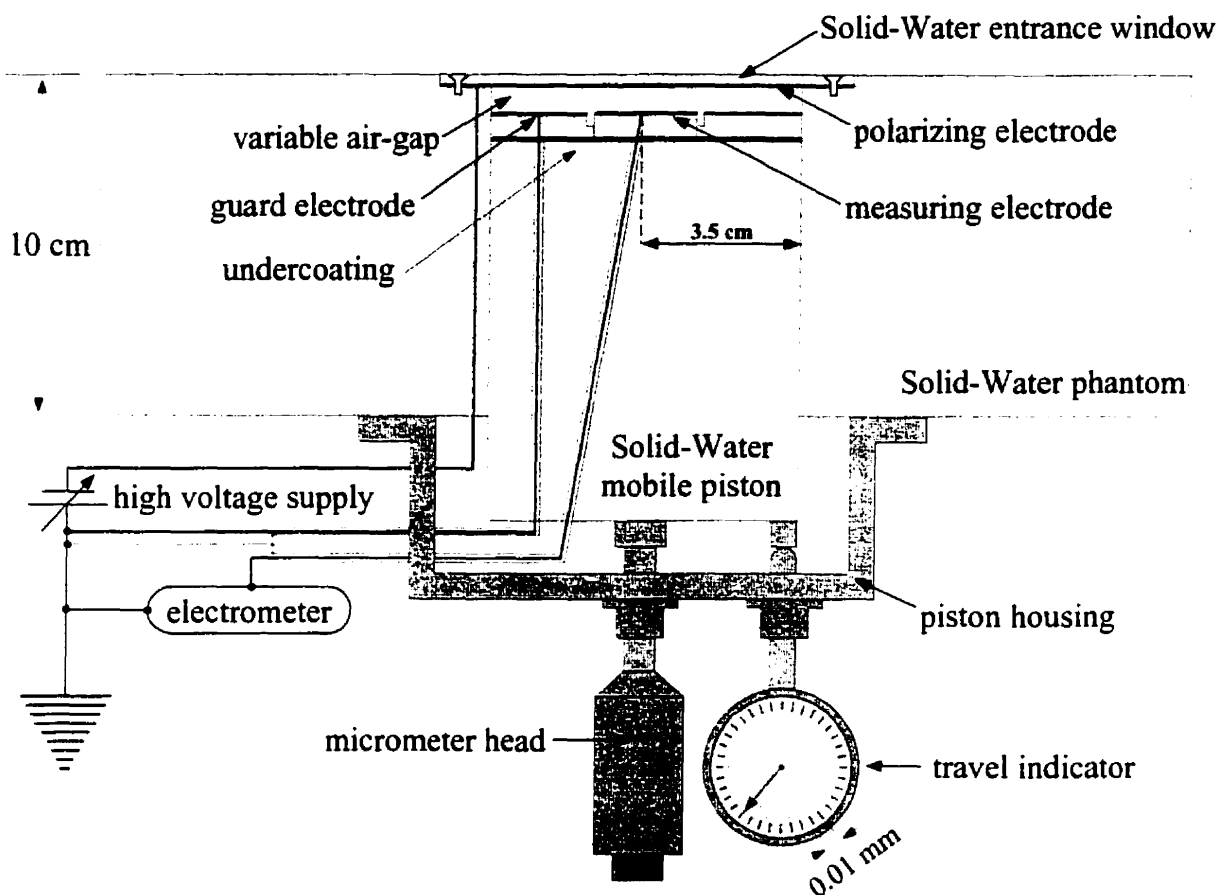
FIGURE 6.1. Schematic drawing of a Solid–Water™ embedded extrapolation chamber.

provides relative electrode separations z ranging from approximately 0.5 to 10 mm. The micrometer head is fastened to the piston housing which is securely mounted to the phantom body. Since some "play" or hysteresis effect is noticeable on typical micrometers, the movement of the piston in the cylinder (*i.e.*, change in the air gap Δz or sensitive air mass $\rho A \Delta z$) is monitored by a mechanical distance travel indicator (model 25-881; Starrett, Athol, Massachusetts) which is also attached to the piston housing. The free end of the distance travel indicator is allowed to contact an aluminum pin connected to the bottom of the piston allowing the relative electrode separation to be monitored with a precision of ±0.002 mm.

Following the standard ionization chamber configuration, the measuring electrode was connected to ground through a calibrated electrometer (model 35617 programmable dosimeter; Keithley, Cleveland, Ohio) and the guard ring was connected to ground directly. Two variable voltage power supplies (model 412B; John Fluke, Seattle, Washington, and model 245; Keithley, Cleveland, Ohio) each providing up to ± 2100 V were connected in series to form a high-voltage source capable of delivering up to ± 4200 V. The electrometer response in the charge collection mode has been verified with a picoampere current source (model 261; Keithley, Cleveland, Ohio) the calibration of which is traceable to a standards laboratory (National Research Council, Ottawa, Canada).

The overall design of the PEEC has several advantages over most commercially available ionization chambers. Firstly, the variable-volume design of the chamber permits the direct measurement of dQ/dm for use in Eq. (1.22), the modified Spencer–Attix equation, circumventing the need to know exactly the sensitive air-mass for absolute dose determination. Consequently, the PEEC does not require a dose calibration factor, such as N_{gas}, from a national standards laboratory. Secondly, the well-guarded, parallel-plate design of the PEEC obviates the replacement correction factors associated with cylindrical ionization chambers that are described in the AAPM-TG21 protocol for the calibration of high-energy photon and electron beams.[3] Thirdly, since the PEEC is built directly into the phantom material, the phantom is the chamber wall and there is no need for correction factors which account for differences in the wall material and the medium. In addition, care was taken to minimize the amount of unwanted backscatter from non-Solid-Water™ components of the chamber: as shown in Fig. 6.1 the piston housing, a cup mounted to the bottom of the phantom body, was machined from aluminum (Z = 13) which produces minimal backscatter; furthermore, all metallic chamber components were located at least 10 cm away from the chamber sensitive volume.

I.A. Electrode construction

The electrodes of the embedded extrapolation chamber were designed to be versatile and durable. It was important to manufacture measuring electrodes of various areas which could be interchanged easily between one electrode and another. With this in mind, the measuring electrode was made from a 7 cm diameter, 0.5 cm thick disc of Solid-Water^{TM} which was fastened to the piston with nylon screws. The electrical connection to the electrode surface was achieved by using small female spring-loaded gold-plated pins that were pushed through small holes so that the flat closed surface of the pins were aligned with the disc surface. A sketch of the electrical connections to the guard and central electrodes is shown in Fig. 6.2. The central signal wires of two triaxial shielded cables were outfitted with small male-pins which could be held tightly by the female pins to form a good electrical connection. Polarizing electrodes were formed on Solid-Water^{TM} entrance windows ranging from 0.5 mm to 2.0 mm in thickness. The polarizing electrodes covered the cylindrical aperture and were attached to the phantom body also with nylon screws. The high-voltage connection to the polarizing electrode was accomplished with a spring-loaded brass pin which contacted the polarizing surface directly from the underside. The thickness of the polarizing electrode used for the measurements in this thesis was 2 mm so that the electrode will not suffer from bending under the influence of high electric fields.

Graphite has low atomic number (Z = 6) and, when evenly deposited on the Solid-Water^{TM} pieces, constitutes an ideal conductor for the purposes of radiation dosimetry. Several coats of graphite dag (Aquadag; Acheson colloids (Canada) Limited, Ontario) of ~10 μm thickness per coat were spray-painted by means of a pressurized airbrush (Eclipse; Iwata, Japan) onto the Solid-Water^{TM} pieces to form the electrode surfaces. Each thin layer was carefully sanded and polished to remove small surface irregularities
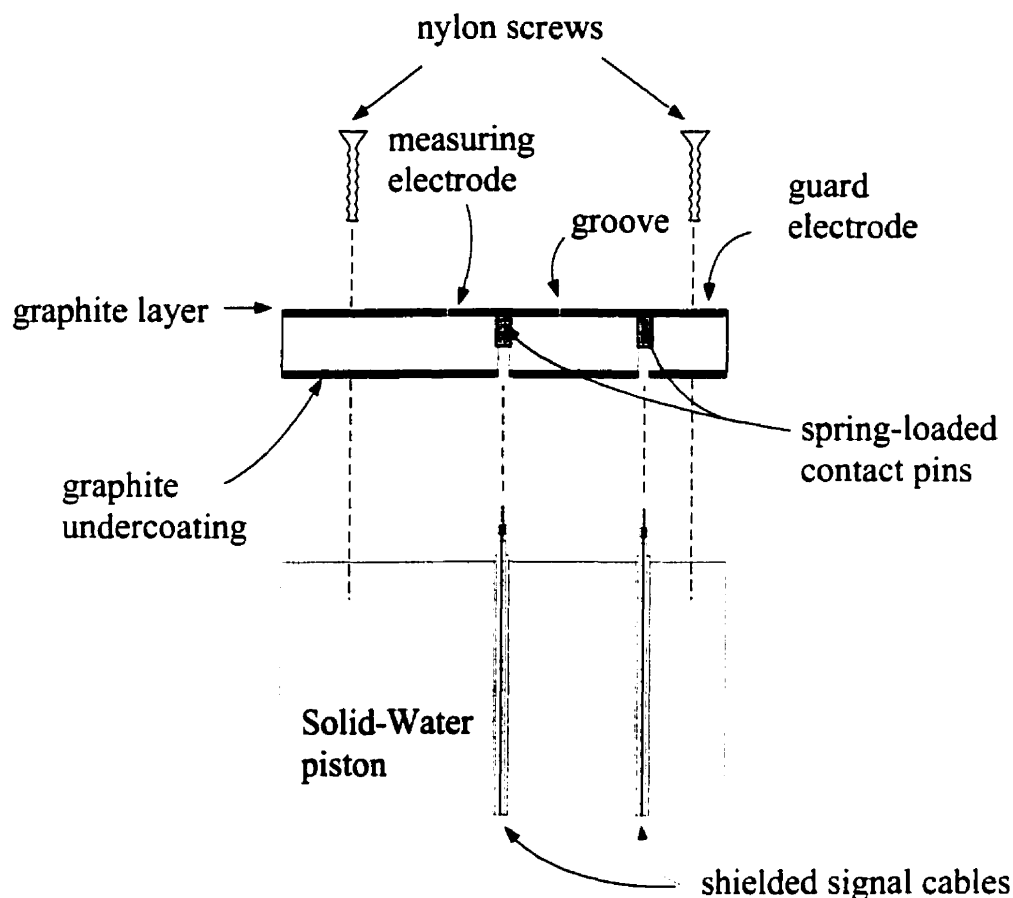
FIGURE 6.2. Schematic diagram of the 7 cm diameter Solid-Water^{TM} mobile piston. The Solid-Water^{TM} electrode disc is fastened to the top of the piston by means of low atomic number nylon screws. Small spring-loaded gold-plated contact pins are used to form the electrical connection between the signal wires and the graphite electrode surface ($\lesssim$ 0.05 mm thick). The measuring and guard electrodes are separated by a thin groove etched into the graphite surface. Graphite is also spray-painted onto the bottom of the electrode to reduce leakage currents coming from beneath the electrode disc.

which are inherent to the spray-painting process, thereby ensuring a uniform deposition of graphite on the Solid-Water^{TM}. This process was repeated until the cross-diameter resistance of the electrode surface fell below 30 Ω. A 30 Ω resistance corresponds to a graphite layer of less than 0.05 mm in thickness. The bottom surface of the Solid-Water^{TM} disc holding the measuring and guard electrodes was also painted with graphite

dag. The bottom surface was connected electrically to the guard electrode. Together the guard electrode and the graphite undercoating prevent leakage currents from reaching the measuring electrode.

Once a sufficient coating of graphite was attained on the top surface of the Solid-Water™ disc, a lathe was used to etch a small circular groove into the graphite layer, producing an electrical separation between the central electrode and the guard electrode. For the data reported in this thesis, the circular groove had a diameter of roughly 2.5 cm. In the next section, the effective area of the measuring electrode is shown to be $A = 4.597 \pm 0.03$ cm^2.

I.B.   Determination of the effective electrode area

Equation (1.22) can be used as a practical approach to radiation dosimetry, provided that one has an accurate knowledge of the effective area A of the measuring electrode. The effective measuring electrode area A may differ slightly from its physical area due to uncertainty in which side of the groove separating the measuring and guard electrodes an electric field line will terminate. It is reasonable then to adopt an electrical method for the determination of A.

An inherent capacitance is associated with any parallel-plate ionization chamber. Assuming that the guard electrode is sufficiently large, there will be no "bowing" of the electric field near the edges of the collecting electrode, thus the capacitance C of the parallel-plate ionization chamber can be approximated by the expression for two infinitely large parallel conducting plates:

$$C = \frac{\Delta Q}{\Delta V} = \varepsilon_o \left(\frac{A}{d}\right),$$ (6.1)

where ϵ_o is the electrical permittivity constant (8.85×10^{-12} F/m), z is the separation between the conducting surfaces, and ΔQ is the change in the charge measured by the

electrometer when the polarizing voltage is changed by an amount ΔV.

For a given electrode separation d, the change in the charge ΔQ on the measuring electrode can be measured for a given change in the applied voltage ΔV. A plot of ΔQ vs ΔV for various ΔV produces a straight line whose slope is equal to the mean chamber capacitance C for a given d.

It is unnecessary to know the absolute electrode separation d for the variable volume PEEC at this stage. For a given *relative* electrode separation z, the capacitance C of the chamber was determined as outlined above. Since the chamber capacitance can be determined very accurately, it can serve as the x–axis, while the unknown *relative* electrode separation z is plotted along the y–axis. Equation. (6.1) can be rearranged so that z can be expressed in terms of C, A, and ε_o as follows:

$$z = \varepsilon_o A \frac{1}{C} . \tag{6.2}$$

It is evident that a plot of the relative electrode separation z as a function of the inverse capacitance $C^{-1} = \Delta V / \Delta Q$ will result in a straight line with a slope equal to $\varepsilon_o A$. By dividing the slope of this line by the electrical permittivity constant ε_o, one arrives at the effective collecting electrode area A.

Data collected for one of the measuring electrodes used by the PEEC are shown in Fig. 6.3. The slope of the line was found to be $(4.068 \pm 0.02) \times 10^{-12}$ F mm which, when divided by ε_o results in an effective electrode area of $A = 4.597 \pm 0.03$ cm^2. This collecting electrode was used in all PEEC measurements reported in this thesis. Incidently, the absolute electrode separation d can be found by calibrating the relative electrode separation z axis such that the solid line in Fig. 6.3 intersects the y–axis at 0. Mathematically, $d = z - z_o$, where z_o is the y–axis intercept.
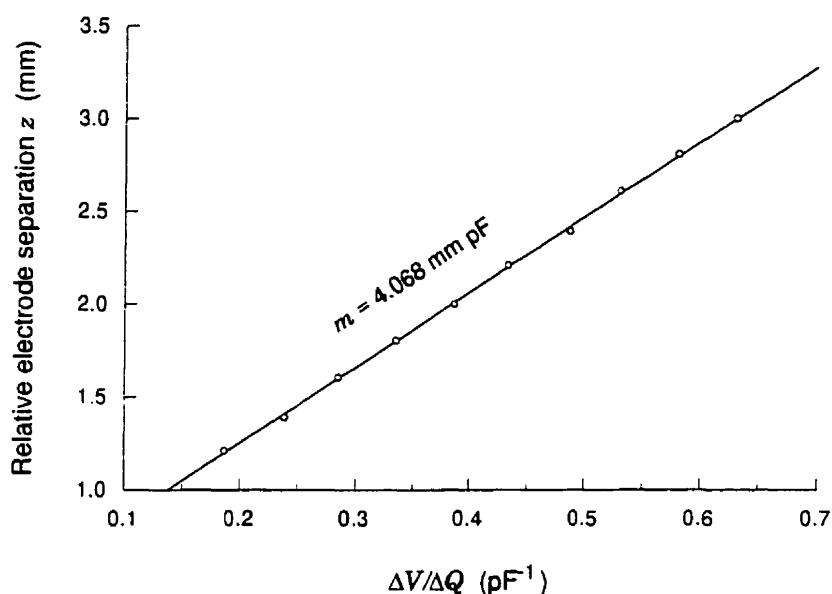
FIGURE 6.3. A plot of the relative electrode separation z as a function of the inverse capacitance $(\Delta Q / \Delta V)^{-1}$. The solid line represents a least-squares fit to the data and has a slope 4.068 mm pF. The electrode area is determined from m/ε_o and equals 4.597 ±0.03 cm^2.

II. Calibration of the electrometer

For dosimetric purposes, it is important that one measures the collected charge in an absolute manner. Consequently, it was necessary to verify the response of our electrometer with a calibrated picoampere current source. A digitally controlled timing circuit (pseudo-arc monitor unit counter) which is normally used to control the beam-on time of the Clinac-18 medical linear accelerator for special treatments at the Montreal General Hospital was modified to serve as a universal timer. The timing circuit includes a relay switch which is triggered by an electronic pulse-counter. For the purpose of electrometer calibration, the pulse-counter was driven by a synchronized internal clock accurate to better than ±1 ms. The calibrated current source (model 261; Keithley, Cleveland, Ohio) was connected to the input of the relay switch which had its output connected directly to the electrometer. The calibrated picoampere source was set to

deliver ±1.000 nA and the timing unit programmed to allow current to flow into the electrometer for 100.0 s resulting ideally in an integrated charge of 100.0 nC reaching the electrometer by the time the relay-circuit was closed by the pulse counter.

The overall uncertainty of the electrometer calibration apparatus including the calibrated current source, the timing circuit, and the analog relay is limited by the time necessary for the relay switch to open an close the circuit. The switching time of the circuit was experimentally determined to be less than 2 ms, and is negligible for times on the order of 100 s. Ten separate measurements in each of the positive and negative current directions were made giving a mean electrometer reading of 99.99 ±0.02 nC where 0.02 nC represents one standard deviation of the measured data. Thus, the electrometer is precise to 0.02% and has a correction factor of 1.00006 ± 0.00002. This is well below the uncertainty in the integrated charge delivered to the electrometer, and therefore, does not need to be considered further.

III. Charge collection potential

Before undertaking a calculation of the absorbed dose using the signal from the PEEC, it is important to experimentally determine the amount of charge recombination that occurs in the chamber sensitive volume for every electrode separation. To achieve this, a series of saturation curves for each radiation modality (*i.e.*, continuous photon, pulsed photon, and pulsed electron beams) was collected as a function of the electrode separation prior to the measurement of the ionization gradient in phantom. Experimentally measured saturation curve data did not agree fully with calculations based on the Boag theory for the general recombination of ions in continuous[4, 5] and pulsed[6, 7] beams (see Chapter 5). In Chapter 7 these relatively minor yet measurable discrepancies are

discussed and a modified theory for ion recombination is developed. Based on the results

obtained in Chapter 7, we conclude that the optimum polarizing potential at which to

collect ions liberated in the chamber sensitive volume lies in the low voltage portion of

the near saturation region $(0.7 \lesssim f \lesssim 0.9)$ where charge multiplication is negligible. It

can be shown that an electric field strength of ~200 V/mm is sufficient to operate the

PEEC in the optimum charge collection region for all electrode separations.

IV. Calibration of therapy machine output

The embedded extrapolation chamber was used to determine the output of var-

ious high-energy photon and electron beams which are in clinical use at the Montreal

General Hospital. Dose measurements made with the PEEC were compared with dose

measurements conducted using calibrated Farmer-type cylindrical ionization chambers.

Irradiations of the PEEC and the calibrated Farmer-type chambers were performed with

a Cobalt-60 gamma source (Theratron 780; AECL, Ottawa, Ontario), x-ray beams in the

energy range from 4 to 18 MV, and electron beams in the nominal energy range from 6

to 22 MeV. All high-energy x-ray and electron beams were provided by a Clinac-2300

linac (Varian, Palo Alto, California) with the exception of the 4 MV and the 10 MV

x-ray sources, which were from a Therapi 4 linac (EMI, Sunnyvale, California), and

a Clinac-18 linac (Varian, Palo Alto, California), respectively. Output calibration mea-

surements for the x-ray beams were made at 5 cm depth in solid water. For electron

beams, the depth of calibration corresponded to the depth of dose maximum for a given

beam. The mean value of the dose determined by two Farmer-type chambers was used

for comparison with the dose determined using the PEEC.

The reference point for determining the chamber depth in phantom was taken

as the depth of the proximal surface of the polarizing electrode (*i.e.*, the bottom of the graphite dag layer). The desired depth in phantom was obtained by adding an appropriate thickness of phantom material to the top of the PEEC and accounting for the thickness of the Solid-Water^{TM} used to hold the polarizing electrode (2 mm). The absorbed dose in Solid-Water^{TM} at the reference depth was determined by substituting the ionization gradient dQ/dz (corrected for charge losses as well as for temperature and pressure) into Eq. (1.22) according to the AAPM-TG21[3] and AAPM-TG25[8] protocols for the determination of absorbed dose using parallel-plate ionization chambers in high-energy photon and electron beams, respectively.

Measurements of the PEEC response to radiation in a given beam of radiation were performed for various relative electrode separations z. The electrode separations were chosen in order to satisfy the Bragg-Gray cavity conditions. The polarizing potential for each electrode separation was selected to produce an electric field in the chamber sensitive volume of approximately 200 V/mm for all dose output measurements. All ionization measurements were corrected for charge recombination and diffusion losses following the method outlined in Chapter 7. Ionization measurements were also corrected for temperature and pressure. At a given electrode separation, the response of the chamber is linear with dose and, for the same dose, reproducible to better than $\pm 0.2\%$.

V. Summary

The Solid-Water^{TM} phantom-embedded extrapolation chamber (PEEC) is a variable air-volume parallel-plate ionization chamber which forms an integral part of a Solid-Water^{TM} water-equivalent phantom. The chamber relative electrode separation can range from 0.5 mm to 10 mm with a precision of ± 0.002 mm. The chamber is designed such as

to minimize the amount of scatter from non Solid-Water^{TM} chamber components. Hence, all metallic chamber components are separated from the sensitive volume by 10 cm of Solid-Water^{TM}.

The design of the PEEC has several advantages over cylindrical Farmer-type chambers that are currently in use for the calibration of high-energy photon and electron beams:

(i)   the PEEC can measure the ionization gradient dQ/dm directly without prior calibration in a known radiation field;

(ii)   the replacement correction factor associated with cylindrical ionization chambers is not required for parallel-plate ionization chambers; and

(iii)   since the phantom is essentially the chamber wall, a wall correction factor is unnecessary.

From capacitance measurements using a calibrated electrometer the effective area A of the PEEC collecting electrode was determined to be $A = 4.597 \pm 0.03$ cm^2. The electrometer was calibrated from a calibrated current source at the Montreal General Hospital using a specially designed digital timing circuit and was found to have a calibration factor of essentially 1.000.

References

1. C. Constantinou, F. Attix, and B. R. Paliwal, "A solid water phantom material for radiotherapy in x–ray and γ–ray beam calibrations," Med. Phys. **9**, 436–441 (1982).

2. A. K. Ho and B. R. Paliwal, "Stopping power and mass energy absorption coefficient ratios for Solid Water," Med. Phys. **13**, 403–404 (1986).

3. AAPM Task Group 21 of the Radiation Therapy Committee, "A protocol for the determination of absorbed dose from high-energy photon and electron beams," Med. Phys. **10**, 741–771 (1983).

4. J. W. Boag, "The saturation curve for ionization measurements in pulsed radiation beams," Br. J. Radiol. **25**, 649–650 (1952).

5. J. W. Boag, in *The Dosimetry of Ionizing Radiation*, edited by K. R. Kase, B. E. Bjärngard, and F. H. Attix, Volume 2, Chapter 3 (Academic Press, Orlando, 1987).

6. J. W. Boag, "Ionization measurements at very high intensities I. Pulsed radiation beams," Br. J. Radiol. **23**, 601–611 (1950).

7. J. W. Boag and J. Currant, "Current collection and ionic recombination in small cylindrical ionization chambers exposed to pulsed radiation," Br. J. Appl. Phys. **53**, 471–478 (1980).

8. AAPM Task Group 25 of the Radiation Therapy Committee, "Clinical electron-beam dosimetry," Med. Phys. **18**, 73–109 (1991).

CHAPTER 7

Determination of ion collection efficiency

I.   Introduction

In currently used radiation dosimetry protocols the relative contributions of initial recombination and ion diffusion to the total charge loss are assumed to be negligible in comparison with the contribution of general recombination, and therefore are not considered when calculating the ionization chamber ion collection efficiency. This assumption may lead to errors in the calculated ion collection efficiency since, strictly speaking, initial recombination and ion diffusion against the applied potential are always present.

In Chapter 5, it was shown that the effects of both general and initial recombination as well as ion diffusion can be incorporated into a comprehensive model for charge loss in an ionization chamber. According to Böhm's comprehensive model for charge loss in an ionization chamber,[1] described in Chapter 5, the total ion collection efficiency in a *continuous radiation beam* f^c may be written as follows:

$$f^c = f_g^c f_i f_d$$

$$= \left\{ 1 + \frac{\Lambda_i + \Lambda_d}{V} + \frac{\Lambda_g^c + \Lambda_i \Lambda_d}{V^2} + \vartheta\left(\frac{1}{V^3}\right) \right\}^{-1}, \qquad (7.1)$$

where Λ_g^c is, in theory, proportional to dose rate $\dot{\rho}_c$ of the continuous radiation and to the fourth power of the electrode separation d, i.e., $\Lambda_g^c \propto \dot{\rho} d^4$; Λ_i is proportional to d and

148

to the linear ion density N_o per charged particle track; and Λ_d is directly proportional to the temperature T of the chamber gas. Thus Λ_g^c depends on both the dose rate and the chamber geometry, Λ_i depends on the chamber geometry but not on the dose rate, and Λ_d is independent of both the chamber geometry and the dose rate.

In a continuous radiation beam, the relative importance of general recombination with respect to ion diffusion $_c\chi_d^g$ may be calculated by taking the ratio of the general recombination term and the ion diffusion term in Eq. (7.1), to obtain

$$_c\chi_d^g = \frac{\Lambda_g^c/V^2}{\Lambda_d/V} \times \frac{\dot{\rho}_c d^4}{V} . \tag{7.2}$$

From Eq. (7.2) it is clear that, for non-zero Λ_d, $_c\chi_d^g$ decreases as the applied potential V is increased and as $\dot{\rho}_c$ or d are decreased. The relative importance of general recombination with respect to initial recombination $_c\chi_i^g$ may be calculated in a similar manner to get

$$_c\chi_i^g = \frac{\Lambda_g^c/V^2}{\Lambda_i/V} \times \frac{\dot{\rho}_c d^3}{V} . \tag{7.3}$$

and similar conclusions to those obtained from Eq. (7.2) may be drawn.

Table 7.1 summarizes the dependence on the dose rate $\dot{\rho}_c$ and the electrode separation d of the various chamber parameters Λ_g^c, Λ_i, and Λ_d for general recombination, initial recombination, and ion diffusion, respectively, in continuous beams of radiation. The relative contributions of the three charge loss mechanisms in terms of $_c\chi_d^j$ and $_c\chi_i^j$, where j is a variable representing the appropriate charge loss mechanism (general recombination, initial recombination, or ion diffusion), are also shown in columns (6) and (7), respectively. The presence of a voltage term in columns (6) and (7) suggest that a deviation from linearity might be observed if one accounts for only general recombination in the chamber and saturation curve data are plotted in the form of $1/Q$ vs $1/V^2$.

149

Table 7.1 Summary of the dependence on polarizing potential V of general recombination, initial recombination, and ion diffusion in continuous radiation beams. The chamber-air parameters for the above charge loss mechanisms, Λ_g^c, Λ_i, and Λ_d, respectively, along with their dependence on the dose rate $\dot{\rho}_c$ and the electrode separation d are also listed. In addition, the relative contributions of each charge loss mechanism in terms of $_c\chi_d^j$ [column (6)] and $_c\chi_i^j$ [column (7)] where j is a variable representing the appropriate charge loss mechanism (general recombination, initial recombination, or ion diffusion) are shown.

(1)	(2)	(3)	(4)	(5)	(6)	(7)
	voltage dependence	chamber-air parameter	dose rate dependence	d dependence	$_c\chi_d^j$	$_c\chi_i^j$
general recombination	V^{-2}	Λ_g^c	$\dot{\rho}_c$	d^4	$\dot{\rho}_c d^4/V$	$\dot{\rho}_c d^3/V$
initial recombination	V^{-1}	Λ_i	—	d	d	1
ion diffusion	V^{-1}	Λ_d	—	—	1	d^{-1}

As shown in Chapter 5, the comprehensive model for charge loss in a *pulsed radiation beam* predicts that the ion collection efficiency f^p is given as:

$$f^p = f_g^p f_i f_d$$

$$= \left\{ 1 + \frac{\Lambda_g^p + \Lambda_i + \Lambda_d}{V} + \vartheta\left(\frac{1}{V^2}\right) \right\}^{-1} . \tag{7.4}$$

where Λ_i and Λ_d were defined above for continuous beams, and Λ_g^p is proportional to the pulse charge density ρ_p and to the square of the electrode separation d, i.e., $\Lambda_g^p \propto \rho_p d^2$.

The relative importance of general recombination for pulsed beams with respect to ion diffusion $_p\chi_d^g$ may be calculated from

$$_p\chi_d^g = \frac{\Lambda_g^p}{\Lambda_d} \propto \rho_p d^2 . \tag{7.5}$$

Table 7.2 Summary of the dependence on polarizing potential V of general recombination, initial recombination, and ion diffusion in pulsed radiation beams. The chamber-air parameters for the above charge loss mechanisms, Λ_g^p, Λ_i, and Λ_d, respectively, along with their dependence on the pulse charge density ρ_p and the electrode separation d are also listed. In addition, the relative contributions of each charge loss mechanism in terms of $_p\chi_d^j$ [column (6)] and $_p\chi_i^j$ [column (7)] where j is a variable representing the appropriate charge loss mechanism (general recombination, initial recombination, or ion diffusion) are shown.

(1)	(2)	(3)	(4)	(5)	(6)	(7)
	voltage dependence	chamber-air parameter	dose rate dependence	d dependence	$_c\chi_d^j$	$_c\chi_i^j$
general recombination	V^{-1}	Λ_g^p	ρ_p	d^2	$\dot\rho_c d^2$	$\dot\rho_c d$
initial recombination	V^{-1}	Λ_i	—	d	d	1
ion diffusion	V^{-1}	Λ_d	—	—	1	d^{-1}

Thus the relative importance of general recombination with respect to ion diffusion is diminished for small electrode separations d and for low pulse charge densities ρ_p.

Table 7.2 summarizes the dependence on the pulse charge density ρ_p and the electrode separation d of the various chamber parameters Λ_g^p, Λ_i, and Λ_d for general recombination, initial recombination, and ion diffusion, respectively, in pulsed beams of radiation. The relative contributions of the three charge loss mechanisms in terms of $_p\chi_d^j$ and $_p\chi_i^j$, where j is a variable representing the appropriate charge loss mechanism, are also shown in columns (6) and (7), respectively. The absence of a voltage term in columns (6) and (7) implies that the relative contributions of general recombination, initial recombination, and diffusion loss cannot be discerned by varying the chamber potential. Thus, no error in the determination of the ion collection efficiency f^p from considerations of general recombination alone (*i.e.*, ignoring initial recombination and diffusion loss) should be observed from a plot of $1/Q$ vs $1/V$ for pulsed beams.

In this Chapter, we study the dependence of the collection efficiency data on the applied chamber polarizing potential for cylindrical Farmer-type ionization chambers and for parallel-plate ionization chambers in both continuous and pulsed radiations beams. By varying the source-detector distance, we were also able to look at the dependence of the ion collection efficiency on the dose rate $\dot{\rho}_c$ in continuous beams and on the pulse charge density ρ_p in pulsed beams. In addition, the dependence of the ion collection efficiency on the electrode separation d in continuous and pulsed radiation beams was studied using the variable-volume phantom-embedded extrapolation chamber (PEEC).

II.   Materials and Methods

II.A.   Ion collection efficiency measurements with a Farmer chamber

The continuous photon beam for our measurements was provided by a Cobalt–60 unit (Theratron-780, AECL, Ottawa, Ontario). The unit is used for routine radiotherapy and produced an exposure rate in air of 160 R/min for a 10×10 cm^2 field at a source-chamber distance (SCD) of 80 cm. The pulsed beams used in our measurements (18 MV photons and 9 MeV electrons) were obtained from a Clinac-2300 medical linear accelerator with a dose rate of ~500 cGy/min at the depth of dose maximum d_{max} in a water phantom for a 10×10 cm^2 field at a source–surface distance (SSD) of 100 cm. The instantaneous charge density produced in the chamber per pulse, *i.e.*, the pulse charge density ρ_p, for this geometry is approximately 1 nC cm^{-3}.

For continuous photon beams, the saturation curves reported below were measured with a commercial 0.6 cm^3 Farmer-type thimble ionization chamber (model 2571 A, Nuclear Enterprises, Beenham, Reading, England). The Farmer chamber was operated in the standard configuration, with the collecting electrode grounded through an electrometer

(model 35617, Keithley, Cleveland, Ohio) and the polarizing electrode connected to a regulated DC power supply (model 412 B, Fluke, Seattle, Washington). The chamber polarizing potentials for the Farmer chamber ranged from 0 to 650 V, and the exposure rates from ~14 R/min (long SCD) to ~5400 R/min (SCD ~15 cm; the chamber inside the cobalt unit multivane collimator), corresponding to dose rates to a small mass of water in air of ~14 cGy/min to ~5400 cGy/min, respectively. The saturation charge results reported in Section III.B were normalized to irradiation times of 1 minute.

Measured leakage charges were essentially linear with applied chamber voltage and amounted to less than 0.01 nC/min at a potential of 600 V. At a potential of 600 V the current collected for a dose rate of 160 cGy/min was on the order of 35 nC/min, thus we estimate the leakage as a percentage of the total measured charge on the order of 0.001%, 0.03%, and 0.3% at dose rates of 5400, 160, and 14 cGy/min, respectively. At potentials below 600 V the ratio of leakage charge to the total measured signal in the near saturation region is proportionally lower. In view of its relatively low contribution to the total signal, the leakage charge has been ignored in the analysis of the data.

A polystyrene cobalt-60 buildup cap was used in all continuous beam irradiations. For each chamber polarity, the mean value of at least four measurements was used for the measured charge. The standard deviation of the measured charge at each point typically was on the order of 0.07% of the mean. The charge Q reported in the data analysis below represents the mean value of the measured charges obtained for positive and negative chamber polarities. The polarity effect for the Farmer-type chamber was on the order of 0.1% of the measured Q.

Measurements of the collection efficiency in the pulsed radiation beams were carried out in the standard calibration geometry for the Clinac-2300 linear accelerator at the Montreal General Hospital, *i.e.*, with a field size of 10×10 cm^2 at an SSD of

100 cm, and at a depth in phantom of 5 cm for the 18 MV photon beam, and at d_{max}

(2.2 cm) for the 9 MeV electron beam. The pulse charge densities ρ_p produced in the

chamber for the 18 MV photon beam and the 9 MeV electron beam at an SSD of 100 cm

were approximately 1 nC cm^{-3}. A second set of collection efficiency data for the 18 MV

photon beam was also collected for an SSD of 500 cm and a field size of 15×15 cm^2

defined at the phantom surface, which produced a ρ_p of approximately 0.04 nC cm^{-3}

(1/25 nC cm^{-3}).

II.B. Ion collection efficiency measurements with a phantom-embedded extrapolation chamber

The characteristics of our phantom-embedd extrapolation chamber (PEEC) were

described in detail in Chapter 6. A series of saturation curves corresponding to various

electrode separations d was collected for continuous photon beams, an 18 MV pulsed

photon beam, and a 9 MeV pulsed electron beam. Ion collection efficiency data were

studied for separations d of 0.5, 1.5, 2.5, and 3.5 mm which span the entire range of d

used in the output calibration of clinical radiotherapy machines.

Saturation curves for continuous radiation beams were measured at a depth of

5 cm in Solid-Water^{TM} phantom with an SSD of 80 cm and field size of 10×10 cm^2

defined at the phantom surface. Measurements in the pulsed radiation beams were done

at an SSD of 100 cm and a field size of 10×10 cm^2 defined at the phantom surface. For

the 18 MV photon beam the depth of measurement in Solid-Water^{TM} phantom was 5 cm

and corresponded to a pulse charge density ρ_p of ~1 nC cm^{-3}. For the 9 MeV electron

beam the depth of measurement was 2.2 cm (d_{max}) also corresponding to a pulse charge

density ρ_p of ~1 nC cm^{-3}. The collection efficiency for an electrode separation of 2.0 mm

was also measured at depth of 5 cm in phantom with an SSD of 500 cm and field size

of 15×15 cm^2 defined at the phantom surface corresponding to ρ_p ~0.04 nC cm^{-3}. The

electric field strength in the chamber sensitive volume ranged from 0 to 400 V/mm for each electrode separation.

Measured leakage charges were negligible for all electric field strengths with this chamber. For each chamber polarity, the mean value of at least four measurements was used for the determination of the measured charge. The standard deviation of the measured charge at each point typically was on the order of 0.05% of the mean. The charge Q reported in the data analysis below represents the mean value of the measured charges obtained for positive and negative chamber polarities. The polarity effect for the PEEC ranged between 0 and 5% of the measured Q, being most severe for small d in the pulsed electron beam and least severe for large d in the pulsed photon beam.

III.   Results for continuous photon beams

III.A.   Collection efficiency for a Farmer chamber in continuous radiation at a constant dose rate

Figure 7.1(a) shows typical saturation curve data measured with a dose rate of 160 cGy/min and plotted in the standard $1/Q$ vs $1/V^2$ format for $0.7 < f < 1$. The dotted line represents a least-squares fit to measured data in the voltage range from 5 to 100 V and fits the $1/V^2$ model with a very high correlation coefficient. This suggests that the assumption of the predominance of general recombination is valid and a linear extrapolation of $1/V^2 \rightarrow 0$ yields a Q_{sat} of 33.76 nC for the particular collection efficiency experiment shown.

However, a closer look at the data points of Fig. 7.1(a) reveals that $1/Q$ deviates from the expected $1/V^2$ dependence at large applied potentials ($1/V^2 \rightarrow 0$). This deviation becomes more evident in Fig. 7.1(b), which presents on an expanded scale

FIGURE 7.1. A plot of $1/Q$ vs $1/V^2$ for saturation curve data measured with a 0.6 cm^3 thimble ionization chamber in a continuous beam of photons with an exposure rate of 160 R/min. Part (a) shows the full data set in the near saturation region where $0.7 \lesssim f < 1.0$. The dotted line represents a least-squares fit to the data indicated by open circles and results in $Q_{sat} = 33.76$ nC. Data within the shaded area of (a) for the near saturation region are shown on an expanded scale in (b). The solid line in (b) represents the curve fit of Eq. (7.6) to the data shown by open circles with $\alpha = 3.79 \times 10^{-3}$ V and $\beta = 2.57 \times 10^{-1}$ V^2, and provides a Q_{sat} of 33.88 nC. The data in the shaded region of (b) for the extreme near-saturation region are shown on an expanded scale in (c). The dotted line in (c) corresponds to the least-squares fit shown in (a). The dashed-dotted line represents the two-voltage technique [Eq. (5.18)] applied to data measured at 150 V and 300 V (identified by double circles) and results in $Q_{sat} = 34.01$ nC.

the near saturation data of Fig. 7.1(a) corresponding to $f \gtrsim 0.97$. The dotted line in Fig. 7.1(b) represents the linear fit to measured data obtained in Fig. 7.1(a). It is obvious that charges measured at large potentials actually exceed the value for Q_{sat} of 33.76 nC as determined from the linear fit to data in Fig. 7.1(a), placing into doubt the conventional wisdom that $1/Q$ vs $1/V^2$ follows a linear relationship in the whole collection efficiency range from 0.7 to 1.0.

As discussed above, in addition to general recombination there are two other processes which contribute to charge loss in an ionization chamber: initial recombination and diffusion loss. These two processes depend on the applied potential but not on the dose rate and are generally ignored in the determination of Q_{sat}. However, they may play a role in the final approach to saturation because they are governed by a $1/Q$ vs $1/V$ linear relationship that saturates more slowly than general recombination which is characterized by a $1/Q$ vs $1/V^2$ linear relationship.

To investigate the possible effects of initial recombination and ion diffusion on the saturation curve, we express Eq. (5.56) in the form of

$$\frac{1}{Q} = \frac{1}{Q_{sat}} + \frac{\alpha}{V} + \frac{\beta}{V^2} . \tag{7.6}$$

where $\alpha = (\Lambda_i + \Lambda_d)/Q_{sat}$ and $\beta = (\Lambda_g + \Lambda_i\Lambda_d)/Q_{sat}$, and carry out a curve fitting to the measured data of Fig. 7.1(a) in the voltage range from 5 to 100 V. As shown by the solid curve in Fig. 7.1(b), Eq. (7.6) applied to the data indicated by open circles, with $\alpha = 3.79\times10^{-3}$ V and $\beta = 2.57\times10^{-1}$ V^2 gives a better agreement with measured data than the $1/Q$ vs $1/V^2$ linear relationship. Equation (7.6) results in a Q_{sat} of 33.88 nC, but still fails to predict the values for Q measured at chamber polarities above 200 V.

The Q_{sat} obtained with Eq. (7.6) exceeds the result obtained from the linear extrapolation of $1/Q$ vs $1/V^2$ by 0.4%. Thus, the breakdown of the $1/Q$ vs $1/V^2$ linear

relationship at high chamber potentials may be explained partially by the contribution of initial recombination and ion diffusion to the total charge lost in the chamber volume. The excess charge measured at potentials above 200 V, however, is probably contributed by non-dosimetric effects and therefore should not be included in the determination of the true saturation charge that is used in the determination of the absorbed dose.

The finding that charge measured above ~200 V contains a small non-dosimetric component is of some interest clinically. Cylindrical ionization chambers are typically operated at potentials of 300 V and Q_{sat} values are determined customarily with the two-voltage technique given by Eq. (5.17) using charge data measured at 300 V and 150 V. Since these two points seem to contain a small non-dosimetric component, as shown in Fig. 7.1(b), the two-voltage technique might result in an erroneous value for Q_{sat}.

To evaluate this potential problem for our ionization chamber we illustrate in Fig. 7.1(c) the results of the two-voltage technique [Eq. (5.18)] advocated by the AAPM[2] and others[3-6] for the determination of Q_{sat}. The dotted line represents the linear fit of $1/Q$ vs $1/V^2$ obtained in Fig. 7.1(a). The dashed–dotted line represents the two-voltage technique through charges measured at 300 V and 150 V. Since the data measured at these two points are already outside the linear region of the $1/Q$ vs $1/V^2$ plot, the linear fit to only these two data points actually produces a larger Q_{sat} (34.01 nC) than did the linear fit of Fig. 7.1(a) accounting for general recombination alone (33.76 nC) or Eq. (7.6) in Fig. 7.1(b) accounting for general recombination, initial recombination, and diffusion loss (33.88 nC). The latter value provides the best estimate for Q_{sat} with the two-voltage technique overestimating the value by 0.4% and the linear fit of $1/Q$ vs $1/V$ underestimating it by 0.4%.

Several effects such as chamber leakage currents, charge multiplication in the chamber sensitive volume, or Schottky effect[7] may be the cause of the non-dosimetric

excess charge at high chamber potentials. Schottky effect is extremely unlikely to affect our measurements at room temperature and chamber potentials below 1000 V. Its estimated contribution to the total measured charge is on the order of 10^{-67} nC/min.

As mentioned above, the chamber leakage currents measured in the absence of radiation were negligible in comparison to the measured signal, except possibly for the highest applied potentials (>600 V) and the lowest dose rate (14 cGy/min) where the leakage current may have accounted for up to 0.3% of the measured signal. Despite the possibility that chamber leakage currents increase under the influence of radiation and adversely affect the measured charge in a manner for which we cannot correct, we conclude that the chamber leakage currents are not responsible for the excess measured charge.

To avoid problems with charge multiplication inside the chamber sensitive volume, Boag recommended that electric fields should not exceed 1000 V/mm anywhere in the chamber volume. The electric field inside our thimble chamber was estimated following the method proposed by Boag.[8] The maximum field strength, corresponding to an applied potential of 650 V, present in the chamber was ~1500 V/mm at the tip of the central electrode (assuming a hemispherical electrode tip) and only ~700 V/mm along its length. One should expect that charge multiplication can be discounted since the maximum electric field present in the chamber (1500 V/mm) is less than 2000 V/mm, the electric field strength at which charge multiplication is believed to become important.[8–10] However, it is possible that the small excess charge measured at high applied potentials is caused by the onset of charge multiplication in the chamber.

Charge multiplication is an exponentially increasing function of the applied voltage and will multiply the measured charge Q such that the collection efficiency $f = Q/Q_{sat}$ is given by $f = Qe^{\gamma V}/Q_{sat}$, where γ is a constant of proportionality for charge

multiplication. Based on Eq. (7.6), accounting for charge multiplication leads to the following approximation for the saturation curve:

$$\frac{1}{Q} = \left[\frac{1}{Q_{sat}} + \frac{\alpha}{V} + \frac{\beta}{V^2}\right] e^{-\gamma V}. \tag{7.7}$$

In Fig. 7.2 we plot the data from Fig. 7.1 in the form $1/Q$ vs $1/V$ for collection efficiency $f > 0.99$. The dotted line in Fig. 7.2 represents the linear fit to measured data obtained in Fig. 7.1(a) assuming the presence of general recombination alone; the solid line represents the fit of Eq. (7.6) [$\alpha = 3.79 \times 10^{-3}$ V, $\beta = 0.257$ V^2, $Q_{sat} = 33.88$ nC] obtained in Fig. 7.1(b) accounting for both general and initial recombination as well as for diffusion loss; and the dashed line represents the curve fit of Eq. (7.7) accounting for
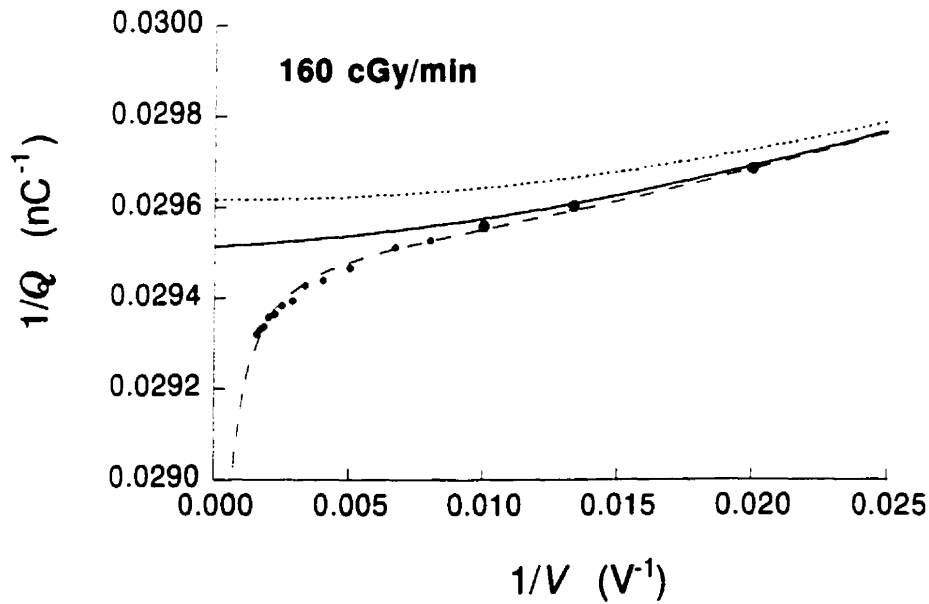
FIGURE 7.2. A plot of the saturation curve data of Fig. 7.1(c) in the extreme near-saturation region in the form of $1/Q$ vs $1/V$. The dotted curve corresponds to the least-squares fit shown in Fig. 7.1(a). The solid curve corresponds the fit of Eq. (7.6) from Fig. 7.1(b). The dashed curve represents the curve fit of Eq. (7.7) with $\alpha = 3.71 \times 10^{-3}$ V, $\beta = 0.257$ V^2, and $\gamma = 1.2 \times 10^{-5}$ V^{-1}, accounting for both general and initial recombination, ion diffusion, as well as charge multiplication, and predicts that $Q_{sat} = 33.87$ nC.

charge multiplication in addition to the three charge loss processes with $\alpha = 3.71 \times 10^{-3}$ V, $\beta = 0.257$ V^2, $Q_{sat} = 33.87$ nC, and $\gamma = 1.2 \times 10^{-5}$ V^{-1}.

It is evident that Eq. (7.7) follows the measured data very well in the whole collection efficiency range from 0.7 to 1. A Q_{sat} of 33.87 nC was determined through the fitting of Eq. (7.7) to the entire range of measured data and is within 0.03% of the value obtained in Fig. 7.1(b) using Eq. (7.6). The excellent agreement between the semi-empirical model of Eq. (7.7) and measured data in the extreme near-saturation region supports the hypothesis that charge multiplication contributes to the measured charge and that this excess charge should not be counted as part of the dosimetric process. Equation (7.7) implicitly contains the true Q_{sat} and allows for its extraction from the measured data by separating the contribution of charge multiplication and the dosimetric signal.

III.B. Dose-rate dependence of the collection efficiency for a Farmer chamber in continuous radiation

The saturation curve of Fig. 7.1 was measured at a dose rate of ~160 cGy/min. Since it is well known that the approach to saturation depends on the dose rate as well as on the applied potential, we carried out collection efficiency experiments on our chamber with various other dose rates from ~14 cGy/min to ~5400 cGy/min. Saturation curve data measured at five dose rates (14, 70, 160, 454, and 5400 cGy/min) are shown in Fig. 7.3 in the form of $1/Q$ vs $1/V$ for the near saturation region (~0.8 $< f <$ 1) in (a), and for the extreme near-saturation region (~0.99 $< f <$ 1) in (b). The dotted curves represent data fits assuming the validity of the $1/Q$ vs $1/V^2$ relationship (general recombination alone); the solid curves represent fits of Eq. (7.6) to measured data indicated by open circles, accounting for all three charge loss processes (recombination and diffusion); and the dashed curves represent fits of Eq. (7.7), which models the three charge loss processes
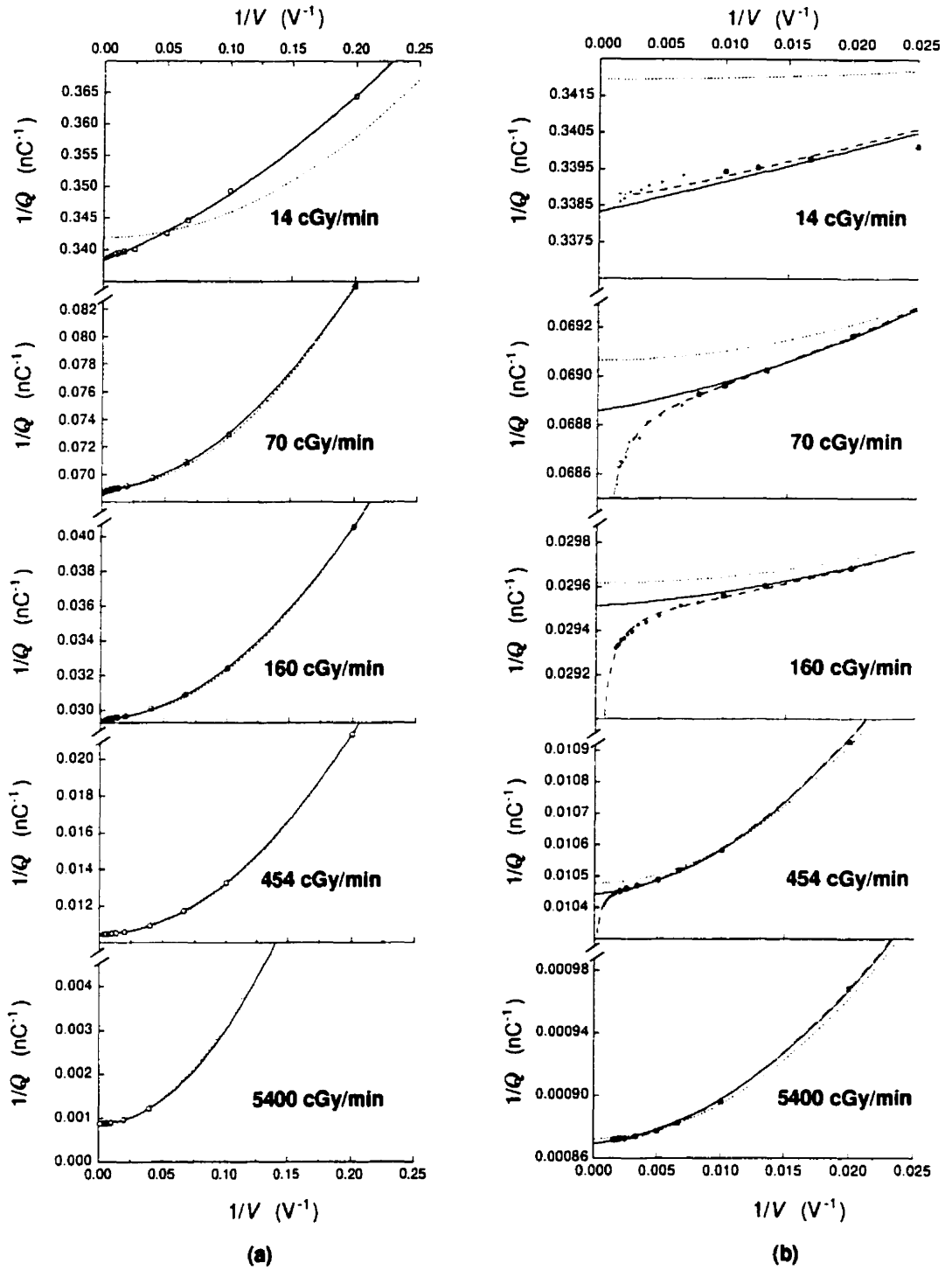
FIGURE 7.3. Saturation curve data for a 0.6 cm^3 thimble ionization chamber plotted as $1/Q$ vs $1/V$ for various dose rates of continuous cobalt-60 irradiation. Part (a) shows the near saturation region where $0.8 < f < 1$ and part (b) shows the extreme near-saturation region where $f > 0.99$. The dotted curves represent data fits assuming the validity of the $1/Q$ vs $1/V^2$ relationship, solid curves represent data fits of Eq. (7.6), and dashed curves represent data fits of Eq. (7.7).

as well as charge multiplication, to all data points.

For all dose rates, similarly to the situation discussed above for data measured at a dose rate of 160 cGy/min, we observe a deviation from the $1/Q$ vs $1/V^2$ relationship at high chamber potentials. The voltage at which the breakdown becomes noticeable generally increases with dose rate, and the breakdown is hardly visible at 5400 cGy/min even at the highest chamber potentials used. With an appropriate choice of parameters α, β, and γ, the semi-empirical model given by Eq. (7.7), which accounts for charge loss and charge multiplication, fits the measured data well for all dose rates.

The curve fitting of Eq. (7.7) to measured data results in values for α that are inversely proportional to the dose rate and values for β that are essentially independent of the dose rate. This finding is consistent with the assumption that general recombination depends on dose rate while initial recombination and diffusion loss do not.

In Table 7.3 we compare saturation charges Q_{sat} determined for our Farmer-type ionization chamber for five different dose rates between 14 and 5400 cGy/min. For each dose rate, Q_{sat} was determined with three methods: Method (i), the extrapolation to $1/V^2 = 0$ of the linear portion of the $1/Q$ vs $1/V^2$ data; Method (ii), the two-voltage technique [Eq. (5.17) with $V_H = 300$ V and $V_L = 150$ V]; and Method (iii), the semi-empirical model given by Eq. (7.7). Irrespective of the dose rate, the semi-empirical model predicts values for Q_{sat} that are ~0.4% higher than those predicted by Method (i). Values for Q_{sat} obtained from Method (ii) are scattered about the values obtained from Method (iii) depending on the degree to which the charges measured at 300 and 150 V are influenced by charge multiplication.

We believe that Eq. (7.7) provides the best approach to the determination of the true Q_{sat} in an ionization chamber irradiated with continuous beams. The two-voltage method currently advocated by the AAPM[2] and others[3-6] may overestimate the saturation

TABLE 7.3. Comparison of saturation charges Q_{sat} (nC) determined for a Farmer-type ionization chamber for various dose rates according to (i) extrapolation of linear region of $1/Q$ and $1/V^2$, (ii) the two-voltage technique [Eq. (5.17) with $V_H = 300$ V and $V_L = 150$ V] in the near-saturation region, (iii) the semi-empirical model given by Eq. (7.7). Values are expressed in parentheses as percentages of Q_{sat} obtained from Method (iii).

Dose rate (cGy/min)	extrapolation $(1/V^2)$	two-volt $(1/V^2)$	semi-empirical model (Eq. 7.7)	α $(10^{-3}$ V)	β (V^2)	γ $(10^{-6}V^{-1})$
5400	1145 (99.6)	1148 (99.8)	1150 (100.0)	0.75	0.206	1.0
454	95.39 (99.7)	95.81 (100.2)	95.66(100.0)	1.64	0.265	6.6
160	33.76 (99.6)	34.01 (100.4)	33.87 (100.0)	3.71	0.257	12
70	14.48 (99.8)	14.56 (100.2)	14.51 (100.0)	7.78	0.330	7.7
14	2.924 (99.0)	2.952 (99.9)	2.955 (100.0)	7.97	0.252	-1.1

charge by as much as 0.5% for dose rates encountered for the calibration of cobalt-60 radiotherapy machines, while a rigorous application of Boag's theory for general recombination in continuous beams will underestimate the saturation charge by -0.4% irrespective of the dose rate.

III.C. Dependence of the collection efficiency on electrode separation for the PEEC in continuous radiation

Figure 7.4 shows collection efficiency data measured for electrode separations ranging from 0.5 to 3.5 mm plotted in the form of $1/Q$ vs $1/V^2$ for $f \geq 0.7$. The dotted lines in Figs. 7.4(b) through 7.4(d) represent least-squares fits to the data measured in the near saturation region. The "goodness" of the linear fit to the data, as indicated on each plot by the correlation coefficient R, improves with increasing electrode separation. This observation is consistent with the theory of Section I, and implies that general recombination assumes a more prominent role in the charge lost within the chamber as the electrode separation d is increased. A linear fit is not presented in Fig. 7.4(a) because
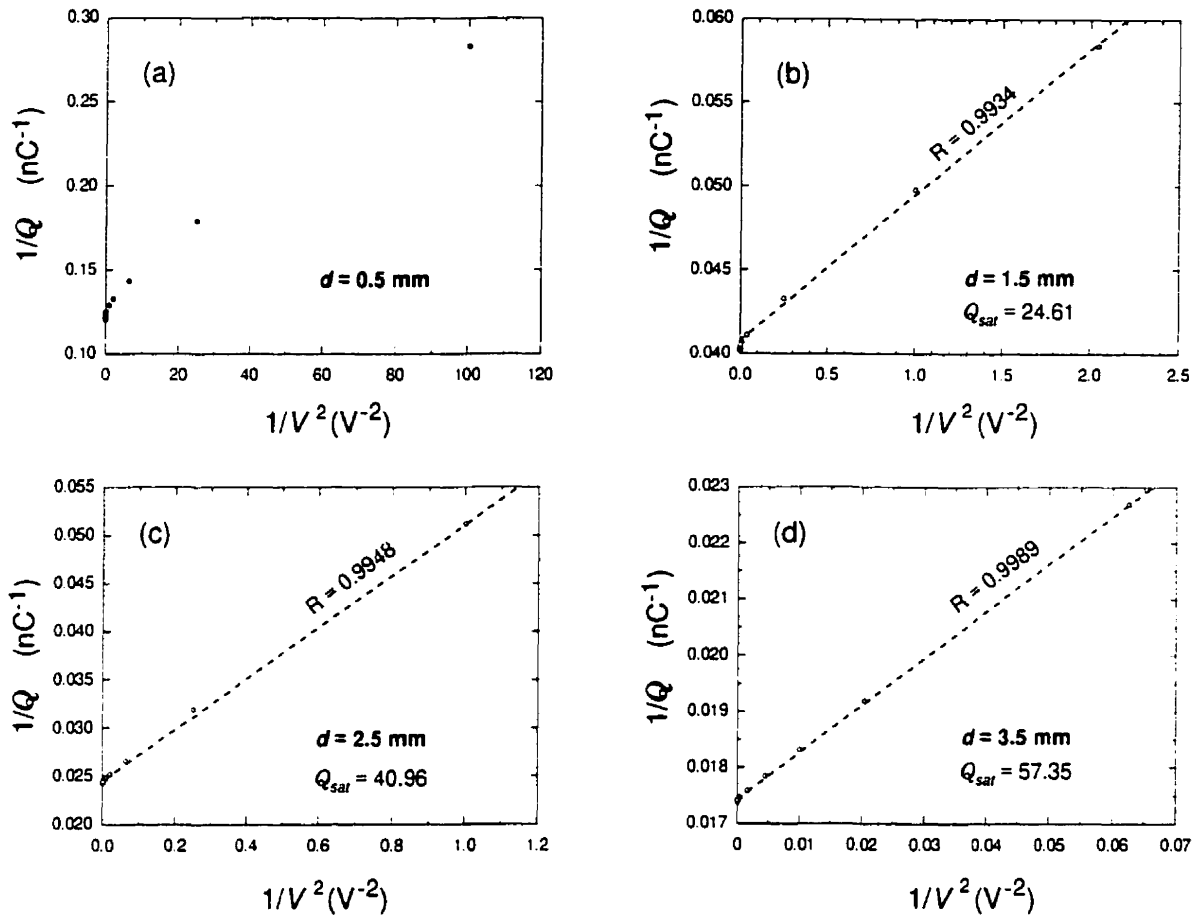
FIGURE 7.4. Saturation curve data measured with a parallel-plate ionization chamber for various electrode separations d in a continuous photon beam. The saturation charge Q_{sat} is found from extrapolating to $1/V^2 = 0$ the dashed lines representing least-squares fits to the linear region of the data. For the 0.5 mm electrode separation, no linear portion on the $1/Q$ vs $1/V^2$ plot could be found, hence no line is shown, and Q_{sat} could not be obtained by linear extrapolation of the data to $1/V^2 = 0$. The correlation coefficient R of the linear fit increases as electrode separation is increased indicating that the contribution of initial recombination and ion diffusion to the total charge loss diminishes with increasing separation d.

no satisfactory region of linearity could be found for an electrode separation of only 0.5 mm, suggesting that for small d the relative contribution of general recombination to the overall charge loss in an ionization chamber is minimal.
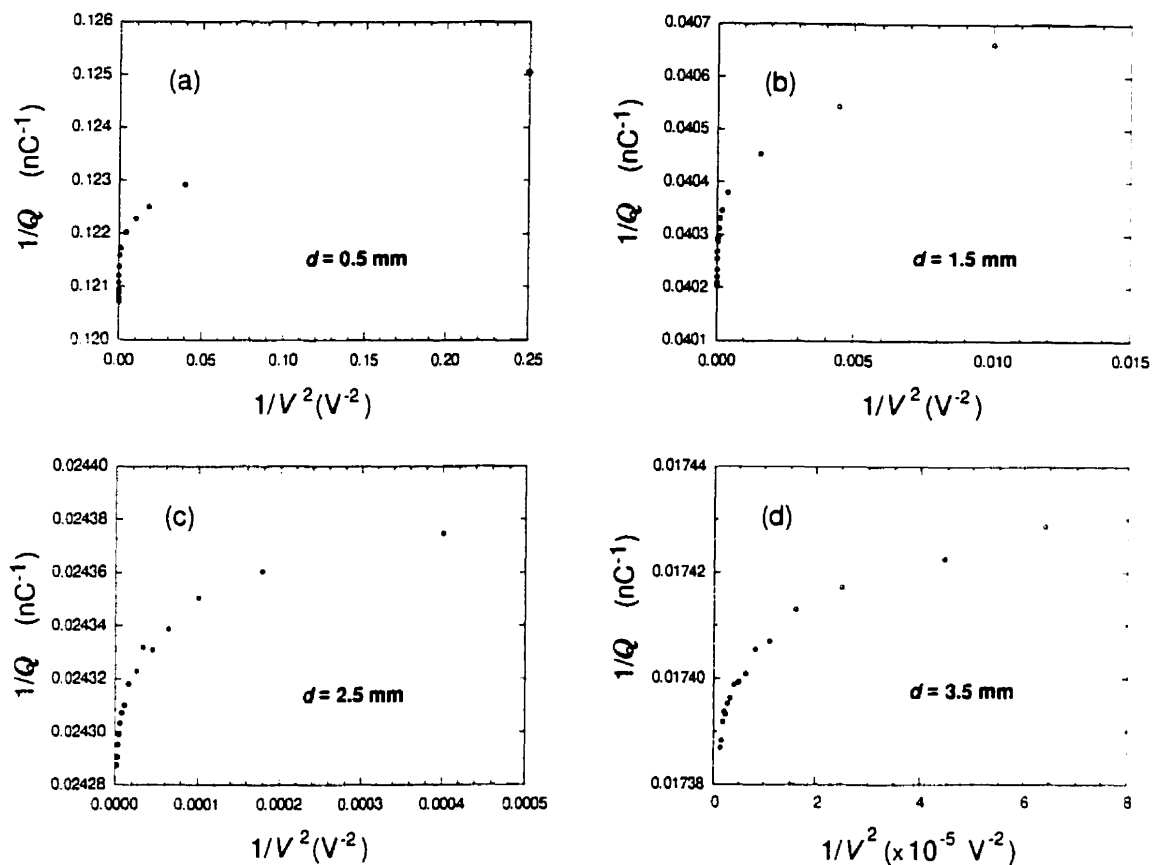
FIGURE 7.5. Collection efficiency data from Fig. 7.4 plotted on expanded scales showing that the $1/Q$ data do not follow a linear relationship with $1/V^2$ in the extreme near-saturation region. Thus, the extrapolation method used to determine Q_{sat} in Fig. 7.4 is unsatisfactory in this region.

Certainly for Figs. 7.4(a) and 7.4(b) which represent electrode separations of 0.5 and 1.5 mm, respectively, it is obvious that the predicted linear relationship between $1/Q$ and $1/V^2$ fails for large applied potentials. This observation is consistent with the comprehensive model for charge loss in a chamber, since Λ_g^c is strongly dependent on the electrode separation. In Fig. 7.5, the data from Fig. 7.4 are plotted on an expanded scale to show the deviation from linearity in more detail. When the data are shown on an expanded scale, it becomes apparent that the linearity between $1/Q$ and $1/V^2$ fails entirely for all electrode separations in the extreme near-saturation region, where

166

$f \geq 0.99$. Thus, it would seem inappropriate, especially for small electrode separations, to exclude the effects of initial recombination and ion diffusion on the overall charge loss in the chamber.

The saturation curve data of Fig. 7.4 are plotted in Fig. 7.6 in the form of $1/Q$ vs $1/E$ (*i.e.*, d/V). The dotted curves represent the least-squares fits accounting only for general recombination ($1/Q$ vs $1/V^2$) from Fig. 7.4. This fit was applied to data measured in the near saturation region which are indicated by open circles. The solid curves represent the curve fit of Eq. (7.6) which accounts for initial recombination and diffusion loss as well as general recombination. The curve fit provided by Eq. (7.6) is in better agreement with the measured data than the $1/Q$ vs $1/V^2$ linear relationship. The data from Fig. 7.6(a) are shown on an expanded scale in Fig. 7.6(b) to show the extreme near-saturation region in more detail. On this scale it is evident that Eq. (7.6) alone is insufficient to predict values for Q measured at electric fields above ~ 50 V/mm.

We hypothesize that the excess measured charge seen in Fig. 7.6(b) is due to charge multiplication in the chamber volume similarly to the case of the Farmer chamber at high polarizing potentials. The dashed curves in Fig. 7.6(b) represent the fits of Eq. (7.7), which includes all three charge loss mechanisms in addition to charge multiplication, to the entire data set. The curve fit of Eq. (7.7) is in excellent agreement with measured data throughout the whole range of electric fields from 1 V/mm to 400 V/mm, supporting our hypothesis that the excess measured charge is due to charge multiplication.

Table 7.4 summarizes the values for Q_{sat} resulting from each of the three curve fits. The values for Q_{sat} obtained from the curve fit to data in the near saturation region of Eq. (7.6), including initial recombination, general recombination, and diffusion loss, agree to within 0.1% with values obtained from the curve fit to all measured data of Eq. (7.7), including charge multiplication in addition to the three charge loss mechanisms, for all
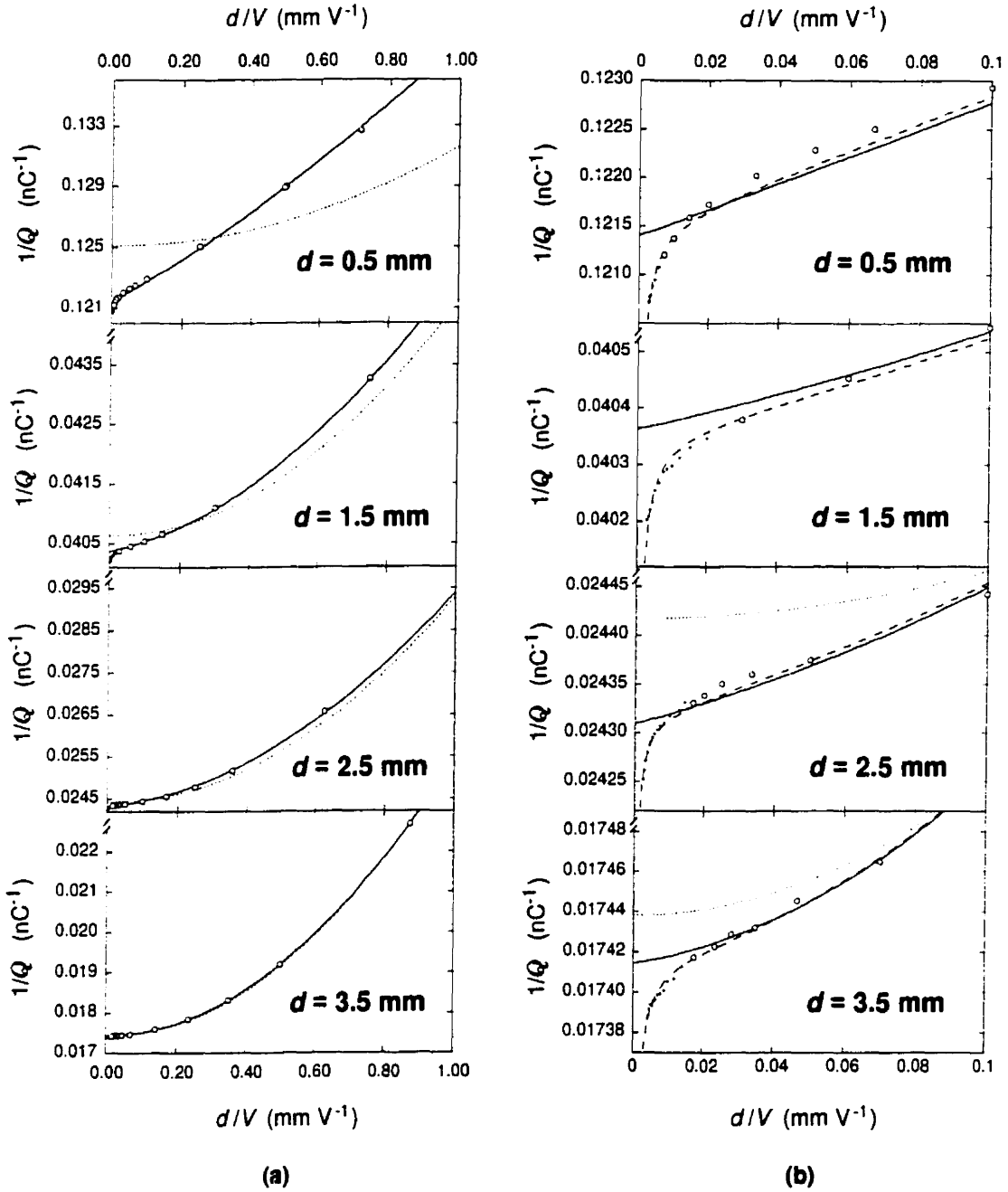
FIGURE 7.6. Saturation curve data from Fig. 7.4 plotted in the form of $1/Q$ vs $1/V$ for the full range of electric fields (a), and in the extreme near-saturation region (b). The dotted curves represent the linear fit to data in the near saturation region (indicated by open circle) of $1/Q$ vs $1/V^2$ accounting for only general recombination. The solid curves represent the curve fit of Eq. (7.6) to data in the near saturation region and include the contributions of initial recombination and diffusion loss as well as general recombination. The dashed curves represent the fit of Eq. (7.7) to all of the data points, including charge multiplication in addition to the three charge loss mechanisms.

TABLE 7.4. Comparison of saturation charges Q_{sat} (nC) for the PEEC for various electrode separations determined from (i) extrapolation of linear region of $1/Q$ and $1/V^2$, (ii) the semi-empirical model given by Eq. (7.6), and (iii) the semi-empirical model given by Eq. (7.7). Values are expressed in parentheses as percentages of Q_{sat} obtained from Method (iii).

electrode separation d (mm)	extrapolation $(1/V^2)$	semi-empirical model (Eq. 7.6)	semi-empirical model (Eq. 7.7)	α $(10^{-4}V))$	β $(10^{-3}V^2)$	γ $(10^{-6}V^{-1})$
0.5	7.993 (97.1)	8.237 (100.1)	8.230 (100.0)	132	3.83	20
1.5	24.61 (99.3)	24.78 (100.0)	24.78 (100.0)	14.4	3.26	13
2.5	40.96 (99.6)	41.14 (100.0)	41.12 (100.0)	9.52	4.13	6.4
3.5	57.35 (99.9)	57.43 (100.0)	57.41 (100.0)	2.66	6.58	8.0

electrode separations d. The values for Q_{sat} resulting from the assumed linear relationship between $1/Q$ and $1/V^2$, considering only general recombination, are consistently lower than values obtained from the other two methods. The agreement between the $1/Q$ vs $1/V^2$ method and the other methods improves from 0.97 to nearly 1.0 as the electrode separation d is increased from 0.5 to 3.5 mm, respectively. This improvement of the $1/Q$ vs $1/V^2$ fit to the data is consistent with the results of Table 7.1 which predict that general recombination becomes increasingly more important for large d. The relatively poor agreement observed between the linear model and Eqs. (7.6) and (7.7) for $d = 0.5$ mm confirms that general recombination is not the dominant mechanism for charge loss in the chamber and that initial recombination and diffusion loss must be included in the analysis of the collection efficiency for small d.

III.D. Consequences of the comprehensive model for charge loss in an ionization chamber for continuous irradiation

We tested the comprehensive model for the charge loss in an ionization chamber exposed to continuous irradiation to see if it correctly predicts the observed behavior of the

experimental data. Given that the product of the collection efficiencies for initial recombination and ion diffusion can be written in the form of $f' = \left(1 + \Lambda/V + \vartheta(1/V^2)\right)^{-1}$ with $\Lambda = \Lambda_i + \Lambda_d$, they are considered together in the following analysis. The theoretical total collection efficiency for ionization chambers in continuous beams was calculated using $f = f_g^c f'$ with the parameter incorporating initial recombination and ion diffusion Λ equal to 10 and for two values of Λ_g^c, namely $\Lambda_g^c = 1$ and $\Lambda_g^c = 1000$. In Fig. 7.7 the theoretical data are plotted in the form of $1/Q$ vs $1/V^2$ as is the current procedure for the determination of Q_{sat}. The theoretical curves are consistent with measured data in that as $1/V^2 \rightarrow 0$ the data deviate from linearity. The straight lines represent least-squares fits to the data indicated by open symbols. The model predicts that regardless of the
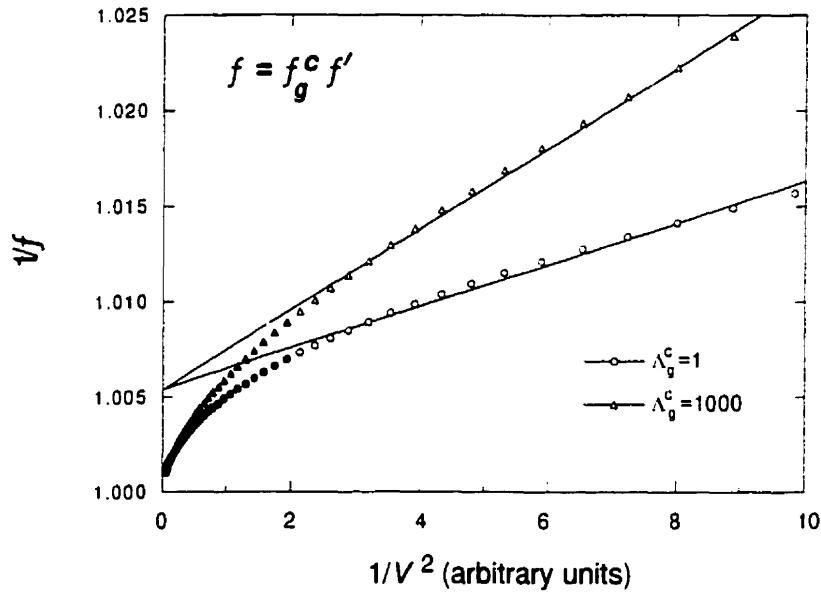
FIGURE 7.7. Plot of the inverse collection efficiency for an ion chamber in a continuous beam as predicted by the comprehensive model for charge loss in an ionization chamber. A linear relationship exists between $1/Q$ and $1/V^2$ in the near saturation region; however, in the extreme near saturation region, the data deviate from linearity. The linear extrapolation of the $1/Q$ vs $1/V^2$ data overestimates collection efficiency of the chamber by a constant factor irrespective of the value of Λ_g^c.

value for Λ_g^c the extrapolation of the lines intersects the same location on ordinate axis implying that Q_{sat} determined from a plot of $1/Q$ vs $1/V^2$ will be underestimated by an amount that is dependent on the parameters for initial recombination and ion diffusion.

This agrees with the results shown in Table 7.3 for the Farmer chamber, where for constant chamber geometry, the Q_{sat} determined from a plot of $1/Q$ vs $1/V^2$ underestimates the true Q_{sat} by -0.4% for all dose rates. The only charge loss parameter that changes with changing dose rate is Λ_g^c. The results obtained with the PEEC for various electrode separations also agree with the model. As pointed out earlier, the results shown in Table 7.4 indicate that the Q_{sat} determined from a plot of $1/Q$ vs $1/V^2$ underestimate the true Q_{sat} by a decreasing margin as the electrode separation is decreased. This is a direct result of the dependence of the parameter for initial recombination Λ_i on d while Λ_d is independent of d as shown in Table 7.1.

IV.   Results for pulsed photon and electron beams

IV.A. Dependence of the collection efficiency on pulse charge density for a Farmer chamber in pulsed radiation

Figures 7.1 through 7.3 deal with collection efficiency properties of a Farmer-type cylindrical ionization chamber irradiated with continuous beams. For comparison, we show in Fig. 7.8 the collection efficiency properties of the Farmer chamber irradiated with pulsed beams of 18 MV photons and 9 MeV electrons from a Clinac 2300 medical linear accelerator (Varian Associates, Palo Alto, CA). According to Böhm's approach, the collection efficiency for pulsed radiation f^p is given by Eq. (7.4), which for large V reduces to

$$f^p \approx \left\{ 1 + \frac{\Lambda_g^p + \Lambda_i + \Lambda_d}{V} \right\}^{-1}, \tag{7.8}$$
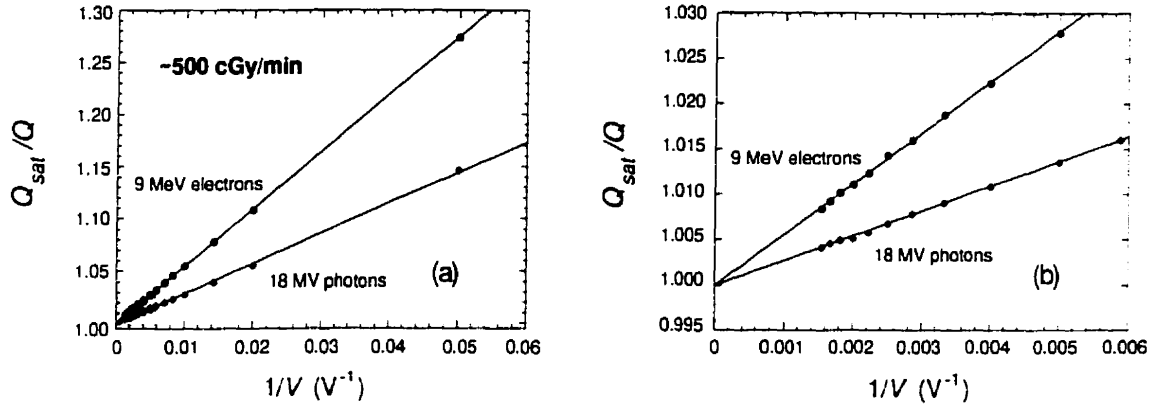
FIGURE 7.8. A plot of the inverse collection efficiency $(Q_{sat}/Q = 1/f)$ for a 0.6 cm^3 thimble ionization chamber as a function of $1/V$ for two pulsed radiation beams: 18 MV photons and 9 MeV electrons $(\rho_p \sim 1$ nC cm$^{-3})$. Part (b) shows the shaded area of part (a) on an expanded scale.

implying that a plot of $1/Q$ vs $1/V$ is linear in the near saturation region.

In Fig. 7.8, a plot of the inverse collection efficiencies $1/f = (Q_{sat}/Q)$ as functions of $1/V$ for the pulsed 18 MV photon and the 9 MeV electron beams results in straight lines in the near saturation region. Figure 7.8(b) shows on an expanded scale the shaded region of Fig. 7.8(a), proving that for a Farmer-type ionization chamber exposed to pulsed radiation producing a pulse charge density ρ_p of ~ 1 nC cm^{-3}, during the final approach to saturation, $1/Q$ is indeed linear with $1/V$ as predicted by Eqs. (5.28) and (7.8) for pulsed radiation beams. Results were plotted in the form of $1/f$ vs $1/V$ so that both sets of data could be shown in the same plot. The choice for Q_{sat} for each beam was determined from a linear extrapolation of the collection efficiency data to $1/V = 0$ and is justified by the fact that no deviation from linearity was observed for either beam.

The linearity between $1/Q$ and $1/V$ even at high applied potentials suggests that charge multiplication may be dose rate dependent and that for high instantaneous dose rates produced by medical linear accelerators charge multiplication may be negligible. To test this hypothesis, we varied the magnitude of the pulse charge density ρ_p by

increasing the SSD and relying on the inverse square law. Measurements of the ion

collection efficiency for various chamber potentials V were made with the Farmer

chamber in a Solid-Water^{TM} phantom located at an SSD of 500 cm, corresponding to

ρ_p ~0.04 nC cm^{-3}. The results of this experiment are shown in Fig. 7.9. The solid

line in Fig. 7.9(a) represents a least-squares fit to the data in the near saturation region,

which, when extrapolated to $1/V = 0$, yields a value for Q_{sat} of 1.025 nC. The linear

relationship between $1/Q$ vs $1/V$ fails for potentials in the extreme near-saturation region

when ρ_p is relatively small. This small deviation from linearity is most likely due to the

onset of charge multiplication in the chamber. The effects of charge multiplication in the

chamber sensitive volume for pulsed beams is readily extracted from the measured data

by the following expression which is similar to Eq. (7.7):

$$\frac{1}{Q} = \left[\frac{1}{Q_{sat}} + \frac{\alpha'}{V}\right] e^{-\gamma V} . \tag{7.9}$$

where $\alpha' = \Lambda_g^p + \Lambda_i + \Lambda_d$. The dashed curve in Fig. 7.9 represents a least-squares fit of

Eq. (7.9) to the measured data and follows the experimental data very well. Thus, for

low pulse charge density ρ_p, charge multiplication affects the charge measured at high

polarizing potentials. The value for Q_{sat} obtained from a fit of Eq. (7.9) to all of the

data points is 1.024 nC which is slightly less than the result of the linear extrapolation

of $1/Q$ vs $1/V$ for data in the near saturation region.

For an SSD of 500 cm, the dose rate was so low (~5 nC/min) that the contribution

of leakage currents in the chamber could not be completely ignored. We estimate

that the leakage charge accounts for roughly 0.2% of the total measured signal at a

chamber potential of 600 V diminishing to nearly 0% for potentials on the order of

50 V. Thus some of the deviation from linearity in the $1/Q$ vs $1/V$ relationship at high

chamber potentials is due to measured leakage currents; however, leakage cannot be used
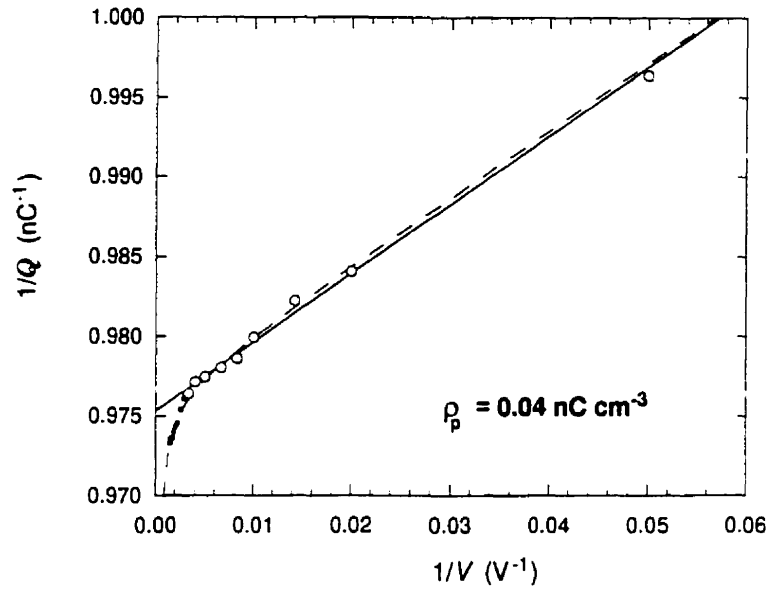
FIGURE 7.9. Saturation curve data for a Farmer-type ionization chamber in an 18 MV pulsed photon beam for ρ_p -0.04 nC cm^{-3} plotted in the form of $1/Q$ vs $1/V$ for $f \gtrsim 0.97$. The solid line represents a least-squares linear fit to the data in the near saturation region and yields a value for Q_{sat} of 1.025 nC when extrapolated to $1/V = 0$. The dashed line represents a least-squares fit of Eq. (7.9) to all data points, including charge multiplication in addition to charge loss mechanisms, and results in a Q_{sat} of 1.024 nC.

exclusively to explain the observed deviation of -0.3 % at the highest applied potential because at this potential, leakage is only on the order of -0.2%. On account of the very low signal and the relatively large contribution of leakage to the total signal at large potentials, the data set shown in Fig. 7.9 is somewhat inconclusive.

IV.B. Dependence of the collection efficiency on electrode separation for the PEEC in pulsed radiation

Ion collection efficiency data were also gathered for various electrode separations d in pulsed radiation beams with the PEEC at a nominal SSD of 100 cm corresponding to a ρ_p of -1 nC cm^{-3}. Because general recombination, initial recombination, and ion diffusion all have the same functional dependence on the applied potential V, in the

absence of spurious charge contributions, the measured data are expected to remain linear when plotted in the form of $1/Q$ vs $1/V$ for all d.

In Fig. 7.10 saturation curve data measured in an 18 MV pulsed photon beam are plotted in the form of $1/Q$ vs $1/E$ (*i.e.*, d/V). As expected, for each electrode separation there exists an extended region of linearity between $1/Q$ and $1/E$. The solid lines in Fig. 7.10 represent least-squares fits to the data measured in the near saturation region as indicated by open circles, which, when extrapolated to $1/V = 0$, results in $1/Q_{sat}$. For small electrode separations, in the extreme near-saturation region there is a deviation from the expected linearity of the $1/Q$ vs $1/E$ relationship. The dashed curves representing the fit of Eq. (7.9), which include the effects of charge loss and charge multiplication, agrees with the measured data throughout the entire range of electric fields from 1 V/mm to 400 V/mm.

In Fig. 7.11, saturation curve data for various electrode separations measured in a beam of 9 MeV pulsed electrons are plotted in the form of $1/Q$ vs $1/E$ in the extreme near-saturation region. The solid lines in Fig. 7.11 represent least-squares fits to the data measured in the near saturation region, as indicated by open circles. The dashed lines represent the curve fit of Eq. (7.9) to data in the entire range of electric fields from 1 V/mm to 400 V/mm. Again, the curve fit of Eq. (7.9) which includes the effects of charge multiplication on the measured data agrees with measurement throughout the entire range of electric fields supporting the hypothesis that the excess measured charge is due to charge multiplication.

Table 7.5 provides a summary of the values for Q_{sat} for pulsed beams of 18 MV photons and 9 MeV electrons determined from a linear extrapolation of $1/Q$ vs $1/V$ to $1/V = 0$ for data in the near saturation region and from the fit of Eq. (7.9) to all of the measured data for various electrode separations d. Both methods yield values for
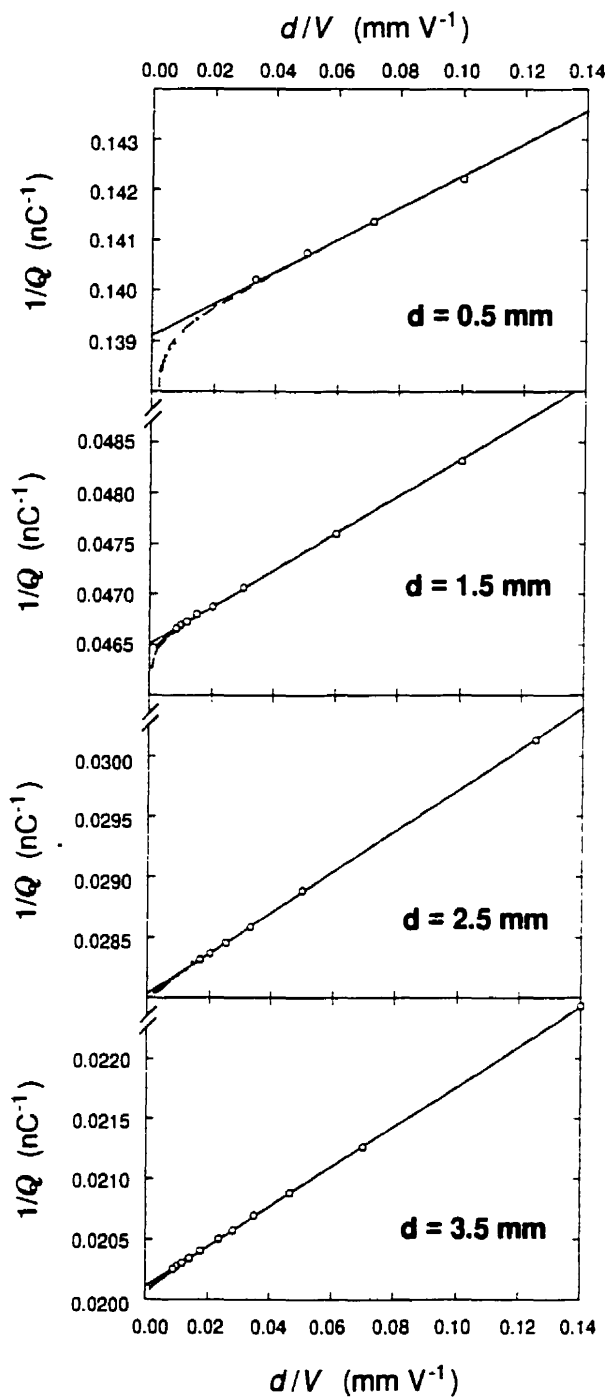
FIGURE 7.10. Saturation curve data measured with a parallel-plate ionization chamber for various electrode separations d in an 18 MV pulsed photon beam. The saturation charge Q_{sat} is found from extrapolating to $1/E = 0$ the solid lines representing least-squares fits to the linear region of the data (indicated by open circles). For the 0.5 mm electrode separation, the linear relationship between $1/Q$ and $1/V$ breaks down noticeably. The dashed curves representing the fit of Eq. (7.9) to the data follows the measured data throughout the entire range of electric fields.
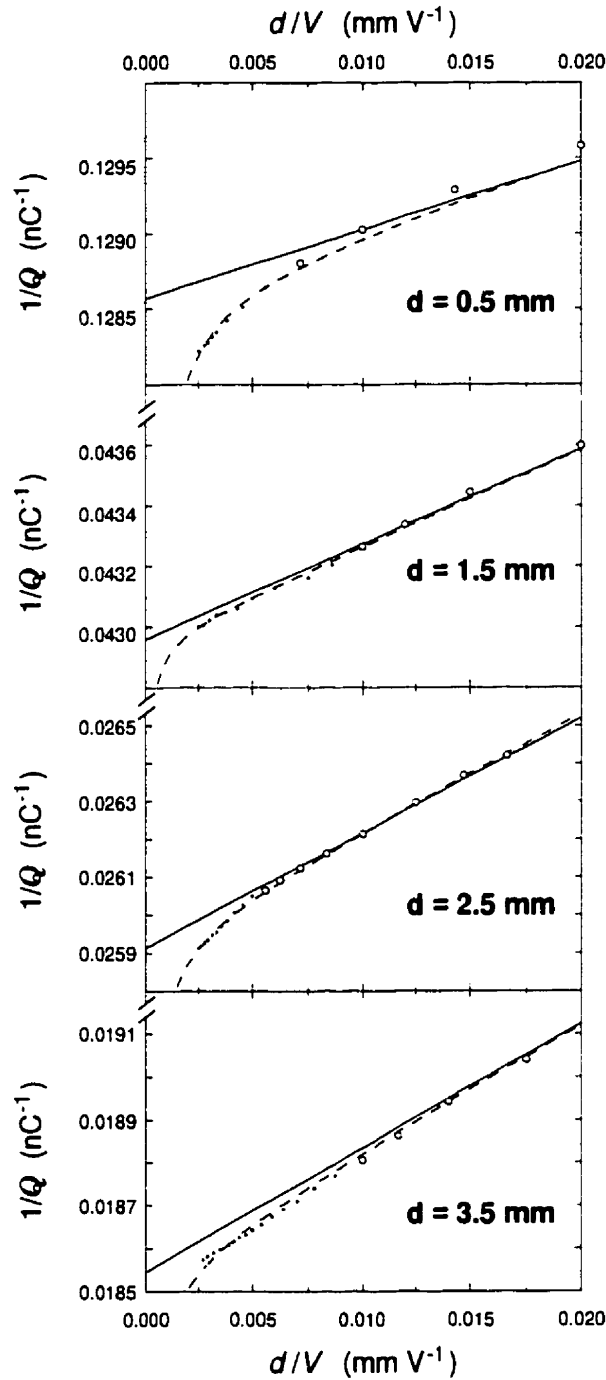
FIGURE 7.11. Saturation curve data measured with a parallel-plate ionization chamber for various electrode separations d in an 9 MeV pulsed election beam. The saturation charge Q_{sat} is found from extrapolating to $1/V = 0$ the solid lines representing least-squares fits to the linear region of the data (indicated by open circles). The curve fits of Eq. (7.9), which include the effects of charge multiplication, agree with the measured data throughout the entire range of electric fields and are indicated by the dashed curves.

Table 7.5 Saturation charge in pulsed beams of 18 MV photons and 9 MeV electrons for various electrode separations d determined from a linear extrapolation of $1/Q$ vs $1/V$ to $1/V = 0$ for data in the near saturation region and from the curve fit of Eq. (7.9) to all data points. Values are expressed in parentheses as percentages of the semi-empirical curve fit of Eq. (7.9).

electrode separation d (mm)	Beam	extrapolation $1/Q$ vs $1/V$	semi-empirical model (Eq. 7.9)
0.5	18 MV	7.189 (100.0)	7.187 (100.0)
	9 MeV	7.778 (100.1)	7.774 (100.0)
1.5	18 MV	21.50 (100.0)	21.49 (100.0)
	9 MeV	23.28 (100.0)	23.28 (100.0)
2.5	18 MV	35.67 (100.0)	35.67 (100.0)
	9 MeV	38.58 (100.1)	38.55 (100.0)
3.5	18 MV	49.72 (100.0)	49.71 (100.0)
	9 MeV	53.93 (100.0)	53.91 (100.0)

Q_{sat} that agree to within 0.1% for all electrode separations d for pulsed 18 MV photons and 9 MeV electrons.

IV.C. Collection efficiency for the PEEC in low pulse charge density pulsed radiation

As saturation curve measurements with the Farmer chamber are very difficult and leakage currents may pose a severe problem at low dose rates (~20 cGy/min), the measurements were repeated with the Solid-Water^{TM} PEEC lying on its side at an SSD of 500 cm to obtain a pulse charge density ρ_p ~0.04 nC cm^{-3}. The PEEC has much better leakage characteristics than the Farmer chamber, and even for very low dose rates, such as these, leakage is entirely negligible. One set of saturation curve data was collected for an electrode separation d of 2.0 mm in order to verify the results obtained with the Farmer chamber.

The results of these measurements are shown in Fig. 7.12, in which measured data are plotted in the form of $1/Q$ vs $1/E$ for $f \gtrsim 0.98$, corresponding to the near saturation region. The solid line represents a least-squares linear fit to the data in the near saturation region indicated by open circles, and yields a value for Q_{sat} of 1.398 when extrapolated to $1/V = 0$. The dashed curve represents the least-squares fit of Eq. (7.9) to the entire data set and yields a value of 1.397 nC for Q_{sat} which is less than the result of linear extrapolation alone. The data support the theory that charge multiplication contributes to the measured charge for low ρ_p for large electric fields.
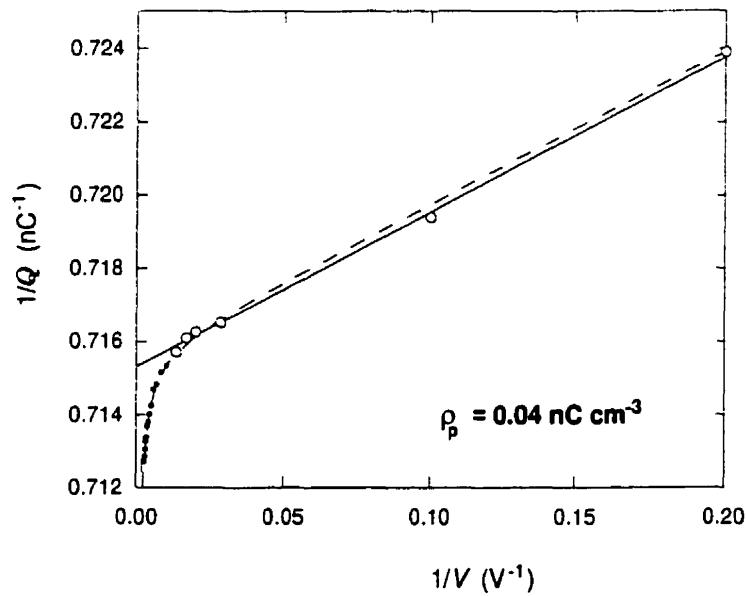
FIGURE 7.12. Saturation curve data for the PEEC with an electrode separation d of 2.0 mm in an 18 MV pulsed photon beam with $\rho_p \sim 0.04$ nC cm^{-3} (SSD of 500 cm) plotted in the form of $1/Q$ vs $1/V$ for $f \gtrsim 0.98$. The solid line represents a least-squares fit to the data in the near saturation region and yields a value for Q_{sat} of 1.398. The dashed line represents a least-squares fit of Eq. (7.9) to all data points and yields a value for Q_{sat} of 1.397 nC which is slightly lower than the value obtained from linear extrapolation alone.

IV.D. Consequences of the comprehensive model for charge loss in an ionization chamber for pulsed irradiation

The theoretical inverse ion collection efficiency data in a pulsed beam of radiation calculated for general recombination in the absence of initial recombination and ion diffusion where $f_g^p = \left(1 + \Lambda_g^p/V\right)^{-1}$ for $\Lambda_g^p = 1$ and $\Lambda_g^p = 10$, and following the comprehensive model for charge loss where $f = f_g^p f'$ in which f' was defined above for continuous beams, are shown in Fig. 7.13. The parameter for initial recombination and ion diffusion was chosen such that $\Lambda = \Lambda_i + \Lambda_d = 5$. From Fig. 7.13, it is evident that in the absence of spurious charge contribution, the comprehensive model predicts a linear relationship between $1/Q$ and $1/V$ in the entire range of $f > 0.7$ and does not predict any deviation from linearity in the extreme near-saturation region.
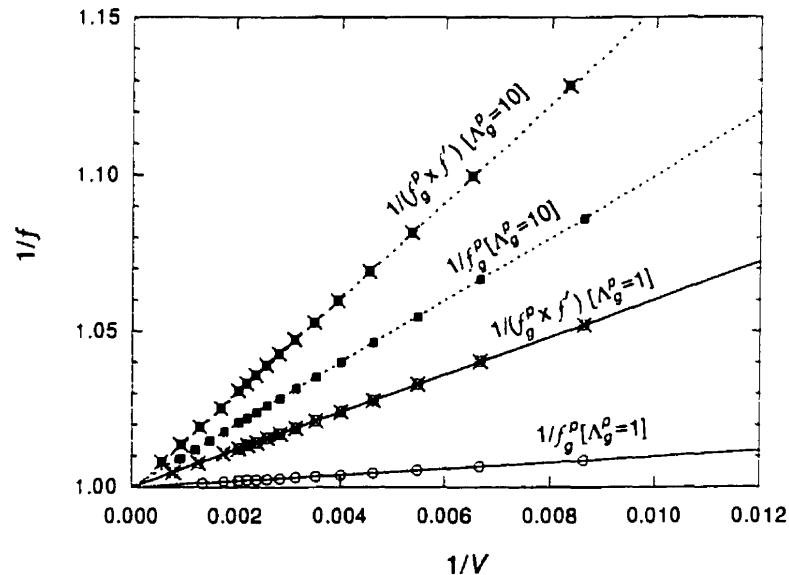
FIGURE 7.13. Theoretical inverse ion collection efficiency $1/f$ in a pulsed beam of radiation for general recombination in the absence of initial recombination and ion diffusion where $f_g^p = \left(1 + \Lambda_g^p/V\right)^{-1}$, and following the comprehensive model for charge loss where $f = f_g^p f'$ for $f \geq 0.9$. The least squares fits to the theoretical data all intercept the ordinate axis at $1/f = 1$ and the data follow the lines well into the extreme near-saturation region ($f \geq 0.99$). The comprehensive model does not predict a deviation from linearity between $1/Q$ and $1/V$ for pulsed radiation beams.

V. Conclusions

We have studied the collection efficiency characteristics of our in-house built variable volume extrapolation chamber and several commercial ionization chambers which are used in standard dosimetry calibration protocols. The $1/Q$ vs $1/V^2$ relationship which is currently used for the determination of collection efficiency f^c and saturation charge Q_{sat} in continuous radiation beams is not entirely valid as it considers only the effect of general recombination in the chamber volume.

For fixed-volume Farmer chambers, in the absence of charge multiplication, failure to account for the effects of initial recombination and ion diffusion on the overall charge loss can lead to an underestimation of Q_{sat} by a nearly constant factor of -0.4%, irrespective of the dose rate. For our extrapolation ionization chamber, the error in the determination of Q_{sat} introduced by ignoring initial recombination and ion diffusion is a function of the electrode separation d, decreasing from -3% to 0.1% as d is increased from 0.5 to 3.5 mm.

Application of the two-voltage technique, which is based on the assumed linearity of $1/Q$ and $1/V^2$ in the near saturation region, for Farmer chambers at potentials of 300 V and 150 V will, in general, overestimate Q_{sat}, because the charge collected even at moderate chamber potentials (*e.g.*, 150 V and above) may be affected by charge multiplication in the chamber volume. For parallel-plate chambers charge multiplication was observed for electric fields as low as 50 V/mm. Contrary to the conventional wisdom that the polarizing potential should be chosen to operate the ionization chamber well into the near saturation region, we suggest that potentials be kept relatively low to avoid complications arising from the onset of charge multiplication in the chamber sensitive volume.

We propose a comprehensive, semi-empirical model that includes the effects of general recombination as well as initial recombination and ion diffusion, and also accounts for the unwanted charge multiplication in the chamber volume. We suggest that in order to determine Q_{sat} a saturation curve be measured for a given ionization chamber, and that Eq. (7.7), with appropriate values for α, β, and γ, be used to fit the measured data to extract the true Q_{sat} and, subsequently, the collection efficiency $f(V)$ for a given chamber potential V. Alternatively, we suggest that for the determination of Q_{sat} in Farmer chambers, the two-voltage technique be used for relatively low chamber potentials of 100 V and 50 V to avoid charge multiplication, and the resulting value be multiplied by 1.004 to account for initial recombination and diffusion loss.

We also showed that in pulsed beams in the absence of charge multiplication in the chamber sensitive volume, the linear relationship between $1/Q$ and $1/V$ that is currently used in the determination of the collection efficiency f^p is valid and introduces no error in the experimentally determined Q_{sat}. Similarly for the case of continuous beams, we suggest that for Farmer-type ionization chambers the two-voltage technique be used for relatively low chamber potentials of 100 V and 50 V to avoid problems arising from the onset of charge multiplication.

References

1. J. Böhm, "Saturation corrections for plane parallel ionization chambers," Phys. Med. Biol. **21**, 754–759 (1976).

2. AAPM Task Group 21 of the Radiation Therapy Committee, "A protocol for the determination of absorbed dose from high-energy photon and electron beams," Med. Phys. **10**, 741–771 (1983).

3. J. W. Boag and J. Currant, "Current collection and ionic recombination in small cylindrical ionization chambers exposed to pulsed radiation," Br. J. Appl. Phys. **53**, 471–478 (1980).

4. P. R. Almond, "Use of a Victoreen 500 electrometer to determine ionization chamber collection efficiencies," Med. Phys. **8**, 901–904 (1981).

5. F. H. Attix, "Determination of A_{ion} and P_{ion} in the new AAPM radiotherapy dosimetry protocol," Med. Phys. **11**, 714–716 (1984).

6. M. S. Weinhouse and J. A. Meli, "Determining P_{ion}, the correction factor for recombination losses in an ionization chamber," Med. Phys. **11**, 846–849 (1984).

7. R. L. Sproull, *Modern Physics* (Wiley & Sons, New York, second edition, 1956).

8. J. W. Boag, in *The Dosimetry of Ionizing Radiation*, edited by K. R. Kase, B. E. Bjärngard, and F. H. Attix, Volume 2, Chapter 3 (Academic Press, Orlando, 1987).

9. F. H. Attix, *Introduction to Radiological Physics and Radiation Dosimetry* (John Wiley & Son, New York, 1986).

10. P. N. Jeffery, J. W. Boag, and H. E. Johns, "Electron avalanche amplification in x-ray imaging devices," Phys. Med. Biol. **19**, 593–604 (1974).

CHAPTER 8

Calibration of photon and electron beams with a phantom-embedded extrapolation chamber

I.   Introduction

An accurate determination of the output produced by photon and electron machines

used in radiotherapy is an important component of the radiotherapeutic process. This

output is generally measured as the dose rate (in cGy/min for radioisotope units and low

energy x-ray units, and in cGy/MU for megavoltage linear accelerators) at a reference

point in a water equivalent phantom with a nominal field size (usually 10×10 cm^2) and

a nominal source—phantom surface distance. Dose rates at any arbitrary point inside

the irradiated patient are then calculated using various pre-measured physical parameters

which relate the dose rate at the point of interest in the patient to the measured absolute

dose rate at the reference point in the water equivalent phantom.   According to the

ICRU,[1] the overall accuracy in dose delivery to the patient should be within 5% based

on an analysis of dose response data and an evaluation of errors in dose delivery. This

constraint requires that the accuracy of the calibration of the absolute machine output be

within 2%. Uncertainties inherent to other measured parameters relating the dose rate

at the reference point in phantom to the dose rate at arbitrary points of interest in the

patient account for the remaining 3%.

As mentioned in Chapter 1, there are currently three known absolute dosimetry

techniques: calorimetry, chemical (Fricke) dosimetry, and dosimetry with standard free

air ionization chambers. Of these three techniques, calorimetry has the highest degree of absoluteness. Since none of these techniques is suitable for routine calibration of radiotherapy machines, radiotherapy clinics most commonly determine the machine output with parallel-plate or cylindrical thimble ionization chambers following one of several national or international protocols (e.g., ICRU,[1, 2] AAPM-TG21,[3] AAPM-TG25,[4] IAEA-WHO,[5] *etc.*). These protocols are based on standard Bragg–Gray[6, 7] or Spencer–Attix[8] cavity theories which were described in Chapter 4. The cavity theories provide simple linear relationships between the dose D_{med} to a point in the medium and the ratio Q/m where Q is the ionization charge collected in a mass m of a gas inside a measuring cavity within the medium.

Unlike the charge Q which is easily measured to a high degree of accuracy with a calibrated electrometer, the effective mass of the cavity gas is difficult to determine experimentally to the required degree of accuracy. The standard method for obviating the problem with the determination of the ratio Q/m is to calibrate the cavity chamber at, or trace its calibration to, a national standards laboratory as described in Chapter 4. The output of a radiotherapy machine is then calculated from the measured ionization in the chamber sensitive air volume using the chamber calibration factor N_x or N_{gas} and a dosimetry protocol (in our case the AAPM-TG21 protocol for high energy photon and electron beams) incorporating various correction factors. These factors account for the effects of chamber geometry and wall composition on the electron fluence in the chamber volume as well as for ion recombination. These correction factors make the determination of the machine output cumbersome and complicated, and introduce uncertainties in the final result.

For sufficiently small cavity gas masses m, the ratio Q/m is a constant when measured as a function of m, and may be replaced by the derivative dQ/dm in the

cavity relationships. In contrast to the ratio Q/m, dQ/dm is relatively easy to measure accurately with specially designed extrapolation chambers, such as our Solid-Water^{TM} phantom-embedded extrapolation chamber (PEEC) described in detail in Chapter 6. Extrapolation chambers permit the variation of the cavity air mass m through a controlled change in the electrode separation.

Since 1937 when Failla[9] designed the first extrapolation chamber, these chambers have been used primarily for the determination of surface doses in orthovoltage[9] and megavoltage[10] photon beams, and also in the dosimetry of β rays[11-13] and low-energy x rays.[12] The use of extrapolation chambers in the measurement of radiotherapy machine output was proposed as early as in 1955 by Genna and Laughlin[14] who calibrated a cobalt beam with a specially designed extrapolation chamber in a polystyrene phantom. Output measurements of megavoltage photon and electron beams with an extrapolation chamber have been described recently by Klevenhagen[15] who called his chamber an ionization gradient chamber.

Similarly to Klevenhagen, we have built an uncalibrated, variable air-volume extrapolation chamber which is capable of measuring directly the photon and electron absorbed dose in phantom. The chamber built by Klevenhagen was made of Lucite and required the use of a water tank for dose measurement; therefore, corrections for the density and fluence differences between Lucite and water had to be considered. Our PEEC was built directly into a Solid-Water^{TM} phantom; consequently, there is no need for any corrections to the measured signal other than for charge losses within the chamber when determining the absorbed dose in Solid-Water^{TM}.

The determination of the absolute absorbed dose or dose rate for clinical photon and electron beams at a given depth in Solid-Water^{TM} with the PEEC is straightforward and agrees well with results obtained with standard calibrated ionization chamber tech-

niques. In this chapter we describe the use of our PEEC for calibration of megavoltage photon and electron beams.

II.   Materials and methods

A detailed description of the Solid-Water^{TM} phantom-embedded extrapolation chamber used in experiments reported in this chapter was provided in Chapter 6. A calibrated high-precision electrometer (model 35617; Keithley, Cleveland, Ohio) was used for all ionization measurements with the PEEC. Measurements of the PEEC response to a given radiation beam were carried out for various relative electrode separations z, ranging from 0.5 to 2.5 mm which will be shown to span the entire Bragg–Gray region. A polarizing electric field of approximately 300 V/mm which is sufficient to operate the chamber in the near saturation region was used. All ionization measurements were corrected for charge losses from ion recombination[16–18] and ion diffusion[19] following the comprehensive model for charge loss proposed by Böhm[20] and discussed in detail in Chapter 7. For continuous beams, Böhm's approach leads to the polynomial relationship

$$\frac{1}{Q} = \frac{1}{Q_{sat}} + \frac{\alpha}{V} + \frac{\beta}{V^2} .$$

(8.1)

where $\alpha = \lambda_i + \lambda_d$ and $\beta = \lambda_g^c$ in which λ_i, λ_d and λ_g^c are the chamber-air parameters describing initial recombination, ion diffusion, and general recombination, respectively. For pulsed beams, the standard two-voltage technique [Eq. (5.29)] was applied to data obtained at polarizing voltages where extracameral currents were minimal.

For each chamber polarity, the mean value of at least 4 measurements was taken as the measured charge. The standard deviation of the measured charge at each point was less that 0.1% of the mean. The charge Q used for the calibration of the photon and

electron beams with the PEEC represents the average of the measured charges obtained for positive and negative chamber polarities.

The reference point for determining the chamber depth in phantom was taken at the center of the inner surface of the polarizing electrode (*i.e.*, on the graphite dag layer). The desired depth in phantom was obtained by adding an appropriate thickness of solid water on top of the PEEC and accounting for the 2 mm thickness of the solid water material holding the polarizing electrode. Irradiations of the PEEC were performed with a cobalt–60 γ–ray source, x–ray beams in the energy range from 4 to 18 MV, and electron beams in the nominal energy range from 6 to 22 MeV.

III. Results and discussion

The modified Spencer–Attix cavity equation for radiation dosimetry is

$$D_{med} = \left(\frac{1}{\rho A}\right)\frac{dQ}{dz}\,\overline{W}_{air}\left(\frac{\overline{L}}{\rho}\right)_{air}^{med} .$$ (8.2)

where ρ is the density of the air in the chamber, A is the area of the collecting electrode, $\overline{W}_{air} = 33.97$ eV [ref. 21] is the mean energy required to produce an ion-pair in air, and $(\overline{L}/\rho)_{air}^{med}$ is the ratio of mean restricted mass collisional stopping powers of the medium and air for the electron spectrum at the point of measurement, with medium referring to the phantom material.

Equation (8.2) forms the basis for absolute radiation dosimetry with a variable air-volume chamber and states that the dose in phantom D_{med} is linearly proportional to the measured ionization gradient dQ/dz. The basic assumptions are: (i) that the four parameters ρ, A, $\overline{W}_{air}$, and $(\overline{L}/\rho)_{air}^{med}$ in the modified Spencer–Attix equation are known accurately and (ii) that the chamber sensitive volume satisfies the Bragg–Gray cavity

conditions described in Chapter 4 (Section III.A). Although humidity is known to affect the values for ρ, $\overline{W}_{air}$, and $(\overline{L}/\rho)_{air}^{med}$ no humidity corrections were made in this work. The reasons for this is that fortuitously, the combined humidity correction factor on the final result is a constant value[22, 23] of 0.997 ± 0.001 for a relative humidity of air ranging from 15% to 75%. As the measurements for with the PEEC and the calibrated chambers were conducted on the same day and usually only minutes apart, the humidity correction factor should apply equally to both measurements and the effect will tend to cancel out in the comparison of the two methods.

The mean ionization energy $\overline{W}_{air}$ and mean restricted collisional stopping power ratio $(\overline{L}/\rho)_{air}^{med}$ for a given photon or electron beam energy are available from the literature. The method for determining the mean energy at a given depth in phantom is described in Section V.D of Chapter 4. The air density ρ is easily determined for a given temperature and pressure; and the effective electrode area A was determined through a chamber capacitance measurement to be 4.597 cm^2, as described in Chapter 6.

The ionization gradient dQ/dz of Eq. (8.2) is determined from a measured relationship between Q_{sat} and z. Three typical examples of the Q_{sat} vs z relationship in the relative electrode separation range between 0 and 3 mm are shown in Fig. 8.1 for a ^{60}Co continuous γ–ray beam, a 6 MV pulsed photon beam, and a 9 MeV pulsed electron beam. A least–squares fit to the measured data in this range results in a straight line with a very high correlation coefficient, and a $Q_{sat} = 0$ intercept at ~ 0.5 mm on the distance travel indicator scale. This value for the $Q_{sat} = 0$ intercept is consistent with the value obtained from the plot of the relative electrode separation versus the inverse capacitance that was used to determine the electrode area (see Fig. 6.3). The intercept could be used to calibrate the absolute electrode separation scale on the distance travel indicator; however, the use of Eq. (8.2) makes this piece of information superfluous.
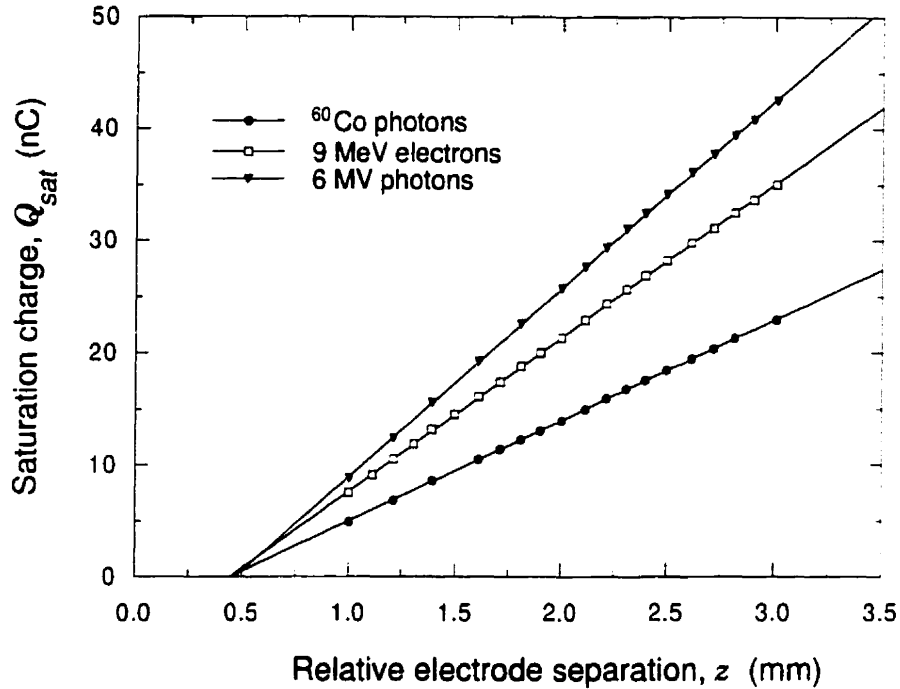
FIGURE 8.1. Saturation charge Q_{sat} as a function of the relative electrode separation measured with the PEEC for ^{60}Co continuous photons, 6 MV pulsed photons, and 9 MeV pulsed electrons. Solid lines represent least-squares fits to all data points shown.

The excellent linear fit to measured data would suggest that we are dealing with a pure Bragg–Gray cavity throughout the entire 3 mm range of z values. To investigate how the chamber meets the Bragg–Gray conditions, the ionization gradients dQ/dz were calculated for various ranges of z between 0 and 3 mm and the results are plotted in Fig. 8.2. The data shown in Fig. 8.2 are for all beams calibrated with the PEEC and represent the normalized ionization gradients as a function of the largest electrode separation included in the particular data set for the least-squares fit analysis. For example, the normalized ionization gradient plotted for a relative electrode separation of 1.5 mm represents the slope of the line including all data points less than or equal to 1.5 mm
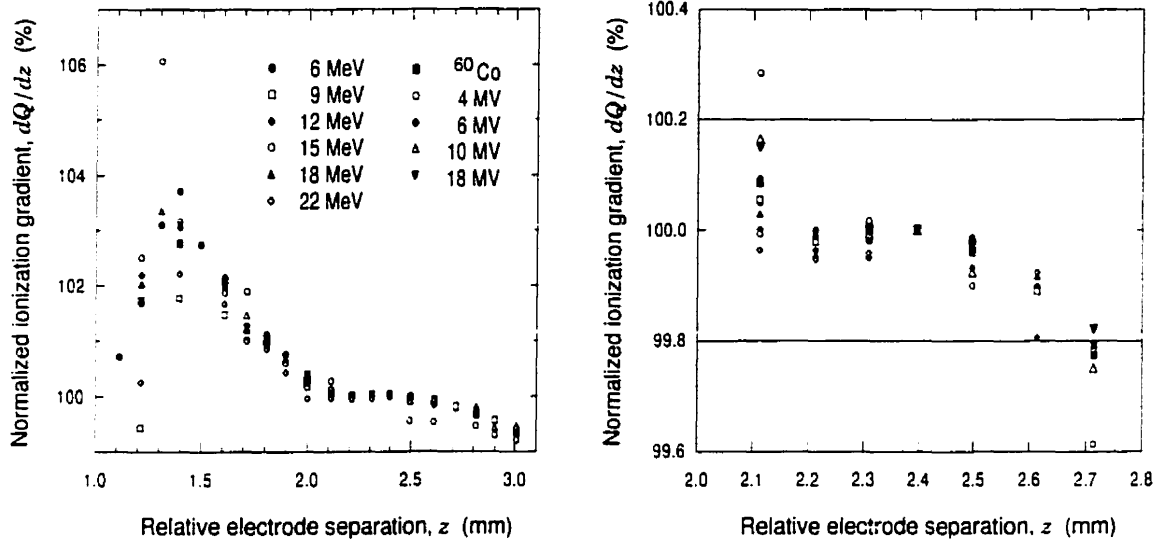
FIGURE 8.2. Normalized ionization gradient as a function of the largest relative electrode separation z included in the data set for the least-squares fit analysis for all radiation beams calibrated with the PEEC for z ranging between 0 and 3.0 mm in (a), and between 2.0 and 2.8 mm in (b).

obtained from a plot of Q_{sat} vs z. The normalized ionization gradient corresponding to a relative electrode separation of 2.5 mm was found by taking the slope of the line fitting all points for which $z \leq 2.5$ mm. The measured dQ/dz vary by about 5% in the entire range of electrode separations; however, the variations are not random. Rather, we observe a particular trend in the dQ/dz values as a function of z. It is possible to identify three distinct regions of the ionization gradients in Fig. 8.2:

region 1 ($0 < z \lesssim 2.0$ mm): Fluctuations of dQ/dz are observed possibly due to the relatively few points available for the least-squares fit analysis and the relatively small air-mass available for electron interaction. The common trend of the measured data suggests a more fundamental physical problem and needs to be

investigated further.

region 2 ($2.0 \lesssim z \lesssim 2.6$ mm): The ionization gradients dQ/dz are essentially constant and can be considered the true Bragg–Gray region; and

region 3 ($z \gtrsim 2.6$ mm): The ionization gradients dQ/dz slowly decrease with increasing z because the cavity is transforming from a Bragg–Gray cavity into an intermediate cavity in which, for photon beams, some of the ionization events are produced by photon interactions within the chamber sensitive volume, and for electron beams, the relatively large electrode separation affects the electron spectrum in the cavity.

The ionization gradient data for the Bragg–Gray cavity region are shown on an expanded scale in Fig. 8.2(b). Since in this region dQ/dz fluctuates by less than $\pm 0.2\%$, gradients measured in this region can be used reliably for the determination of dose in conjunction with the modified Spencer–Attix relationship given in Eq. (8.2).

We observed the same behaviour for all photons in the range from 4–18 MV, cobalt–60 γ rays, as well as for electrons in the range from 6–22 MeV. Therefore, for the purposes of dosimetry with our extrapolation chamber, the slope of the Q vs z relationship was determined including only data with *relative electrode separations* of up to 2.4 mm which falls within the region where the Bragg–Gray conditions are adequately met. The actual size of the Bragg–Gray cavity can be determined from the data in Fig. 8.2 by subtracting 0.5 mm (the $Q_{sat} = 0$ intercept) from the relative electrode separation scale. We conclude that the Bragg–Gray condition is met for *absolute electrode separations* of up to 2.0 mm, which is consistent with data obtained for the Solid-Water$^{\text{TM}}$ PEEC equipped with different electrodes.[24]

In Tables 8.1 and 8.2 we show how the PEEC meets its main objective, the determination of absolute dose in clinical photon and electron beams, respectively. In

Table 8.1 Comparison of photon dose at a depth of 5 cm in a Solid-Water™ (SW) phantom measured with the phantom-embedded extrapolation chamber (PEEC) and two Farmer chambers. (1) Photon beam type and energy; (2) ratio of mean restricted mass stopping powers ($\Delta = 10$ keV) for Solid-Water™ and air[25]; (3) measured ionization gradient averaged over positive and negative chamber polarities and corrected charge loss, temperature, and pressure; (4) dose determined with the PEEC and Eq. (8.2); (5) average dose determined with two calibrated Farmer ionization chambers and the AAPM-TG21 protocol[3]; (6) percent difference between columns (4) and (5).

(1)	(2)	(3)	(4)	(5)	(6)
Photon beam	$\overline{L}_{air}^{SW}$	dQ/dz	Dose [PEEC]	Dose [Farmer]	difference
		(nC mm⁻¹)	(cGy)	(cGy)	(%)
Co-60	1.117	9.019	57.58	57.65	-0.1
4 MV	1.112	12.785	81.26	81.67	-0.5
6 MV	1.106	13.647	87.72	87.71	+0.0
10 MV	1.090	7.156	44.58	44.67	-0.2
18 MV	1.071	15.534	98.20	97.81	+0.4

Table 8.1, for a given photon beam, doses determined at a depth of 5 cm in Solid-Water™ phantom with two calibrated Farmer chambers in conjunction with the AAPM-TG21 protocol are compared with doses determined with our PEEC under the same irradiation conditions. The discrepancies between doses determined with our uncalibrated extrapolation chamber and doses obtained with the calibrated Farmer chambers are shown in column (6). For photon beam output calibration measurements, the dose determined with the uncalibrated PEEC agrees with the dose determined with the Farmer chambers to within ±0.5%, clearly showing the suitability of the PEEC for direct measurement of beam outputs in megavoltage photon beams.

In Table 8.2, doses determined using the uncalibrated PEEC [column (7)] and the calibrated Farmer chambers [column (8)] for a given electron beam are compared. The mean energy at the phantom surface $\overline{E}_o$ listed in column (2) was determined experimentally from a plot of the depth ionization curve as outlined in Chapter 4, Section V.D.

The mean electron energy $\overline{E}(d)$ is obtained from published TG21[3], and the mean restricted mass stopping power ratio of Solid-Water™ and air [column (5)] was evaluated at this energy. The discrepancies between doses determined with our uncalibrated extrapolation chamber and doses obtained with the calibrated Farmer chambers are shown in column (9). For all electron beam dose output measurements, the discrepancies between the uncalibrated PEEC and the calibrated Farmer chambers are smaller than ±1%. The results shown in Tables 8.1 and 8.2 indicate that a properly designed, uncalibrated extrapolation chamber, such as the PEEC, is a reliable dosimeter for measuring outputs of megavoltage photon or electron beams.

Table 8.2 Comparison of electron dose at depth of dose maximum in a Solid-Water™ (SW) phantom measured with the phantom-embedded extrapolation chamber (PEEC) and two Farmer chambers. (1) Electron beam nominal energy; (2) mean electron energy at phantom surface [see Ch.4 §V.D]; (3) depth d of measurement; (4) mean electron energy E at d [see Ch.4 §V.D]; (5) ratio of mean restricted mass stopping powers ($\Delta = 10$ keV) for Solid-Water™ and air[5, 26] for $E(d)$; (6) measured ionization gradient averaged over positive and negative chamber polarities and corrected for charge loss, temperature, and pressure; (4) dose determined with the PEEC and Eq. (8.2); (5) average dose determined with two calibrated Farmer ionization chambers and the AAPM-TG21[3] protocol; (9) percent difference between columns (7) and (8).

(1)	(2)	(3)	(4)	(5)	(6)	(7)	(8)	(9)
Electron beam	$\overline{E}_o$	Depth	$\overline{E}(d)$	$\overline{L}_{air}^{SW}$	dQ/dz	Dose [PEEC]	Dose [Farmer]	difference
	(MeV)	(cm)	(MeV)		(nC mm⁻¹)	(cGy)	(cGy)	(%)
6 MeV	6.0	1.4	3.1	1.075	16.681	102.49	101.51	+1.0
9 MeV	8.7	2.2	4.2	1.061	16.863	102.26	101.92	+0.3
12 MeV	11.7	2.8	6.2	1.041	17.163	102.12	101.73	+0.4
15 MeV	14.8	2.8	9.3	1.013	17.658	102.24	102.45	-0.2
18 MeV	17.5	2.8	12.2	0.997	18.067	102.96	102.60	+0.4
22 MeV	20.9	1.8	17.4	0.970	18.233	101.09	101.15	-0.1

IV. Conclusions

Both in precision and accuracy, our uncalibrated phantom-embedded extrapolation chamber (PEEC) provides results that are comparable to those obtained with calibrated ionization chambers. Uncalibrated variable air-volume extrapolation chambers, built as an integral part of the phantom in which the dose is measured, can serve as radiation dosimeters in output calibrations of megavoltage photon and electron beams in radiotherapy. In contrast to the dosimetry with calibrated thimble chambers, the dosimetry with extrapolation chambers is simple and does not require troublesome correction factors which account for chamber properties, for perturbation of the electron fluence, and for the unavailability of high energy photon and electron calibrations at standards laboratories.

Our phantom-embedded extrapolation chamber is simple in design and forms an integral part of a Solid-Water^{TM} phantom. With the particular chamber design, it is unnecessary to measure the electrode separation in an absolute manner; only easy to obtain measurements of the *relative* electrode separations are required for dose calculations. For relative electrode separations in the range from 2.0 and 2.6 mm, the PEEC behaves as a Bragg–Gray cavity, and as such, can be used reliably in the determination of the absorbed dose in the medium.

The dose measured with a Bragg–Gray cavity is not only proportional to the difficult-to-measure ratio Q/m of charge Q collected per unit mass m of cavity air, but is also proportional to the slope dQ/dz obtained from the functional relationship between the measured charge Q and the electrode separation z. The proportionality constant in Eq. (8.2) contains four parameters and can be determined with a high degree of accuracy. Of course, the dose determined with the PEEC, just like in the case of calibrated ionization chambers, depends on the agreed upon values for $\overline{W}_{air}$, the average energy to produce

an ion-pair in air, and on the tabulated restricted mass collisional stopping powers for a given electron spectrum in the chamber cavity.

Dose measurements with carefully designed and precisely built extrapolation chambers can be regarded as a practical alternative to other currently known dosimetry techniques for all clinical megavoltage photon and electron beams. The use of uncalibrated extrapolation chambers provides a simple means to either verify independently machine outputs measured with standard calibration techniques or to determine machine outputs directly when calibrated chambers are not available.

References

1. ICRU, "Measurement of absorbed dose in a phantom irradiated by a single beam of x or gamma rays," Report 23, International Commission on Radiation Units and Measurement, Washington, D.C., 1973.

2. ICRU, "Radiation dosimetry: electron beams with energies between 1 and 50 MeV," Report 35, International Commission on Radiation Units and Measurement, Washington, D.C., 1984.

3. AAPM Task Group 21 of the Radiation Therapy Committee, "A protocol for the determination of absorbed dose from high-energy photon and electron beams," Med. Phys. **10**, 741–771 (1983).

4. AAPM Task Group 25 of the Radiation Therapy Committee, "Clinical electron-beam dosimetry," Med. Phys. **18**, 73–109 (1991).

5. I. A. E. A. (IAEA), "Absorbed dose determination in photon and electron beams; an international code of practice," Technical report 277, IAEA, Vienna, 1987.

6. W. H. Bragg, *Studies in Radioactivity* (Macmillan, New York, 1912).

7. L. H. Gray, "An ionization method for the absolute measurement of γ-ray energy," Proc. R. Soc. A. (London) **156**, 578–596 (1936).

8. L. V. Spencer and F. H. Attix, "A theory of cavity ionization," Radiat. Res. **3**, 239–254 (1955).

9. G. Failla, "Measurement of tissue dose in terms of the same unit for all ionizing radiations," Radiology **29**, 202–215 (1937).

10. J. Manson, D. Verkly, J. A. Purdy, and G. D. Oliver, "Measurement of surface dose using build-up curves obtained with an extrapolation chamber," Radiology **115**, 473–474 (1975).

11. R. Loevinger, "Extrapolation chamber for the measurement of beta sources," Rev. Sci. Instrum. **24**, 907–914 (1953).

12. J. Böhm and U. Schneider, "Review of extrapolation chamber measurements of beta rays and low energy x rays," Radiat. Prot. Dosim. **14**, 193–198 (1986).

13. C. G. Soares, "Calibration of ophthalmic applicators at NIST: A revised approach," Med. Phys. **18**, 787–793 (1991).

14. S. Genna and J. S. Laughlin, "Absolute calibration of a cobalt-60 gamma-ray beam," Radiology **65**, 394–405 (1955).

15. S. C. Klevenhagen, "Determination of absorbed dose in high energy photon and electron radiation by means of an uncalibrated ionization chamber," Phys. Med. Biol. **36**, 239–253 (1991).

16. G. Mie, "Der elektrische Strom in ionisierter Luft in einem ebenen Kondensator," Ann. Physik **13**, 857–889 (1904).

17. J. W. Boag, in *Radiation Dosimetry*, edited by F. H. Attix and W. C. Roesh, Chapter 1 (Academic Press, New York, 1966).

18. P. B. Scott and J. R. Greening, "The determination of saturation currents in free-air ionization chambers by extrapolation methods," Phys. Med. Biol. **8**, 51–57 (1963).

19. P. Langevin, "Mesure de la valence des ions dans les gaz," Le Radium **10**, 113–124 (1913).

20. J. Böhm, "Saturation corrections for plane parallel ionization chambers," Phys. Med.

Biol. **21**, 754–759 (1976).

21. M. Boutillon and A. M. Perroche, "Effect of a change of stopping-power values on the *W* value recommended by ICRU for electrons in dry air," Report CCEMRI(I)85–8, Bureau International des Poids et Mesures, Sèvres, 1985.

22. F. H. Attix, *Introduction to Radiological Physics and Radiation Dosimetry* (John Wiley & Son, New York, 1986).

23. D. W. O. Rogers, in *Advances in Radiation Oncology Physics*, edited by J. A. Purdy, pp. 181–223 (American Institute of Physics, Lawrence, Kansas, 1990), Proceedings of the AAPM 1990 summer school.

24. C. Zankowski and E. B. Podgorsak, "Calibration of photon and electron beams with an extrapolation chamber," Med. Phys. **24**, 497–503 (1997).

25. A. K. Ho and B. R. Paliwal, "Stopping power and mass energy absorption coefficient ratios for Solid Water," Med. Phys. **13**, 403–404 (1986).

26. RMI customer documentation, *Epoxy based phantom material*, Radiation Measurements Inc., Middleton, WI, 1986.

CHAPTER 9

Proton beam calibration

I.   Introduction

In previous chapters we discussed in detail the calibration of photon and electron beams with the phantom-embedded extrapolation chamber (PEEC). In this chapter, we describe our attempt at using the PEEC to calibrate a clinical proton beam at the Loma Linda University Medical Center (LLUMC) in Loma Linda California.

Models for determining the absorbed dose in clinical proton beams are based on protocols provided by Task Group 20 of the American Association of Physicists in Medicine[1] (AAPM-TG20) and the European Heavy Particle Dosimetry Group[2,3] (ECHED). Both groups recommend the use of air-filled ionization chambers calibrated in terms of exposure or air kerma in a ^{60}Co beam. Similarly to the photon and electron beam dosimetry, proton beam dosimetry is based on the Bragg-Gray cavity theory, and the absorbed dose to the medium D_{med} is given by:

$$D_{med} = Q_{corr} \cdot N_{gas}^{\gamma} \cdot \overline{W}_{\gamma}^{p} \cdot \left(\frac{\overline{S}}{\rho}\right)_{air}^{med} . \tag{9.1}$$

where Q_{corr} is the measured charge, corrected for temperature, pressure, and ion recombination; N_{gas}^{γ} is the cavity gas calibration factor determined in a ^{60}Co γ–ray beam; $\overline{W}_{\gamma}^{p}$ is the ratio of the mean energy required to produce an ion pair in air for protons (34.3 eV/ion pair [ref. 4]) and for ^{60}Co γ rays (33.97 eV/ion pair [ref. 5]), respectively;

and $(\overline{S}/\rho)_{air}^{med}$ is the ratio of the mean mass collisional stopping powers of the medium to air, averaged over the spectrum of protons at the point of measurement in the medium.

In contrast to the situation with photon and electron beams, absolute dosimetry of clinical proton beams is more ambiguous because of inherent uncertainties in basic physics data relevant to proton beam dosimetry. Recently, Vatnitsky *et. al.*[6] published the results of an intercomparison of proton beam dosimetry techniques from several institutions around the world involved in the clinical use of proton beams. Representatives from various institutions used their own ionization chambers and calibration protocols to determine the proton beam output at LLUMC. An intercomparisons of results showed discrepancies of up to 6% between various institutions.

To test the behaviour of our extrapolation chambers in proton beams, we took the polystyrene version of the PEEC to LLUMC and carried out a basic dose output measurement procedure on the 200 MeV experimental proton beam. The results of the PEEC measurements were compared with standard ionization chamber techniques in practice at LLUMC. The goal of the proton beam experiment was to determine whether or not the PEEC design is suitable for the calibration of high-energy proton beams. Based on our work with photon and electron beams we believe that the PEEC should also provide a simple and reliable method for the calibration of high-energy proton beams used clinically.

II.   Background

Heavy charged particles, such as protons, follow relatively straight lines as they traverse the medium, slowing down by interactions with atomic electrons in the medium and by occasional nuclear collisions. The depth dose characteristics of heavy charged

particles are markedly different from those of high-energy photon and electron beams. Depth doses obtained from monoenergetic proton beams are characterized by a region of almost constant dose over most of the beam range in the medium, rising to a sharp Bragg peak at the end of the proton range. A few millimeters beyond the Bragg peak, practically no dose is delivered to the medium, making it possible to conform the dose distribution from proton beams to the tumour volume much better than is possible with photon beams which are essentially exponentially attenuated, or with high-energy electron beams which suffer from bremsstrahlung contamination which contributes to the dose at depths beyond the physical range of electrons in the medium.

For a monoenergetic proton beam, the dose at the Bragg peak is approximately four times greater than the entrance dose. The width of the Bragg peak is on the order of a few millimeters depending on the energy spread of the proton beam. An illustration of a typical proton beam percent depth dose curve is shown in Fig. 9.1. Since a Bragg peak of a few millimeters width is normally too narrow to be of use clinically, the beam is purposely degraded by a beam spreader or bolus to widen the Bragg peak to span the dimensions of the tumour. Widening of the Bragg peak comes at the cost of increasing the surface dose to the patient, as is shown in Fig. 9.2.

III.   Materials and Methods

In the early 1990's, the Department of Radiation Sciences at Loma Linda University Medical Center designed and constructed the first dedicated, hospital-based proton treatment facility. LLUMC contains three treatment rooms having rotating gantries, a treatment room containing two horizontal beam delivery systems, and a fifth beam room dedicated to physics and radiobiological research. Calibration of the unmodulated mono-

Monoenergetic proton beam
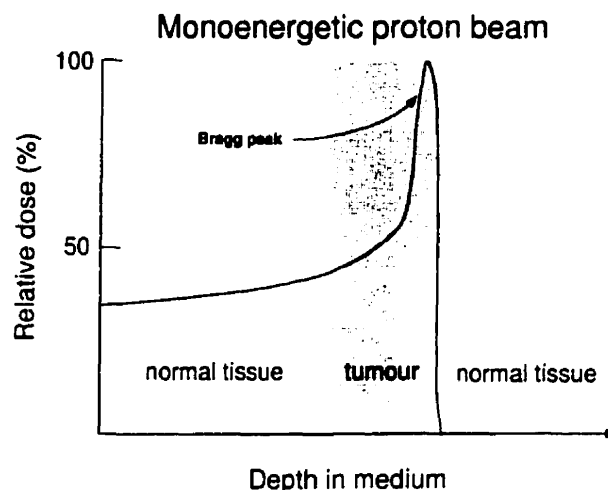
FIGURE 9.1. Typical percent depth dose curve of a high-energy monoenergetic proton beam as it traverses a medium. The PDD of a proton beam is characterized by an entrance region of nearly constant dose followed by a narrow region of concentrated dose deposition known as the Bragg peak. Beyond the Bragg peak no dose is delivered to the medium by the proton beam.

energetic 250 MeV proton beam with our extrapolation chamber was conducted using the horizontal beam line of the LLUMC proton therapy facility.

Proton beams are generated by a zero gradient synchrotron capable of accelerating protons in a continuously variable manner to kinetic energies ranging from 70 to 250 MeV. The proton beam is initially accelerated to 2 MeV by a radiofrequency quadrupole linear accelerator and subsequently injected into the synchrotron ring. Shortly after the ring is filled, the beam is accelerated to its final energy in an rf cavity located diametrically opposite to the injection point. The proton beam is then extracted from the synchrotron and directed toward the beam transport lines which guide the proton beam into the appropriate treatment room. This method permits the treatment of patients with a low-frequency pulse-mode duty cycle providing a beam for approximately 300 ms every

Modulated proton beam

Depth in medium
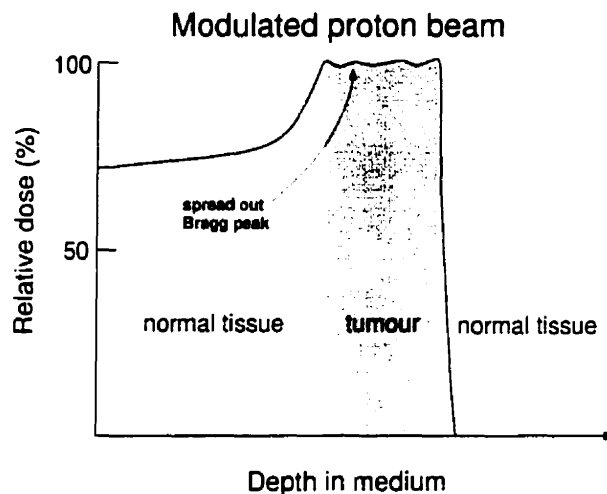
FIGURE 9.2. Percent depth dose curve of a high-energy proton modulated to spread out the Bragg peak. The Bragg peak of a modulated proton beam can be spread out to cover the entire tumour volume at the cost of increasing the relative entrance dose considerably over that of the unmodulated beam.

2.2 s. Beam intensity is approximately 5×10^{10} protons per pulse.

The horizontal proton beam enters the treatment room as a narrowly focussed pencil beam that is unsuitable for most clinical applications. To make it useful for our experiment, the pencil beam is made to impinge on two lead scattering foils to produce a 15 cm diameter uniform proton field at the location of the ionization chamber. For clinical use, the proton beam Bragg peak is modulated using a variable thickness Lucite propeller. The propeller contains nine sections of Lucite with 0.8 cm thickness increments between adjacent sections. Each section reduces the range of protons in water by approximately 1 cm. The propeller rotates at a speed of 310 rpm in order to avoid any resonance effects arising from the 60 Hz or higher harmonic structure in the extracted beam.

The sensitive volume of the polystyrene PEEC was positioned at a water equivalent

depth of 10 cm in a polystyrene phantom. Thus, the calibration depth was located in the flat entrance dose region of the 250 MeV proton beam which then has a range of 31.8 cm in polystyrene. The field size at the depth of measurement was 15×15 cm^2 and the distance from the last bending magnet to the phantom surface was approximately 300 cm.

The polystyrene-embedded extrapolation chamber was originally the prototype chamber for the Solid-Water^{TM} PEEC. The overall design of the chamber is similar to that of the Solid-Water^{TM} PEEC (see Chapter 6). The performance of the polystyrene-embedded extrapolation chamber in high-energy electron and photon beams was already experimentally verified and the results published.[7] The sensitive chamber volume for this chamber is shielded from micrometer head and the piston housing by 8 cm of polystyrene. The electrode design was updated to conform with the design specifications of the Solid-Water^{TM} PEEC. The measuring electrode was connected to ground via a shielded triaxial cable through an electrometer (model 35617; Keithley, Cleveland, OH) and the guard electrode was connected to ground directly. In a manner similar to that described in Chapter 6, in Fig. 9.3 the relative electrode separation z was plotted as a function of the inverse capacitance. From the plot, the effective collecting electrode area of the polystyrene PEEC was determined to be 3.36 ± 0.02 cm^2.

Measurement of the ionization resulting from the proton beam irradiations were taken at various electrode separations with the electric field maintained at ~ 400 V/mm. A variable voltage power supply (model 412B; John Fluke, Seattle, WA) capable of providing up to ± 2100 V was used to provide the desired chamber polarizing potential. Measurements were concentrated in the range of electrode separations for, 0.50 to 2.50 mm, except for one measurement which was made with an electrode separation of 5.50 mm corresponding to the maximum electrode separation which could be biased
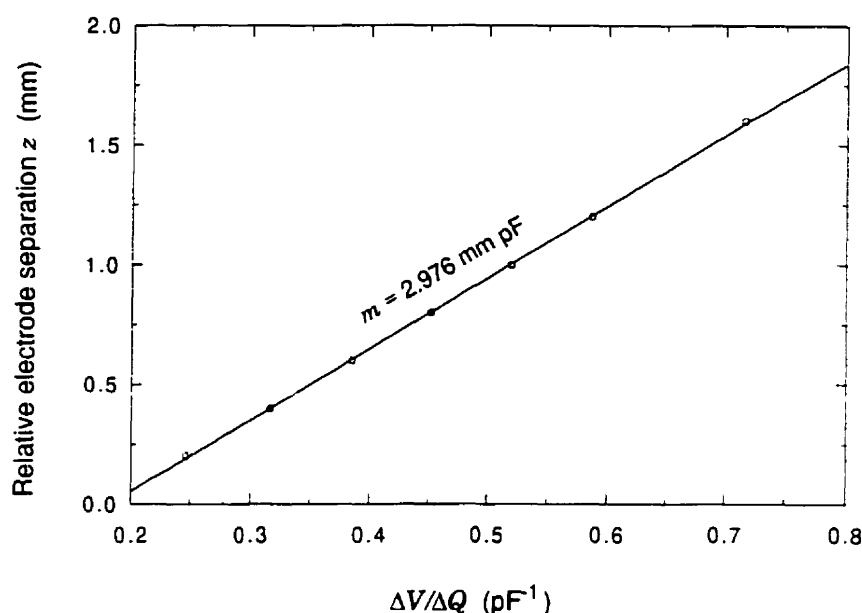
FIGURE 9.3. A plot of the relative electrode separation z as a function of the inverse capacitance $(\Delta Q/\Delta V)^{-1}$. The solid line represents a least-squares fit to the data and has a slope 2.976 mm pF. The electrode area is determined from m/ε_o and equals 3.36 ±0.03 cm^2.

at 400 V/mm by our power source. Measurements were repeated for both positive and negative chamber polarities and all readings were corrected for ambient temperature and pressure. The polystyrene PEEC was subsequently replaced by a calibrated Farmer-type cylindrical ionization chamber (model 30001, PTW, Freiburg, Germany) at the same depth in polystyrene phantom for independent dose verification and comparison. The ^{60}Co calibration factor of the cylindrical chamber was traceable to a national standards laboratory. Ion recombination for both the PEEC and the Farmer chamber was estimated using the standard two-volt technique for continuous radiation.[8, 9]

At LLUMC, beam output is reported in terms of dose to muscle, therefore, for the purposes of this study all doses will be reported as such.

IV.   Results

The absorbed dose in the polystyrene D_{poly} when the PEEC is exposed to proton

beam irradiation is given by the usual Bragg-Gray relationship:

$$D_{poly} = \frac{dQ}{dm} \overline{W}^p_{air} \left(\frac{\overline{S}}{\rho}\right)^{poly}_{air} , \qquad (9.2)$$

in which $\overline{W}^p_{air}$ is the mean energy required to produce an ion-pair in air by proton

irradiation (34.3 eV/ion-pair), and $dm = \rho A\, dz$ where ρ is the density of air in the

chamber sensitive volume, A is the area of the collecting electrode, and z is the relative

electrode separation.

To convert the dose absorbed in polystyrene to that which would be absorbed

in muscle under identical beam conditions, the dose to polystyrene is multiplied sim-

ply by the ratio of mass stopping powers of muscle to polystyrene, or $D_{muscle} = $

$D_{poly}(\overline{S}/\rho)^{muscle}_{poly}$. In this conversion, it is assumed that the proton fluences at the

equivalent depths of measurement in polystyrene and muscle are identical. This means

that Eq. (9.2) can be modified to read

$$D_{muscle} = \frac{dQ}{dm} \overline{W}^p_{air} \left(\frac{\overline{S}}{\rho}\right)^{muscle}_{air} , \qquad (9.3)$$

even though the ionization measurements were made in polystyrene and not in muscle.

For the 250 MeV proton beam used in this experiment, a mean stopping power ratio of

muscle to air equal to 1.148 was used for a depth of 10 cm. [ref.6]

Figure 9.4 is a plot of the polystyrene PEEC response to proton irradiation as a

function of the relative electrode separation averaged over positive and negative chamber

polarities and corrected for charge recombination. The slope of the line in Fig. 9.4

is 9.247±0.016 nC/(10^6 MU mm) where MU refers to the proton accelerator monitor
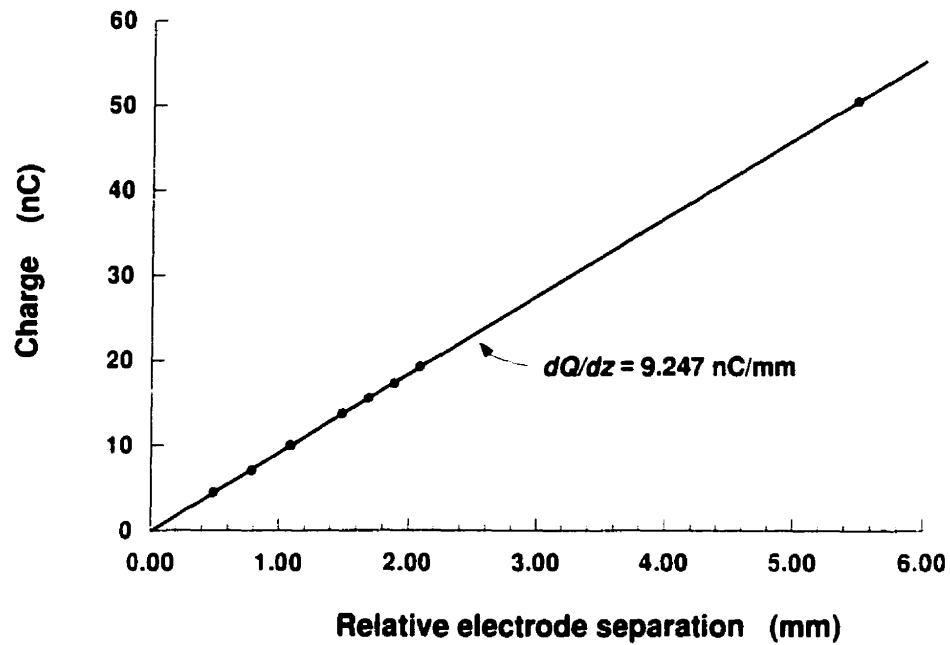
FIGURE 9.4. Plot of the polystyrene-embedded extrapolation chamber ionization response to a proton beam of 250 MeV nominal energy, measured at a water equivalent depth of 10 cm in polystyrene and a field size of 10×10 cm^2. Data represent the mean response of the chamber operated at both positive and negative polarities, corrected for temperature, pressure, and ion recombination using the two-voltage technique for continuous radiation.

units. Substitution of dQ/dz into Eq. (9.2) results in an absorbed dose to muscle of 93.3 cGy/10^6 MU at a depth of 10 cm.

Three ionization measurements were taken with a Farmer ionization chamber at the same depth in polystyrene phantom as the PEEC and the mean value of the ionization, corrected for temperature, pressure, and ion recombination, was used in Eq. (9.1). The beam output determined from this method was for the dose in muscle 98.7 cGy/10^6 MU. Comparison with the results found using the PEEC show a 5% discrepancy between the two dose measurements.

IV.A. Discussion of uncertainties

The AAPM-TG20 protocol states that ionization chambers yield absolute dose

measurements in proton beams with total uncertainties of ±3%.[1] Therefore the difference of 5% between the preliminary extrapolation chamber measurements and the calibrated thimble chamber measurements is not completely unexpected. During the time of our experiments we did not investigate the ion recombination properties of the polystyrene extrapolation chamber exposed to the proton beam. Based on our subsequent work involving the ion recombination in continuous photon beams we speculate that the use of the quasi-continuous proton beam will underestimate the actual ionization produced in the chamber. Initial recombination and ionic diffusion against the electric field in the chamber may be significant in chambers exposed to proton irradiation; however, these two charge loss mechanisms were not included in the analysis of the data obtained in the 250 MeV proton beam. The omission of the contributions of initial recombination and ion diffusion to the total charge loss will certainly result in an underestimation of the actual saturation ionization. The exact amount of this effect is currently unknown.

Other potential sources of discrepancy between measurement of dose with the extrapolation chamber and the PTW chamber are the fluence correction factor and the replacement factor which account for the cylindrical geometry of the PTW chamber but were not used in our dose calculations. The uncertainty due to perturbation of the radiation field from the PTW chamber will be small and cannot be used to explain the 5% discrepancy. Since the PTW chamber is in excellent agreement with proton doses determined with calorimetry, we conclude that the 5% discrepancy is for the most part attributable to the polystyrene extrapolation chamber.

V.   Conclusions

The uncalibrated phantom-embedded extrapolation chamber design determines the absorbed dose-to-muscle to within 5% of standard calibrated Farmer-type ionization chamber for the 250 MeV proton therapy beam. More work is needed to determine the ion recombination characteristics of the PEEC exposed to proton beams before a meaningful comparison with standard techniques can be made. Uncertainties in the dosimetry of high-energy charged-particle therapy beams preclude accurate evaluation of the performance of the PEEC at this time, and further work will be required to elucidate the source of discrepancies between proton doses determined with the PEEC and Farmer chambers.

References

1. AAPM Task Group 20 of the Radiation Therapy Committee, "Protocol for heavy charged-particle therapy beam dosimetry," Report 16, AAPM (American Association of Physicists in Medicine) New York 1986.

2. S. Vynckier, D. E. Bonnett, and D. T. L. Jones, "Code of practice for clinical proton dosimetry," Radiother. Oncol. **20**, 53–63 (1991).

3. S. Vynckier, D. Bonnett, and D. Jones, "Supplement to the code of practice for clinical proton dosimetry," Radiother. Oncol. **32**, 174–179 (1994).

4. L. J. Verhey, A. M. Koehler, J. C. McDonald, M. Goiten, I. C. Ma, R. J. Schneider, and M. Wagner, "The determination if absorbed dose in a proton beam for the purposes of charged particle radiation therapy," Radiat. Res. **79**, 34–54 (1979).

5. M. Boutillon and A. M. Perroche, "Effect of a change of stopping-power values on the *W* value recommended by ICRU for electrons in dry air," Report CCEMRI(I)85–8, Bureau International des Poids et Mesures Sèvres 1985.

6. S. Vatnitsky, J. Seibers, D. Miller, M. Moyers, M. Schaefer, D. Jones, S. Vynckier, Y. Hayakawa, S. Delacroix, U. Isacsson, J. Medin, A. Kacperek, A. Lomax, A. Coray, H. Kluge, J. Heese, L. Verhey, I. Daftari, K. Gall, G. Lam, T. Beck, and G. Hartmann, "Proton dosimetry intercomparison," Radiother. Oncol. **41**, 169–177 (1996).

7. C. Zankowski and E. B. Podgorsak, "Ionization gradient chamber in absolute photon and electron dosimetry," Radiol. Oncol. (Slovenia) **30**, 138–141 (1996).

8. J. W. Boag, in *Radiation Dosimetry*, edited by F. H. Attix and W. C. Roesh, chapter 1

Academic Press New York 1966).

9.   F. H. Attix, "Determination of A_{ion} and P_{ion} in the new AAPM radiotherapy dosimetry protocol," Med. Phys. **11**, 714–716 (1984).

CHAPTER 10

Conclusions

I. Summary

The objective of radiation dosimetry is to determine the energy per unit mass imparted to a medium from directly or indirectly ionizing radiations. Currently, only three dose measurement techniques are considered as absolute, in that they do not require calibration in a known radiation field. In order of "absoluteness" these are calorimetry, chemical dosimetry, and free-air ionization chamber dosimetry. We propose to introduce a fourth absolute dosimetry technique based on the use of phantom-embedded extrapolation chambers, or PEECs.

The phantom-embedded extrapolation chamber (PEEC) is an uncalibrated, variable air-volume, parallel-plate ionization chamber which forms an integral part of a Solid-Water^{TM} phantom and may be used for the determination of absorbed dose in Solid-Water^{TM} phantoms. The unique design of the Solid-Water^{TM} PEEC allows for the direct measurement of the ionization gradient dQ/dm. This gradient can be substituted for the ratio of Q/m in the Spencer–Attix cavity relationship, obviating the requirement for calibration of the chamber in a known radiation field. In this regard, the PEEC can be considered an absolute ionization chamber equivalent in absoluteness to the free-air ionization chamber. Moreover, the PEEC is superior to the free-air ionization chamber in that it is relatively small, easily portable from one machine to another, and may be used

for calibration not only of all megavoltage photon and electron beams used in radiotherapy but also of proton beams. The design of the PEEC also eliminates or reduces many of the correction factors associated with the use of cylindrical Farmer-type chambers that are currently recommended by the AAPM–TG21 protocol for the calibration of high-energy photon and electron beams.

In current radiation dosimetry protocols initial recombination and diffusion loss are ignored and the collection efficiency is determined assuming that the approach to saturation for both continuous and pulsed beams is governed by general recombination. This approach can result in errors in the determination of the collection efficiency f^c for Farmer-type chambers in continuous beams on the order of 0.5%, irrespective of the dose rate. For parallel-plate ionization chambers, the error in the determination of Q_{sat} introduced by ignoring initial recombination and ion diffusion is a function of the electrode separation d, decreasing from ~3% to 0.1% as d is increased from 0.5 to 3.5 mm, respectively.

For Farmer chambers operated at moderate chamber potentials (*e.g.*, 150 V and above), charge multiplication affects the measured charge and should be accounted for. In parallel-plate chambers charge multiplication was observed for electric fields as low as 50 V/mm. Consequently, we suggest that chamber potentials be kept relatively low to avoid complications arising from the onset of charge multiplication in the chamber sensitive volume.

When the appropriate polarizing potential is used, and charge multiplication is accounted for, our extrapolation chamber meets its ultimate goal— the ability to measure the absorbed dose in phantom without requiring an exposure calibration in a known radiation field. Both in precision and accuracy, our uncalibrated phantom-embedded extrapolation chamber provides results that are comparable to those obtained

with calibrated ionization chambers. Measurements made with our uncalibrated PEEC and those made with calibrated Farmer-type ionization chambers agree to within ±0.5% for high-energy photon beams ranging from cobalt-60 gamma rays to 18 MV x rays and electron beams in the energy range from 6 to 22 MeV.

Thus, uncalibrated variable air-volume extrapolation chambers, built as an integral part of the phantom in which the dose is measured, can serve as radiation dosimeters in output calibrations of megavoltage photon and electron beams in radiotherapy and also of proton beams. The dosimetry with phantom-embedded extrapolation chambers is simple and does not require troublesome correction factors which account for chamber properties, for perturbation of the electron fluence, and for the unavailability of high energy photon and electron calibrations at standards laboratories.

Dose measurements with carefully designed and precisely built extrapolation chambers can be regarded as a practical alternative to other currently known dosimetry techniques for all clinical megavoltage photon and electron beams. The use of uncalibrated extrapolation chambers provides a simple means to either verify independently machine outputs measured with standard calibration techniques or to determine machine outputs directly when calibrated chambers are not available.

II.   Future work

Work is currently underway to automate many of the procedures necessary to operate the PEEC. A computer controlled step-motor is being designed to turn the micrometer screw so that changes in the electrode separation can be accurately controlled down to 10 μm. It is possible to transfer the control of the electrometer and power supply to an external computer. A program can be written to unite the three systems (step-

motor, electrometer reading, and power-supply) into one functional unit so that output calibration measurements with the PEEC can be performed in one step. Such an integrated measurement system would make the PEEC a very viable chamber for clinical use.

Already, we have fashioned from bone-equivalent phantom material electrode buttons which can be painted with graphite-dag for use in bone–tissue interface studies. With a thin entrance window made of bone-equivalent material, the absorbed dose near a Solid-Water^{TM}–bone interface can be measured. By making the bone-equivalent entrance window and collecting electrode button sufficiently thick, the PEEC will approximate a solid bone-equivalent phantom and direct measurement of the dose-to-bone can be made.

It might be possible to improve the dosimetry with the variable-volume extrapolation chamber by using mean restricted mass stopping power ratios for which the cutoff energy Δ corresponds to the actual electrode separation. Use of the appropriate restricted mass stopping power may extend the region in which the Bragg–Gray cavity conditions are satisfied. In principle, the mean restricted mass stopping powers in any material can be calculated if the electron spectrum is accurately known. The electron spectrum generated from any medical linear accelerator can, in principle, be calculated from Monte Carlo simulations. The transport of the radiation beams through a given medium can also be calculated using Monte Carlo methods, hence the electron spectrum at any depth in the medium can also be determined.

Several possibilities exist in the study of the relative contribution of general recombination, initial recombination, and ion diffusion to the overall charge loss in an ionization chamber. For such studies a more rigorous set of measurements than those described in this thesis could be performed with the goal of accurately determining the parameters α, β, and γ which characterize the effects of initial recombination and diffusion, general recombination, and charge multiplication in the chamber sensitive

volume. Moreover, by looking at the collected charge as a function of the electrode separation d for constant potential V, the effects of each of the three charge loss mechanisms of the measured signal should be resolvable, since each mechanism has a different dependence on d.

More work is needed to determine the ion recombination characteristics of the PEEC exposed to proton beams before a meaningful comparison with standard dosimetric techniques on proton beams can be made. Firstly, for a given electrode separation of the PEEC, a saturation curve must be measured so that the optimum polarizing potential in proton beams can be determined. Secondly, a detailed investigation of the chamber response as a function of the electrode separation should be made to establish the correct electrode separations to satisfy the Bragg–Gray conditions. In our measurements we assumed that the Bragg-Gray region in photon and electron beams corresponded to that in proton beams. However, the Bragg–Gray conditions in proton beams are satisfied by cavities of different dimensions than those in photon and electron beams.

Appendix A: List of Figures

222

FIGURE 7.1   A plot of $1/Q$ vs $1/V^2$ for saturation curve data measured with a 0.6 cm^3 thimble ionization chamber in a continuous beam of photons with an exposure rate of 160 R/min. Part (a) shows the full data set in the near saturation region where $0.7 \lesssim f < 1.0$. The dotted line represents a least-squares fit to the data indicated by open circles and results in $Q_{sat} = 33.76$ nC. Data within the shaded area of (a) for the near saturation region are shown on an expanded scale in (b). The solid line in (b) represents the curve fit of Eq. (7.6) to the data shown by open circles with $\alpha = 3.79 \times 10^{-3}$ V and $\beta = 2.57 \times 10^{-1}$ V^2, and provides a Q_{sat} of 33.88 nC. The data in the shaded region of (b) for the extreme near-saturation region are shown on an expanded scale in (c). The dotted line in (c) corresponds to the least-squares fit shown in (a). The dashed-dotted line represents the two-voltage technique [Eq. (5.18)] applied to data measured at 150 V and 300 V (identified by double circles) and results in $Q_{sat} = 34.01$ nC. . 157

FIGURE 7.2   A plot of the saturation curve data of Fig. 7.1(c) in the extreme near-saturation region in the form of $1/Q$ vs $1/V$. The dotted curve corresponds to the least-squares fit shown in Fig. 7.1(a). The solid curve corresponds the fit of Eq. (7.6) from Fig. 7.1(b). The dashed curve represents the curve fit of Eq. (7.7) with $\alpha = 3.71 \times 10^{-3}$ V, $\beta = 0.257$ V^2, and $\gamma = 1.2 \times 10^{-5}$ V^{-1}, accounting for both general and initial recombination, ion diffusion, as well as charge multiplication, and predicts that $Q_{sat} = 33.87$ nC. . . 161

Appendix B: List of Tables

Appendix C: Bibliography

AAPM Task Group 20 of the Radiation Therapy Committee, "Protocol for heavy charged-particle therapy beam dosimetry," Report 16, AAPM (American Association of Physicists in Medicine), New York, 1986, [200, 209].

AAPM Task Group 21 of the Radiation Therapy Committee, "A protocol for the determination of absorbed dose from high-energy photon and electron beams," Med. Phys. **10**, 741–771 (1983) [16, 89, 117, 121, 130, 137, 145, 158, 163, 185, 194].

A. T. G. . of the Radiation Therapy Committee, "Clinical electron-beam dosimetry," Med. Phys. **18**, 73–109 (1991) [16, 145, 185].

P. R. Almond, "Use of a Victoreen 500 electrometer to determine ionization chamber collection efficiencies," Med. Phys. **8**, 901–904 (1981) [116, 158, 163].

F. H. Attix, "Determination of A_{ion} and P_{ion} in the new AAPM radiotherapy dosimetry protocol," Med. Phys. **11**, 714–716 (1984) [116, 158, 163, 206].

F. H. Attix, *Introduction to Radiological Physics and Radiation Dosimetry* (John Wiley & Son, New York, 1986), [34–38, 40, 46, 52, 59, 110, 159, 189].

M. J. Berger and S. M. Seltzer, "Stopping powers and ranges of electrons and positrons,"

Report NBSIR 82-2451-A, National Bureau of Standards, Washington, D.C.,
1982, [100, 101].

M. J. Berger and S. M. Seltzer, "Stopping powers and ranges of electrons and positrons,"
Report NBSIR 82-2550-A, National Bureau of Standards, Washington, D.C.,
1983, [58].

H. A. Bethe, "Zur Theorie des Durchgangs schneller Korpuskularstrahlen durch
Materie," Ann. Physik 5, 325 (1930) [56].

H. A. Bethe, "Bremsformel für Elektronen relativistischer Geschwindigkeit," Z. Physik
76, 293 (1932) [56].

H. Bethe and W. Heitler, "On the stopping of fast particles and on the creation of
positive electrons," Proc. Roy. Soc. A. (London) 146, 83–112 (1934) [36].

J. W. Boag, "Ionization measurements at very high intensities I. Pulsed radiation beams,"
Br. J. Radiol. 23, 601–611 (1950) [111, 120, 143].

J. W. Boag, "The saturation curve for ionization measurements in pulsed radiation
beams," Br. J. Radiol. 25, 649–650 (1952) [111, 143].

J. W. Boag, in *Radiation Dosimetry*, edited by F. H. Attix and W. C. Roesh, Chapter 1
(Academic Press, New York, 1966), [98, 118, 187, 206].

J. W. Boag, in *The Dosimetry of Ionizing Radiation*, edited by K. R. Kase, B. E.
Bjärngard, and F. H. Attix, Volume 2, Chapter 3 (Academic Press, Orlando,

1987), [110, 111, 118, 121, 128, 143, 159].

J. W. Boag and J. Currant, "Current collection and ionic recombination in small cylindrical ionization chambers exposed to pulsed radiation," Br. J. Appl. Phys. **53**, 471–478 (1980) [116, 143, 158, 163].

J. W. Boag and T. Wilson, "The saturation curve at high ionization intensity," Br. J. Appl. Phys. **3**, 222–229 (1952) [111, 112].

J. Böhm, "Saturation corrections for plane parallel ionization chambers," Phys. Med. Biol. **21**, 754–759 (1976) [111, 121, 127, 148, 187].

J. Böhm and U. Schneider, "Review of extrapolation chamber measurements of beta rays and low energy x rays," Radiat. Prot. Dosim. **14**, 193–198 (1986) [186].

M. Boutillon and M. T. Niatel, "A study of a graphite cavity chamber for absolute exposure measurements of Co-60 gamma rays," Metrologica **9**, 139–146 (1973) [111, 121, 128].

M. Boutillon and A. M. Perroche, "Effect of a change of stopping-power values on the W value recommended by ICRU for electrons in dry air," Report CCEMRI(I)85-8, Bureau International des Poids et Mesures, Sèvres, 1985, [11, 80, 188, 200].

M. Boutillon and A. M. Perroche, "Re-evaluation of the w value for electrons in dry air," Phys. Med. Biol. **32**, 213–219 (1987) [80].

W. H. Bragg, "Consequences of the corpuscular hypothesis of the gamma and x rays,

and the ranges of beta rays," Phil. Mag. **20**, 385 (1910) [78].

W. H. Bragg, *Studies in Radioactivity* (Macmillan, New York, 1912), [16, 185].

A. Brahme and H. Svensson, "Specification of electron beam quality from the central-axis depth absorbed-dose distribution," Med. Phys. **3**, 95–102 (1976) [100].

E. H. S. Burhop, *The Auger Effect* (Cambridge University Press, England, 1952), [30].

C. Constantinou, F. Attix, and B. R. Paliwal, "A solid water phantom material for radiotherapy in x–ray and γ–ray beam calibrations," Med. Phys. **9**, 436–441 (1982) [135].

G. Ding and D. Rogers, "Mean energy, energy-range relationships and depth-scaling factors for clinical electron beams," Med. Phys. **23**, 361–376 (1996) [102].

R. D. Evans, *The Atomic Nucleus* (Krieger, Malabar, Florida, 1955), [34].

G. Failla, "Measurement of tissue dose in terms of the same unit for all ionizing radiations," Radiology **29**, 202–215 (1937) [186].

S. Genna and J. S. Laughlin, "Absolute calibration of a cobalt-60 gamma-ray beam," Radiology **65**, 394–405 (1955) [186].

L. H. Gray, "Absorption of penetrating radiation," Proc. R. Soc. A. (London) **122**, 647 (1929) [78].

L. H. Gray, "An ionization method for the absolute measurement of γ-ray energy," Proc. R. Soc. A. (London) **156**, 578–596 (1936) [16, 185].

J. R. Greening, "Saturation characteristics of parallel-plate ionization chambers," Phys. Med. Biol. **9**, 143–154 (1964) [55, 111, 115].

J. R. Greening, *Fundamentals of Radiation Dosimetry (Medical Physics Handbook 6)* (Adam Hilger Ltd., Bristol, Great Briton, 1981), [24].

E. J. Hall, *Radiobiology for the Radiologist* (Harper & Row, Maryland, 1973), [5].

A. K. Ho and B. R. Paliwal, "Stopping power and mass energy absorption coefficient ratios for Solid Water," Med. Phys. **13**, 403–404 (1986) [92, 135, 193, 194].

J. Hubbell, "Photon cross sections, attenuation coefficients from 10 keV to 100 GeV," Report NSRDS-NBS29, U.S. National Bureau of Standards, Washington, D.C., 1969, [34].

ICRU, "Radiation quantities and units," Report 19, International Commission on Radiation Units and Measurement, Bethesda, Maryland, 1971, [2].

ICRU, "Measurement of absorbed dose in a phantom irradiated by a single beam of x or gamma rays," Report 23, International Commission on Radiation Units and Measurement, Washington, D.C., 1973, [16, 184, 185].

ICRU, "Radiation quantities and units," Report 33, International Commission on Radiation Units and Measurement, Bethesda, Maryland, 1980, [11, 68, 69].

ICRU, "Radiation dosimetry: electron beams with energies between 1 and 50 MeV," Report 35, International Commission on Radiation Units and Measurement, Washington, D.C., 1984, [16, 59, 61, 185].

International Atomic Energy Agency (IAEA), "Absorbed dose determination in photon and electron beams; an international code of practice," Technical report 277, IAEA, Vienna, 1987, [185].

J. D. Jackson, *Classical Electrodynamics* (Wiley, New York, second edition, 1975), [53].

G. Jaffé, "On the theory of ionization in columns, I. (in German)," Ann. Physik (Leipzig) **42**, 303–344 (1913) [121].

G. Jaffé, "Collumnar ionization. (in French)," Le Radium **10**, 126–134 (1913) [121].

G. Jaffé, "On the theory of ionization in columns, II. (in German)," Ann. Physik (Leipzig) **1**, 977–1008 (1929) [121].

G. Jaffé, "On the theory of recombination," Phys. Rev. **58**, 968–976 (1940) [121].

P. N. Jeffery, J. W. Boag, and H. E. Johns, "Electron avalanche amplification in x-ray imaging devices," Phys. Med. Biol. **19**, 593–604 (1974) [110, 159].

K. Johansson, L. Mattson, L. Lindborg, and H. Svensson, Report SM-222/35, IAEA, Vienna, Austria, 1977, [99].

H. E. Johns and J. R. Cunningham, *The Physics of Radiology* (Charles C. Thomas,

Springfield, Illinois, 4th edition, 1983), [36, 40, 111].

W. R. Kanne and J. A. Bearden, "Collumnar ionization," Phys. Rev. **50**, 935–938 (1936) [122].

F. H. Khan, *The Physics of Radiation Therapy* (Williams and Wilkins, Maryland, second edition, 1992), [130].

O. Klein and Y. Nishina, Physik **52**, 853 (1929) [36].

S. C. Klevenhagen, "Determination of absorbed dose in high energy photon and electron radiation by means of an uncalibrated ionization chamber," Phys. Med. Biol. **36**, 239–253 (1991) [186].

P. Langevin, "Mesure de la valence des ions dans les gaz," Le Radium **10**, 113–124 (1913) [111, 123, 187].

D. Lea, "The theory of ionization measurements in gasses at high pressures," Proc. Cambridge Philos. Soc. **30**, 80–101 (1934) [121].

C. M. Lederer and V. S. Shirley, *Table of Isotopes* (Wiley-Interscience, New York, 7th edition, 1979), [30].

G. Lempert, R. Nath, and R. J. Shulz, "Fraction of ionization from electrons arising in the wall of an ionization chamber," Med. Phys. **10**, 1–3 (1983) [89].

M. S. Livingston and H. A. Bethe, "Nuclear physics," Rev. Mod. Phys. **9**, 245 (1937)

[56].

R. Loevinger, "Extrapolation chamber for the measurement of beta sources," Rev. Sci. Instrum. **24**, 907–914 (1953) [186].

R. Loevinger, C. Karzmark, and M. Weissbluth, Radiology **77**, 906 (1961) [101].

J. Manson, D. Verkly, J. A. Purdy, and G. D. Oliver, "Measurement of surface dose using build-up curves obtained with an extrapolation chamber," Radiology **115**, 473–474 (1975) [186].

P. Marmier and E. Sheldon, *Physics of Nuclei and Particles* Volume 1 (Academic Press, New York, 1969), [56].

G. Mie, "Der elektrische Strom in ionisierter Luft in einem ebenen Kondensator," Ann. Physik **13**, 857–889 (1904) [111, 112, 115, 187].

A. Muller, "On the behaviour of columnar ionization in pure gasses (in German)," Z. Physik **145**, 469–485 (1956) [122].

NACP, "Electron beams with mean energies at the phantom surface below 15 MeV," Acta Radiol. Oncol. Rad. Phys. **20**, 402–415 (1981) [100].

R. K. Pathria, *Statistical Mechanics* (Pergamon Press, Oxford, 1972), [127].

V. H. Ritz and F. H. Attix, "An ionization chamber for kilocalorie source calibrations," Radiat. Res. **16**, 401–415 (1962) [123].

RMI customer documentation, *Epoxy based phantom material*, Radiation Measurements Inc., Middleton, WI, 1986, [194].

D. W. O. Rogers, in *Advances in Radiation Oncology Physics*, edited by J. A. Purdy, pp. 181–223 (American Institute of Physics, Lawrence, Kansas, 1990), Proceedings of the AAPM 1990 summer school. [63, 104, 189].

D. W. O. Rogers, in *Teletherapy: present and future*, edited by T. R. Mackie and J. R. Palta, pp. 319–356 (Advanced Medical Publishing, Madison, Wisconsin, 1996), Proceedings of the AAPM 1996 summer school. [17].

D. W. O. Rogers and A. F. Bielajew, "Differences in electron depth-dose curves calculated with EGS and ETRAN and improved energy-range relationships," Med. Phys. **13**, 687–691 (1986) [100].

P. B. Scott and J. R. Greening, "The determination of saturation currents in free-air ionization chambers by extrapolation methods," Phys. Med. Biol. **8**, 51–57 (1963) [111, 121, 123, 128, 187].

C. G. Soares, "Calibration of ophthalmic applicators at NIST: A revised approach," Med. Phys. **18**, 787–793 (1991) [186].

L. V. Spencer and F. H. Attix, "A theory of cavity ionization," Radiat. Res. **3**, 239–254 (1955) [16, 81, 108, 185].

R. L. Sproull, *Modern Physics* (Wiley & Sons, New York, second edition, 1956), [158].

241

R. M. Sternheimer, "The density effect for the ionization loss in various materials," Phys. Rev. **88**, 851–859 (1952) [59].

W. F. G. Swann, "Theory of energy loss of high energy particles," J. Franklin Inst. **226**, 598 (1938) [58].

J. S. Townsend, *Electricity in Gasses* (Clarendon Press, Oxford, 1915), [111].

E. L. Travis, *Primer of Medical Radiobiology* (Year Book Medical, Chicago, 1982), [5].

E. A. Uehling, "Penetration of heavy charged particles in matter," Annual Rev. Nucl. Sci. **4**, 315–350 (1954) [58].

S. Vatnitsky, J. Seibers, D. Miller, M. Moyers, M. Schaefer, D. Jones, S. Vynckier, Y. Hayakawa, S. Delacroix, U. Isacsson, J. Medin, A. Kacperek, A. Lomax, A. Coray, H. Kluge. J. Heese, L. Verhey, I. Daftari, K. Gall, G. Lam, T. Beck, and G. Hartmann, "Proton dosimetry intercomparison," Radiother. Oncol. **41**, 169–177 (1996) [200, 207].

L. J. Verhey, A. M. Koehler, J. C. McDonald, M. Goiten, I. C. Ma, R. J. Schneider, and M. Wagner, "The determination if absorbed dose in a proton beam for the purposes of charged particle radiation therapy," Radiat. Res. **79**, 34–54 (1979) [200].

S. Vynckier, D. Bonnett, and D. Jones, "Code of practice for clinical proton dosimetry," Radiother. Oncol. **20**, 53–63 (1991) [200].

S. Vynckier, D. Bonnett, and D. Jones, "Supplement to the code of practice for clinical proton dosimetry," Radiother. Oncol. **32**, 174–179 (1994) [200].

M. S. Weinhouse and J. A. Meli, "Determining P_{ion}, the correction factor for recombination losses in an ionization chamber," Med. Phys. **11**, 846–849 (1984) [116, 158, 163].

G. N. Whyte, *Principles of Radiation Dosimetry* (Wiley, New York, 1959), [23].

E. J. Williams, "The passage of α– and β–particles through matter and Born's theory of collisions," Proc. Roy. Soc. A (London) **135**, 108–142 (1932) [56].

H. Wyckoff and F. Attix, "Design of free-air ionization chambers," Handbook 64, National Bureau of Standards, Washington, DC, 1957, [12].

C. Zankowski and E. B. Podgorsak, "Ionization gradient chamber in absolute photon and electron dosimetry," Radiol. Oncol. (Slovenia) **30**, 138–141 (1996) [205].

C. Zankowski and E. B. Podgorsak, "Calibration of photon and electron beams with an extrapolation chamber," Med. Phys. **24**, 497–503 (1997) [192].

H. Zanstra, "A rapid method for determining the saturation current by the Jaffé theory of columnar ionization," Physica (Amsterdam) **2**, 817–824 (1935) [111, 121].